Effect of Parameter Variations on the Electromagnetic Response of a Metafilm Comprised of Resonant Elements

by

K. L. Kumley

B.S., University of Colorado, 2002

M.S., South Dakota School of Mines and Technology, 2005

A thesis submitted to the

Faculty of the Graduate School of the

University of Colorado in partial fulfillment

of the requirements for the degree of

Doctor of Philosophy

Department of Electrical, Computer, and Energy Engineering

2018

This thesis entitled:
Effect of Parameter Variations on the Electromagnetic Response of a Metafilm Comprised of Resonant Elements
written by K. L. Kumley
has been approved for the Department of Electrical, Computer, and Energy Engineering

Edward Kuester

Christopher Holloway

Date

The final copy of this thesis has been examined by the signatories, and we find that both the content and the form meet acceptable presentation standards of scholarly work in the above mentioned discipline.

Kumley, K. L. (Ph.D., Electrical Engineering)

Effect of Parameter Variations on the Electromagnetic Response of a Metafilm Comprised of Resonant Elements

Thesis directed by Prof. Edward Kuester

A metafilm is a 2-dimensional version of a metamaterial which consists of a single layer of resonators. The elements resonate with changes in frequency and are arranged periodically in an array. In this thesis, a theory describing the characteristics of arrays of resonant scatterers is thoroughly developed using analytical techniques (which have the advantages of providing physical insight and being computationally inexpensive) and demonstrated by numerical analysis. The analysis is based on a dipole interaction model, and is validated using independent full-wave numerical simulations. The technique derived in this work, the interaction polarizability approximation, takes into account variations in the parameters of the elements in such a way that it can accurately predict both weak and strong coupling. For a metafilm, this leads to expressions for reflection and transmission coefficients that correctly predict the existence of Fano bands. Experimental measurements are carried out that confirm the existence of Fano resonances for a metafilm mounted in a waveguide, bearing out the practical significance of the predictions of this thesis. This thesis demonstrates that the Fano bands, or regions of rapid asymmetric frequency variation in an otherwise smooth curve, are not simply the result of measurement errors but are in fact an inherent behavior for a metafilm, one that simply results from manufacturing errors that cause variations in parameters that affect resonant behavior.

Dedication

My adorable children Franchesca and Fiona and my handsome husband Matthew.

Acknowledgements

My thesis advisor Professor Edward Kuester, whose incredible patience, tutelage, and mentorship has allowed me to finally fulfill a scholarly quest. My quest began when I started noticing equations that describe some phenomenon in nature, whose details of origin were hidden, and I longed to understand the path that lead to such important equations that I'm so privileged to take for granted. I'm grateful to have finally taken that journey, with success thanks to my advisor.

Dr. Christopher Holloway, for making the time to not only serve on my committee, support my measurements at NIST, his collaboration with publications, but also took the time to review my thesis. Professor Zoya Popovic for giving me my start at CU and serving on my committee. Professor Dejan Filipovic for serving on my committee and providing equipment for measurements. Professor James Curry and Dr. Maxim Ignatenko for serving on my committee. Dr. Sung Kim, for his support of measurements performed at NIST and collaboration with publications.

Professor Rodger Ziemer and Professor Ramaswami Dandapni for their instruction and mentorship during my undergraduate years. Dr. Neil Chamberlain of NASA Jet Propulsion Lab, Dr. Mohammed D. Abouzahra of MIT Lincoln Labortory, Dr. Krishna Pande of Rockwell Collins, and Farzin Lalezari of First RF, for allowing me to work on interesting projects and their mentorship.

My marvelous children with their breathtaking distractions from this work. My husband and best friend Matt, who has shown immeasurable patience, love and support which have been invaluable. My parents and siblings for their unwavering love and encouragement.

Contents

Tables

Table

Figures

Figure

Chapter 1

Introduction

1.1 Metamaterials, Metasurfaces and Metafilms

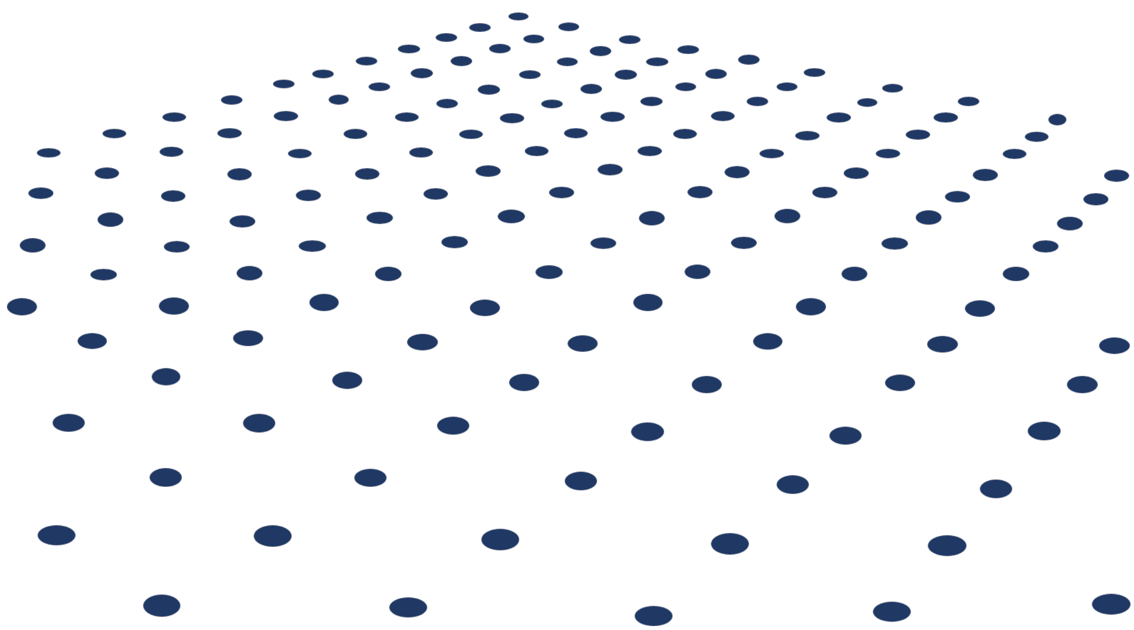

Figure 1.1: Depiction of a cermet topology metafilm: a 2D square array of elements of infinite extent.

The widely-used term metamaterial, generally describes materials that are designed to have some novel behavior or achieve ordinary behavior in a novel way. Topologies usually involve some sort of periodic pattern. To better understand the goal of metamaterials, one should consider what are classified as ordinary materials. Ordinary bulk materials consist of molecules and atoms that are very small compared to the wavelength of the field in the surrounding medium, and to the spacing between them. When a field is applied, on a microscopic level, the charges are stretched apart and become polarized, creating an induced field. The permittivity of the material is the macroscopic response of an applied electric field. When describing their electromagnetic behavior, some kind of effective medium theory can be used.

But, what if the atoms or molecules could be engineered? Might something new occur? Perhaps the engineered particles should become physically larger and polarized so that they can be designed to resonate as frequency changes, but remain small compared to a free space wavelength. This way they can still be modeled using some sort of effective medium theory that could characterize the material properties, such as an effective permittivity and permeability. This idea has added new degrees of freedom in designing new materials, which are currently referred to as metamaterials. Note that if the particles or the spacing between them became too large, on the order of wavelength, then their electromagnetic behavior would require Bragg theory and would exhibit properties more like antenna arrays.

There are many metamaterials currently being designed such as electromagnetic bandgap materials, negative index of refraction materials, nonlinear metamaterials, wire-mesh structures, and fishnet structures to name a few. Exciting applications have been explored such as a planar (perfect) lens, cloaking materials, extreme-impedance media, perfect conductor media, zero-index materials, doubly negative media, and perfect lens etc. [34], [49], and [51]. One metamaterial implementation that received a lot of attention is based on the split ring resonator [45].

One disadvantage of a metamaterial is its many layers. When a uniform field is applied to the material, each particle's resonances result in lost energy. Therefore, the more layers of planar arrays in the metamaterial, the more loss of the bulk material there will be. A simple solution to this problem might be to restrict the metamaterial to a single layer or one two-dimensional particle array. This surface array is an example of a metasurface.

One such metasurface is the two-dimensional equivalent of a "fishnet" topology called a metascreen [22]. One disadvantage of the metascreen is it has a lot more conductor and therefore more loss. Other topologies can yield metasurface behavior, such as a grating topology made of parallel conducting wires which performs as a metascreen in the direction parallel to the wires' axes and as a metafilm in the perpendicular direction [22]. More generally, "any periodic two-dimensional structure the thickness and periodicity of which are small compared to a wavelength in the surrounding media is a metasurface". Due to the stated restrictions, the next higher-order Floquet-Bloch mode won't propagate and a dispersive effective medium theory can be used to model the metasurface behavior [22].

A metafilm is a special subclass of a metasurface. It has been defined by Kuester et al. [28] as a "two-dimensional equivalent of metamaterial". It has a cermet topology, in which the elements remain disconnected and are sized and spaced small compared to the wavelength of the background medium.

An experimentally proven design of a metasurface is a fluid controllable surface [22]. The elements are periodically placed in a 2D lattice. Each element is a resonator with a capacitive gap in the center. A fluid channel is placed continuously across the gaps of the resonators. When the material properties of the fluid going through the channel changes, so does the resonant frequency of the element [22].

Another application where the use of a metasurface is advantageous over a metamaterial is the reduction of the size of a cavity. If a cavity is partially filled with a negative-index metamaterial, one could reduce the size of the cavity as done in [11] and [15]. Instead of a bulk metamaterial placed in the cavity, one could use a single layer or metasurface and reduce the size of the cavity even further [22].

1.2 Modeling Electromagnetic Behavior

When modeling a metamaterial, many numerical approaches are available. The advantage of a numerical code is the flexibility in the design. However, the more complicated the design, such as geometrically complicated resonators, the more computationally expensive they become to simulate. Additionally, key physical insights can be sometimes be overlooked. On the other hand, analytical models can give the most physical insight, at the expense of being restricted to a simpler element configuration and having some limitations on when they give accurate results. However, in many applications of electromagnetics, simple models are used to make predictions about more complicated designs. Decisions about how to pursue a design using a numerical modeling tool, can be crafted more carefully when they are based on the physical insight gained from understanding the simpler model, thus greatly reducing design efforts.

In general, analytical models of metamaterials, metasurfaces, and metafilms are based upon how large the elements are and how far apart they are spaced in comparison to the wavelength of the background medium. Figure 1.2 illustrates one way of classifying various approaches. Floquet-Bloch homogenization techniques are the most general but also the most complicated [54]. Multiscale homogenization techniques are also complicated to implement for many cases and requires the element spacing to be small compared to wavelength [3]. Dispersive effective medium theory places limits of element size and spacing but is more easily implemented [27]. Finally, classical effective medium theory is easy to implement, however the elements are limited to being nonresonant [8]. This work will utilize dispersive effective medium theory.

Analytical models of metasurfaces and metafilms have unique challenges compared to those of bulk materials since they are only two-dimensional. Consider the properties of a bulk material. A quantity that relates the polarization of the material as a response to an applied field is the volume susceptibility. It's a way to quantify how easily the bound charges of the material become displaced when a field is applied, and is a unitless quantity. However, the 2D equivalent or surface susceptibility has units of meters so it cannot be used in the same way. This is inconvenient, and two approaches to dealing with this have been considered. In one a person could assign a thickness to the film. In the other, boundary conditions can be applied so that an equivalent infinite sheet model can be used. As demonstrated by [22], the first approach does not fix the thickness of the film, and only the second one leads to a unique solution.

For example, Senior and Volakis have shown how a very thin layer of highly conducting non-magnetic material can be modeled by the resistivity of an equivalent impedance sheet [48]. If the layer resides in free space, the volume equivalence principle allows it to be replaced by an equivalent layer of polarization current. The researchers derive boundary conditions that lead to the resistivity equations. Their equations relate the macroscopic property of sheet impedance to the electric field by using a jump condition. The sheet impedance is a property that can be measured in a laboratory and verified.

This type of model can also be applied to the metafilm by replacing it with an infinitely thin sheet of polarization immersed in free space. We assume the scatterers are small compared to the wavelength of the background medium, the spacing is less than a quarter of that wavelength and they are not allowed to touch. Using these assumptions, Kuester et al. derived boundary conditions [28] called the generalized sheet transition conditions (GSTCs) that contained the surface susceptibilities as parameters, expressions for which were also derived. The surface susceptibilities are macroscopic properties that are related to the microscopic properties of the elements. Then in [20] Holloway et al. derived the plane-wave S-parameters, which can be used to measure the performance of a metafilm, in terms of the surface susceptibilities. These equations will be introduced in Chapter 4.

1.3 Fano Resonances

A Fano resonance (named after U. Fano's paper in 1961 [12]) is a sharp asymmetric peak that is the result of wave interference. Recently, publications (such as this review article [38]) focus on creating and controlling Fano resonances using particles in an array. There are many applications for Fano resonances, one that is attracting much attention is the use of nonlinear Fano resonances for the design of optimal bistable switching for nonlinear photonic crystals (e.g. optical transistors, switches and logic gates) [40]. In the optics community, some designs are chosen such that the scattering particles are chosen to comprise of two different shapes so that the fields of both are asymmetric with each other. This creates sharp asymmetric resonances. However, the work does not include the Fano resonances created due to small variations among the particles with the same shape. This thesis will demonstrate the existences of Fano resonances induced by scatterers that are nearly identical, how they come about in a metafilm, and how to control their sharpness.

In [50], (whose authors refer to their design as a metasurface) the design of a perfect lens is considered. It is designed so that the lattice spacing is on the order of one third to two thirds of a wavelengths. This leads to resonances that are due to lattice spacing, and occur for both periodic and aperiodic spacing. They only go so far as to note that for a region of frequency, multiple rapid variations in frequency occur due to the perturbed lattice. The resonances they found occur when the lattice constant is around a half wavelength, and so according to our definition the structure cannot be regarded as a metasurface, but is rather a photonic bandgap surface or frequency selective surface. Chapter 6 will demonstrate how the multiple rapid variations in frequency come about for a true metafilm, though the ideas certainly can be extended to a this type of metasurface.

Another similar example is that of a frequency selective surfaces (FSS). They are similar periodic arrays to those of metafilms, though the elements and spacing are larger in comparison to a wavelength. Again the lattice is on the order of a half wavelength, so the lattice resonates. In [16], Munk shows that if a FSS has two elements with different frequencies or different periods in spacing, resonances will occur in the reflection coefficient where it would otherwise had been smooth. We would call this a Fano resonance. Although the researchers didn't explore the matter further, this thesis will do so. For a metafilm, we will explain why Fano resonances occur, how they present themselves in arrays with multiple variations in resonant frequencies, how to model metafilms with any number of variations in resonant frequencies, demonstrate that these Fano resonances occur within specific bands of frequencies, and prove their existence from measurement results.

1.4 Thesis Overview

The scattering element used as the basis for most of the structures considered in this thesis is the dielectric sphere. This continuity will allow for conclusions between various chapters to be directly correlated. While this work can be extended to other scatterer shapes (as demonstrated in the experimental results of Chapter 7), the sphere is very convenient to work with analytically. It will be used for the isolated cluster pair studies of Chapter 3, as well as the metafilm studies in Chapters 4 and 6. It will be designed to resonate with changes in frequency such that it becomes polarized and exhibits dipole moment fields and remain small compared to the wavelength of the background medium. Chapter 2 will give the reader a good idea of what to expect from an isolated magnetodielectric sphere with dipole fields.

Chapter 3 considers the case of an isolated pair of scatterers that exhibits dipole modes. The field produced by the dipole moment induced in one scatterer by an incident field will induce an additional dipole moment in another. What are the implications of this? If the two elements are identical, the individual and total induced dipole moments are shown to exhibit one resonance with a wider bandwidth than that of a single element. If the scatterers differ in such a manner the resonant frequency of each is different, what will happen? If the variation is small enough, will the pair act as though they have the same properties? An analytical model that accounts for weak and small coupling will be derived and compared with other models, so that the details on how the pair interacts can be studied. We'll find that when they couple, they interact in such a way that one resonance becomes narrow, exhibiting Fano resonance properties.

In Chapter 4, analytical (GSTC) models from previous works will be used to investigate the case of a metafilm whose lattice has been perturbed. Instead of periodic spacing, the elements are now aperiodically spaced. This chapter will validate the analytical models with that of a commercially available finite element method software (*HFSS*). We will find that periodic spacing is a very good approximation for aperiodically placed elements, so long as they don't touch. It simply results in a slight shift in the reflection coefficient versus frequency plot, and no change in shape.

To take into account variations of the resonant frequencies of the elements of a metafilm, Chapter 5 derives the interaction dipole approximation equations (IPA) which are based on the quasi-static cluster pair equations of Chapter 3 and the GSTC's derived in previous works discussed in Chapter 4. Previous works used the average dipole approximation (APA) model [28]. Both are compared mathematically. The case of two resonant frequencies (as results from a checkerboard spacing) is examined, then the case of four different resonant frequencies, and finally a matrix equation for any number of varying resonant frequencies is derived.

The implications of the behavior of a dipole pair to that of a sheet of them (a metafilm) are examined next in Chapter 6. Both the APA and IPA models are compared with *HFSS*. For a sheet of identical resonators, the frequency response of the reflection and transmission coefficients will result in smooth lines and curves. However, when the elements of the metafilm have different resonant frequencies with small or large variations, the weak and strong coupling observed in Chapter 3 causes interference that manifests itself as a collection of sharp dips (Fano resonances) in an otherwise smooth curve. These dips appear in the frequency response of the S-parameters (reflection and transmission coefficients) near the individual element resonant frequency. This restricts the range of frequencies in which the Fano resonances will appear, which will be referred to as a Fano band. Outside the Fano band, the reflection and transmission coefficients have a smooth frequency dependence, like that of a uniform sheet. When modeling weak coupling, APA and IPA have very good agreement with *HFSS*. However for strong coupling only the IPA is proven to have excellent agreement with *HFSS*.

In chapter 7, measurements are performed on a metafilm comprised of dielectric cubes. Its behavior was predicted with HFSS and the S-parameters were shown to exhibit a Fano band when the parameters of the cubes that affect resonant frequency differ between elements. This was experimentally verified by using a PNA to measure the S-parameters of the metafilm placed in a waveguide, after performing a TRL calibration. The final chapter summarizes the contributions of the thesis, and indicates a number of future directions that research on this problem could take.

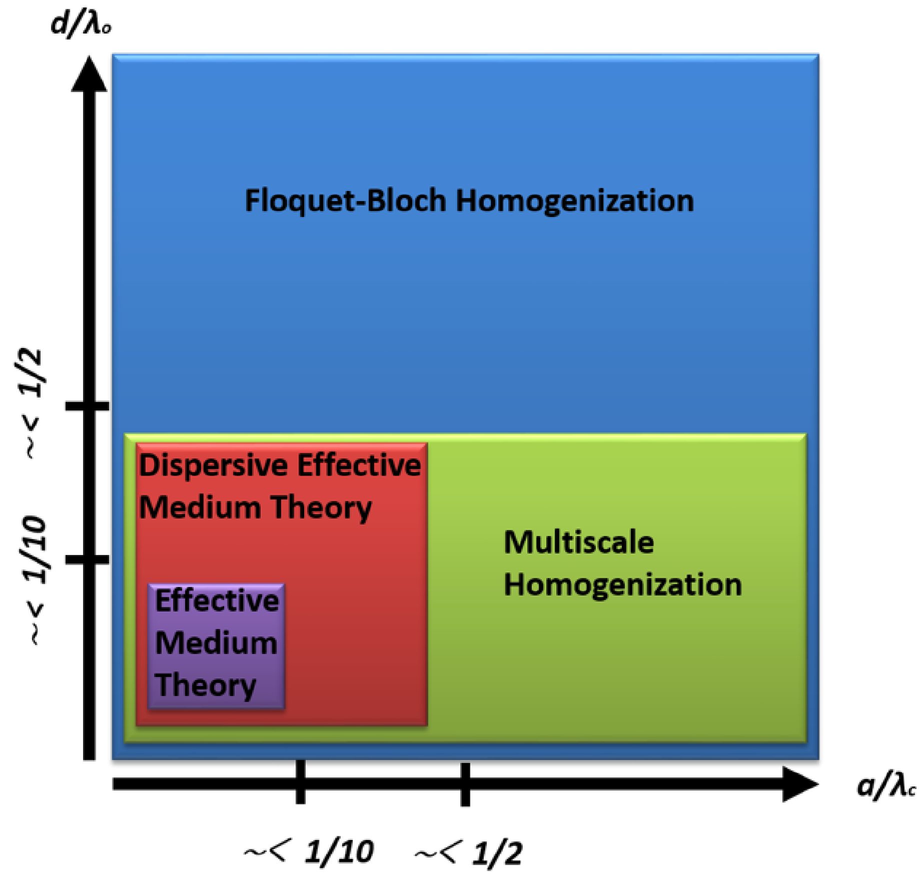

Figure 1.2: Plot of analytical models of 2D arrays by characteristic size a versus spacing d, normalized by wavelength.

Chapter 2

The Isolated Resonant Sphere Dipole Modes

2.1 Background

The scattering element of a metafilm must be large enough to resonate but small compared to a wavelength in the background medium. The magnetodielectric sphere is a very easy element to work with, when developing an analytical model for a metafilm. Equations that represent the frequency dependent polarizabilities have already been derived by Lewin [37]. The equations account for the dependence on frequency as well as the sphere's radius, permittivity, and permeability. The special properties the sphere possesses based on its highly symmetrical shape have been studied by Van Bladel [5] - [4]. The example of a high-permittivity dielectric sphere will be used extensively throughout this thesis. While this many not be the most practical shape to manufacture, the analysis of it will certainly provide useful insight into the fundamental behavior of other more practical elements. Here, previous work [37], [5], [4] will be utilized to study the behavior of the magnetodielectric sphere, the effects manufacturing errors will have, and the that effects material loss will have on resonance.

In 1975, Van Bladel [5] - [4] explored the analytically, the problem of a lossless dielectric resonator with high permittivity. He looked at the problem in two ways: one where the excitation is outside the resonator, and the other where the excitation is inside the resonator. In both cases he came to the same conclusion: that two types of modes can exist within the resonator, confined and nonconfined. All resonant modes of any generally shaped dielectric resonator that are nonconfined, except when a resonator has a high degree of rotational symmetry (such as a sphere). In that special case, the modes for which the normal component of the electric field is zero over the entire surface would be that of the confined type. Meaning they would remain confined to the interior region of the dielectric body and decay rapidly outside.

In [5] - [4], field equations we derived to determine how well the incident field couples with the modes of the resonator. They are given below: for nonconfined modes, equation (2.1) and for confined modes, equation (2.2). In these equations, the incident magnetic field is $\mathbf{H_i}$ and the magnetic field of the mode is $\mathbf{H_m}$. k is the operating wave number and k_m is the complex resonant wavenumber of the mode (which takes into account radiation losses). As k approaches k_m, then the factor $k^2/(k^2 - k_m^2)$ becomes large but radiation losses prevent it from actually reaching infinity.

Nonconfined modes:

$$\frac{k^2}{k^2 - k_m^2} \frac{\iint_S \psi_m(\mathbf{u_n} \cdot \mathbf{H_i})\, dS - \iiint_V \mathbf{H_i} \cdot \mathbf{H_m}, dV}{\iiint_{V+V'} |\mathbf{H_m}|^2, dV} \tag{2.1}$$

Confined modes:

$$-\frac{k^2}{k^2 - k_m^2} \frac{\iiint_V \mathbf{H_{i1}} \cdot \mathbf{H_m} dV - (1/R_0^2) \iint_S \phi_{0i} E'_{n1}, dS}{N \iiint_V |\mathbf{H_m}|^2, dV} \tag{2.2}$$

Next, the quality factor or Q of the resonator derived in [5] - [4], is shown in equations (2.3) - (2.4) for the nonconfined and confined modes respectively. Here N is the index of refraction. These equations indicate that modes of the confined type have a much higher Q than the nonconfined type. One can expect the confined type of modes to have sharper resonances, since their fields are highly confined to the inside of the sphere, than do the nonconfined type whose fields don't decay as quickly outside the resonator.

Nonconfined modes:

$$Q = \frac{N^3}{2k_m a} \tag{2.3}$$

Confined modes:

$$Q = \frac{N^5}{2k_m^3 a^3} \tag{2.4}$$

Later in the chapter, Van Bladel's conclusions will be extended to show that not only do confined modes exist for high dielectric spheres [5] - [4], but they are also present for a sphere with a high permeability or both a high permttivity and permeability.

The dynamic polarizabilities of a magnetodielectric sphere that are extensively used in this thesis, stem from Lewin's derivation for a three-dimensional material loaded with spherical particles [37]. They were based on Stratton's [55] (page 415) presentation of the work of Mie, Debye, and Sommerfeld work for a sphere, and made two assumptions: 1) The particle is electrically small compared with the wavelength in its background medium. In other words the radius of the sphere, a times the propagation constant of the background material k_0 must be small. 2) The spheres are far enough apart that coupling can be based on dipole interactions. With this simplification, one can use a small argument limit to derive a function called $F(\phi)$ as shown in equation (2.5) which is convenient for expressing the dynamic electric and magnetic polarizabilities.

$$F(\phi) = \frac{2(\sin\phi - \phi\cos\phi)}{(\phi^2 - 1)\sin\phi + \phi\cos\phi} \tag{2.5}$$

$$\phi = k_0 a \sqrt{\varepsilon_r \mu_r} \tag{2.6}$$

The variables ε_r and μ_r are the relative permittivity and permeability of the sphere, respectively.

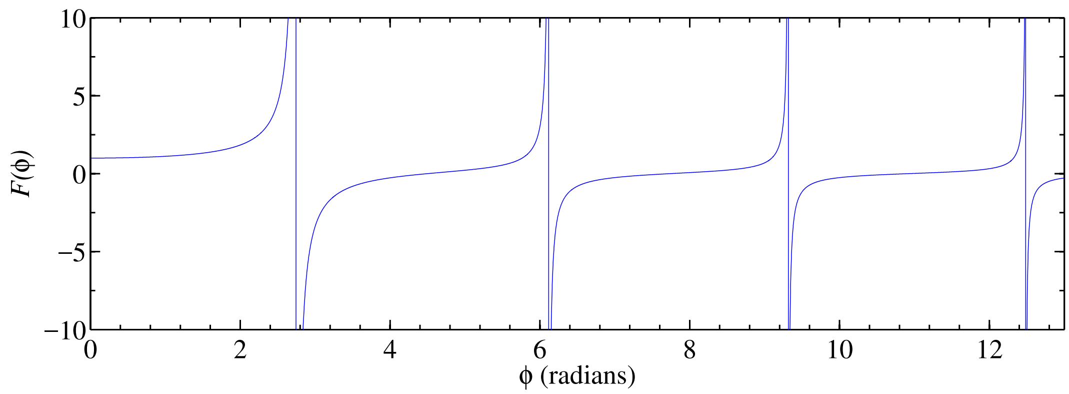

Figure 2.1: Plot of the function $F(\phi)$ vs. ϕ in radians. This function is used in the analytical equations for the electric polarizability, α_E and magnetic polarizability, α_M of a single sphere.

Lets take a moment to consider the behavior of the function $F(\phi)$ given in (2.5). This is an even unitless function of ϕ containing sines, cosines, and powers of ϕ. The variable ϕ is dependent on the following physical properties of the sphere: the radius a, relative permittivity ε_r, and relative permeability μ_r. To take into account variations with frequency, it is also dependent on the free space wavenumber $k_0 = 2\pi f\sqrt{\varepsilon_0\mu_0}$ with units of radians per meter. The function $F(\phi)$ is plotted in Figure 2.1. $F(\phi)$ behaves similarly to a tangent function. For small ϕ, $F(\phi)$ is approximately equal to one and primarily has a flat response until ϕ becomes large enough that the denominator becomes zero or infinite. These asymptotes occur when ϕ is approximately equal to multiples of π.

Based on Lewin's work [37], and later the work of Holloway *et al.* [20] Lewin's equations are written into a more explicit form, for the dynamic electric polarizability α_E and magnetic polarizability α_M of a single magneto-dielectric sphere or equations (2.7) and (2.8) respectively. They depend on the function $F(\phi)$, ε_r, μ_r, and the volume of the sphere $V = 4\pi a^3/3$:

$$\alpha_E = 3V\frac{F(\phi)\varepsilon_r - 1}{F(\phi)\varepsilon_r + 2} \qquad (\mathrm{m}^3) \tag{2.7}$$

$$\alpha_M = 3V\frac{F(\phi)\mu_r - 1}{F(\phi)\mu_r + 2} \qquad (\mathrm{m}^3) \tag{2.8}$$

Variations in the polarizabilities with frequency stem from their dependence upon $F(\phi)$. For the non-resonant case ($\phi \to 0$), $F(\phi) \to 1$ and static expressions for the polarizabilities hold. As frequency increases, for appropriate physical values, the spheres will resonate when the denominators of their expressions become zero. This occurs for α_E when $F(\phi) = -2/\varepsilon_r$ and for α_M when $F(\phi) = -2/\mu_r$. Only the electric and magnetic dipole moments are modeled here. Quadrapoles and other higher order multipoles can be accounted for by improving upon the expression of the function F by using an approach of Van Bladel [5] - [4], at the expense of a more complicated expression. Next, in order to further explore the behavior of equations (2.7) and (2.8), physical values will be assigned based on current material technology, for materials that are good candidates to be used as an element in a metafilm.

2.2 Behavior of the Lossless Sphere

Since the intended application for the resonator will be the metafilm, the scatterer will need to be electrically small compared to the surrounding medium ($k_0a \ll 1$), but large enough to resonate. To simplify the analysis, the surrounding medium will be free space and the sphere will be dielectric only ($\mu_{r0} = 1$). With current technology, a high dielectric material with loss tangents on the order of 10^{-4} [44], [43], and [42], have been achieved. As well as a quote from a paper in 1989 regarding a Trans-Tech material [25]. This applied to a relative permittivity, ε_{r0} close to 100. This is probably the best trade-off for current technology between a high dielectric constant and a low material loss tangent. Finally, a radius of $a_0 = 10$ mm was chosen, so that resonances will occur in the low microwave frequency range. These physical parameters will be used heavily through out the majority of this thesis. In what follows these values will be used to plot $F(\phi)$, α_E, α_M based on equations (2.5), (2.7) and (2.8) respectively. The lossless dielectric sphere will be considered first.

The Figure 2.2 is a plot of the real function $F(\phi)$, α_E/V, and α_M/V vs. frequency in a) and in b) the corresponding magnitudes. The frequency span of the graphs covers the first three asymptotes and resonances. In the static operating region, which occurs at very low frequencies, the sphere radius is electrically too small for resonance. Here $F(\phi)$, α_E/V and α_M/V all have nearly constant values, $F(\phi)$ and α_E/V are positive while α_M begins at zero.

As frequency increases, the spheres become electrically large enough that asymptotes occur for $F(\phi)$ at 1.3092, 2.9185, and 4.4453 GHz, and resonances occur for α_E and α_M. When $F(\phi) = -2/\varepsilon_r = -0.02$ as indicated on the graph by red circles, α_E resonates at 2.1228, 3.6495, and 5.1515 GHz. At $F(\phi) = -2/\mu_r = -2$ as shown by blue circles, then α_M goes through resonances at 1.4989, 2.9979, and 4.4969 GHz.

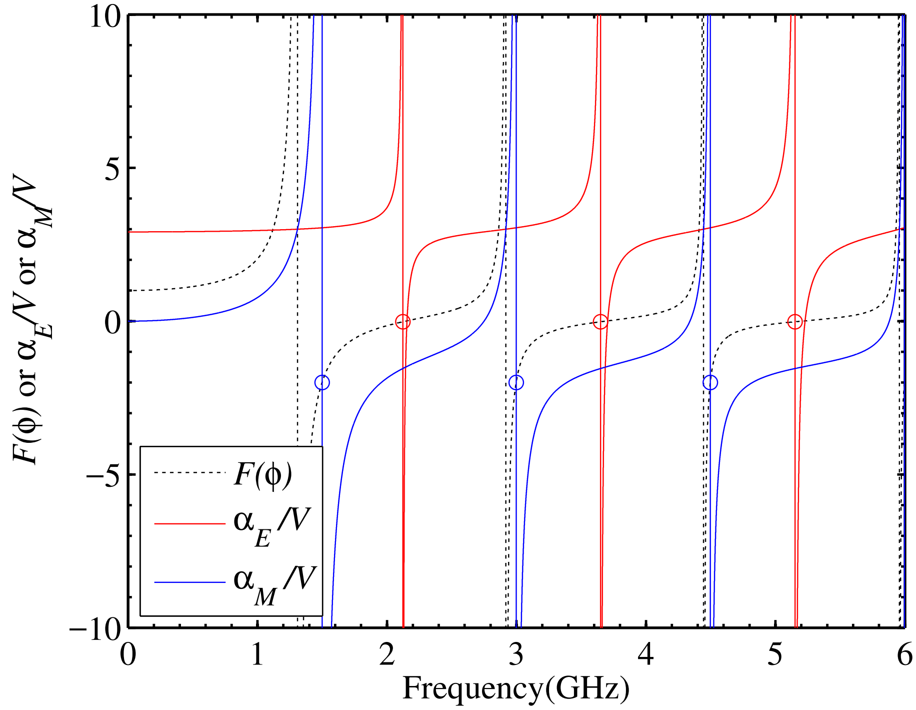

(a)

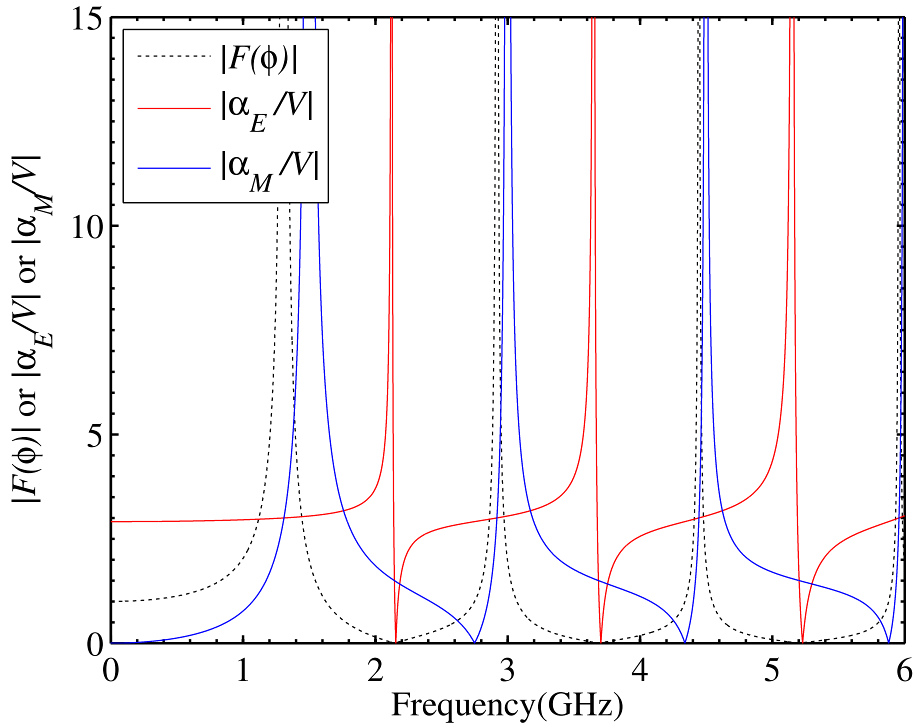

(b)

Figure 2.2: Plots of a) $F(\phi)$ (black dashes), α_E/V (red lines) and α_M/V (blue lines) and b) their respective absolute values versus frequency. The lossless sphere has $\varepsilon_{r0} = 100$, $\mu_{r0} = 1$ and, $a = 10$ mm.

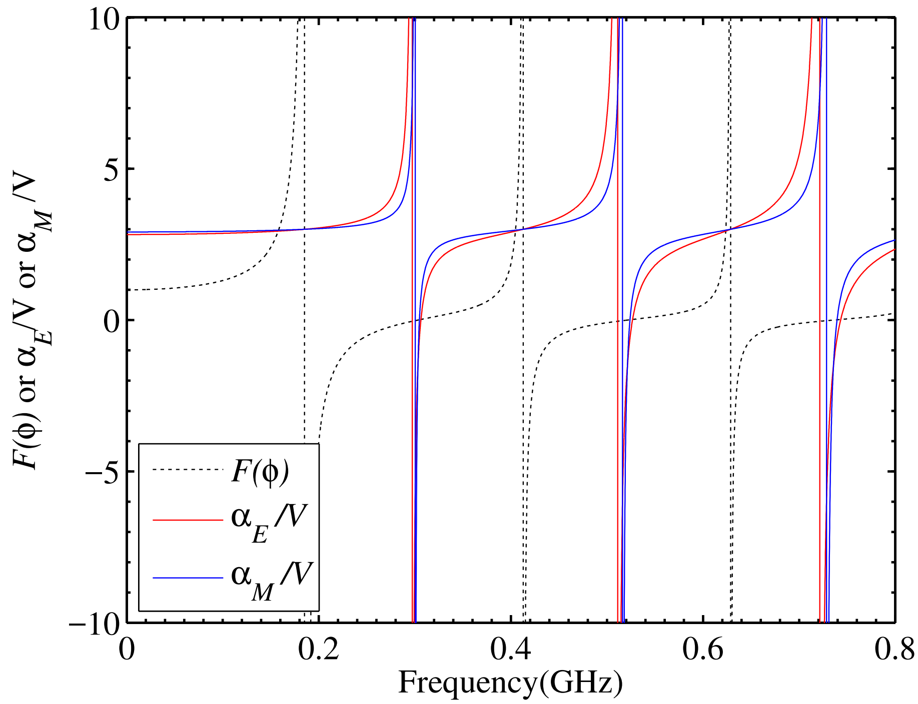

(a) $\varepsilon_{r0} = 100$, $\mu_r = 50$

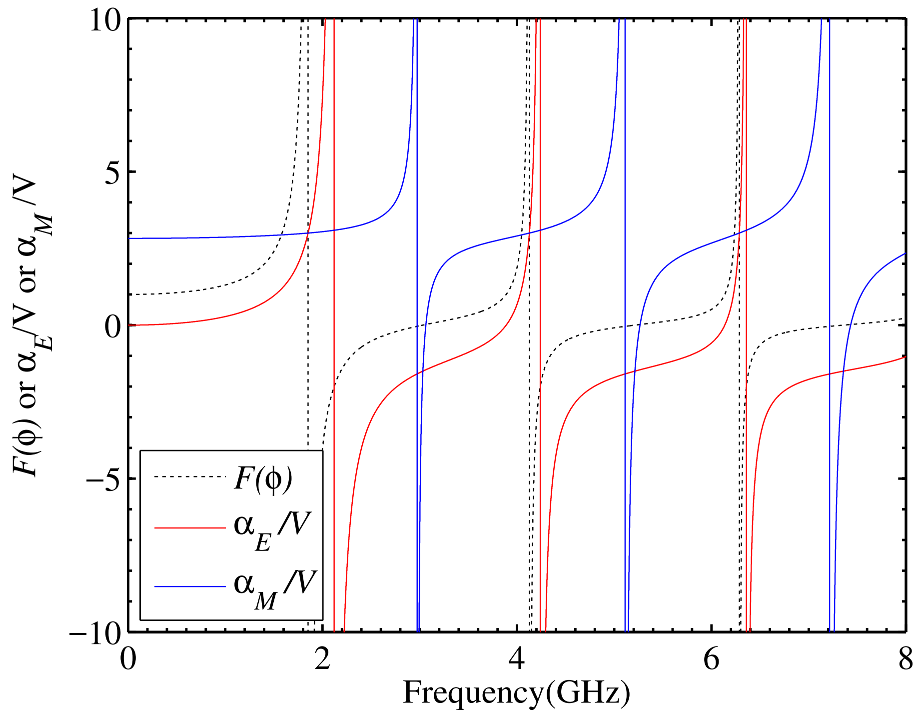

(b) $\varepsilon_r = 1$, $\mu_r = 50$

Figure 2.3: Plots of a) $F(\phi)$ (the black dashes), α_E/V (the red lines) and α_M/V (the blue lines) and b) their absolute values versus frequency. The lossless sphere has $a = 10$ mm, $\mu_r = 50$ and (a) $\varepsilon_{r0} = 100$ and (b) $\varepsilon_{r0} = 1$.

Note that the overall behaviors of the $F(\phi)$ and α_M/V are very similar. The resonances of α_M occur at slightly higher values of frequency than the asymptotes of $F(\phi)$. This means that α_M goes through a resonance when $F(\phi)$ has a rapidly increasing slope, as compared to α_E which goes through a resonance when $F(\phi)$ is nearly constant. The bandwidth of the resonances of α_M is fairly wide compared with those of α_E, whose bandwidth is sharper. For subsequent resonances, the bandwidth of α_M uniformly decreases while α_E has nearly the same bandwidth for all three resonances shown.

The plot of Figure 2.2 is for a high permittivity sphere with a low permeability. Based on the work of Van Bladel in [5] - [4], one can conclude that the sharpness of the electric polarizability resonance indicates it corresponds to a mode of the confined type, while the magnetic polarizability corresponds to a nonconfined mode. What if the permeability is increased to a high value such as 50? Now, the sphere would be magnetodielectric. Figure 2.3 a) illustrates what $F(\phi)$, α_E/V, and α_M/V would look like for the first three corresponding asymptotes and resonances. They are spaced closer together and at lower frequencies than for the dielectric sphere. Clearly both α_E/V, and α_M/V show confined type mode behavior. Now, if the permittivity is lowered to a value of 1, but the permeability is still 50. The behavior shown in Figure 2.3 b) occurs. The locations of the resonant frequencies are more spread out than for the dielectric and magnetodielectric sphere. For the magnetic sphere, α_M shows confined mode behavior, while α_E exhibits nonconfined mode behavior.

In conclusion, for small values of μ_r or ϵ_r, α_E and α_M will both resonate with nonconfined modes near the asymptotes of $F(\phi)$ where $F(\phi)$ varies rapidly, and therefore have a wide bandwidth that decreases with subsequent resonances. In the static region, α_E and α_M will be nearly or at zero value. For large values of μ_r or ϵ_r, α_M and α_E will have a confined type mode behavior and resonate away from the asymptotes where $F(\phi)$ is nearly constant. These resonances have a narrow bandwidth that remains approximately constant at subsequent resonances and have a positive initial value in the static region.

If the radius of the sphere is changed, the function $F(\phi)$ and the polarizabilities maintain their shape, but the locations of the resonant frequencies are shifted. If the radius of the sphere is larger, the resonances become closer together, while if the radius is smaller, the resonant frequencies are further apart. In the next section, the shift in resonant frequency will be quantified for a lossless sphere whose radius, permittivity, and permeability are varied by small amounts.

2.3 Effects of Variations in Radius and Material Parameters of a Lossless Sphere

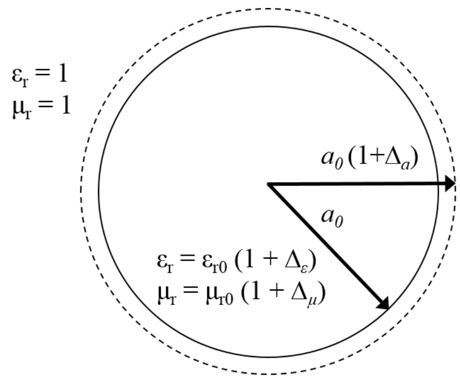

Figure 2.4: Illustration of a magneto-dielectric sphere with small variations in the physical parameters.

Now we consider the effects of small variations in the physical parameters of the sphere. Let a_0 represent the nominal value of the sphere's radius. In practice, manufactured spheres will undoubtedly have radii that are slightly different from the nominal value by some fraction we'll call Δ_a, as shown in Figure 2.4. Similarly, let ε_{ro} and μ_{ro} represent the nominal values of the permittivity and permeability that vary by fractions Δ_ε and Δ_μ respectively. Putting these slight variations into equations (2.6) and V, equations (2.9) and (2.10) become modified as follows:

$$\phi_\Delta = k_0 a_0(1+\Delta_a)\sqrt{\varepsilon_{r0}(1+\Delta_\varepsilon)\mu_{r0}(1+\Delta_\mu)} \tag{2.9}$$

$$V_\Delta = 4\pi a_0^3(1+\Delta_a^3)/3 \qquad (\mathrm{m}^3) \tag{2.10}$$

$$\alpha_E = 3V_\Delta \frac{F(\phi_\Delta)\varepsilon_{r0}(1+\Delta_\varepsilon)-1}{F(\phi_\Delta)\varepsilon_{r0}(1+\Delta_\varepsilon)+2} \qquad (\mathrm{m}^3) \tag{2.11}$$

$$\alpha_M = 3V_\Delta \frac{F(\phi_\Delta)\mu_{r0}(1+\Delta_\mu)-1}{F(\phi_\Delta)\mu_{r0}(1+\Delta_\mu)+2} \qquad (\mathrm{m}^3) \tag{2.12}$$

Looking at equations (2.7) and (2.8), the sphere's induced polaziabilities will have a nominal resonance at $F_0(\phi) = -2/\varepsilon_{r0}$ and $-2/\mu_{r0}$. However, when the physical parameters vary slightly (see equations (2.11) and (2.12)), resonances will occur at $F(\phi) = -2/(\varepsilon_{r0}(1+\Delta_\varepsilon))$ and $F(\phi) = -2/(\mu_{r0}(1+\Delta_\mu))$. Looking at equation (2.9) for ϕ, the radius appears as a mulitplicative term, whereas variations in permittivity and permeability occur under the square root sign. Therefore, it is expected that size variation will have a bigger fractional impact on the resonant frequency than variations in material properties.

Table 2.1: The resonant frequency values of the polarziability of an isolated dielectric sphere, as the permittivity and radius are varied by +/- 10%.

Polarizability α	Sphere Radius a_2 (mm)	Sphere Permittivity ϵ_r	Resonant Frequency f_r (GHz)	Shift in f_r (%)
α_E	$0.90a_0 = 9.0$	ε_{r0}	2.359	-11.1
α_E	$0.95a_0 = 9.5$	ε_{r0}	2.234	-5.2
α_E	$0.99a_0 = 9.9$	ε_{r0}	2.144	-1.0
α_E	$1.00a_0 = 10.0$	ε_{r0}	2.123	0
α_E	$1.01a_0 = 10.1$	ε_{r0}	2.102	1.0
α_E	$1.05a_0 = 10.5$	ε_{r0}	2.022	4.8
α_E	$1.10a_0 = 11.0$	ε_{r0}	1.930	9.1
α_E	a_0	$0.90\epsilon_{r0} = 90$	2.235	-5.3
α_E	a_0	$0.95\epsilon_{r0} = 95$	2.177	-2.5
α_E	a_0	$0.99\epsilon_{r0} = 99$	2.133	-0.5
α_E	a_0	$1.00\epsilon_{r0} = 100$	2.123	0
α_E	a_0	$1.01\epsilon_{r0} = 101$	2.112	0.5
α_E	a_0	$1.05\epsilon_{r0} = 105$	2.073	2.4
α_E	a_0	$1.10\epsilon_{r0} = 110$	2.026	4.6
α_M	$0.90a_0 = 9.0$	ε_{r0}	1.666	-11.1
α_M	$0.95a_0 = 9.5$	ε_{r0}	1.578	-5.3
α_M	$0.99a_0 = 9.9$	ε_{r0}	1.514	-1.0
α_M	$1.00a_0 = 10.0$	ε_{r0}	1.499	0
α_M	$1.01a_0 = 10.1$	ε_{r0}	1.484	1.0
α_M	$1.05a_0 = 10.5$	ε_{r0}	1.428	4.8
α_M	$1.10a_0 = 11.0$	ε_{r0}	1.363	9.1
α_M	a_0	$0.90\epsilon_{r0} = 90$	1.580	-5.4
α_M	a_0	$0.95\epsilon_{r0} = 95$	1.538	-2.6
α_M	a_0	$0.99\epsilon_{r0} = 99$	1.507	-0.5
α_M	a_0	$1.00\epsilon_{r0} = 100$	1.499	0
α_M	a_0	$1.01\epsilon_{r0} = 101$	1.492	0.5
α_M	a_0	$1.05\epsilon_{r0} = 105$	1.463	2.4
α_M	a_0	$1.10\epsilon_{r0} = 110$	1.429	4.7

Nominal values: $\varepsilon_{r0} = 100$, $\mu_{r0} = 1$, $a_0 = 10$mm.

Next, variations in the physical properties of the sphere versus changes in the resonant frequency of the polarizabilities of the sphere will be investigated. Again, a dielectric sphere in free space with the following nominal values: $\varepsilon_{r0} = 100$, $\mu_{r0} = 1$, $a_0 = 10$mm will be used. The radius and permittivity of the sphere will be varied up to +/- 10%. Table 2.1 demonstrates how these variations cause a shift in the resonant frequency.

Increases in radius and permittivity result in an upward shift in the resonant frequency of both the electric and magnetic polarizability, while a decrease in a and ε_{r0} results in downward shift in the resonant frequencies of the polarizabilities. The amount of variation in radius will result in a similar amount of shift the resonant frequency of the polarizability. On the other hand the amount of variation in the permittivity will result in half of that amount of shift in the resonant frequency of the polarizability. Therefore, the sphere is about two times more sensitive to variations in the radii than to variations in the permittivity.

2.4 Effects of Material Loss in the Dielectric Sphere

This section is devoted to the effects loss has on the dielectric sphere. It's expected that the resonances of the polarizabilities will be dampened. However, it will be illustrated that effect of material loss depends on whether the modes present are confined or nonconfined. This is very apparent when considering the first three resonances of the polarizabilities α_E/V, α_M/V. The first three asymptotes of $F(\phi)$ and first three resonances of α_E/V, α_M/V versus frequency will be plotted for three values of dielectric loss tangents, δ_t of 10^{-2}, 10^{-3}, and 10^{-4}.

First, consider $F(\phi)$ as shown in Figure 2.5. As expected, the asymptote in the amplitude plot, no longer continues to infinity but is truncated to a large but finite maximum value. The truncation is greatest for the highest values of material loss. As frequency increases, the maxima of the asymptotes are reduced even further. For example, when the material loss tangent of the sphere is 10^{-4}, the first asymptote at 1.3092 GHz has a high amplitude, but for the third asymptote at 4.4453 GHz, the amplitude is significantly reduced. The phase has a similar trend, but a much less dramatic one than the amplitude plots. The corners of the phase become more rounded as material loss and frequency increase. Overall, as loss and frequency increases, so does the reduction in amplitude and to a lesser extent the rounding of the phase.

Next, the magnitude and phase of the magnetic polarizability is plotted in Figure 2.6 versus frequency,

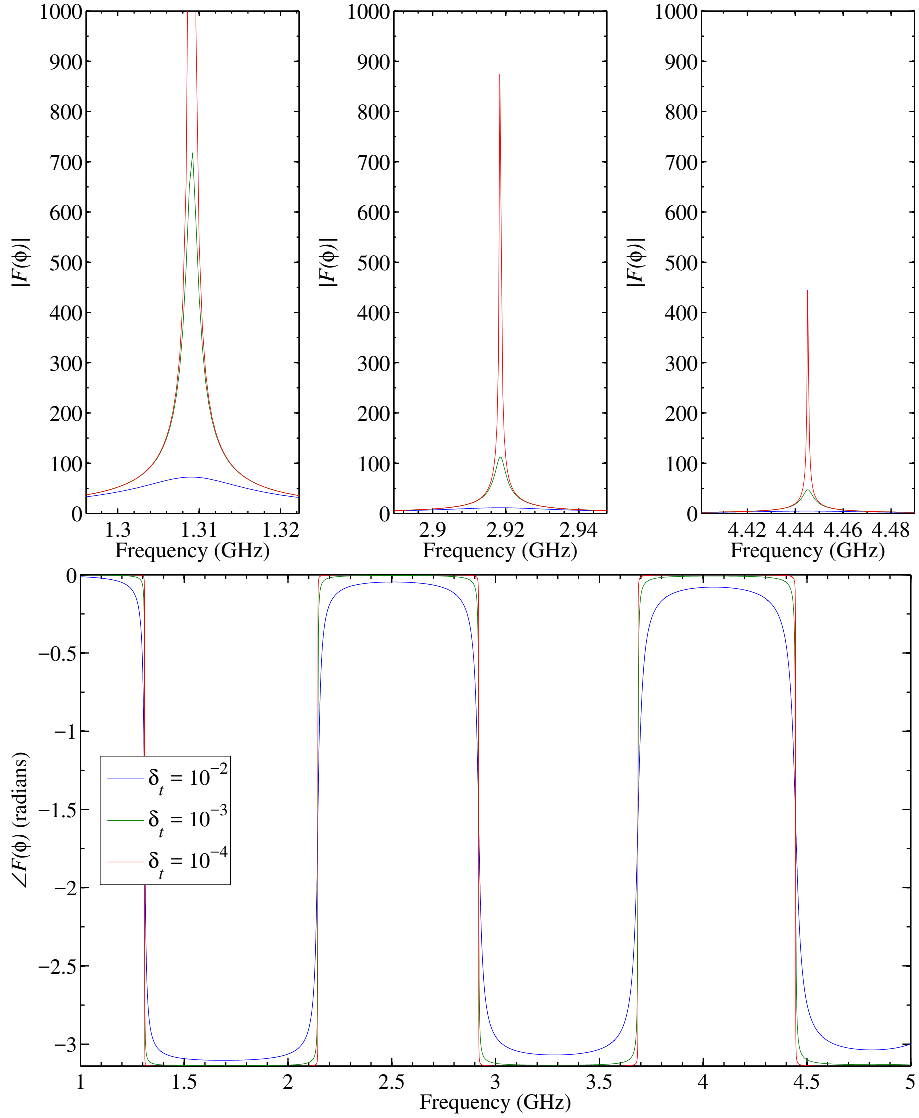

Figure 2.5: Plots of absolute value and phase of the function $F(\phi)$ vs. frequency of a sphere with a dielectric loss tangent δ_t when ε_{r0} = 100 - j100δ_t, μ_{r0} =1 and, a_0 = 10mm.

as material loss tangent varies. Recall that for a small permeability, the modes of α_M/V are of the nonconfined type. The amplitude of α_M/V has a similar trend as $F(\phi)$, in that the amplitude reduces as material loss and frequency increase. As frequency increases, the reduction in the amplitude of the resonances in most dramatic for δ_t of 10^{-2} and 10^{-3}. However, when δ_t is 10^{-4}, α_M maintains a very strong amplitude for the first three resonances shown. The phase of the magnetic polarizability also deviates less from zero at resonance as frequency and material loss increase, and again when δ_t is 10^{-4} the effects are very small.

In Figure 2.7, we illustrate how material loss effects the amplitude and phase of the electric polariz-

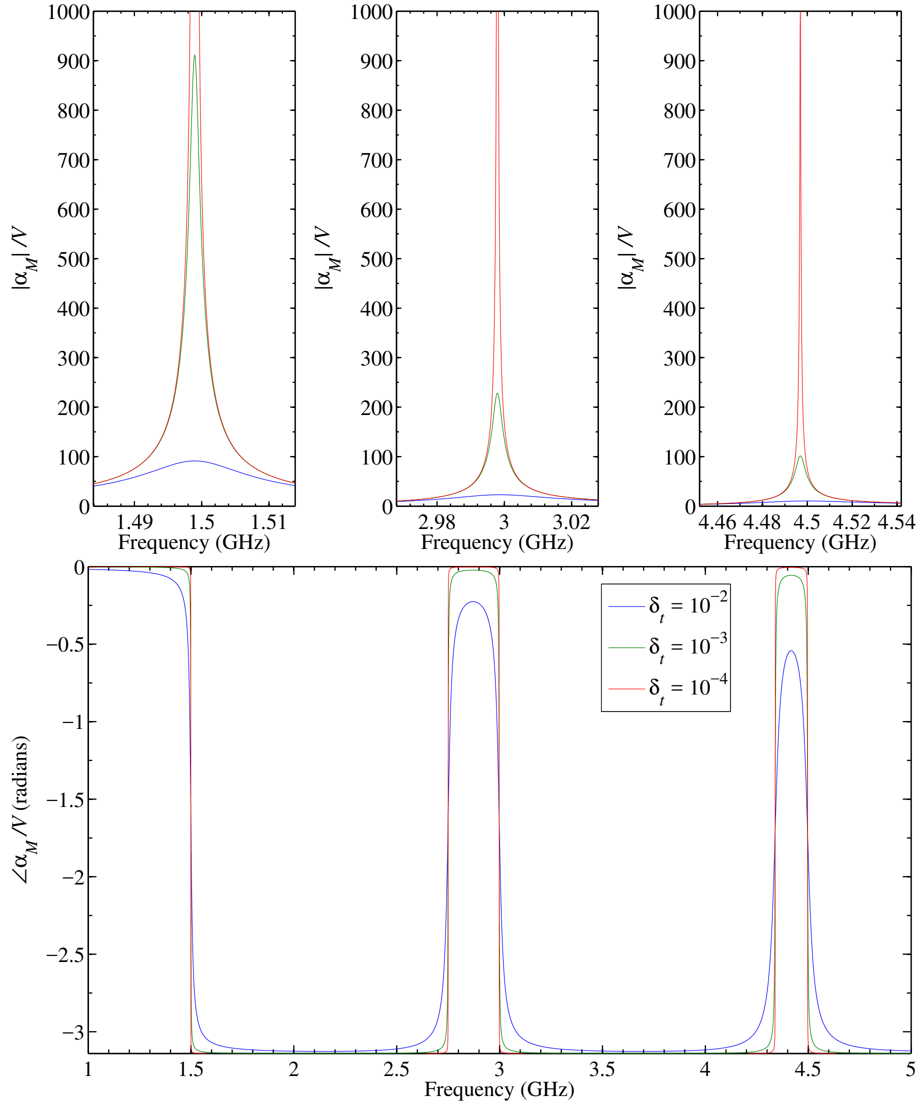

Figure 2.6: Plot of absolute value of magnetic polarizability α_M/V vs. frequency, for a lossy dielectric sphere with variations in dielectric loss tangent, δ_t when ε_{r0} = 100 - j100δ_t, μ_{r0} =1 and a_0 = 10mm.

ability over the same range of frequences as the previous plots of $F(\phi)$ in Figure 2.5 and α_M/V in Figure 2.6. Recall that since the sphere has a high dielectric constant, the modes affecting α_E will be confined. As material loss increases, at resonance the amplitude is reduced. However, the effect on α_E is more dramatic than that on α_M in Figure 2.6. This is to be expected for modes that are of the confined type, because the fields are more confined to the inside of the sphere where all the loss is and decay rapidly outside the sphere where the medium is lossless.

One interesting thing to note, the material loss for α_E is nearly the same for all three resonances

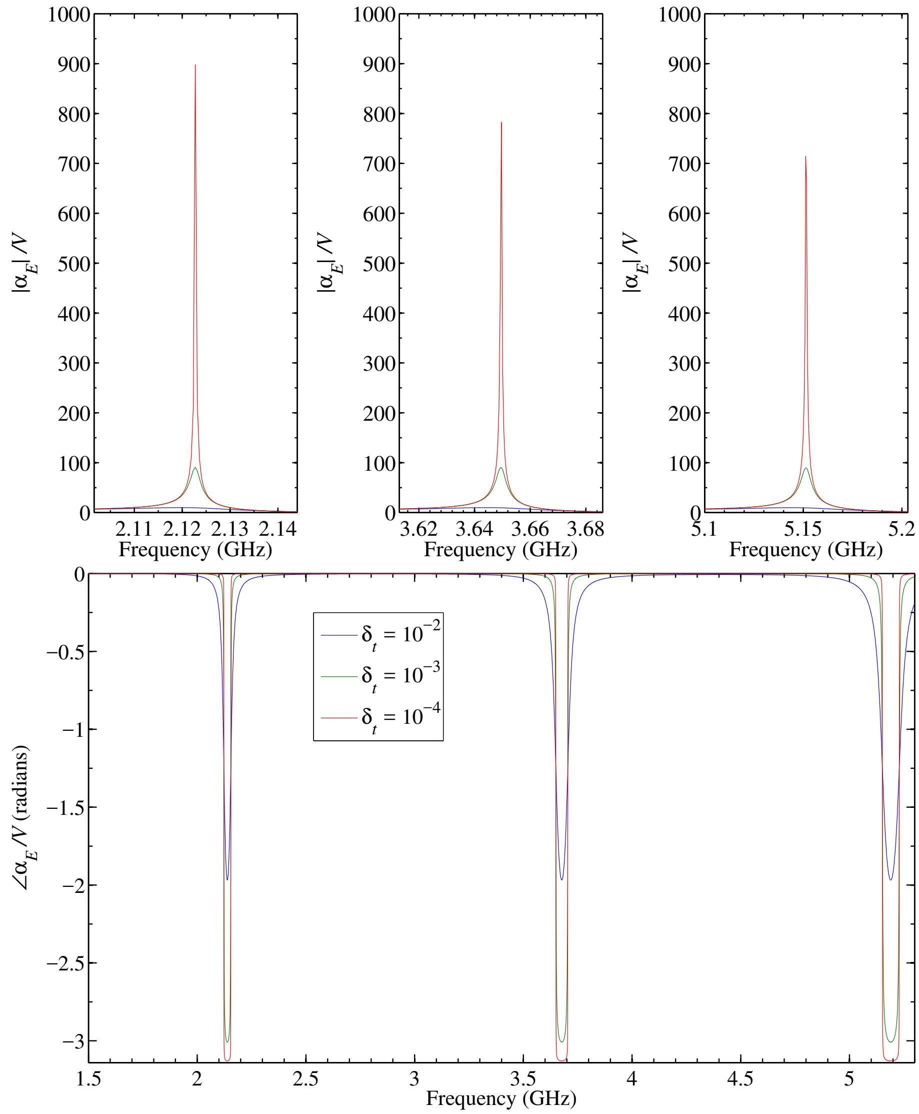

Figure 2.7: Plots of the absolute value of the magnitude and phase of the electric polarizability α_E/V versus frequency for a lossy dielectric sphere with varitions in dielectric loss tangent, δ_t when ε_{r0} = 100 - j100δ_t, μ_{r0} =1 and a_0 = 10mm.

plotted. In contrast, α_M and $F(\alpha)$ first three resonances are effected more strongly by loss as frequency increases.

2.5 Conclusion

This chapter thoroughly investigated magnetodielectric sphere dipole moment behavior, for the first three resonances. The examples in the following chapters will focus on the high permittivity nonmagnetic sphere. However, enough intuition should have been gained as a result of this chapter to extend the results of later chapters to other sphere designs. It was demonstrated, for physical values used throughout this thesis, that the dielectric sphere resonant frequency is the most sensitive to changes in radius. This will be a very important matter in the up coming chapters. Another important thing to note is that the sphere has high rotational symmetry that results in confined modes. For dipole moments that resonate with confined mode behavior, it will not couple easily with its neighbor. This is an important thing to note when studying the coupling between more than one scatterer.

Chapter 3

Cluster Pair of Polarizable Scatterers

3.1 Background

When any scatterer is manufactured, variations from the nominal physical values are unavoidable. These small variations will shift the resonate frequencies of the scatterer. Manufacturing imperfections will prevent a cluster pair of two scatterers designed to be identical, from actually being so; they will only be almost identical, and their resonant frequencies will be close but different. As a pair of nonidentical elements, how would the overall behavior of the pair be affected? Would they behave as though they are identical? If not, would the bandwidth of the resonance simply widen, or will something more complicated be going on? If so, are there any significant implications for a larger group of scatterers, such as those in a metafilm? In this chapter, two resonant scatterers will be treated as a cluster pair that coupled with each other. For the examples examined in this chapter, the physical parameters chosen for the scatterers can be comparable to elements of a metasurface. That way, in the next chapters, the ideas explored here can be extended to a metafilm.

In 1917, Silberstein [29], [30], and [31] attempted to model the interaction between two nonidentical molecules using classical physics. He found it "very remarkable" that Lorentz's additive law of optical refractivities (what we now call polarizabilities) holds, which is simply that, for example, a cluster of two molecules would have an total refractivity of $N = N_1 + N_2$, where N_1 and N_2 are the refractivities of the individual molecules. He challenged whether this simple law was sufficient for the case of nonidentical atoms. He used a Lorentzian frequency dependent model for N_1 and N_2 to derive expressions for the interaction between two nonidentical molecules:

Axial molecular refractivity (electric field along the axis between molecules):

$$N_a = \frac{N_1 + N_2 + 2sN_1N_2}{1 - s^2N_1N_2} \tag{3.1}$$

Transversal molecular refractivity (electric field perpendicular to the axis between molecules):

$$N_t = \frac{N_1 + N_2 + sN_1N_2}{1 - (1/4)s^2N_1N_2} \tag{3.2}$$

where $s = \alpha/(2\pi R^3)$.

He concluded that the terms including the resonant behaviors of N_1 and N_2 would have a considerable contribution. His model of atoms, disagrees with that of quantum physics, which was yet to be formulated at the time. In fact, he had looked at a pair of scalar isotropic dipole moments which are electrically polarized and nonidentical, where N_1 and N_2 are the polarizabilities of each dipole and N_a and N_t are the total polarizabilities pointing in two different directions. His assertion that the additional coupling terms involving N_1N_2 are significant, is correct near and at resonance. When the scatterers are designed to meet the conditions for a metafilm, the distance between them is small enough that they do couple with each other, one and or both are going through a resonance, and their resonant frequencies are close enough together that their fields couple. This will be demonstrated in this chapter.

Now, Silberstein's analysis handles the near field interaction in a static manner. Later, in 1999 Gadomskii and Voronov [13] also suspected the cluster pair deserves a nontrivial solution and re-derived the formulas for a pair of dipole moments also using the Lorentzian model in a much more rigorous manner. Their formulas do take into account the non-static near field interactions, therefore incorporating phase shifts and radiation losses. More details will be discussed later in the chapter.

In 1981 Collin [9] proved that the dipole interaction models, such as the one utilized by Gadomskii and Voronov, make assumptions that end up violating power conservation. Collin states that "In order to conserve power, the reaction of the radiation field back on the motion of the particle must be taken into account". He derives equations that could be incorporated into Gadomskii and Voronov work to correct this issue at the expense of complicating the equations further. These correction terms are only negligible when the particle is not resonating. Despite this, dipole interaction models are still useful in a qualitative way.

Therefore in the analysis section of this chapter, the dipole interaction model will be used without Collin's correction terms while keeping in mind that power is not strictly conserved.

In 1982 Van Bladel [6], considered the case of two identical resonators regarded as a coupled system. He considered that two scatterers brought into proximity with each other will exhibit two different modes: An even mode (when the dipole moments of both resonators point in the same direction), and an odd mode (when the directions of both resonators point in opposite directions). He concluded that both modes had different resonant frequencies. How these modes relate to the works of Silberstein [29], [30], and [31] and Gadomskii and Voronov [13] will be explored later in the chapter.

Now, lets reconsider the findings of Chapter 2. In 1975, Van Bladel in [5] - [4] classified two types of modes: Those that are nonconfined (which exist for arbitrarily shaped scatterers) and those are the confined type. Confined type modes have fields that are primarily confined to the scatterers interior, and rapidly decay outside the element. Van Bladel derived expressions demonstrating that confined modes have a much higher Q than the nonconfined type equations (2.3) - (2.4). When considering coupling, one can imagine the nonconfined type coupling more easily than the confined type.

Recent works on the isolated coupled pair include an eigenmode solution [57], for an asymmetric group of two and four [36] determines radar cross section and doesn't compare with any analytical models. A comparison can made by calculating the polarizabilities with [56].

In light of all these works, we ask what does happen to a pair of scatterers when the parameters that affect their resonance, cause their resonances to occur at nearly equal frequency points? Will this broaden the bandwidth, as is the case for the identical pair? Or does something more complicated happen? Answers to these questions will be explored in this chapter.

3.2 Quasi-static (QS) Dipole Approximation Model Derivation with Interaction Terms

The works of Silberstein, Gadomskii and Voronov both use a Lorentzian model to derive an expression for the interaction between two dipole moments. In this section, equations that generalize the polarizabilities beyond the Lorentzian model will be derived so that the polarizabilities can have any arbitrary frequency dependence.

The cluster pair refers to two scatterers placed in a medium. In this chapter they will be placed so that they are nontouching, but close enough together that the distance between them is considered small compared to the wavelength of the surrounding medium. The resonators will be designed to have an induced dipole moment when a uniform plane wave is impressed upon them. The dipole moment will be derived for three different orientations as illustrated in Figure 3.1. The coordinate system is oriented such that one dipole's center is placed at the origin and the other is placed along the positive y-axis.

The directions of the two dipole moments $\mathbf{p_1}$ and $\mathbf{p_2}$ will be collinear and directed along the direction of the electric field $\mathbf{E}$ that is orthogonal to the propagating wave vector $\mathbf{k}$. The separation distance between both dipole moments will be represented by the vector R_y with a magnitude of d. In Figure 3.1 Case I, the dipole moments point along the y-axis. The direction of the propagating wave will be in either the x- or z-direction. In Case II, Figure 3.1, $\mathbf{p_1}$ and $\mathbf{p_2}$, point along the x- or z- direction and direction of propagation will point orthogonally in the z- or x- directions. Lastly, in Figure 3.1 Case III, the dipole moments point along the x- or z- direction, while $\mathbf{k}$ points along the y- axis and will therefore experience a phase delay between the elements.

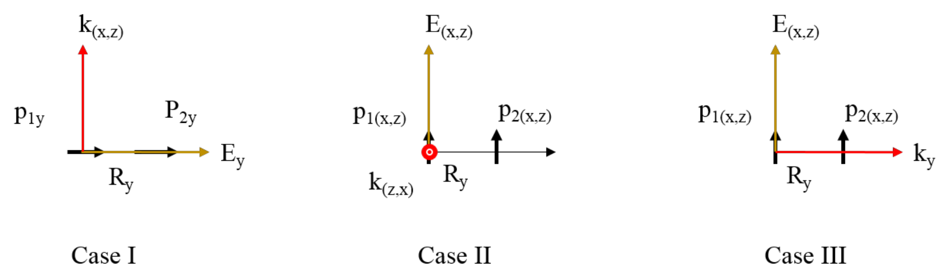

Figure 3.1: Cluster of a dipole pair with three different orientations. The pair is collinear along the y-axis. Case I: the propagation direction $\mathbf{k}$ of the the wave, is in the x- or z- direction and the electric field $\mathbf{E}$ and dipole moments $\mathbf{p_1}$ and $\mathbf{p_2}$ point along the y-axis. Case II: The direction of the propagating wave is in the z- or x- direction and $\mathbf{E}$, p_1, and p_2 point in the x- or z- direction. Case III: The direction of $\mathbf{k}$ is along the y-axis and the electric field and dipole moments point in either the x- or z- direction.

The static potential V of an electric dipole, is written in terms of the dipole moment as follows: $V = (\mathbf{p} \cdot \mathbf{r})/(4\pi\epsilon r^3)$. Here ϵ is the permittivity of the background medium, and $\mathbf{r}$ is the distance vector between the center of the dipole moment and the observation point. Then $\mathbf{E} = -\nabla V$ is used to express the static electric field due to a single dipole moment $\mathbf{p}$ as

$$\mathbf{E} = \frac{1}{4\pi\epsilon}[\frac{-\mathbf{p}}{r^3} + \frac{(\mathbf{p}\cdot\mathbf{r})3\mathbf{r}}{r^5}] \tag{3.3}$$

This formulation can be written more compactly as

$$\mathbf{E} = \frac{1}{4\pi\epsilon}\overleftrightarrow{\mathbf{T}}(\mathbf{r})\cdot\mathbf{p} \tag{3.4}$$

by utilizing a dyadic $\overleftrightarrow{\mathbf{T}}(\mathbf{r})$:

$$\overleftrightarrow{\mathbf{T}}(\mathbf{r}) = \frac{1}{r^3}[-\overleftrightarrow{\mathbf{1}} + 3\frac{\mathbf{rr}}{r^2}] \tag{3.5}$$

where the unit dyadic in the rectangular coordinate system is $\overleftrightarrow{\mathbf{1}} = \mathbf{a}_x\mathbf{a}_x + \mathbf{a}_y\mathbf{a}_y + \mathbf{a}_z\mathbf{a}_z$.

For a pair of dipoles, one will be placed at location a and the other at site b. Since the dipoles are placed collinearly, the distance vector between their centers is $\mathbf{r} = d\mathbf{a}_y$. Using equation (3.4), the electric field at site a due to the electric dipole moment at site b can be represented as

$$\mathbf{E}^{at\ site\ a} = \frac{I}{\epsilon}(C_x(\mathbf{a}_x\mathbf{a}_x + \mathbf{a}_z\mathbf{a}_z) + C_y\mathbf{a}_y\mathbf{a}_y)\cdot\mathbf{p_b} \tag{3.6}$$

Similarly the electric field at site b due to the dipole at site a is

$$\mathbf{E}^{at\ site\ b} = \frac{I}{\epsilon}(C_x(\mathbf{a}_x\mathbf{a}_x + \mathbf{a}_z\mathbf{a}_z) + C_y\mathbf{a}_y\mathbf{a}_y)\cdot\mathbf{p_a} \tag{3.7}$$

where the constants are defined as

$$I = \frac{1}{4\pi d^3},\ C_x = C_z = -1,\ C_y = 2 \tag{3.8}$$

Let the dyadic electric polarizability of the dipole be represented as the electric polarizability $\overleftrightarrow{\boldsymbol{\alpha}}_{\boldsymbol{E}}$ and defined by the equation:

$$\mathbf{p} = \epsilon\overleftrightarrow{\boldsymbol{\alpha}}_{\boldsymbol{E}}\cdot\mathbf{E}^{act} \tag{3.9}$$

Therefore, the polarizability of the dipole at site a can be defined by

$$\mathbf{p_a} = \epsilon\overleftrightarrow{\boldsymbol{\alpha}}_{\boldsymbol{Ea}}\cdot(\mathbf{E}^{at\ site\ a} + \mathbf{E}^{inc}) \tag{3.10}$$

and similarly for the dipole at site b by

$$\mathbf{p_b} = \epsilon\overleftrightarrow{\boldsymbol{\alpha}}_{\boldsymbol{Eb}}\cdot(\mathbf{E}^{at\ site\ b} + \mathbf{E}^{inc}) \tag{3.11}$$

To simplify the algebra, we will assume sufficient symmetry of the scatterers such that $\overleftrightarrow{\boldsymbol{\alpha}}_{\boldsymbol{Ea}} = \alpha_{Ea}\overleftrightarrow{\mathbf{1}}$ and $\overleftrightarrow{\boldsymbol{\alpha}}_{\boldsymbol{Eb}} = \alpha_{Eb}\overleftrightarrow{\mathbf{1}}$. This will restrict the scatterers to a simple shape, such as spheres or cubes.

Now, only consider the y-component

$$p_{ay} = \epsilon\alpha_{Ea}(E_y^{at\ site\ a} + E_y^{inc}) \tag{3.12}$$

$$p_{by} = \epsilon\alpha_{Eb}(E_y^{at\ site\ b} + E_y^{inc}) \tag{3.13}$$

Put equations (3.6) and (3.7) into equation (3.12) and (3.13)

$$p_{ay} = \alpha_{Ea}(IC_y p_{by} + \epsilon E_y^{inc}) \tag{3.14}$$

$$p_{by} = \alpha_{Eb}(IC_y p_{ay} + \epsilon E_y^{inc}) \tag{3.15}$$

and then solve for p_{ay} and p_{by}:

$$p_{ay} = p_{by}\frac{(\frac{1}{\alpha_{Eb}} + IC_y)}{(\frac{1}{\alpha_{Ea}} + IC_y)} \tag{3.16}$$

$$p_{by} = p_{ay}\frac{(\frac{1}{\alpha_{Ea}} + IC_y)}{(\frac{1}{\alpha_{Eb}} + IC_y)} \tag{3.17}$$

Putting equations (3.16) and (3.17) into (3.14) and (3.15) gives expressions for the induced dipole moments at sites a and b with respect to the polarizabilities and separation distance:

$$p_{ay} = \frac{\alpha_{Ea}(1 + \alpha_{Eb}IC_y)}{1 - \alpha_{Ea}\alpha_{Eb}I^2C_y^2}\epsilon E_y^{inc} \tag{3.18}$$

$$p_{by} = \frac{\alpha_{Eb}(1 + \alpha_{Ea}IC_y)}{1 - \alpha_{Ea}\alpha_{Eb}I^2C_y^2}\epsilon E_y^{inc} \tag{3.19}$$

These equations will be used to express the dipole moments for Case I from Figure 3.1. Similarly, for when the orientations of the dipole moments are perpendicular to the line between the dipole centers, as in Case II illustrated in Figure 3.1, the induced dipole moments are:

$$p_{ax} = \frac{\alpha_{Ea}(1 + \alpha_{Eb}IC_\beta)}{1 - \alpha_{Ea}\alpha_{Eb}I^2C_\beta^2}\epsilon E_x^{inc} \tag{3.20}$$

$$p_{bx} = \frac{\alpha_{Eb}(1 + \alpha_{Ea}IC_\beta)}{1 - \alpha_{Ea}\alpha_{Eb}I^2C_\beta^2}\epsilon E_x^{inc} \tag{3.21}$$

Therefore, equations for the total dipole moments of a cluster pair of dipoles based on a quasi-static approximation that takes into account the interactions between the pair is expressed in terms of their polarizabilities and separation distance take the forms:

Case I:

$$p_y^{QS} = p_{ay}^{QS} + p_{by}^{QS} = (\alpha_{Epair,I}^{QS})\epsilon E_y^{inc} \tag{3.22}$$

Case II:

$$p_x^{QS} = p_z^{QS} = p_{ax}^{QS} + p_{bx}^{QS} = (\alpha_{Epair,II}^{QS})\epsilon E_x^{inc} \tag{3.23}$$

The superscript of QS for "quasi-static" approximation will distinguish them from the two other approaches to be considered: AD and GV. The cluster pair polarizability for the dipole moments in the orientations of Case I, $\alpha_{pair,I}^{QS}$ and Case II, $\alpha_{pair,II}^{QS}$ are given below:

$$\alpha_{Epair,I}^{QS} = \frac{\alpha_{Ea} + \alpha_{Eb} + 2\alpha_{Ea}\alpha_{Eb} I C_y}{1 - \alpha_{Ea}\alpha_{Eb} I^2 C_y^2} \tag{3.24}$$

$$\alpha_{Epair,II}^{QS} = \frac{\alpha_{Ea} + \alpha_{Eb} + 2\alpha_{Ea}\alpha_{Eb} I C_x}{1 - \alpha_{Ea}\alpha_{Eb} I^2 C_x^2} \tag{3.25}$$

For dipoles orientated as shown in Case II and Case III, the expressions are identical. The equations (3.22), (3.23) are similar to Silberstein's Lorentzian model, given in equations (3.1) and (3.2) [31].

The coupling terms in the numerator of equation (3.24) are $2\alpha_{Ea}\alpha_{Eb}(1/4\pi d^3)C_y$ and in the denominator $\alpha_{Ea}\alpha_{Eb}(1/4\pi d^3)^2 C_y^2$. If, $d^3 \gg \sqrt{|\alpha_{Ea}\alpha_{Eb}|}$ holds, then the coupling terms become negligible and equations (3.24) and (3.25) simply become the sum of the two individual polarizabilities. Thus, when the particles are not resonating, the polarizabilities become small and the total dipole moment becomes approximately:

$$p^{AD} = (p_a^{AD} + p_b^{AD}) = (\alpha_{Epair}^{AD})\epsilon E_y^{inc} \tag{3.26}$$

where the cluster pair polarizability for the quasi-static additive approach is

$$\alpha_{Epair}^{AD} = (\alpha_{Ea} + \alpha_{Eb}) \tag{3.27}$$

The superscript AD used in equation (3.26), distinguish this quasi-static "additive" approach from other approaches in this chapter.

Similarly for the magnetic case, the quasi-static magnetic dipole moments with respective orientations are given as:

Case I:

$$m_y^{QS} = m_{ay}^{QS} + m_{by}^{QS} = (\alpha_{Mpair,I}^{QS})H_y^{inc} \tag{3.28}$$

Case II:

$$m_x^{QS} = m_z^{QS} = m_{ax}^{QS} + m_{bx}^{QS} = (\alpha_{Mpair,II}^{QS})H_x^{inc} \tag{3.29}$$

where the magnetic cluster pair polarizability for the magnetic dipole moments are:

$$\alpha_{Mpair,I}^{QS} = \frac{\alpha_{Ma} + \alpha_{Mb} + 2\alpha_{Ma}\alpha_{Mb}IC_y}{1 - \alpha_{Ma}\alpha_{Mb}I^2C_y^2} \tag{3.30}$$

$$\alpha_{Mpair,II}^{QS} = \frac{\alpha_{Ma} + \alpha_{Mb} + 2\alpha_{Ma}\alpha_{Mb}IC_x}{1 - \alpha_{Ma}\alpha_{Mb}I^2C_x^2} \tag{3.31}$$

Finally, for the quasi-static additive approach, the cluster pair magnetic dipole moments are

$$m^{AD} = (m_a^{AD} + m_b^{AD}) = (\alpha_{Mpair}^{AD})H_y^{inc} \tag{3.32}$$

where the magnetic polarizability for the quasi-static additive approach is

$$\alpha_{Mpair}^{AD} = (\alpha_{Ma} + \alpha_{Mb}) \tag{3.33}$$

3.2.1 Example: Pair of Dielectric Spheres Comparing the QS Model with the AD Model

In this section we compare, the total dipole moment quasi-static additive equation (3.26) will be compared with the quasi-static interaction equations (3.22) and (3.23) by assigning realistic physical parameter values to a pair of resonators. The pair will be dielectric spheres spaced 0.03 meters apart with a relative permittivity $\epsilon_r = 100$ each, placed in free space. The sphere's radius a and b, and the frequency dependent electric polarizabilities α_{Ea} and α_{Ea} will be calculated utilizing Lewin's equation (2.7). The main physical parameters of the dielectric sphere that affect the resonant frequency of the sphere are ϵ_r and the radius. In Chapter 2, it was demonstrated that sphere is more sensitive to changes in radius. We'll chose the radius of sphere b to be larger than sphere $a = 0.01m$ by a small percent.

At this juncture, only the magnitudes of the normalized electric dipole moments are plotted versus frequency. They are normalized such that $\epsilon E^{inc} = 1$ (i. e., they equal the polarizability). Dipoles oriented in the Case I direction are plotted in Figure 3.2, and for the Case II and Case III directions in Figure 3.3. The first column of the figures designated (a), (c) and (e) are plots calculated in Case I using equation (3.24) and for Case II using equation (3.25). The second column (b), (d) and (f) shows the results of the AD equation (3.26). Each row of the figures indicates a different amount of variance of the radii between the two spheres.

The radius of sphere b is larger than that of sphere a by 0.5% in plots (a) and (b), 0.2% in (c) and (d), and 0.1% in (e) and (f).

Immediately, one will notice that each plot of the normalized total dipole moment contains two resonances, and not simply one resonance with a wider bandwidth as an identical pair would have. Also, the two resonances are spaced a little further apart in the QS model than the AD model. As the radius of sphere b gets smaller and approaches that of a, the bandwidths of the resonances begin to overlap each other. The AD equations predict that their bandwidths remain the same, but maintains two distinct resonances. On the other hand, the QS model predicts the bandwidth of one resonance will become larger, while the other becomes narrower indicating a highly coupled system. Since the modes with electric dipole moment are confined (as defined by Van Bladel [5] - [4]) they cause the narrow resonance to become strong and sharp. The sharp resonance has been previously observed [24]. Sharp asymmetric peaks as a result of wave interference, are referred to as a Fano resonances named after U. Fano's paper in 1961 [12].

In case I, the Fano resonance appears in the second resonance, however in Case II the Fano resonance occurs in the first (lower frequency) resonance. Only the quasi-static model that includes interaction terms, treating the dipole pair as a coupled system, predicts the Fano resonance that occurs when the variations in the parameters that affect resonance are sufficiently small. On the other hand, AD predictions suggest something more complicated could be going on, completely missing the Fano resonance. In the next section, a full wave dipole interaction model derived by Gadomskii and Voronov [13] will be compared to the QS equations. They are also based on the Lorentzian model used by Silberstein, but are more rigorous since they take into account the near-field interaction more accurately.

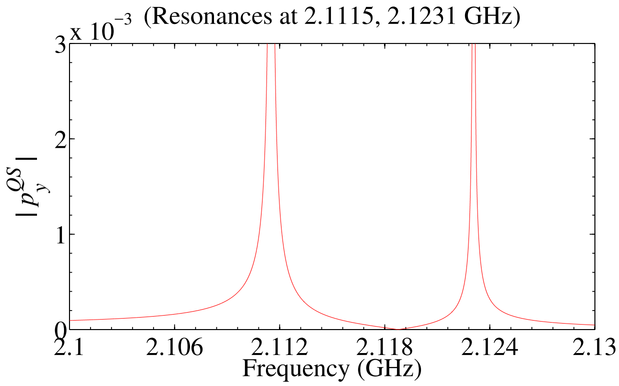

(a) Radius varies 0.5%

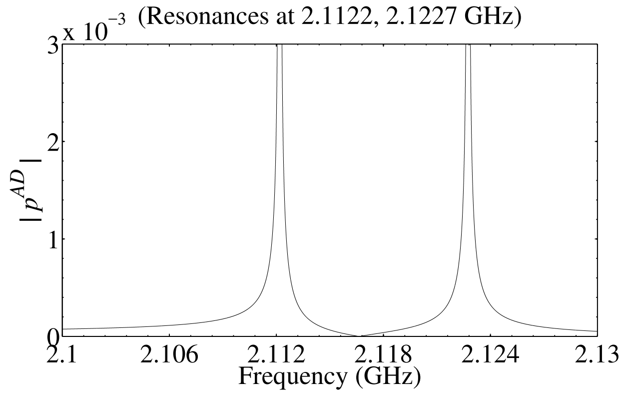

(b) Radius varies 0.5%

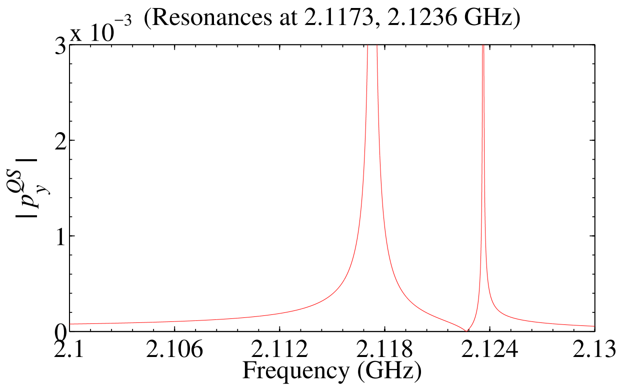

(c) Radius varies 0.2%

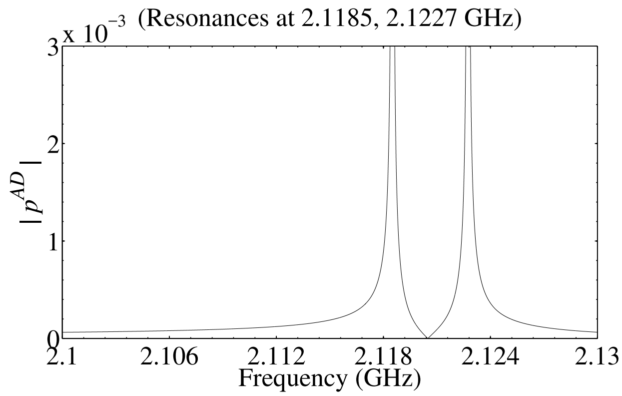

(d) Radius varies 0.2%

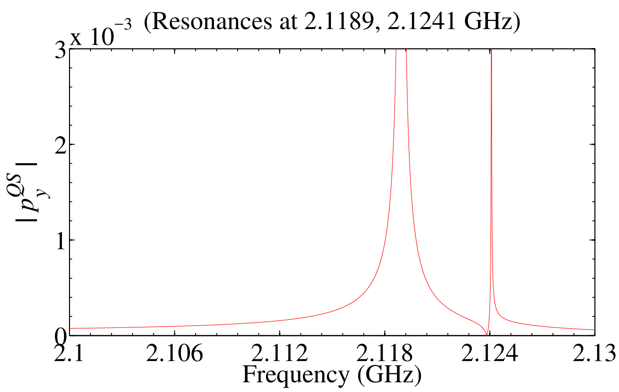

(e) Radius varies 0.1%

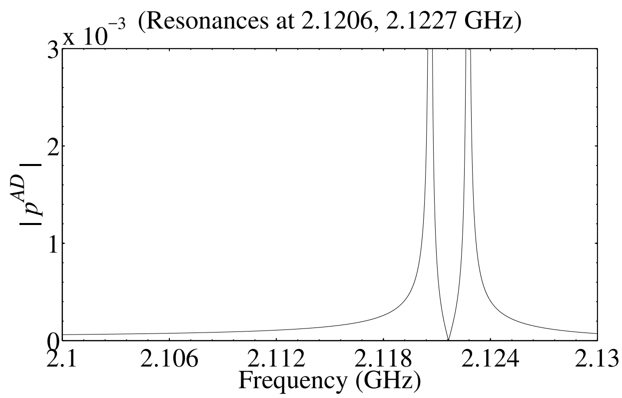

(f) Radius varies 0.1%

Figure 3.2: Pair of dielectric spheres: Case I orientation, spacing 0.03 m, $\epsilon_r = 100$, and lossless. The radius of a is 0.01 m, where b is larger by (a) - (b) 0.5%, (c) - (d) 0.2%, and (e) - (f) 0.1%. Comparison of QS equation (red lines) used in (a), (c) and (e) versus AD equations (black lines) in (b), (d) and (f). Total dipole moments are normalized such that $\epsilon E^{inc} = 1$.

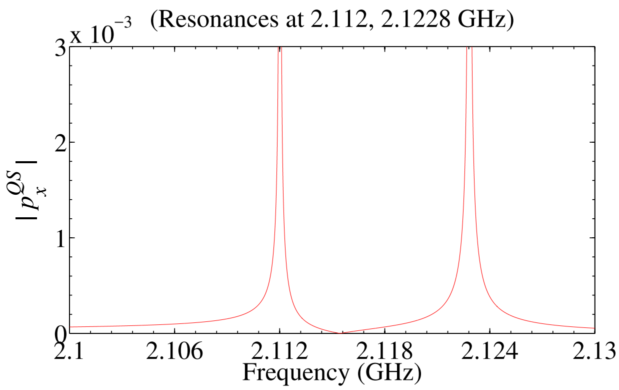

(a) Radius varies 0.5%

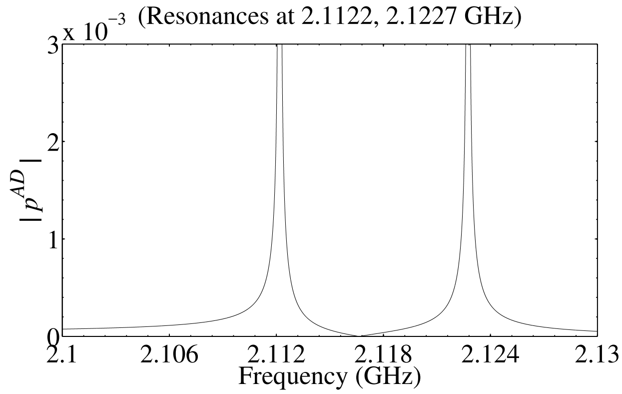

(b) Radius varies 0.5%

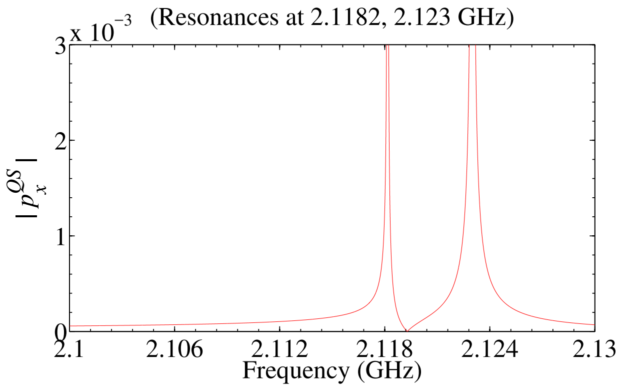

(c) Radius varies 0.2%

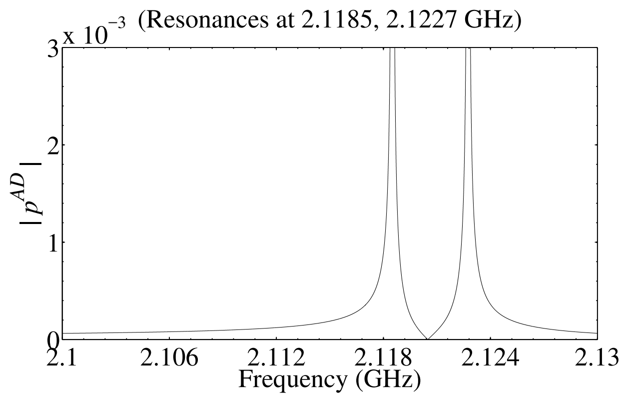

(d) Radius varies 0.2%

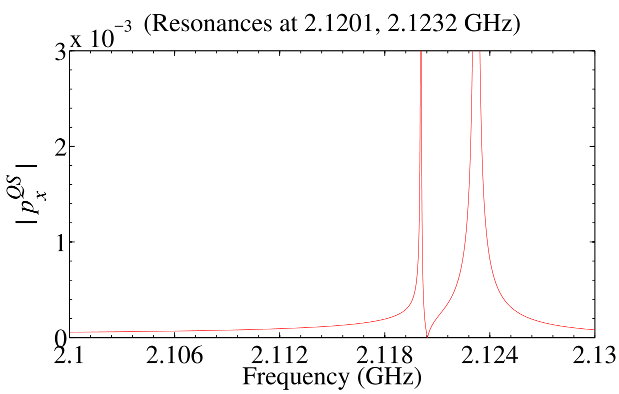

(e) Radius varies 0.1%

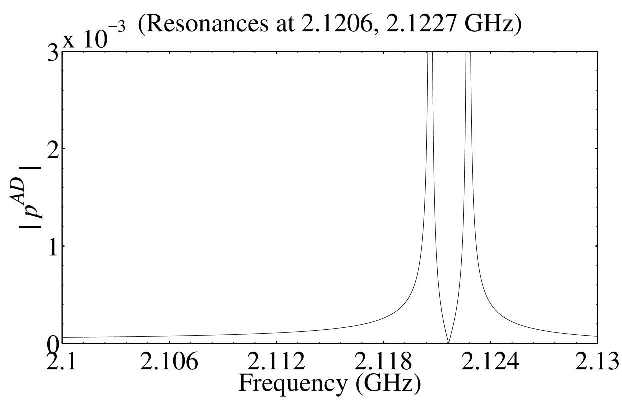

(f) Radius varies 0.1%

Figure 3.3: Pair of dielectric spheres: Case II orientation, spacing 0.03 m, $\epsilon_r = 100$, and lossless. The Radius of a is 0.01 m, where b is larger by (a) - (b) 0.5%, (c) - (d) 0.2%, and (e) - (f) 0.1%. Comparison of QS equation (red lines) used in (a), (c) and (e) versus AD equations (black lines) in (b), (d) and (f). Total dipole moments are normalized such that $\epsilon E^{inc} = 1$.

3.3 Full-wave Dipole Approximation GV Model compared with QS Model

A full-wave solution (in the dipole-interaction approximation) for the dipole moments of a pair of particles was derived by Gadomskii and Voronov in [13]. The model, like Silberstein's uses a Lorentzian function of frequency. The electric dipole moments are given below in SI units (using the notation of this chapter) in equations (3.34) - (3.37).

$$p_{ay}^{GV} = \alpha_{Ea} \frac{1 + 2\alpha_{Eb} G e^{-j(kd+\mathbf{k}\cdot\mathbf{r})}}{1 - 4\alpha_{Ea}\alpha_{Eb} G^2 e^{-j2kd}} \epsilon E_y^{inc} \tag{3.34}$$

$$p_{by}^{GV} = \alpha_{Eb} \frac{e^{-j\mathbf{k}\cdot\mathbf{r}} + 2\alpha_{Ea} G e^{-jkd}}{1 - 4\alpha_{Ea}\alpha_{Eb} G^2 e^{-j2kd}} \epsilon E_y^{inc} \tag{3.35}$$

$$p_{ax}^{GV} = \alpha_{Ea} \frac{1 - \alpha_{Eb} F e^{-j(kd+\mathbf{k}\cdot\mathbf{r})}}{1 - \alpha_{Ea}\alpha_{Eb} F^2 e^{-j2kd}} \epsilon E_x^{inc} \tag{3.36}$$

$$p_{bx}^{GV} = \alpha_{Eb} \frac{e^{-j\mathbf{k}\cdot\mathbf{r}} - \alpha_{Ea} F e^{-jkd}}{1 - \alpha_{Ea}\alpha_{Eb} F^2 e^{-j2kd}} \epsilon E_x^{inc} \tag{3.37}$$

where

$$G = \frac{1}{4\pi}\left(\frac{1}{d^3} + \frac{jk}{d^2}\right) \qquad (\mathrm{m}^{-3}) \tag{3.38}$$

$$F = G - \frac{k^2}{4\pi d} \qquad (\mathrm{m}^{-3}) \tag{3.39}$$

Equations (3.38) and (3.39) for G and F contain two types of fields according to Gadomskii and Voronov. The $1/R$ and $1/R^2$ terms refer to the retarded dipole fields and the term $1/R^3$ refers to the Coulomb fields. Notice that when only the Coulomb fields are taken into account, G and F reduce the GV equations (3.40) and (3.41) to the QS equations (3.22) and (3.23). This occurs when $kd \ll 1$.

Again, the dipoles are collinear along the y-axis. Note that x in equation (3.36) - (3.37) could be replaced by z to describe dipoles directed along the z- direction. The dipole orientations illustrated in Figure 3.1, can be modeled by equations (3.34) - (3.37). For Case I, $\mathbf{k}\cdot\mathbf{r} = 0$, and applying this simplification to equations (3.34) and (3.35) leads to equation (3.40) below. Case II is also realized when $\mathbf{k}\cdot\mathbf{r} = 0$, applies this to equations (3.36) and (3.37) leads to the total dipole moment equation (3.41). Lastly in Case III, the direction of propagation imparts a phase shift, $\mathbf{k}\cdot\mathbf{r} = kd$, and when applied to equations (3.36) and (3.37) leads to (3.42).

Case I:

$$p_y^{GV} = p_{ay}^{GV} + p_{by}^{GV} = (\alpha_{pair,I}^{GV})\epsilon E_y^{inc} \tag{3.40}$$

Case II:

$$p_x^{GV} = p_{ax}^{GV} + p_{bx}^{GV} = (\alpha_{pair,II}^{GV})\epsilon E_y^{inc} \tag{3.41}$$

Case III:

$$p_x^{GV} = p_{ax}^{GV} + p_{bx}^{GV} = (\alpha_{pair,III}^{GV})\epsilon E_y^{inc} \tag{3.42}$$

Therefore the full wave dipole moment cluster pair polarizability for dipole orientations for Cases I - III are respectively:

$$\alpha_{pair,I}^{GV} = \frac{\alpha_{Ea} + \alpha_{Eb} + 4\alpha_{Ea}\alpha_{Eb}Ge^{-jkd}}{1 - 4\alpha_{Ea}\alpha_{Eb}G^2e^{-j2kd}} \tag{3.43}$$

$$\alpha_{pair,II}^{GV} = \frac{\alpha_{Ea} + \alpha_{Eb} - 2\alpha_{Ea}\alpha_{Eb}Fe^{-jkd}}{1 - \alpha_{Ea}\alpha_{Eb}F^2e^{-j2kd}} \tag{3.44}$$

$$\alpha_{pair,III}^{GV} = \frac{\alpha_{Ea} + \alpha_{Eb}e^{-jkd} - \alpha_{Ea}\alpha_{Eb}Fe^{-jkd}(e^{-jkd} + 1)}{1 - \alpha_{Ea}\alpha_{Eb}F^2e^{-j2kd}} \tag{3.45}$$

In [33], another full-wave expression to that of Gadomskii and Voronov in [13] was derived using Green's tensor. Their work is for an arbitrary number of scatterers without studing the interactions of resonances. Next, both dipole interaction models will be assigned physical values for a direct comparison.

3.3.1 Example: Pair of Dielectric Spheres Comparing the QS Model with the GV Model

We again use a pair of dielectric spheres of permittivity of 100 each spaced 0.03 meters apart in free space, the radius of sphere $a = 0.01$ m and sphere b radius will vary by a small amount. Lewin's equations for a frequency dependent polarizability, equations (2.11) - (2.12) will be used. Small variations in radii and the sphere material loss tangent will be investigated using the two dipole moment interaction equations: the full wave model or GV equations (3.40) - (3.42) with the quasi-static approximation equations or the QS equations (3.22) and (3.23).

Figures 3.4 - 3.42 present a comprehensive comparison of the individual normalized dipole moments illustrated by their (a) magnitudes, (b) phases in radians, (c) Imaginary part, (d) real part, and similarly for the normalized total dipole moments (e) - (h). Again, the dipole moments are normalized such that $\epsilon E^{inc} = 1$. The main graphs will have the same frequency range for all plots, though the scales of the vertical axes are generally different. The insets will highlight the resonances, such that the frequency range will be shorter and center around a resonant frequency point. The results of the QS equations are shown in red and GV equations are shown in blue. (a) - (d) Are plots of the individual dipole moment of sphere a, p_a (straight line) and sphere b, p_b (dashed line) and (e) - (h) total dipole moments. Overall, there is good qualitative agreement between the QS and GV equations. The primary difference is that GV takes into account radiation losses which dampen the peaks and cause a slight shift in the resonant frequency.

The plots in Figures 3.4 - 3.15 are the results for lossless dielectric spheres. This demonstrates the contributions of radiation losses taken into account by the GV equations. In Figures 3.4 - 3.7 the dipole orientation is that of Case I and each figure shows the result of the radius of sphere b being larger than sphere a by 3.0%, 0.5%, 0.2% and 0.1%. Similarly, Case II is plotted for the same variations in radii in Figures 3.8 - 3.11 and Case III in Figures 3.12 - 3.15.

As the sphere radii variation decreases, the difference between the two resonant frequencies decreases and their corresponding bandwidths overlap and interfere with each other. At 3% radii variation, the difference of the resonant frequencies is large enough that the spheres weakly couple and radiation losses are small, as compared to a variation of 0.1%, when the spheres strongly couple and the radiation losses become much greater. Interestingly, in Case I $|p_{ax}^{QS}|$, and in Case II and III $|p_{bx}^{QS}|$ maintains the distinction between the two resonances despite the increase in coupling between the two spheres.

As the radius variation decreases, one resonance increases in bandwidth forming a main resonance and the other resonance bandwidth narrows, forming the characteristics of a Fano resonance. Consider the plots of the real and imaginary part of the individual dipole moments p_a and p_b. Van Bladel considers an identical pair to be a coupled system capable of creating two modes: odd and even [6]. Near and at the main resonance, p_a and p_b are either both positive or both negative. This is the even mode. On the other hand, near or at the Fano resonance, p_a and p_b have opposite signs (the odd mode). Their interference creates sharp asymmetric resonances in this case. As the radius of sphere b approaches that of sphere a, the Fano resonance of the QS equations becomes sharper, while the GV equations predict that the radiation losses significantly dampen out the Fano resonance.

In Case I the higher frequency resonance is the Fano resonance, while in Case II and Case III the lower frequency resonance is the Fano resonance. Interestingly, the main resonance strongly dominates the Fano resonance in Case I, more so than Case II and and much more so than in Case III.

Next, material loss is introduced into both dielectric spheres (the same loss tangent for both) will be applied and the results are illustrated in Figures 3.16 - 3.42. When the sphere radii differ by 0.2%, Figures 3.16 - 3.20 show Case I when the loss tangent of the sphere is $\delta_t = 10^{-4}, 10^{-3.5}, 10^{-3}, 10^{-2.95}$, and $10^{-2.5}$ respectively. For the same loss tangents, Case II is shown in Figures 3.21 - 3.25, and Case III in Figures 3.26 - 3.30

For a loss tangent of $\delta_t = 10^{-4}$, there is little change except for the Fano resonance predicted by the QS equations, whose peaks become dampened. As the sphere material loss tangent increases to $\delta_t = 10^{-3}$, in both QS and GV equations, the main resonance becomes somewhat dampened while the Fano resonance is significantly dampened. Then at $\delta_t = 10^{-2.95}$, unexpectedly a sharp Fano resonance is predicted by the GV equations. When the material is very lossy, $\delta_t = 10^{-2.5}$ the Fano resonances are unidentifiable and the main resonance has significantly reduced peaks.

The Fano resonance that is induced by small changes in dielectric sphere material loss tangent δ_t, occurs in the GV equations for Case I - III for 0.2% variation in radius at $\delta_t = 10^{-3}$ in Figures 3.31 - 3.36. When the radii vary by 0.5%, Figures 3.37 - 3.36 demonstrates a Fano resonance due to small variations in losstangent occurs at $\delta_t = 10^{-3.4}$ for all three dipole orientations Case I - III.

Notice, that in many of the plots of the imaginary terms for QS and GV equations, the peaks are positive, indicating a violation of the conservation of energy. It was shown in [9] that this is a result of certain dipole model approximations, and so the behavior near resonances may not be accurately predicted. (For example, as changes in loss tangent inducing Fano resonances.) However, Collin does provide equations that add extra terms to the polarizabilities that could be used to increase accuracy, so that conservation of energy will be maintained, at the expense of more complicated equations [9]. Although we do not pursue this here, this is the path to take to determine if changes in sphere material loss tangent can induce Fano resonances.

Lastly for this example, consider the magnetic dipole case in Figures 3.43 - 3.54. The radius is varied by 3%, 2%, 1%, and 0.2%, for Case I in Figures 3.43 - 3.46, Case II in Figures 3.47 - 3.50, and Case III in

Figures 3.51 - 3.54. The overall behavior of the magnetic dipoles is very similar to that of the electric dipoles. There are two resonances, that can be classified as even and odd modes, wherein the odd mode can produce a Fano resonance. Recall in Chapter 2, that the magnetic polarizabilities have nonconfined mode behavior. The bandwidth is wider and has a more gradual slope, they are stronger, and the fields aren't constricted to the interior of the resonator. Therefore, the fields of one particle will couple more easily with it's neighbor. Whether they are close together physically or their resonances are close enough together to excite each other. Thus, the interference of the odd mode occurs for larger variations in the physical parameters that effect the resonant frequency, than shown for the electric dipoles.

For example, a 3% variation in the radius of the spheres will produce a Fano resonance for magnetic dipoles pointed in the directions of Case I, while Case II and Case III have yet to have enough interference to do so. At 1% radius variation, Cases I-III all have a main resonance and a Fano resonance. On the other hand, the GV equations predict that for Case I with 2% or less variation, the Fano resonance is completely dampened out by radiation losses alone and only one main resonance exists. This also occurs in Case II and III, for radius variations of 0.2 % or less.

Lastly, what happens if the distance between the spheres varies for spacing less than a quarter wavelength but non-touching. For an identical pair of scatterers, no new behavior is observed. If the pair of scatterers are nonidentical, distance determine how much the resonant frequencies need to vary to get strong coupling. When the spheres are closer than that of the example, strong frequency coupling occurs for higher differences in resonant frequency. On the other hand, when they are spaced physically farther apart, strong frequency coupling occurs for lower differences in resonant frequency. Therefore, a closer physically spaced pair of nonidentical scatters, results in stronger coupling in frequency. If one is looking for very sharp resonances, but for larger variations in the sphere radii, they would need to space them closer together.

3.4 Conclusion

This chapter is a comprehensive study of the behavior of a pair of scatterers, that exhibit dipole moments. This chapter demonstrated that a pair of resonators spaced less than a quarter wavelength apart will couple when the scatterer properties that effect resonance varies between them. When the scatterers have nonidentical resonant frequencies, the combined dipole moments results in two resonances: 1) a main resonance with the widest bandwidth (that results from constructive interference of the individual dipole moments), and 2) a Fano resonance with the narrowest bandwidth (that results from destructive interference). The bandwidth of both resonances is directly related to how strongly the pair couples. Strong coupling in frequency results in sharp Fano resonances and a wider main resonance. The weaker the coupling, the closer the bandwidth of both the main and Fano resonance become comparable to each other. Therefore, to accurately characterize the behavior of a pair of scatterers that couples, more rigorous equations like that of the QS equations derived in this chapter and the GV equations of previous work [13] should be used.

If the distance between two identical scatterers changes, no new behavior is observed, so long as they are spaced less than a quarter wavelength apart and are non-touching. If the parameters that effect the resonant behavior of the scatterer, differs between the pair, resulting in different resonant frequencies, then distance determines how much the parameters need to vary to result in strong coupling.

A sphere has special properties, due to it's high rotational symmetry. Therefore it can support modes that are confined, as discussed in Chapter 2 and demonstrated in this chapter. The confined modes remain weakly coupled for even small variations in resonant frequency. It takes very small variations in resonant frequency to create sharp Fano resonances.

The theory demonstrated in this chapter will be extended to that of a 2D array of scatterers (a metafilm) in the remaining chapters.

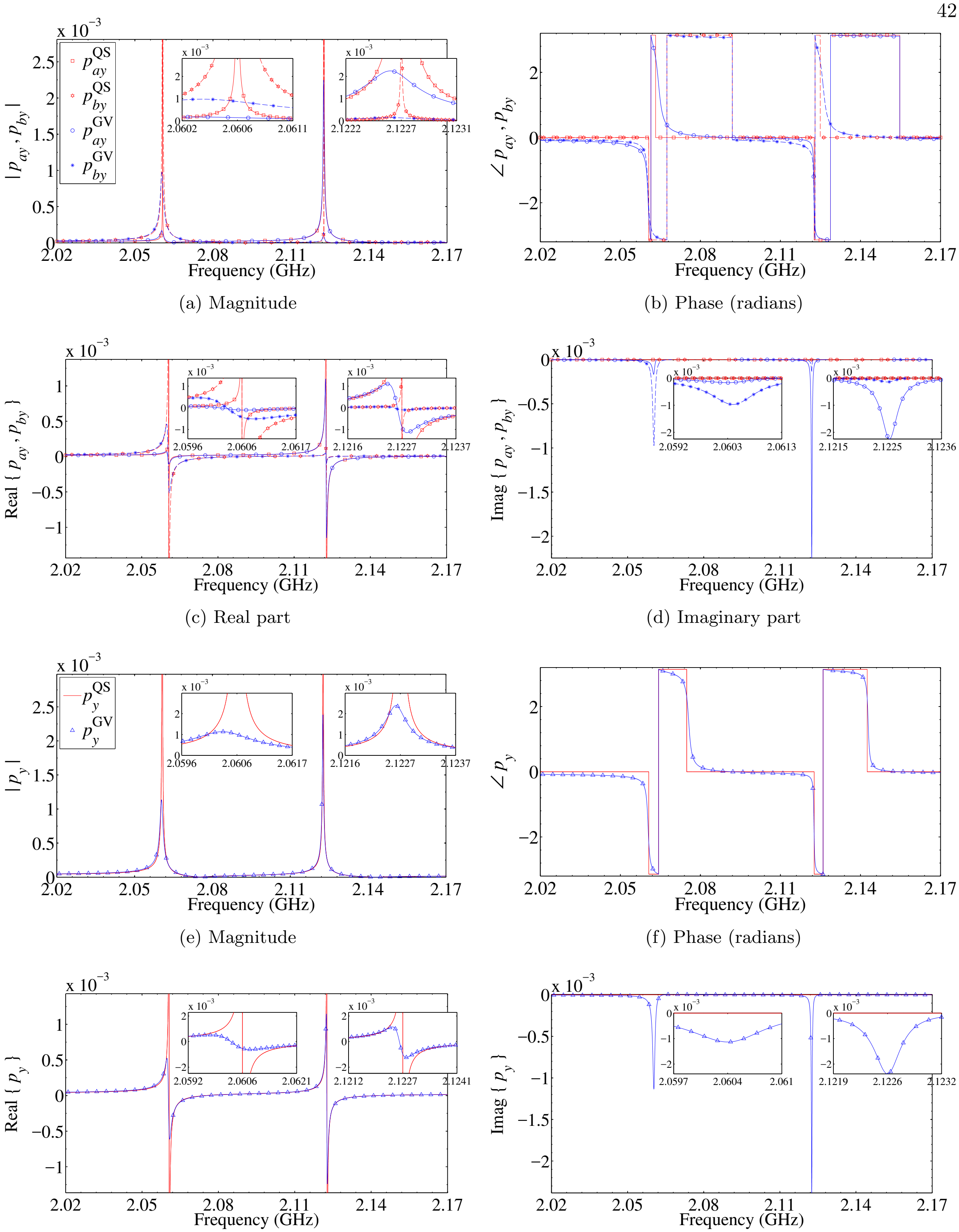

(a) Magnitude

(b) Phase (radians)

(c) Real part

(d) Imaginary part

(e) Magnitude

(f) Phase (radians)

(g) Real part

(h) Imaginary part

Figure 3.4: Pair of dielectric spheres: Case I orientation, radius of b is 3.0% larger than a, spacing 0.03 m $\epsilon_r = 100$, and lossless. Electric dipole moments normalized such that $\epsilon E^{inc} = 1$.

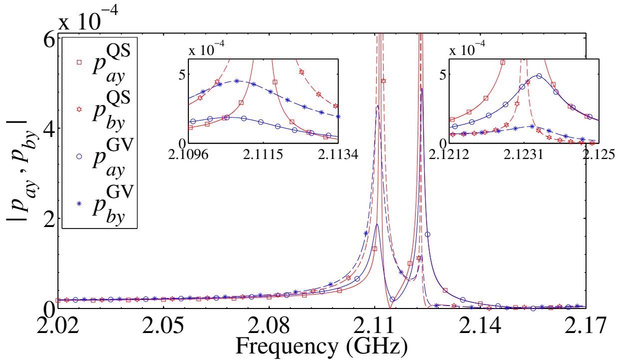

(a) Magnitude

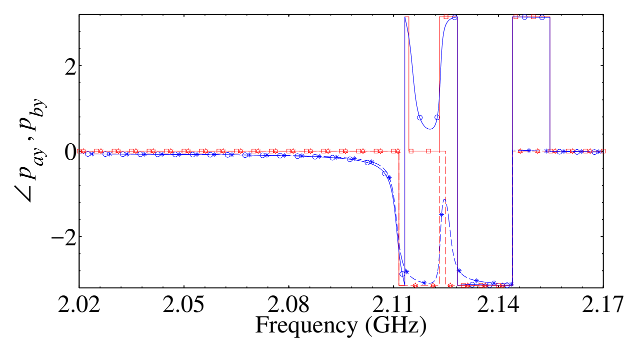

(b) Phase (radians)

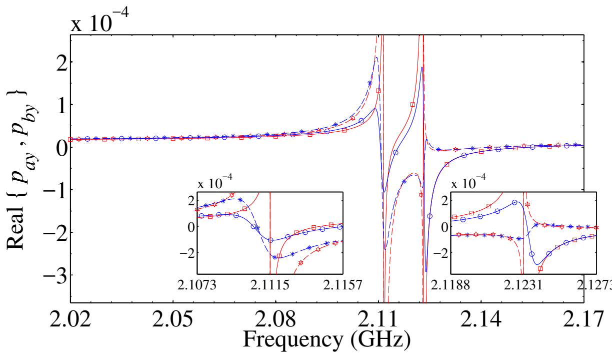

(c) Real part

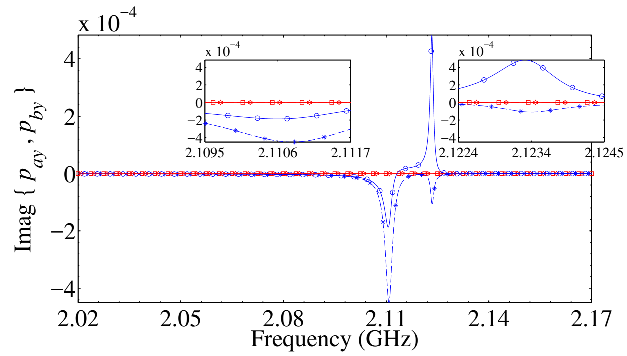

(d) Imaginary part

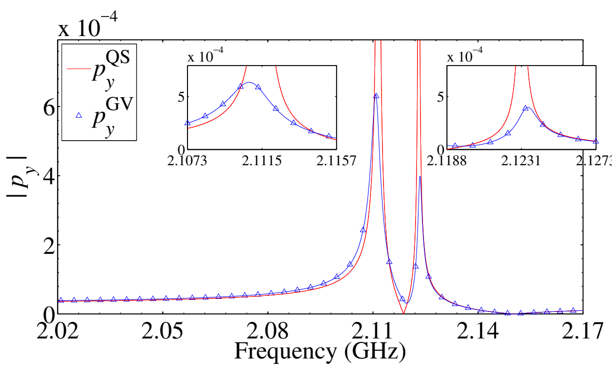

(e) Magnitude

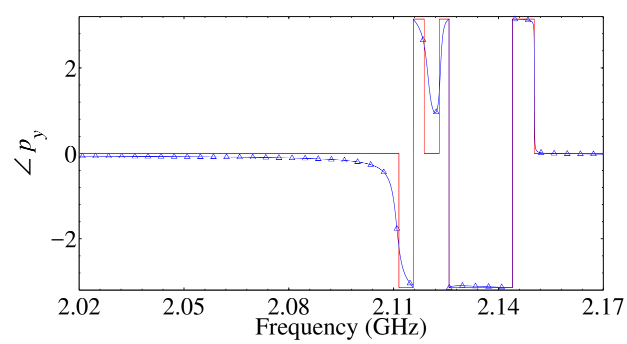

(f) Phase (radians)

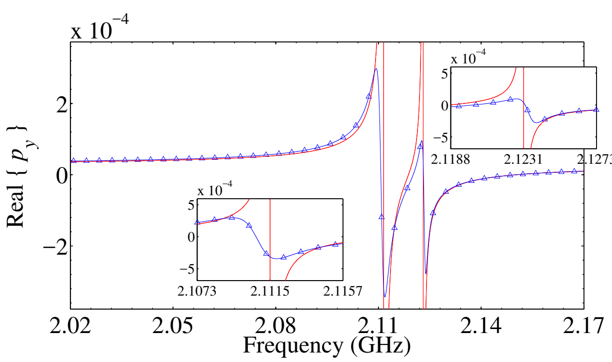

(g) Real part

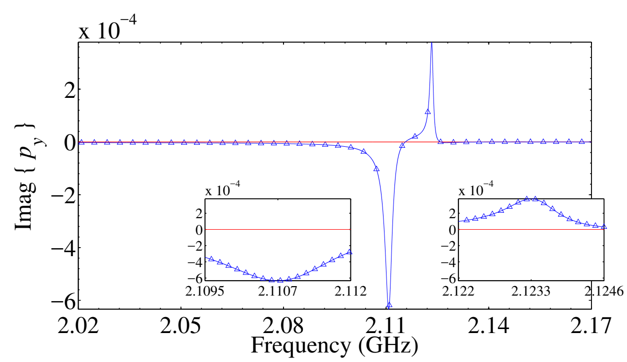

(h) Imaginary part

Figure 3.5: Pair of dielectric spheres: Case I orientation, radius of b is 0.5% larger than a, spacing 0.03 m, $\epsilon_r = 100$, and lossless. Electric dipole moments normalized such that $\epsilon E^{inc} = 1$.

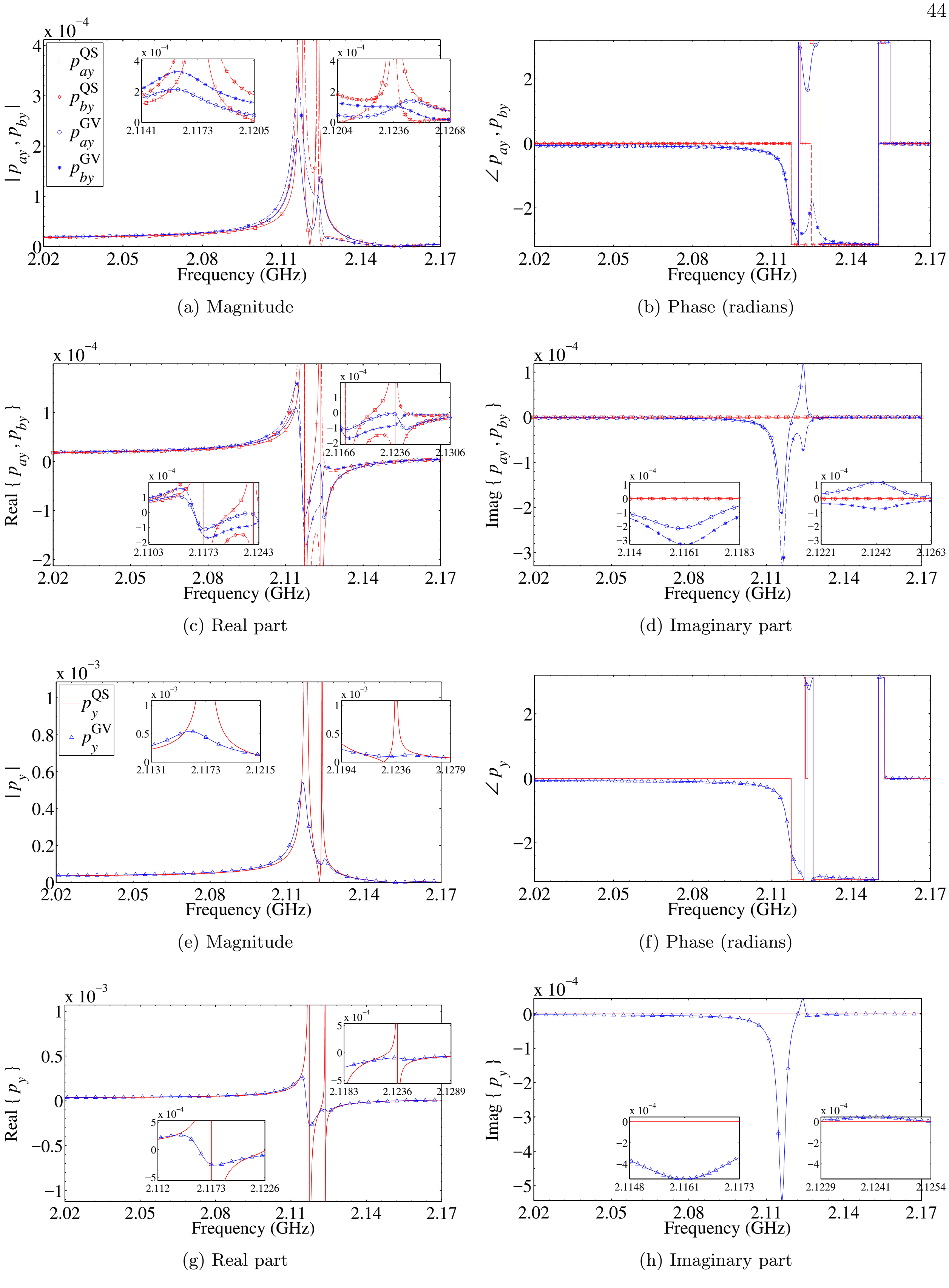

(a) Magnitude

(b) Phase (radians)

(c) Real part

(d) Imaginary part

(e) Magnitude

(f) Phase (radians)

(g) Real part

(h) Imaginary part

Figure 3.6: Pair of dielectric spheres: Case I orientation, radius of b is 0.2% larger than a, spacing 0.03 m, $\epsilon_r = 100$, and lossless. Electric dipole moments normalized such that $\epsilon E^{inc} = 1$.

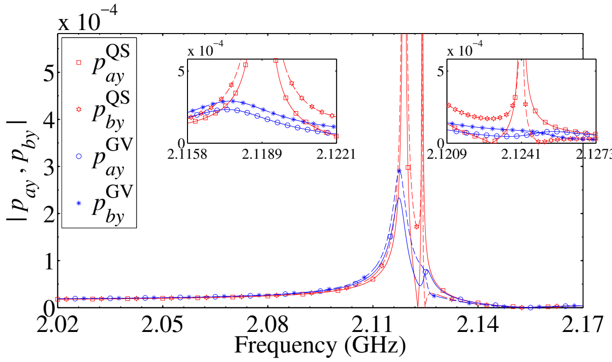

(a) Magnitude

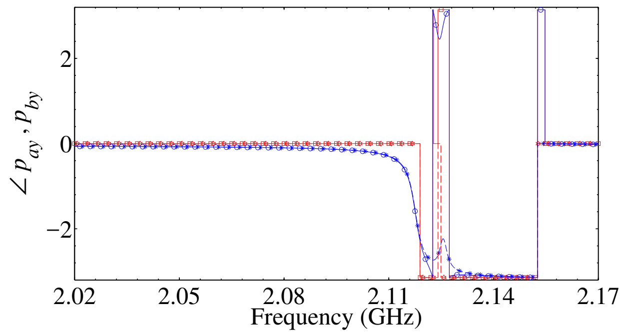

(b) Phase (radians)

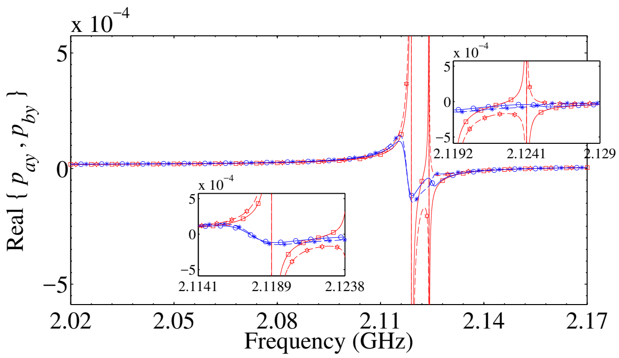

(c) Real part

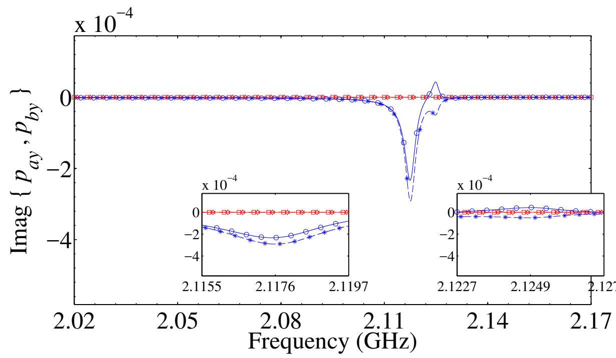

(d) Imaginary part

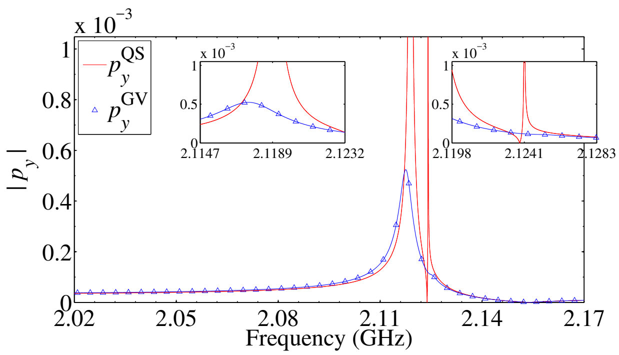

(e) Magnitude

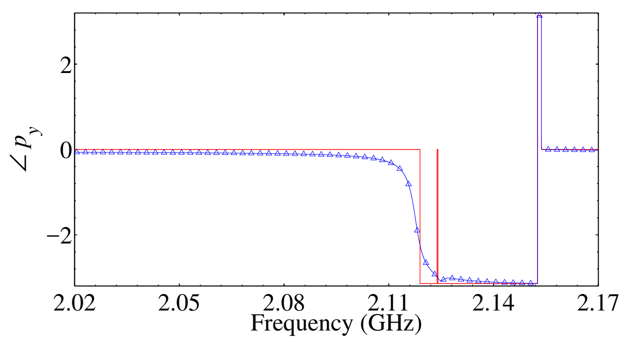

(f) Phase (radians)

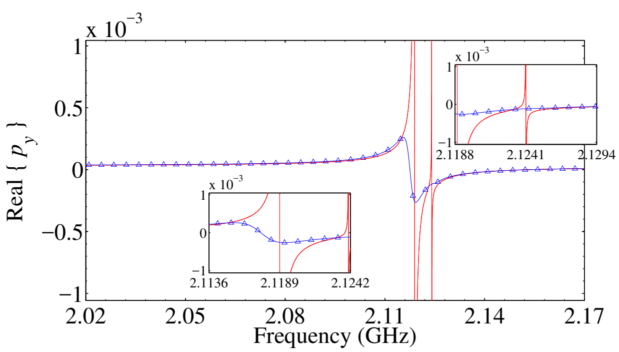

(g) Real part

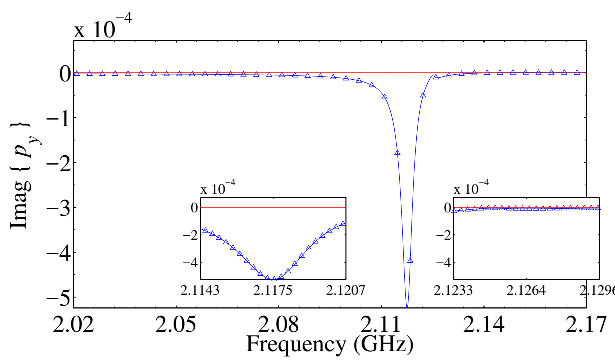

(h) Imaginary part

Figure 3.7: Pair of dielectric spheres: Case I orientation, radius of b is 0.1% larger than a, spacing 0.03 m, $\epsilon_r = 100$, and lossless. Electric dipole moments normalized such that $\epsilon E^{inc} = 1$.

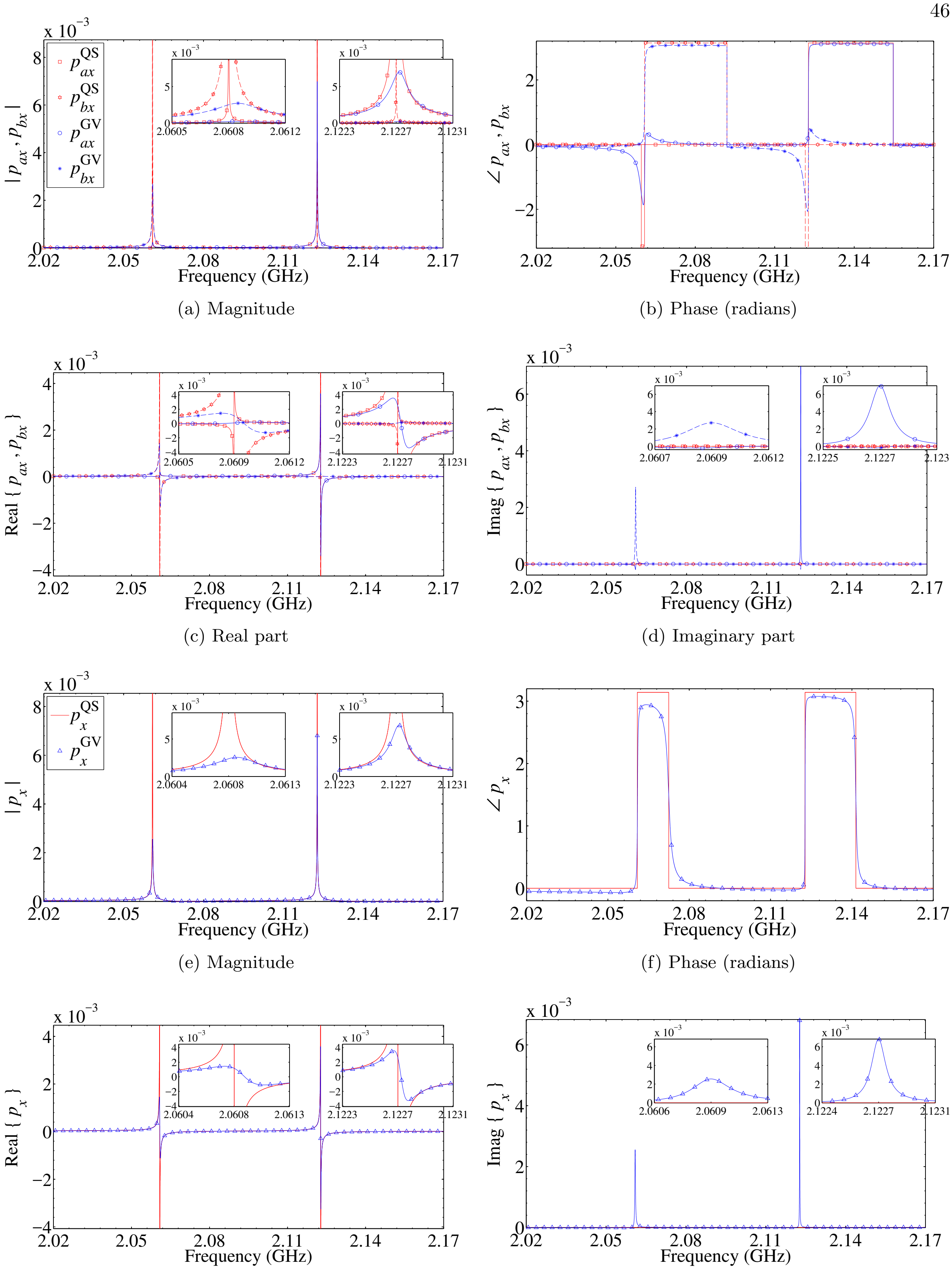

(a) Magnitude

(b) Phase (radians)

(c) Real part

(d) Imaginary part

(e) Magnitude

(f) Phase (radians)

(g) Real part

(h) Imaginary part

Figure 3.8: Pair of dielectric spheres: Case II orientation, radius of b is 3.0% larger than a, spacing 0.03 m, $\epsilon_r = 100$, and lossless. Electric dipole moments normalized such that $\epsilon E^{inc} = 1$.

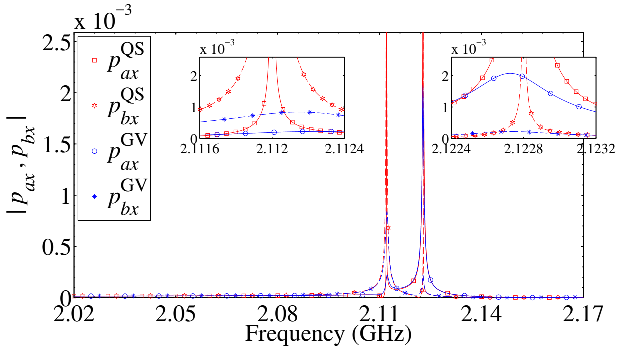

(a) Magnitude

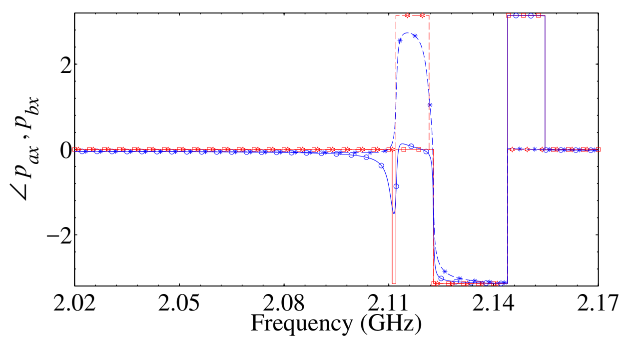

(b) Phase (radians)

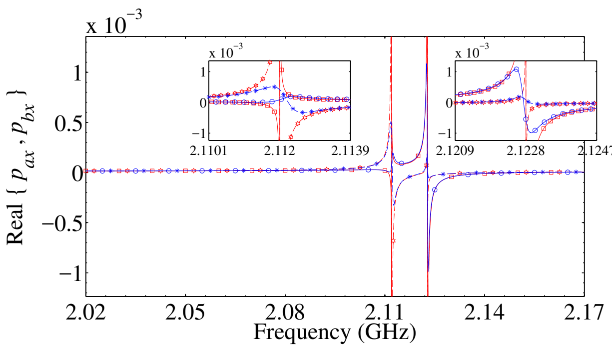

(c) Real part

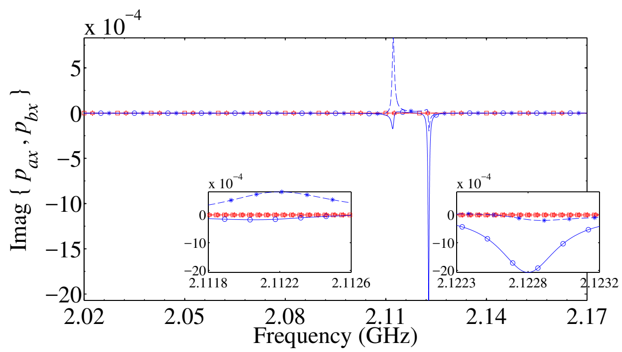

(d) Imaginary part

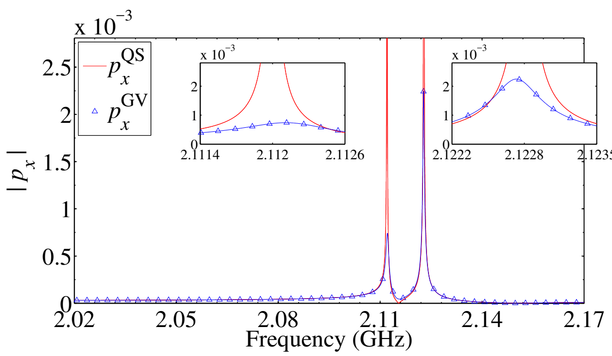

(e) Magnitude

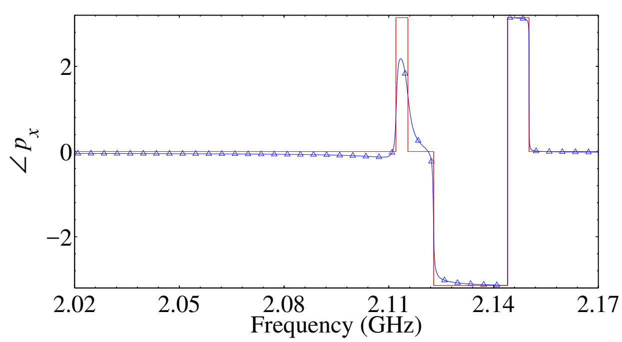

(f) Phase (radians)

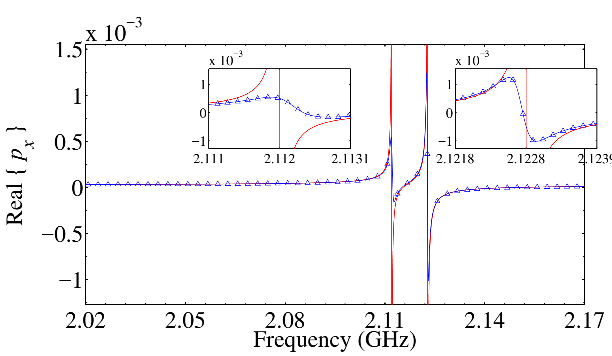

(g) Real part

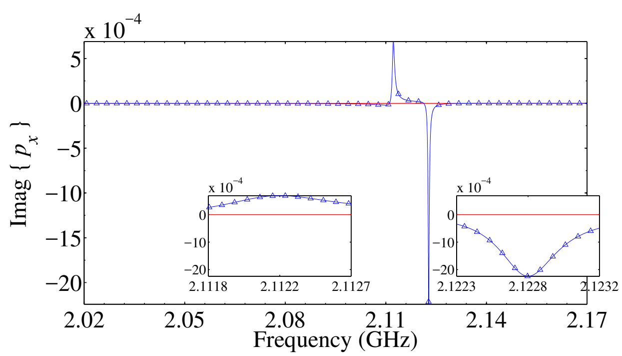

(h) Imaginary part

Figure 3.9: Pair of dielectric spheres: Case II orientation, radius of b is 0.5% larger than a, spacing 0.03 m, $\epsilon_r = 100$, and lossless. Electric dipole moments normalized such that $\epsilon E^{inc} = 1$.

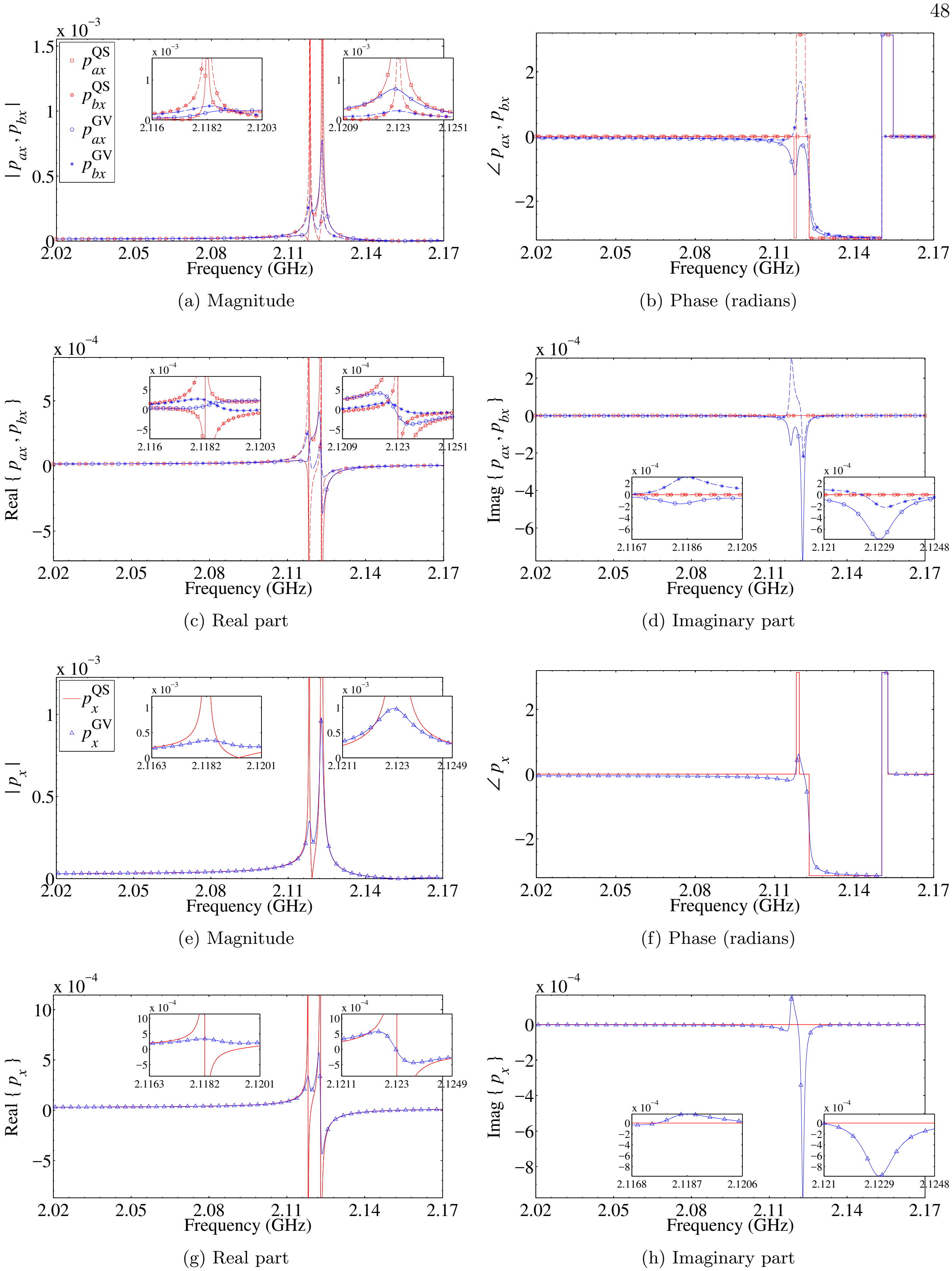

(a) Magnitude

(b) Phase (radians)

(c) Real part

(d) Imaginary part

(e) Magnitude

(f) Phase (radians)

(g) Real part

(h) Imaginary part

Figure 3.10: Pair of dielectric spheres: Case II orientation, radius of b is 0.2% larger than a, spacing 0.03 m, $\epsilon_r = 100$, and lossless. Electric dipole moments normalized such that $\epsilon E^{inc} = 1$.

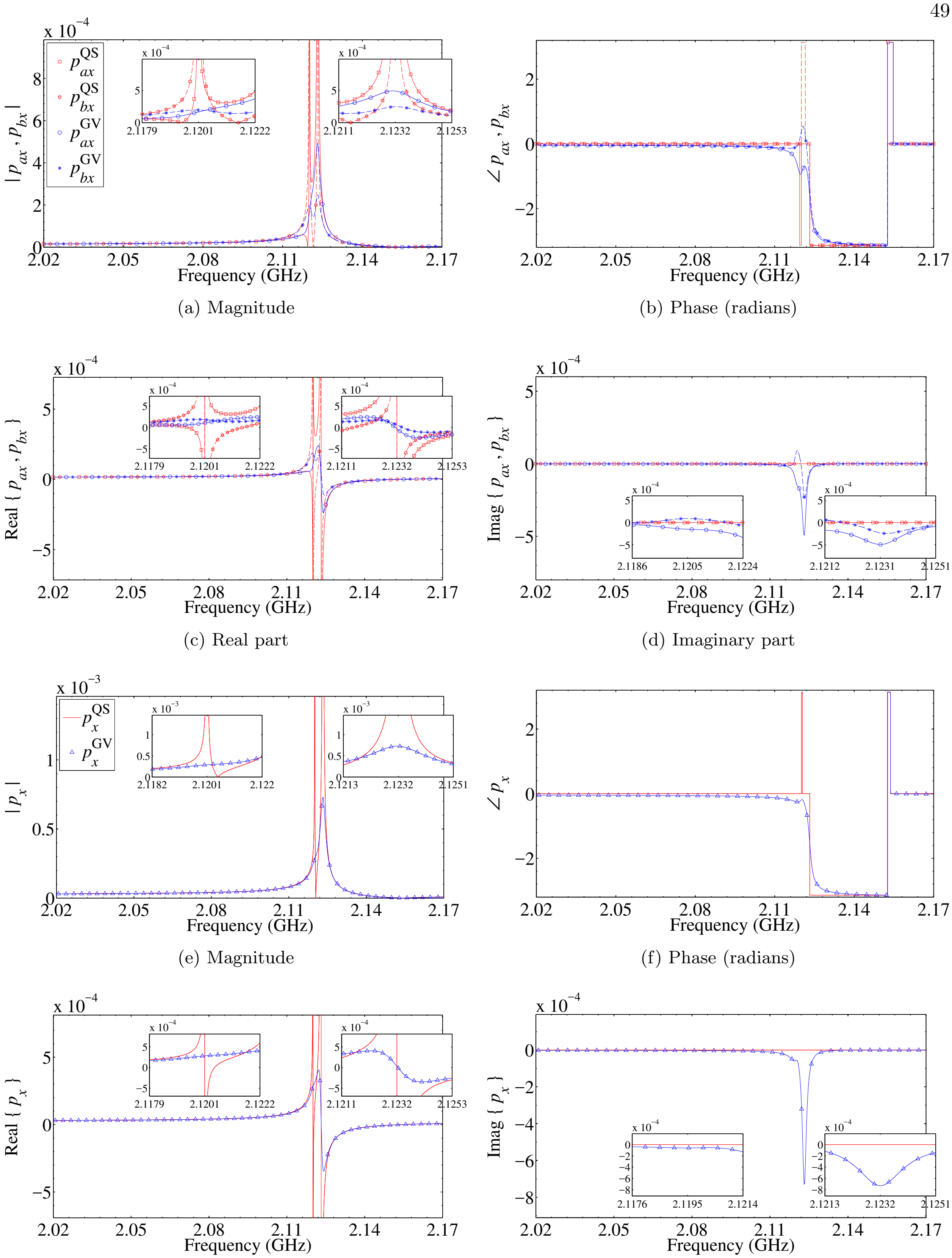

(a) Magnitude

(b) Phase (radians)

(c) Real part

(d) Imaginary part

(e) Magnitude

(f) Phase (radians)

(g) Real part

(h) Imaginary part

Figure 3.11: Pair of dielectric spheres: Case II orientation, radius of b is 0.1% larger than a, spacing 0.03 m, $\epsilon_r = 100$, and lossless. Electric dipole moments normalized such that $\epsilon E^{inc} = 1$.

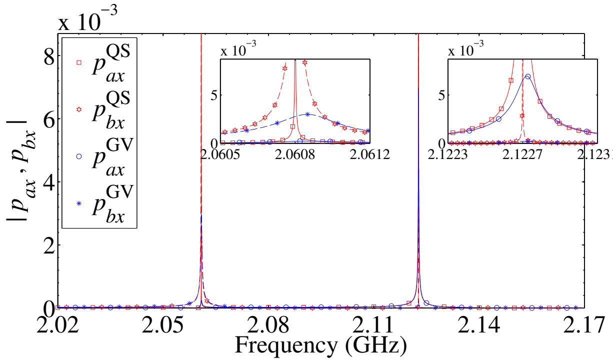

(a) Magnitude

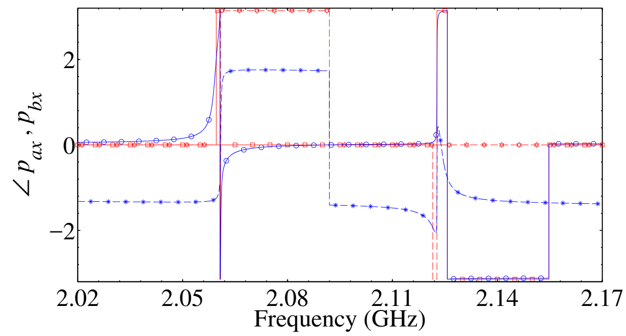

(b) Phase (radians)

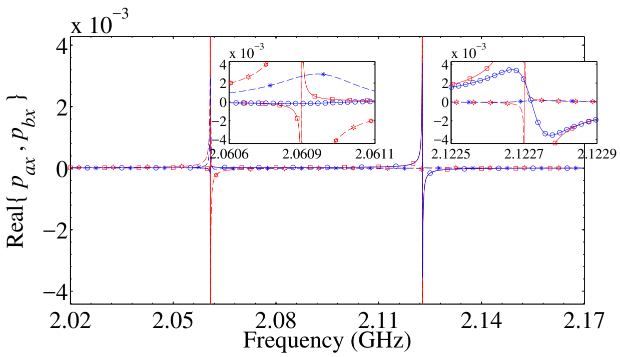

(c) Real part

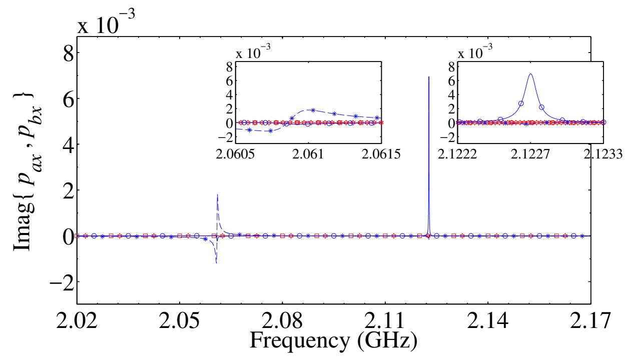

(d) Imaginary part

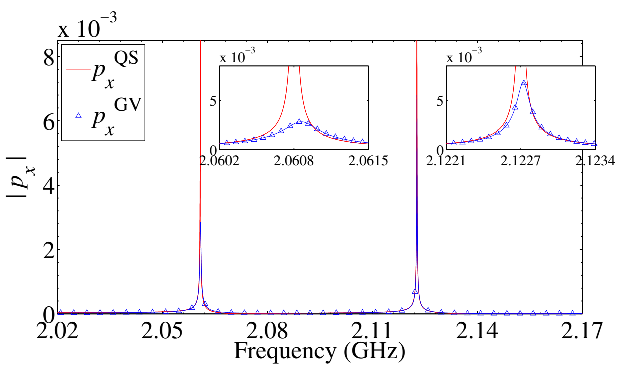

(e) Magnitude

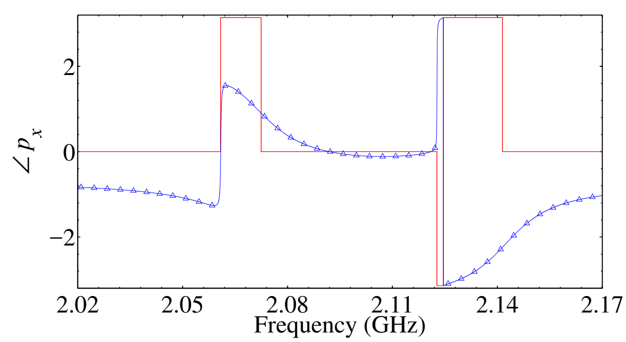

(f) Phase (radians)

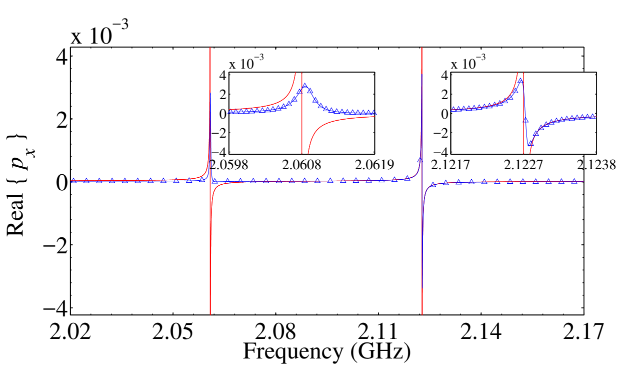

(g) Real part

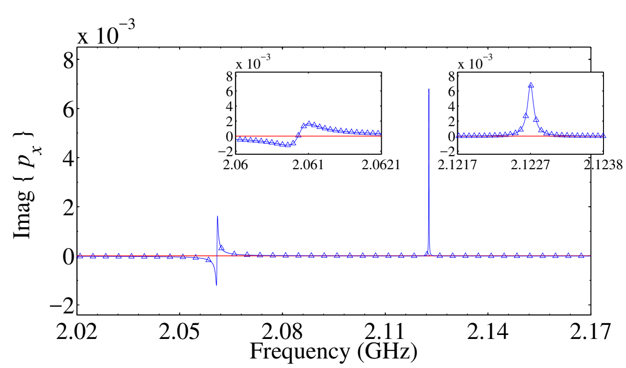

(h) Imaginary part

Figure 3.12: Pair of dielectric spheres: Case III orientation, radius of b is 3.0% larger than a, spacing 0.03 m, $\epsilon_r = 100$, and lossless. Electric dipole moments normalized such that $\epsilon E^{inc} = 1$.

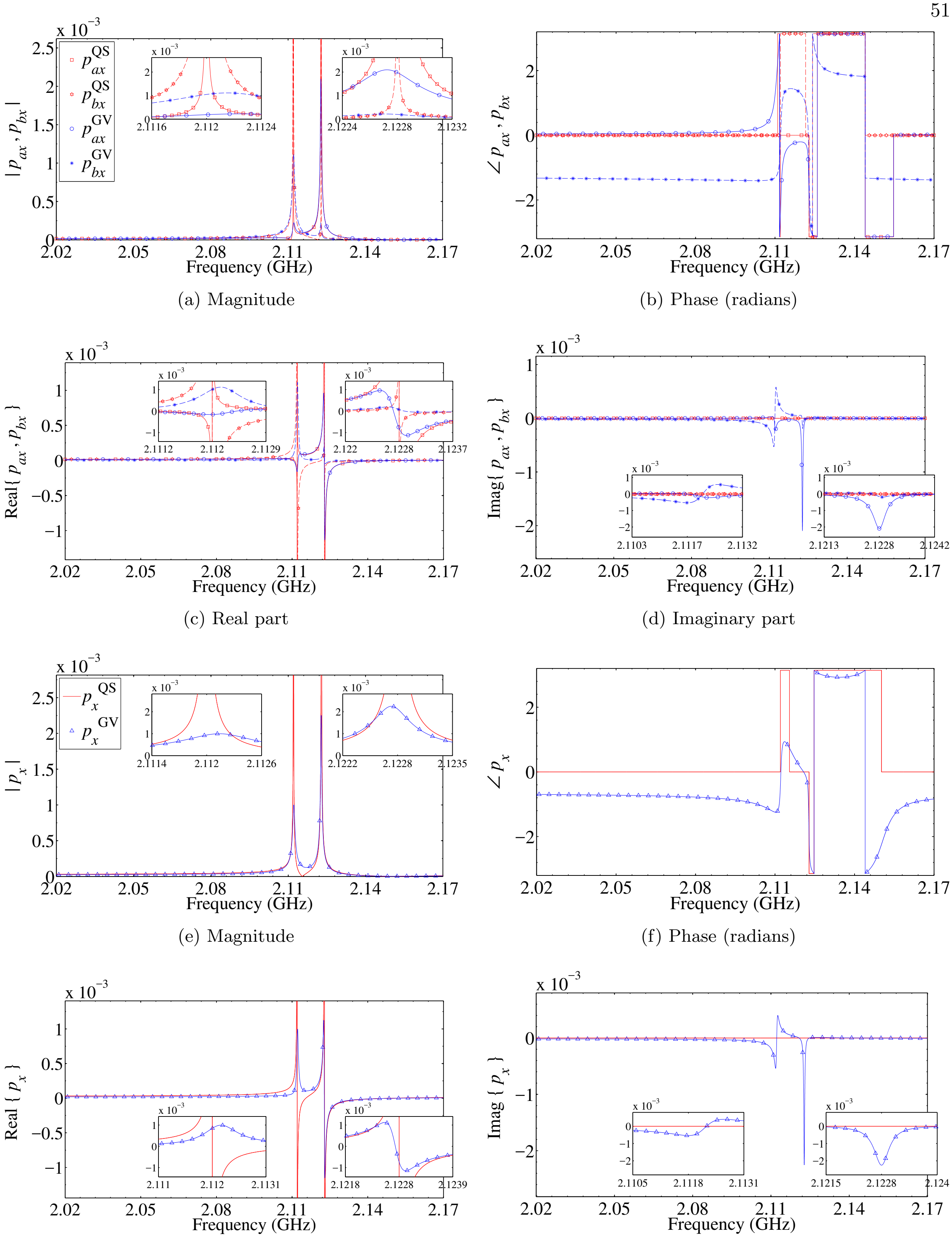

(a) Magnitude (b) Phase (radians)

(c) Real part (d) Imaginary part

(e) Magnitude (f) Phase (radians)

(g) Real part (h) Imaginary part

Figure 3.13: Pair of dielectric spheres: Case III orientation, radius of b is 0.5% larger than a, spacing 0.03 m, $\epsilon_r = 100$, and lossless. Electric dipole moments normalized such that $\epsilon E^{inc} = 1$.

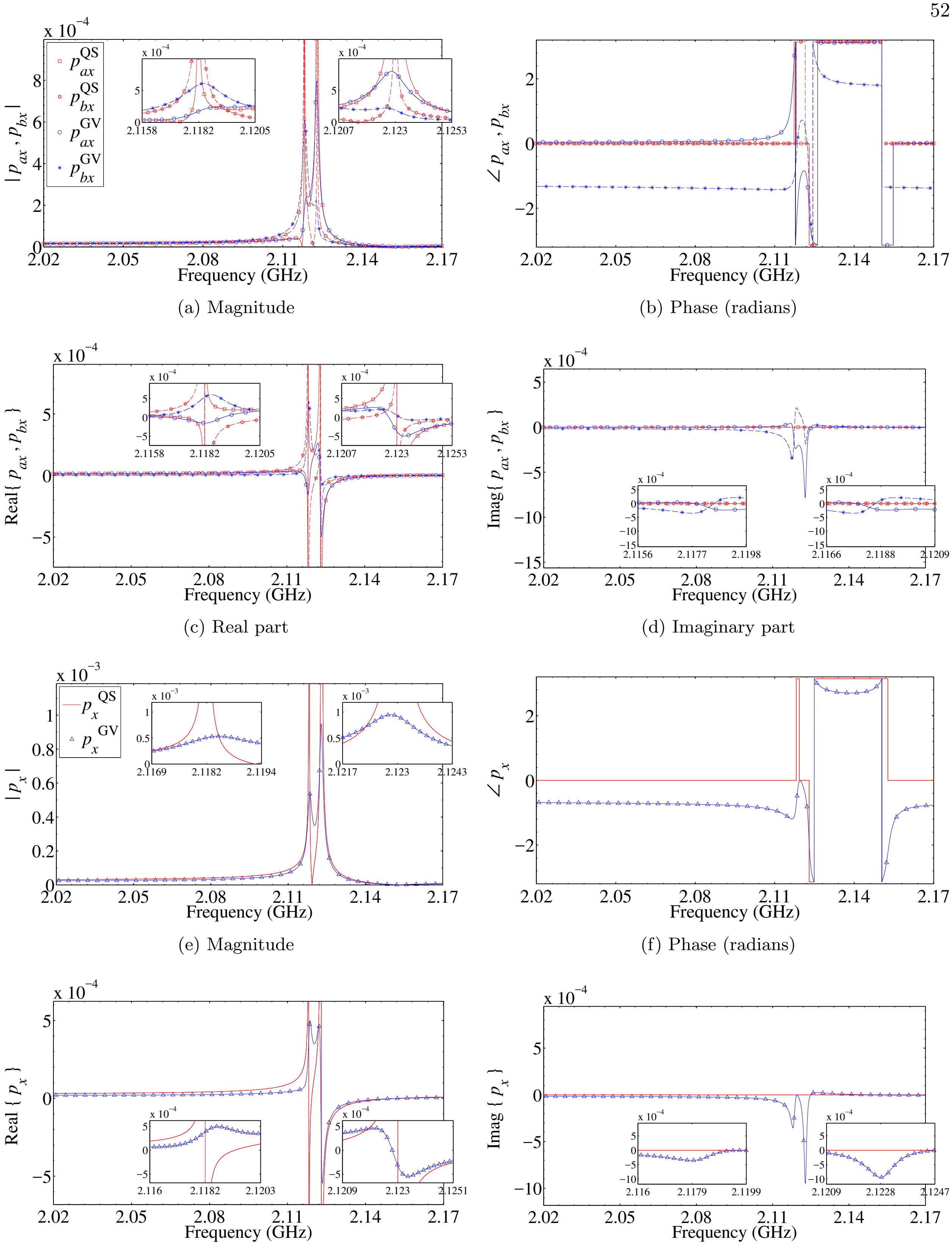

(a) Magnitude

(b) Phase (radians)

(c) Real part

(d) Imaginary part

(e) Magnitude

(f) Phase (radians)

(g) Real part

(h) Imaginary part

Figure 3.14: Pair of dielectric spheres: Case III orientation, radius of b is 0.2% larger than a, spacing 0.03 m, $\epsilon_r = 100$, and lossless. Electric dipole moments normalized such that $\epsilon E^{inc} = 1$.

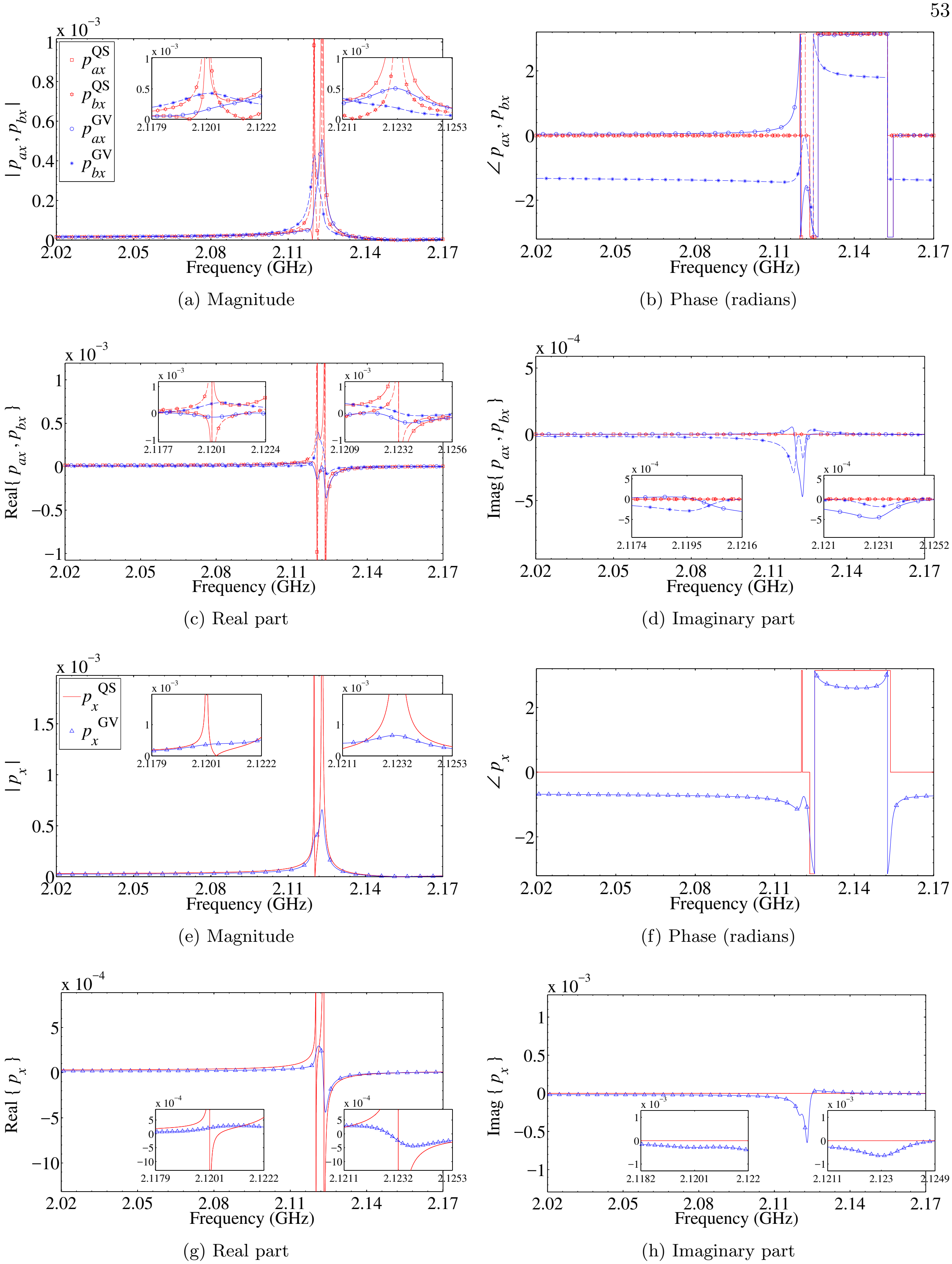

(a) Magnitude (b) Phase (radians)

(c) Real part (d) Imaginary part

(e) Magnitude (f) Phase (radians)

(g) Real part (h) Imaginary part

Figure 3.15: Pair of dielectric spheres: Case III orientation, radius of b is 0.1% larger than a, spacing 0.03 m, $\epsilon_r = 100$, and lossless. Electric dipole moments normalized such that $\epsilon E^{inc} = 1$.

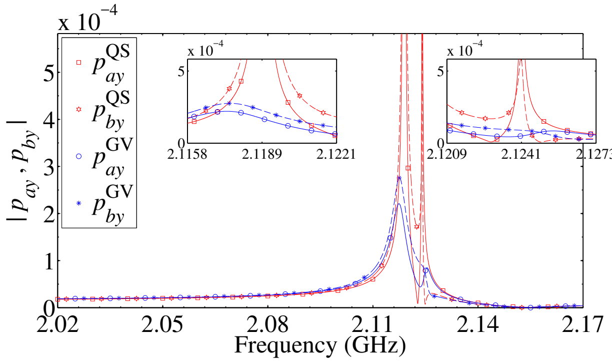

(a) Magnitude

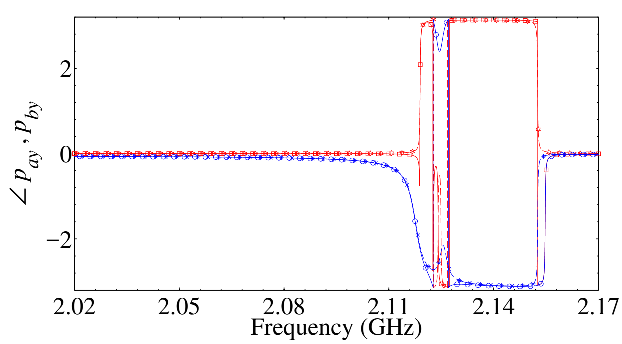

(b) Phase (radians)

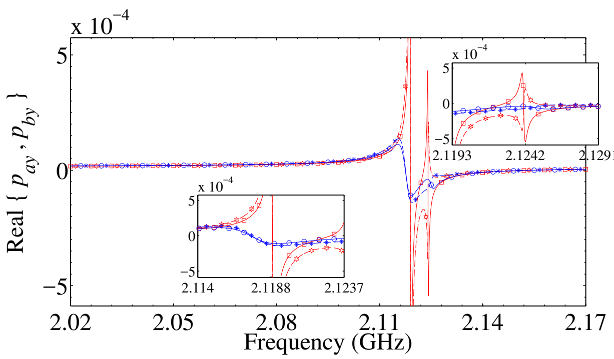

(c) Real part

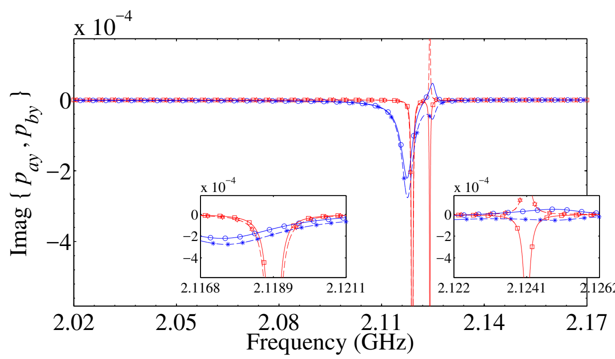

(d) Imaginary part

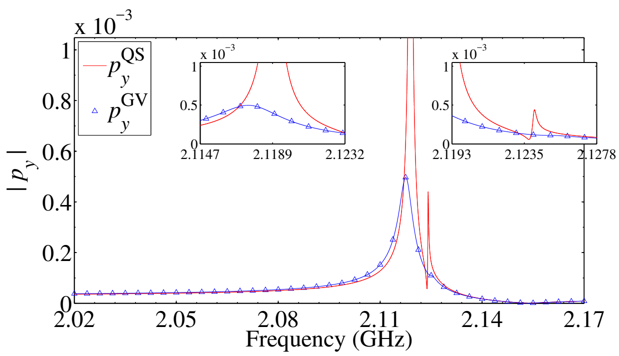

(e) Magnitude

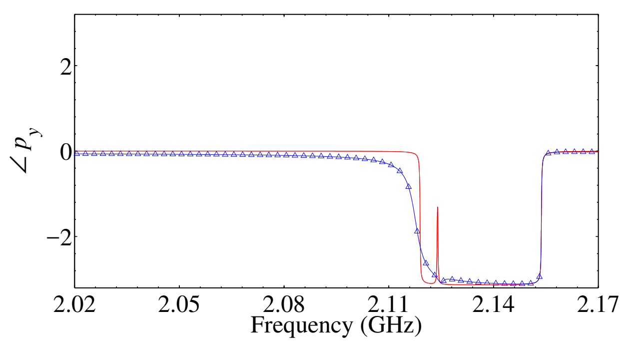

(f) Phase (radians)

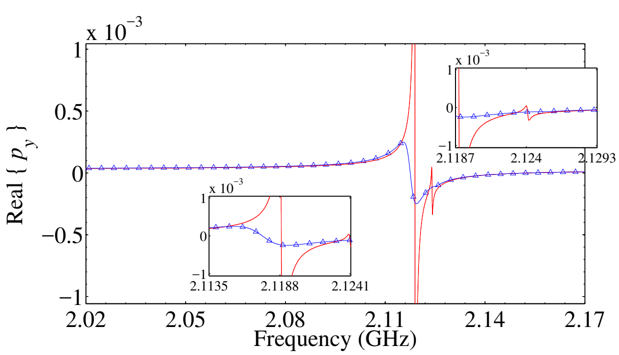

(g) Real part

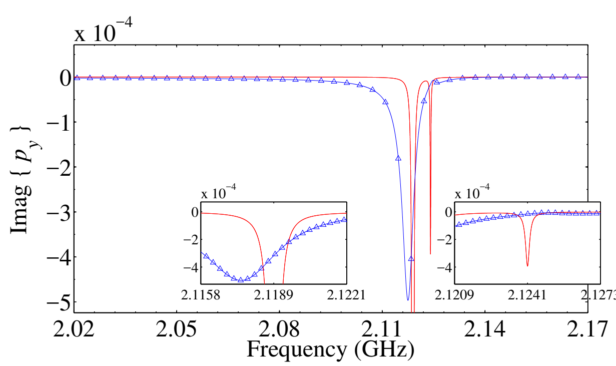

(h) Imaginary part

Figure 3.16: Pair of dielectric spheres: Case I orientation, radius of b is 0.1% larger than a, spacing 0.03 m, $\epsilon_r = 100$, and $\delta_T = 10^{-4}$. Electric dipole moments normalized such that $\epsilon E^{inc} = 1$.

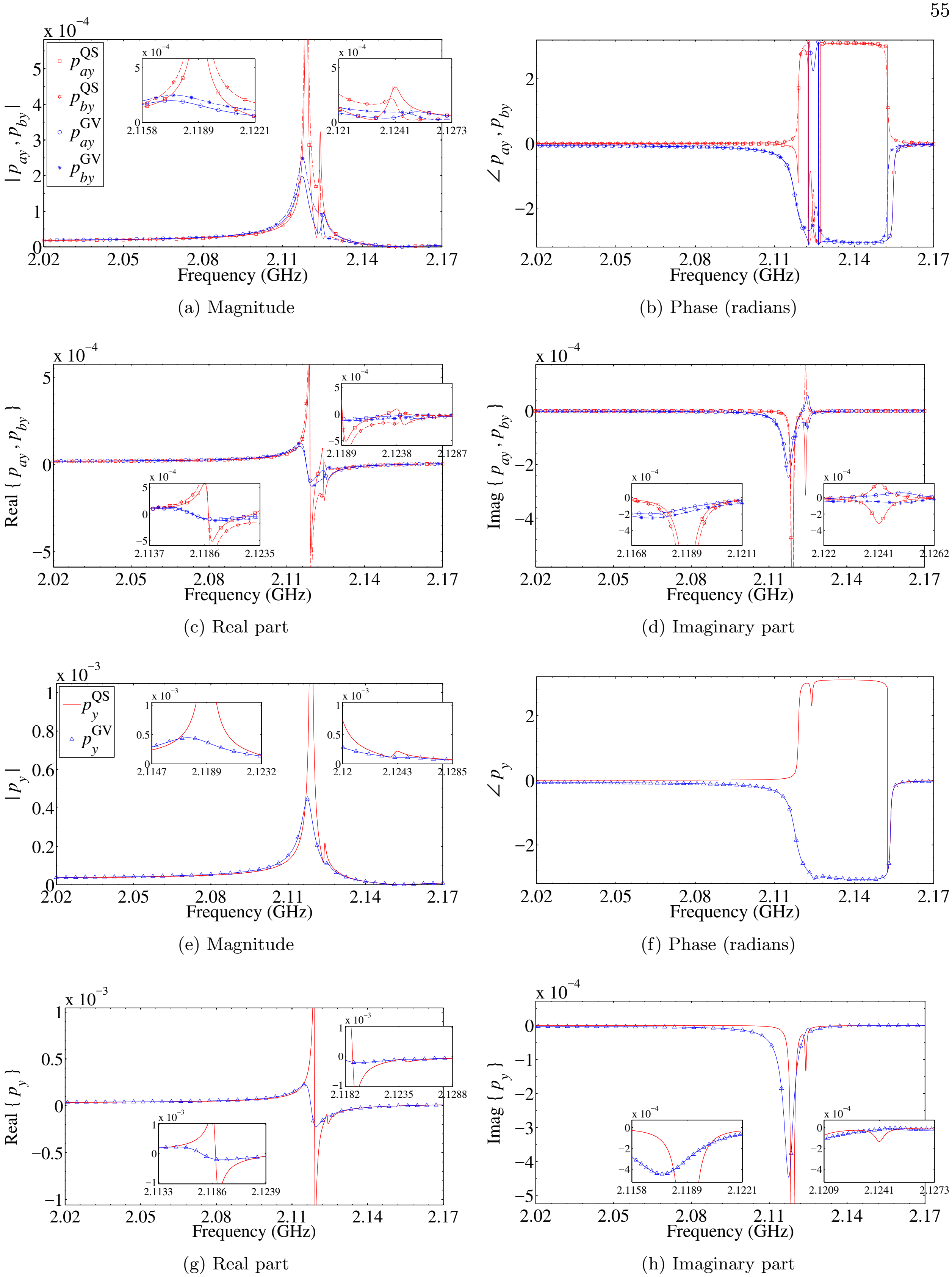

(a) Magnitude (b) Phase (radians)

(c) Real part (d) Imaginary part

(e) Magnitude (f) Phase (radians)

(g) Real part (h) Imaginary part

Figure 3.17: Pair of dielectric spheres: Case I orientation, radius of b is 0.1% larger than a, spacing 0.03 m, $\epsilon_r = 100$, and $\delta_T = 10^{-3.5}$. Electric dipole moments normalized such that $\epsilon E^{inc} = 1$.

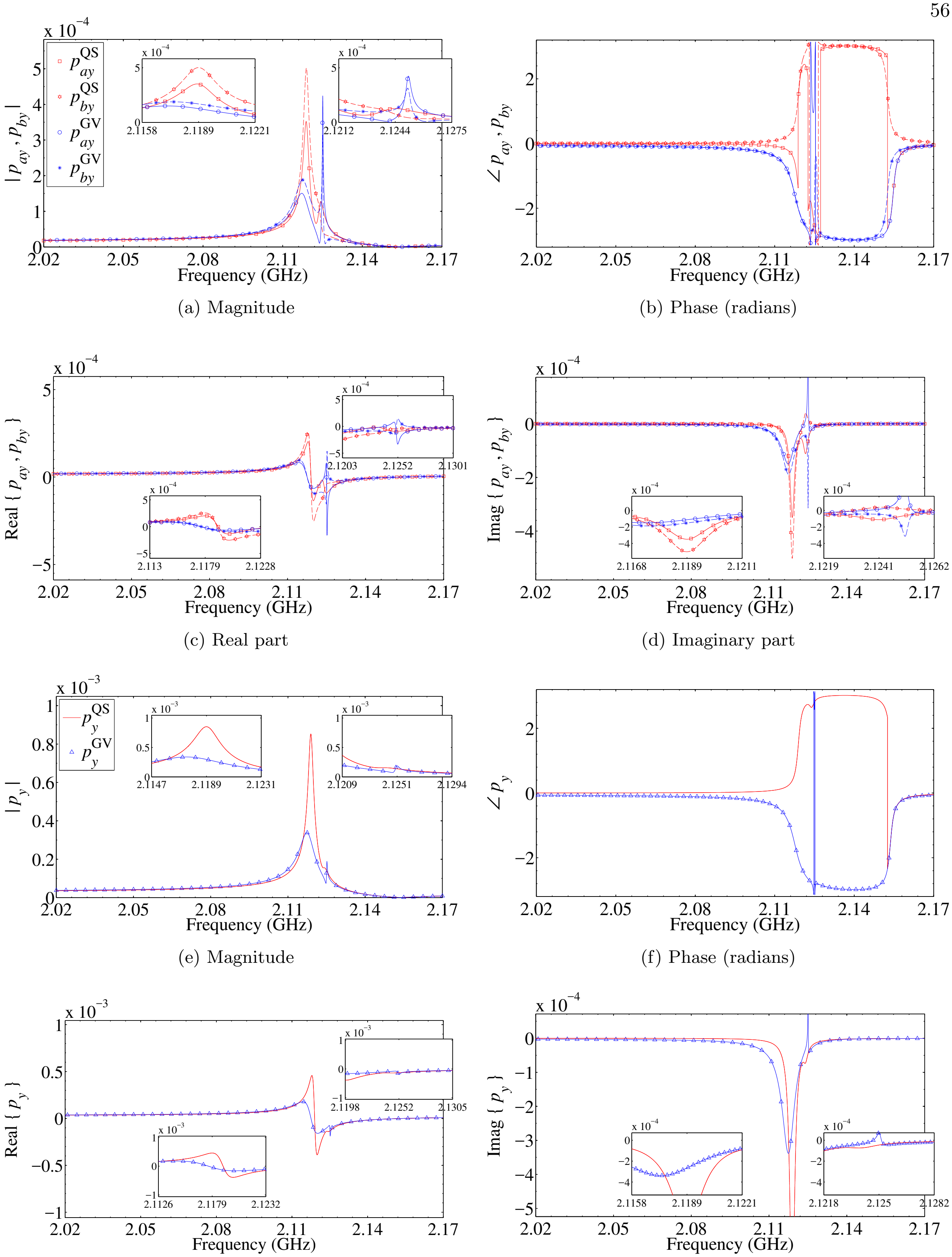

(a) Magnitude

(b) Phase (radians)

(c) Real part

(d) Imaginary part

(e) Magnitude

(f) Phase (radians)

(g) Real part

(h) Imaginary part

Figure 3.18: Pair of dielectric spheres: Case I orientation, radius of b is 0.1% larger than a, spacing 0.03 m, $\epsilon_r = 100$, and $\delta_T = 10^{-3}$. Electric dipole moments normalized such that $\epsilon E^{inc} = 1$.

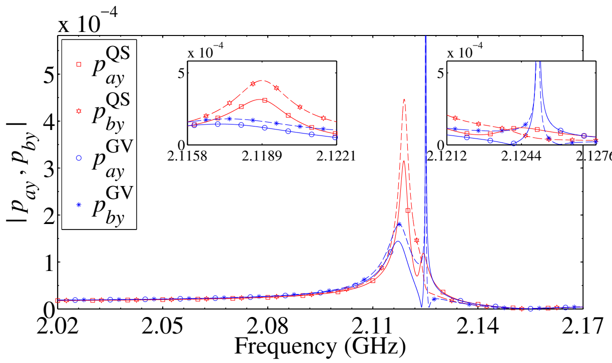

(a) Magnitude

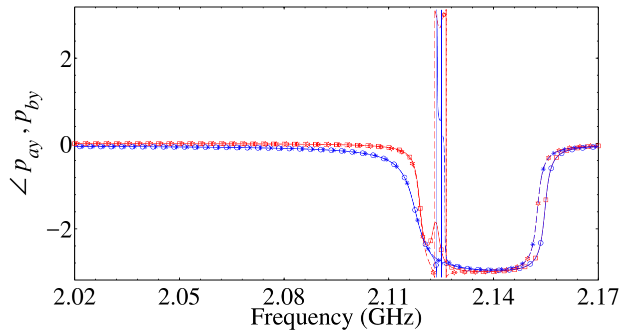

(b) Phase (radians)

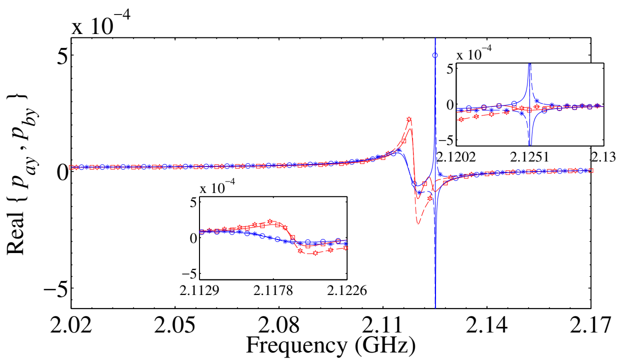

(c) Real part

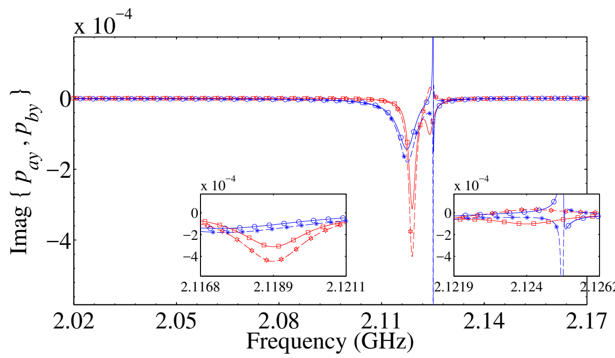

(d) Imaginary part

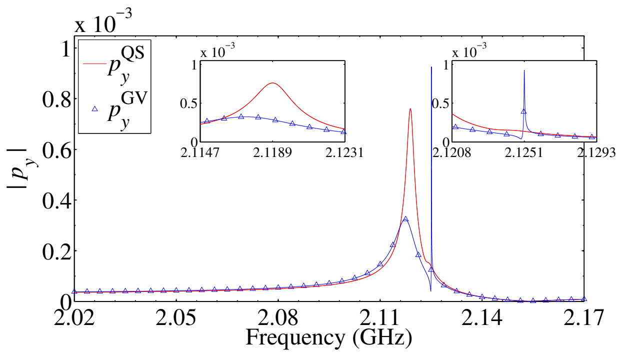

(e) Magnitude

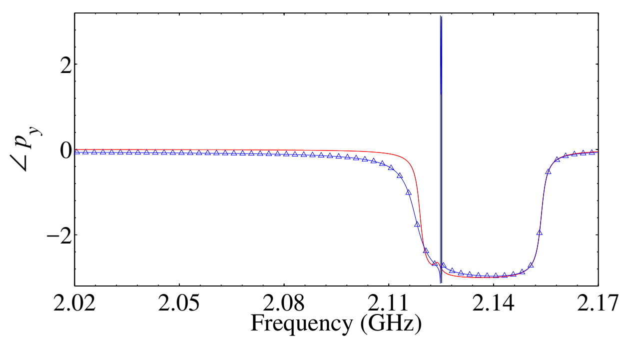

(f) Phase (radians)

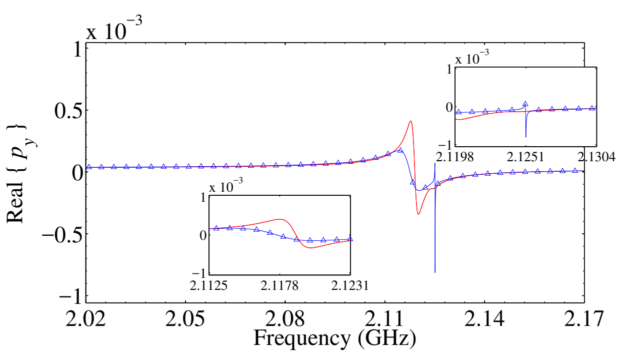

(g) Real part

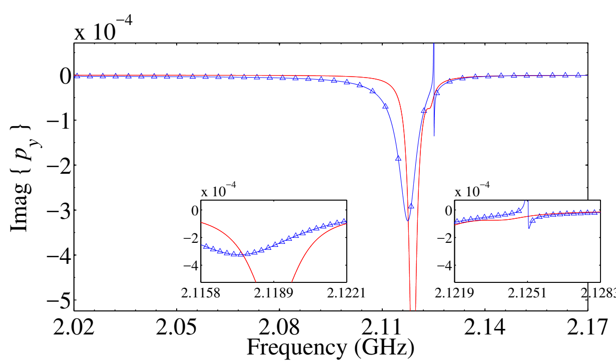

(h) Imaginary part

Figure 3.19: Pair of dielectric spheres: Case I orientation, radius of b is 0.1% larger than a, spacing 0.03 m, $\epsilon_r = 100$, and $\delta_T = 10^{-2.95}$. Electric dipole moments normalized such that $\epsilon E^{inc} = 1$.

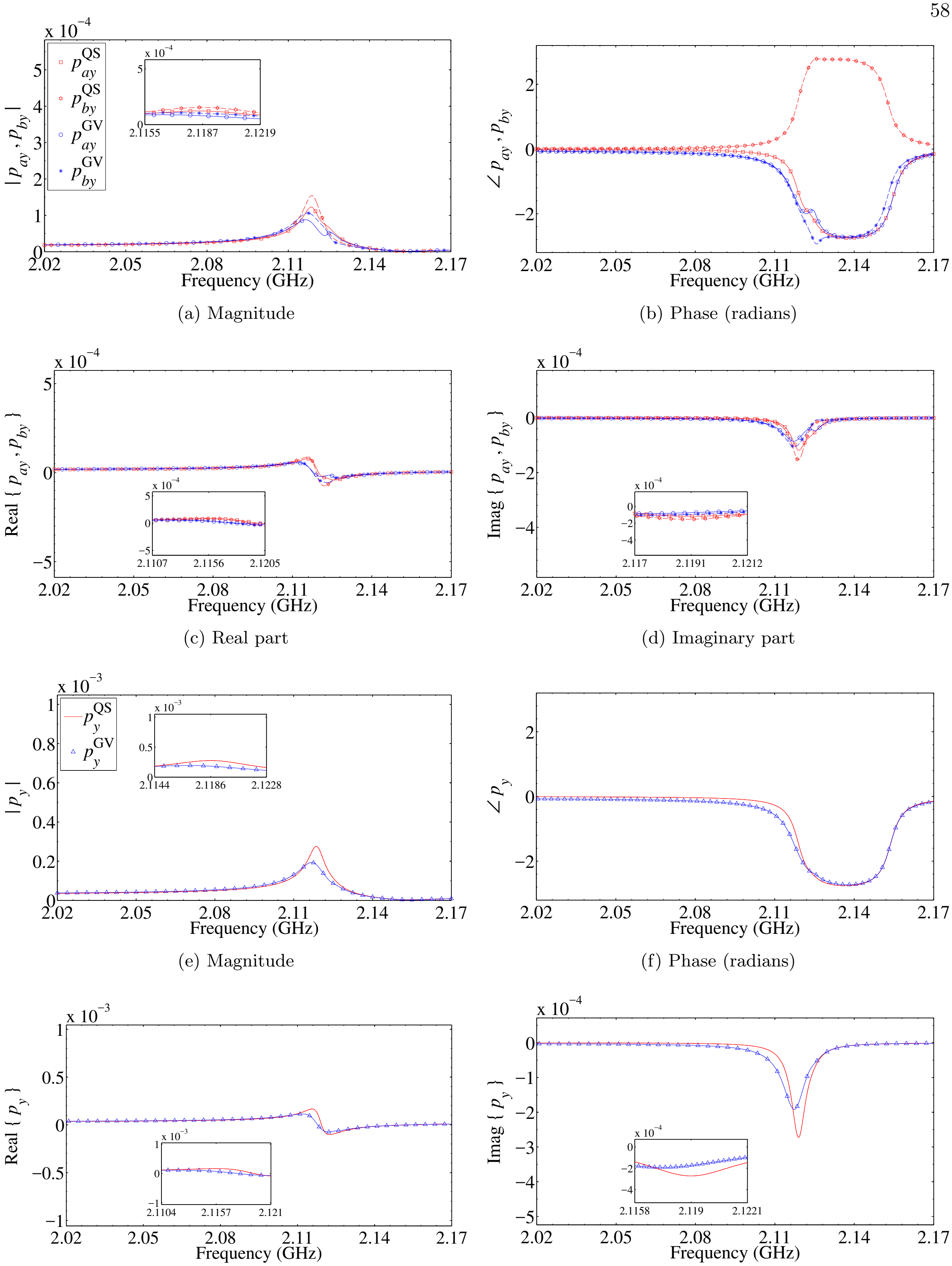

(a) Magnitude

(b) Phase (radians)

(c) Real part

(d) Imaginary part

(e) Magnitude

(f) Phase (radians)

(g) Real part

(h) Imaginary part

Figure 3.20: Pair of dielectric spheres: Case I orientation, radius of b is 0.1% larger than a, spacing 0.03 m, $\epsilon_r = 100$, and $\delta_T = 10^{-2.5}$. Electric dipole moments normalized such that $\epsilon E^{inc} = 1$.

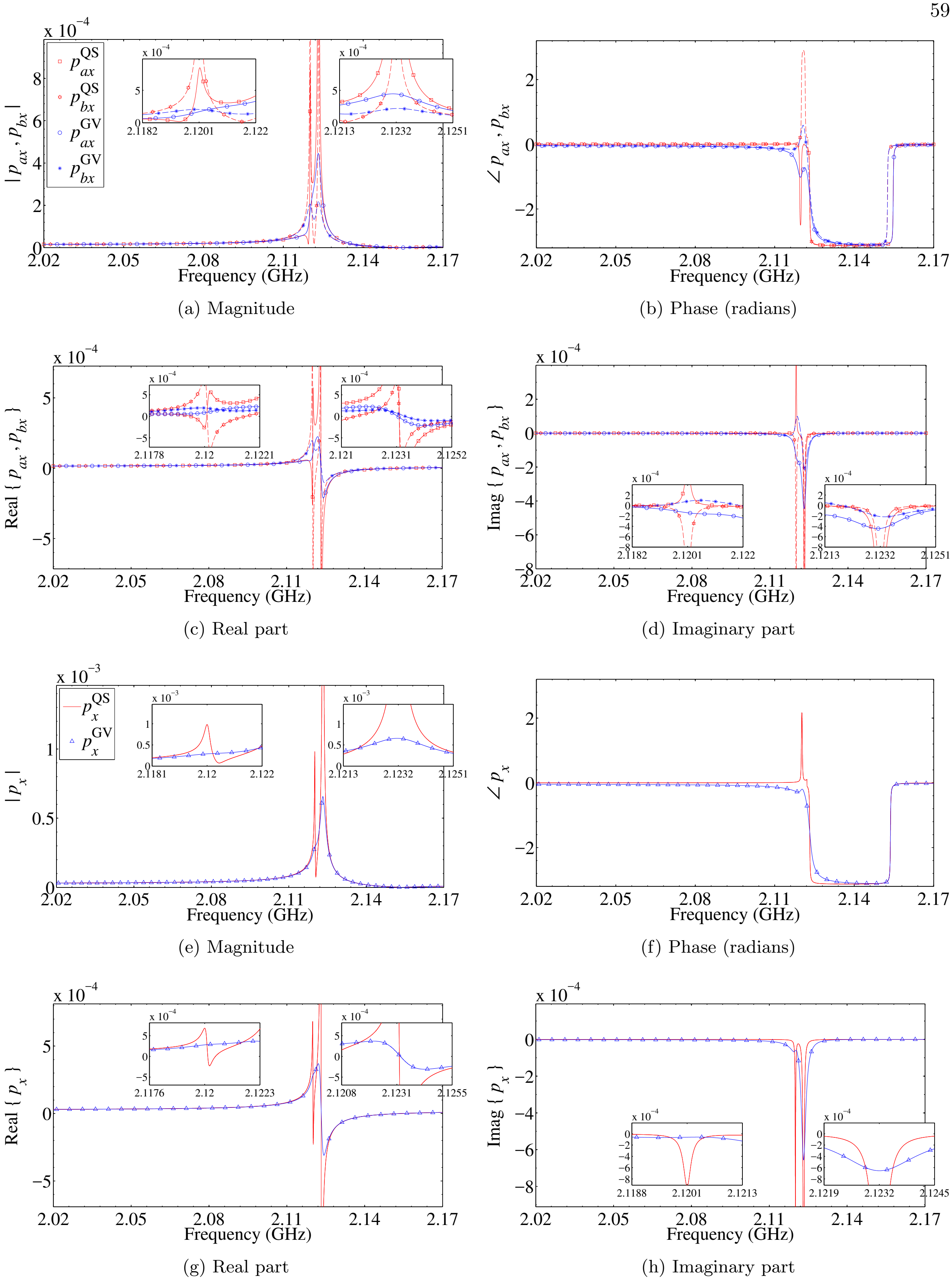

(a) Magnitude

(b) Phase (radians)

(c) Real part

(d) Imaginary part

(e) Magnitude

(f) Phase (radians)

(g) Real part

(h) Imaginary part

Figure 3.21: Pair of dielectric spheres: Case II orientation, radius of b is 0.1% larger than a, spacing 0.03 m, $\epsilon_r = 100$, and $\delta_T = 10^{-4}$. Electric dipole moments normalized such that $\epsilon E^{inc} = 1$.

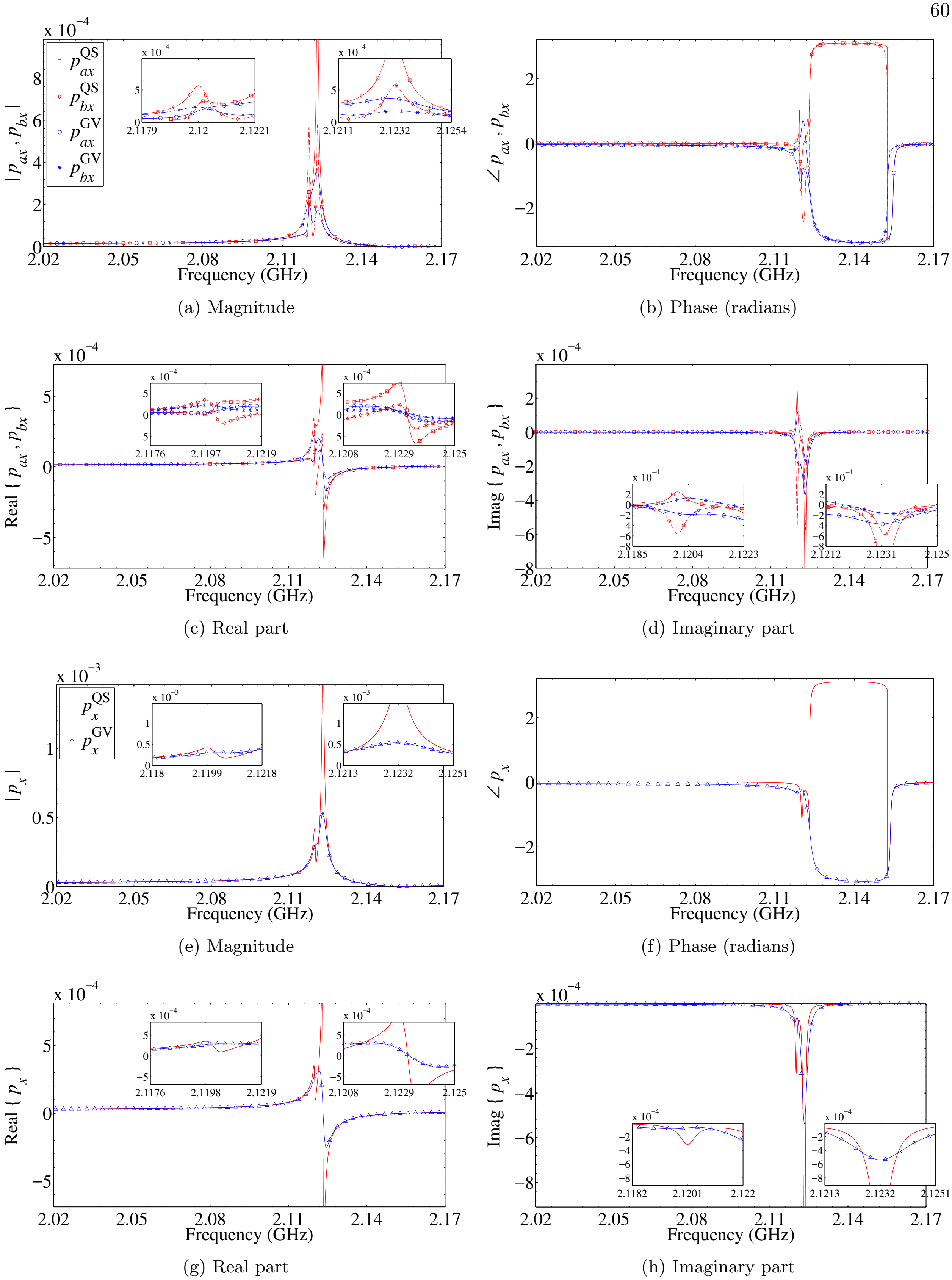

(a) Magnitude

(b) Phase (radians)

(c) Real part

(d) Imaginary part

(e) Magnitude

(f) Phase (radians)

(g) Real part

(h) Imaginary part

Figure 3.22: Pair of dielectric spheres: Case II orientation, radius of b is 0.1% larger than a, spacing 0.03 m, $\epsilon_r = 100$, and $\delta_T = 10^{-3.5}$. Electric dipole moments normalized such that $\epsilon E^{inc} = 1$.

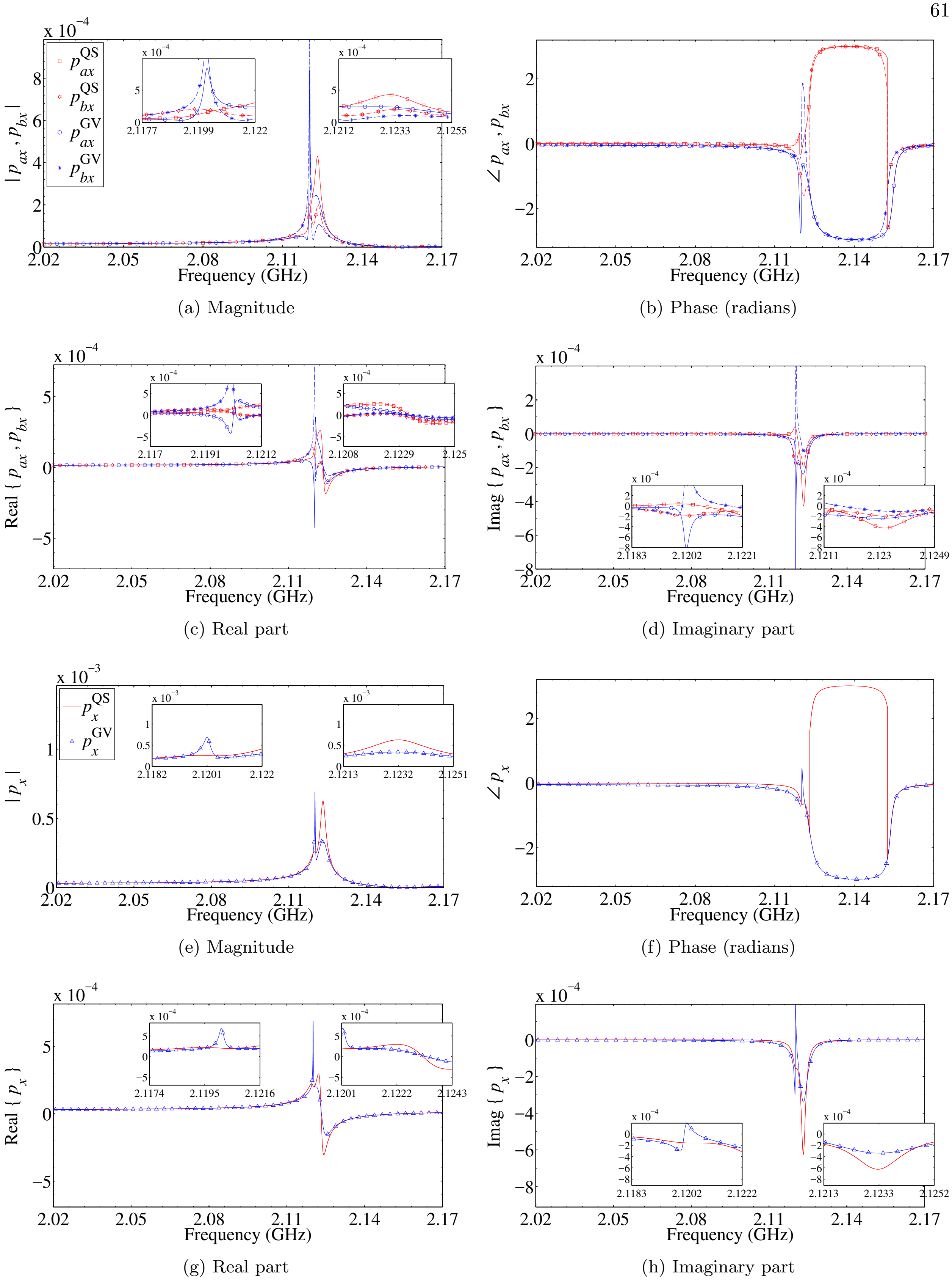

(a) Magnitude

(b) Phase (radians)

(c) Real part

(d) Imaginary part

(e) Magnitude

(f) Phase (radians)

(g) Real part

(h) Imaginary part

Figure 3.23: Pair of dielectric spheres: Case II orientation, radius of b is 0.1% larger than a, spacing 0.03 m, $\epsilon_r = 100$, and $\delta_T = 10^{-3}$. Electric dipole moments normalized such that $\epsilon E^{inc} = 1$.

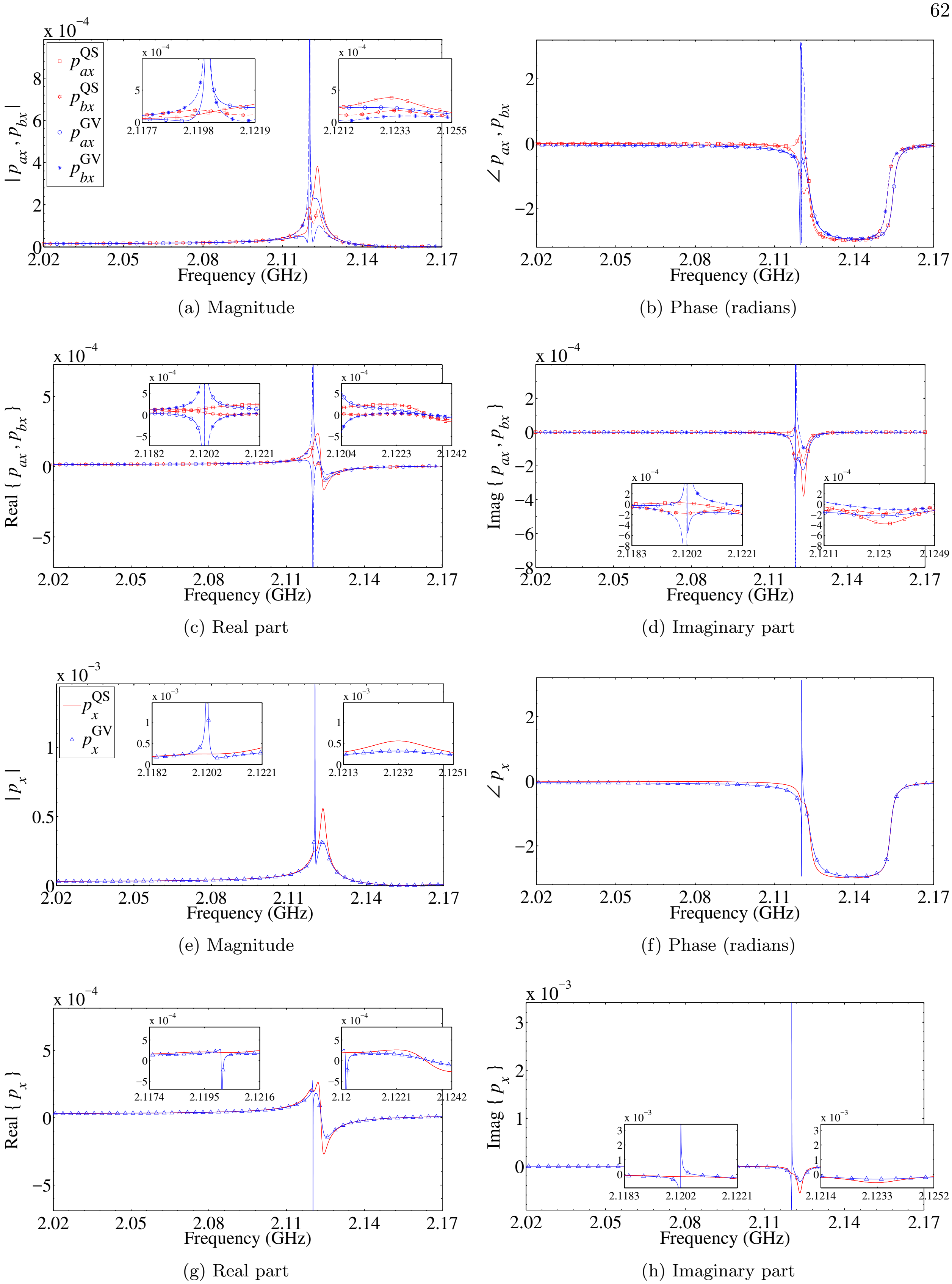

(a) Magnitude

(b) Phase (radians)

(c) Real part

(d) Imaginary part

(e) Magnitude

(f) Phase (radians)

(g) Real part

(h) Imaginary part

Figure 3.24: Pair of dielectric spheres: Case II orientation, radius of b is 0.1% larger than a, spacing 0.03 m, $\epsilon_r = 100$, and $\delta_T = 10^{-2.95}$. Electric dipole moments normalized such that $\epsilon E^{inc} = 1$.

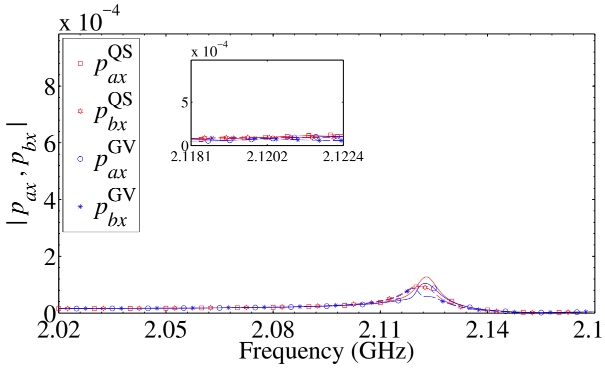

(a) Magnitude

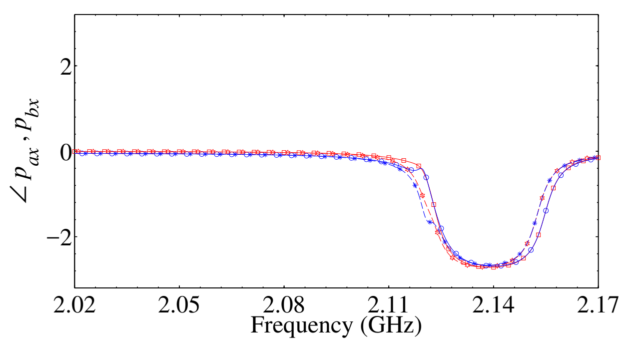

(b) Phase (radians)

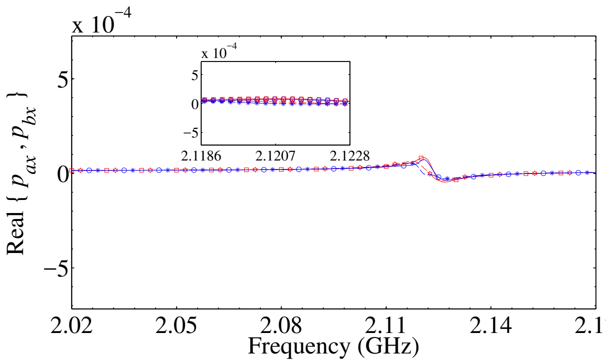

(c) Real part

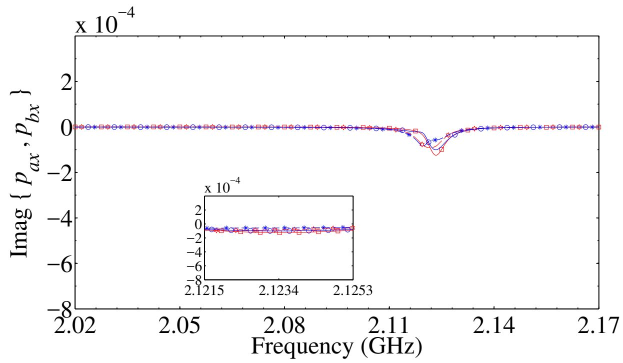

(d) Imaginary part

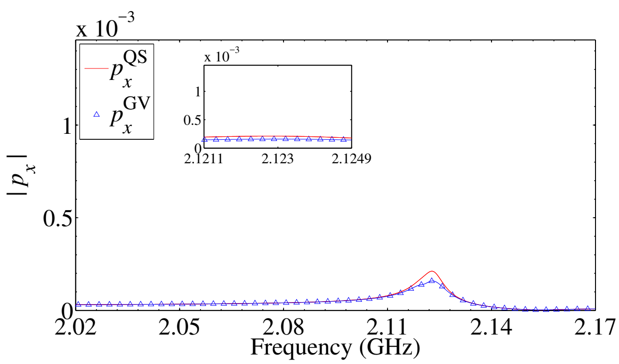

(e) Magnitude

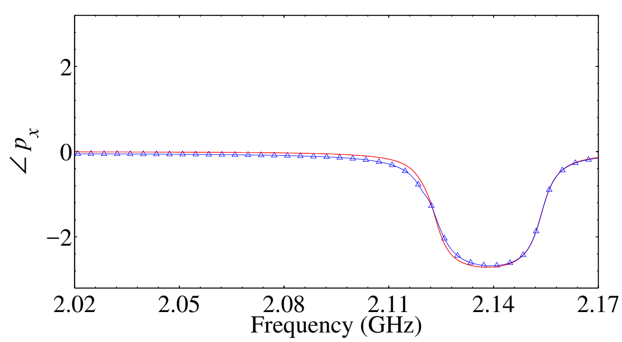

(f) Phase (radians)

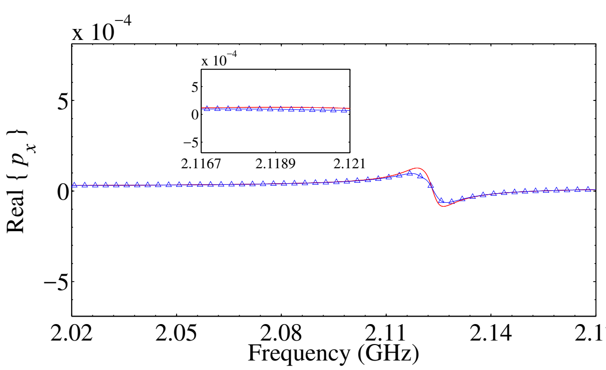

(g) Real part

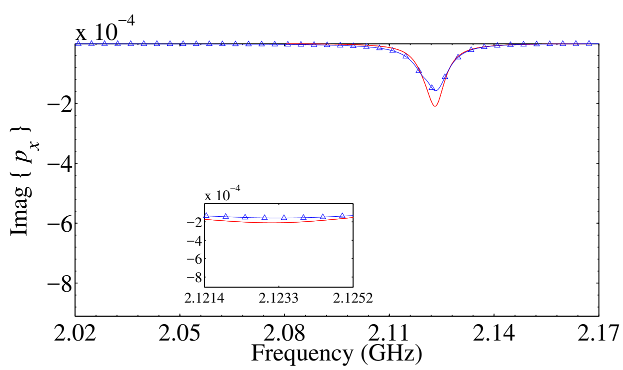

(h) Imaginary part

Figure 3.25: Pair of dielectric spheres: Case II orientation, radius of b is 0.1% larger than a, spacing 0.03 m, $\epsilon_r = 100$, and $\delta_T = 10^{-2.5}$. Electric dipole moments normalized such that $\epsilon E^{inc} = 1$.

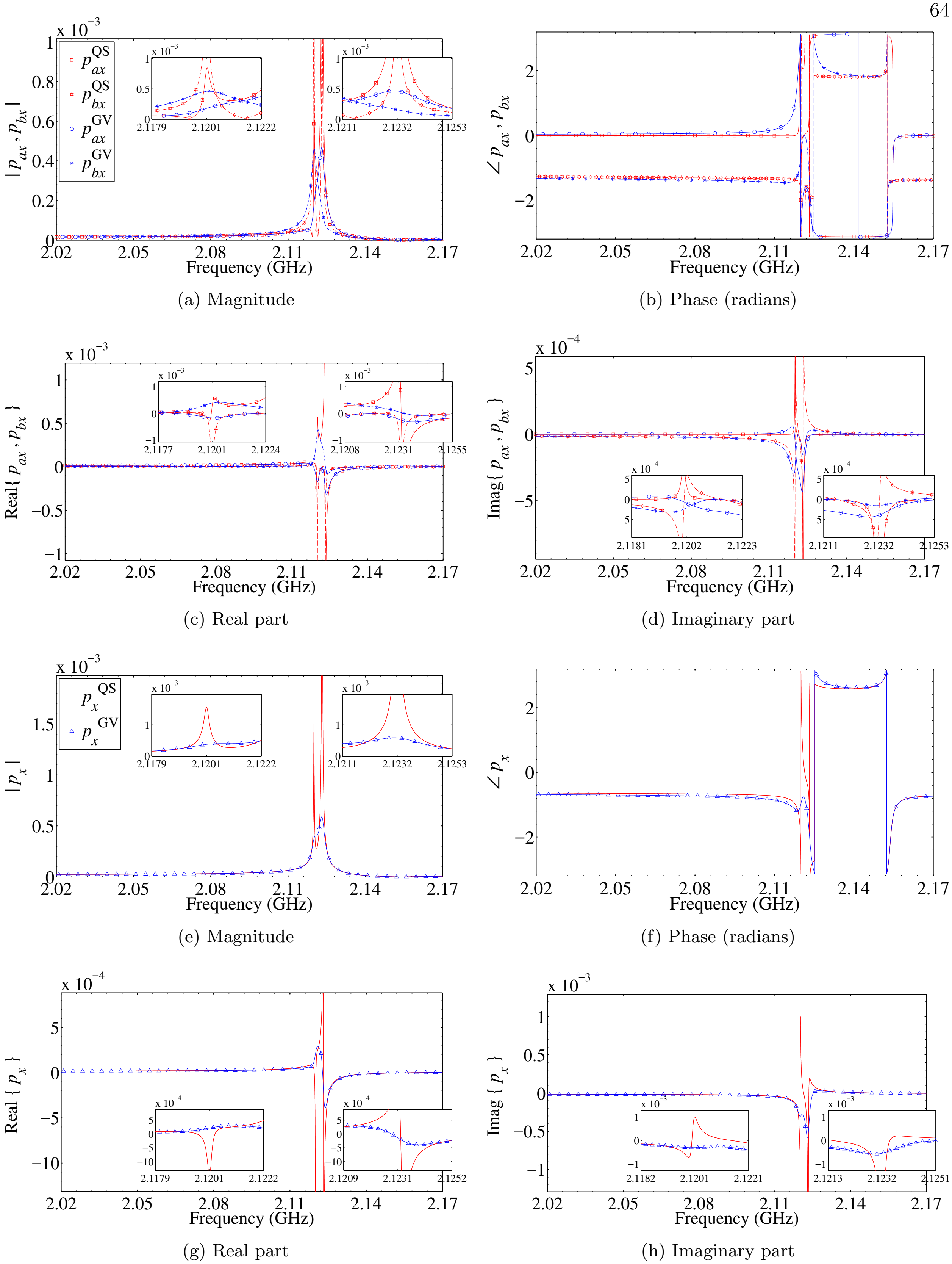

(a) Magnitude (b) Phase (radians)

(c) Real part (d) Imaginary part

(e) Magnitude (f) Phase (radians)

(g) Real part (h) Imaginary part

Figure 3.26: Pair of dielectric spheres: Case III orientation, radius of b is 0.1% larger than a, spacing 0.03 m, $\epsilon_r = 100$, and $\delta_T = 10^{-4}$. Electric dipole moments normalized such that $\epsilon E^{inc} = 1$.

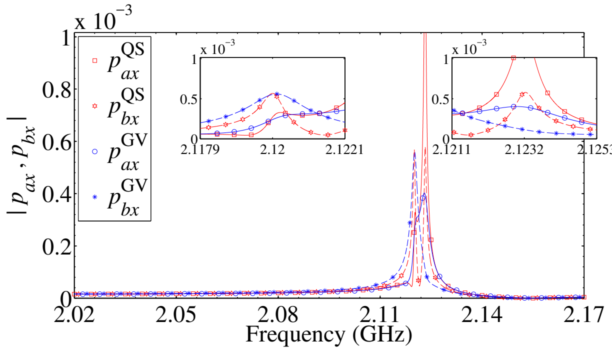

(a) Magnitude

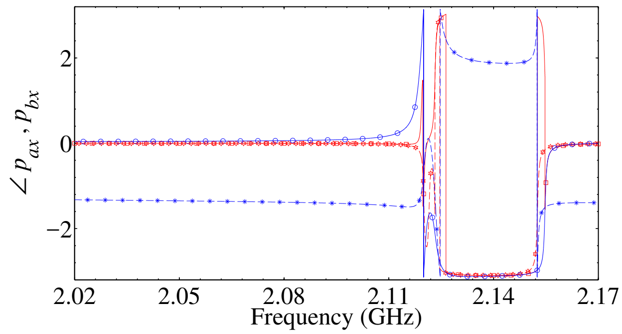

(b) Phase (radians)

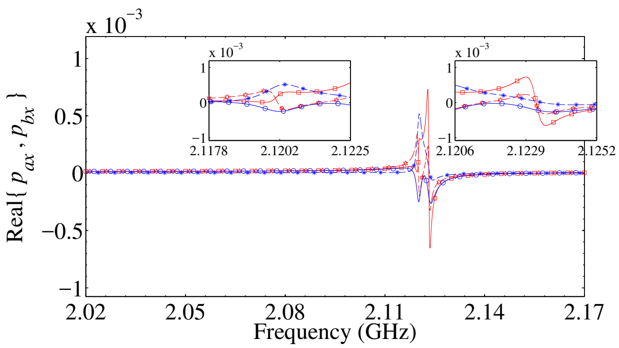

(c) Real part

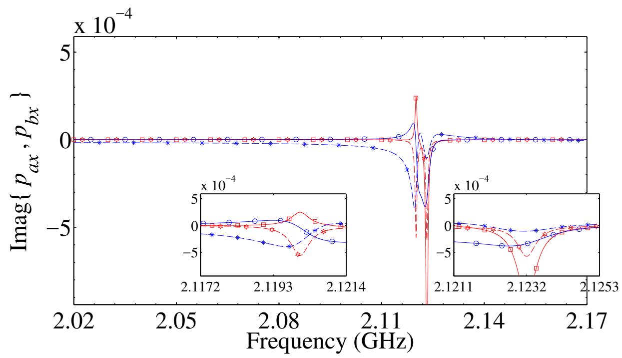

(d) Imaginary part

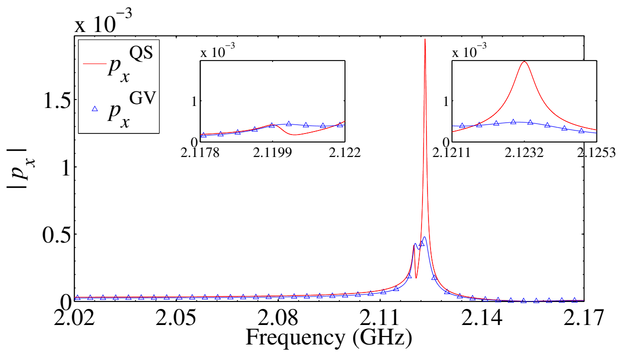

(e) Magnitude

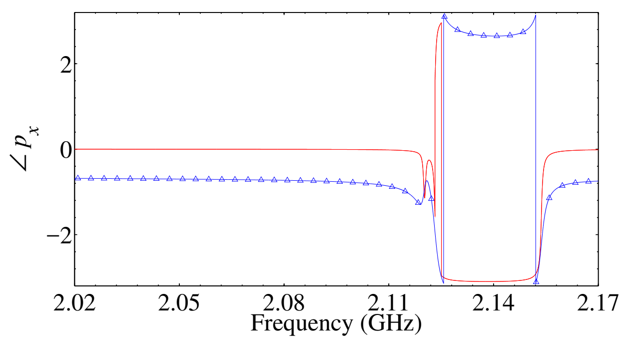

(f) Phase (radians)

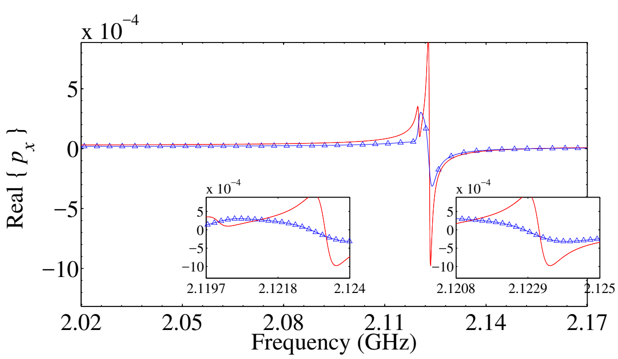

(g) Real part

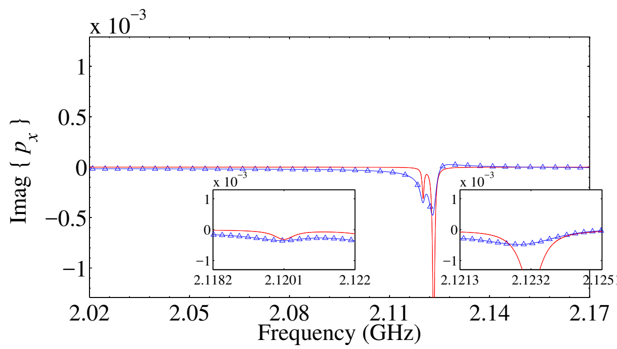

(h) Imaginary part

Figure 3.27: Pair of dielectric spheres: Case III orientation, radius of b is 0.1% larger than a, spacing 0.03 m, $\epsilon_r = 100$, and $\delta_T = 10^{-3.5}$. Electric dipole moments normalized such that $\epsilon E^{inc} = 1$.

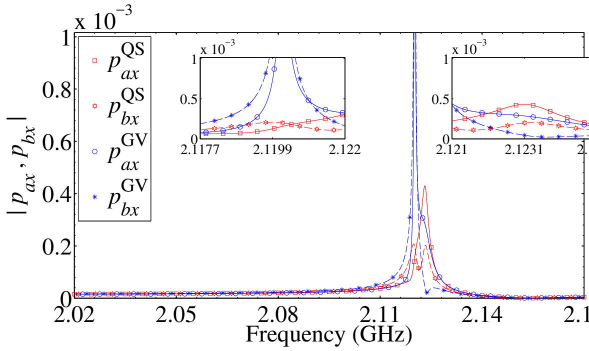

(a) Magnitude

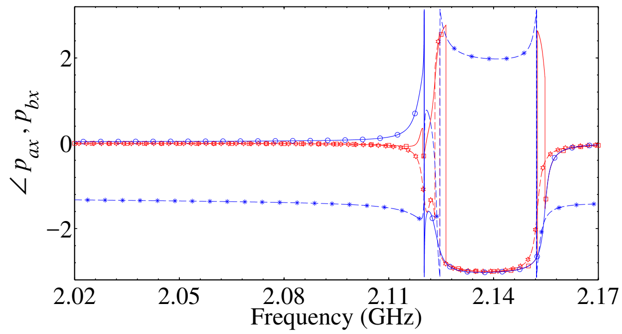

(b) Phase (radians)

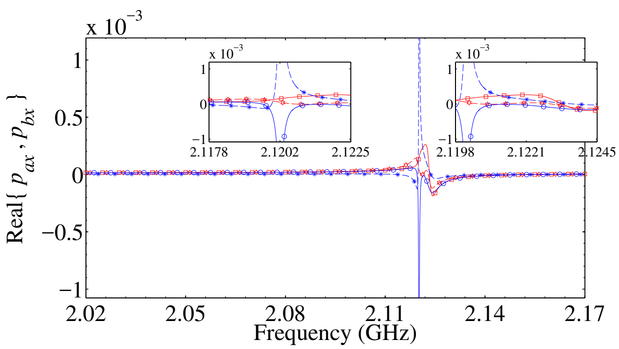

(c) Real part

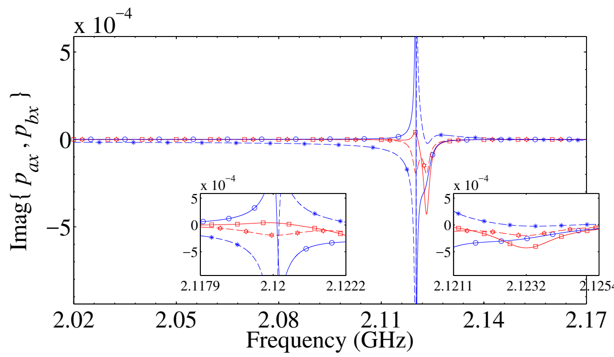

(d) Imaginary part

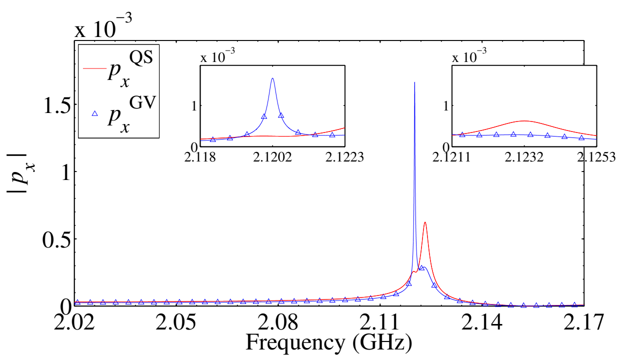

(e) Magnitude

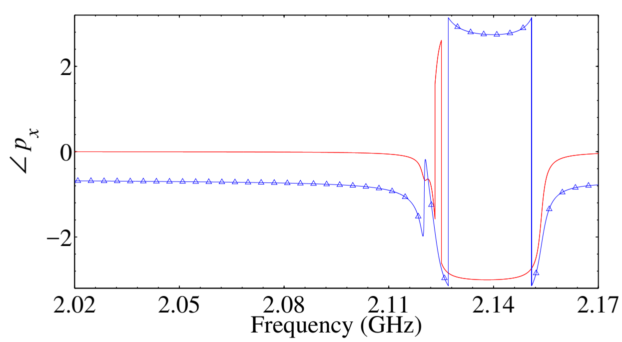

(f) Phase (radians)

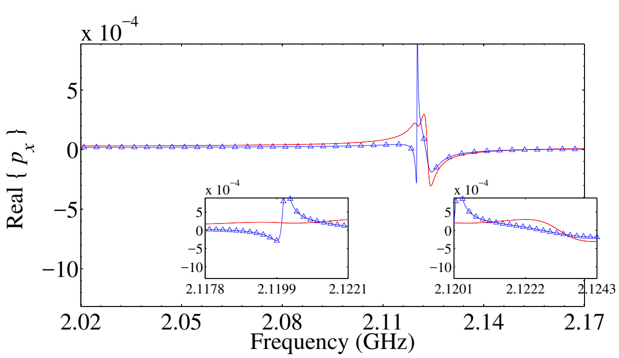

(g) Real part

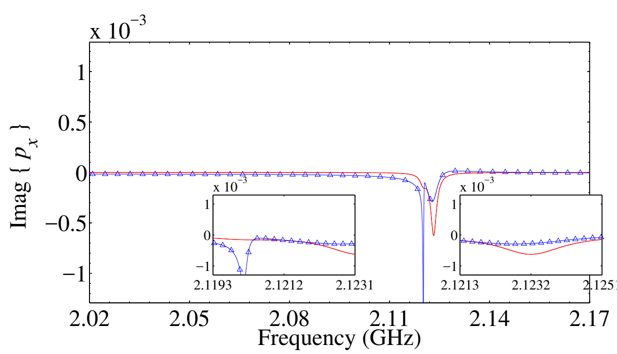

(h) Imaginary part

Figure 3.28: Pair of dielectric spheres: Case III orientation, radius of b is 0.1% larger than a, spacing 0.03 m, $\epsilon_r = 100$, and $\delta_T = 10^{-3}$. Electric dipole moments normalized such that $\epsilon E^{inc} = 1$.

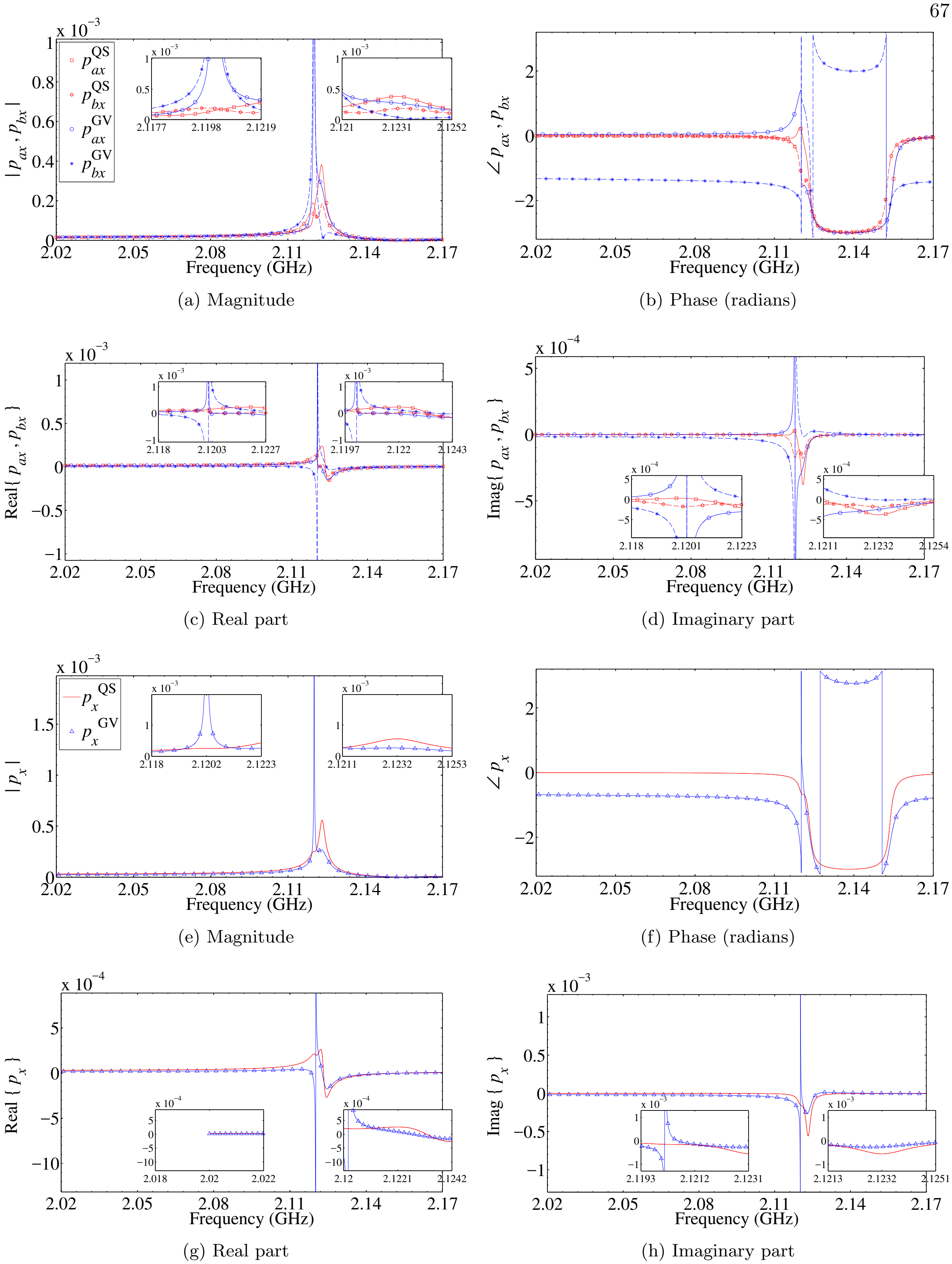

(a) Magnitude (b) Phase (radians)

(c) Real part (d) Imaginary part

(e) Magnitude (f) Phase (radians)

(g) Real part (h) Imaginary part

Figure 3.29: Pair of dielectric spheres: Case III orientation, radius of b is 0.1% larger than a, spacing 0.03 m, $\epsilon_r = 100$, and $\delta_T = 10^{-2.95}$. Electric dipole moments normalized such that $\epsilon E^{inc} = 1$.

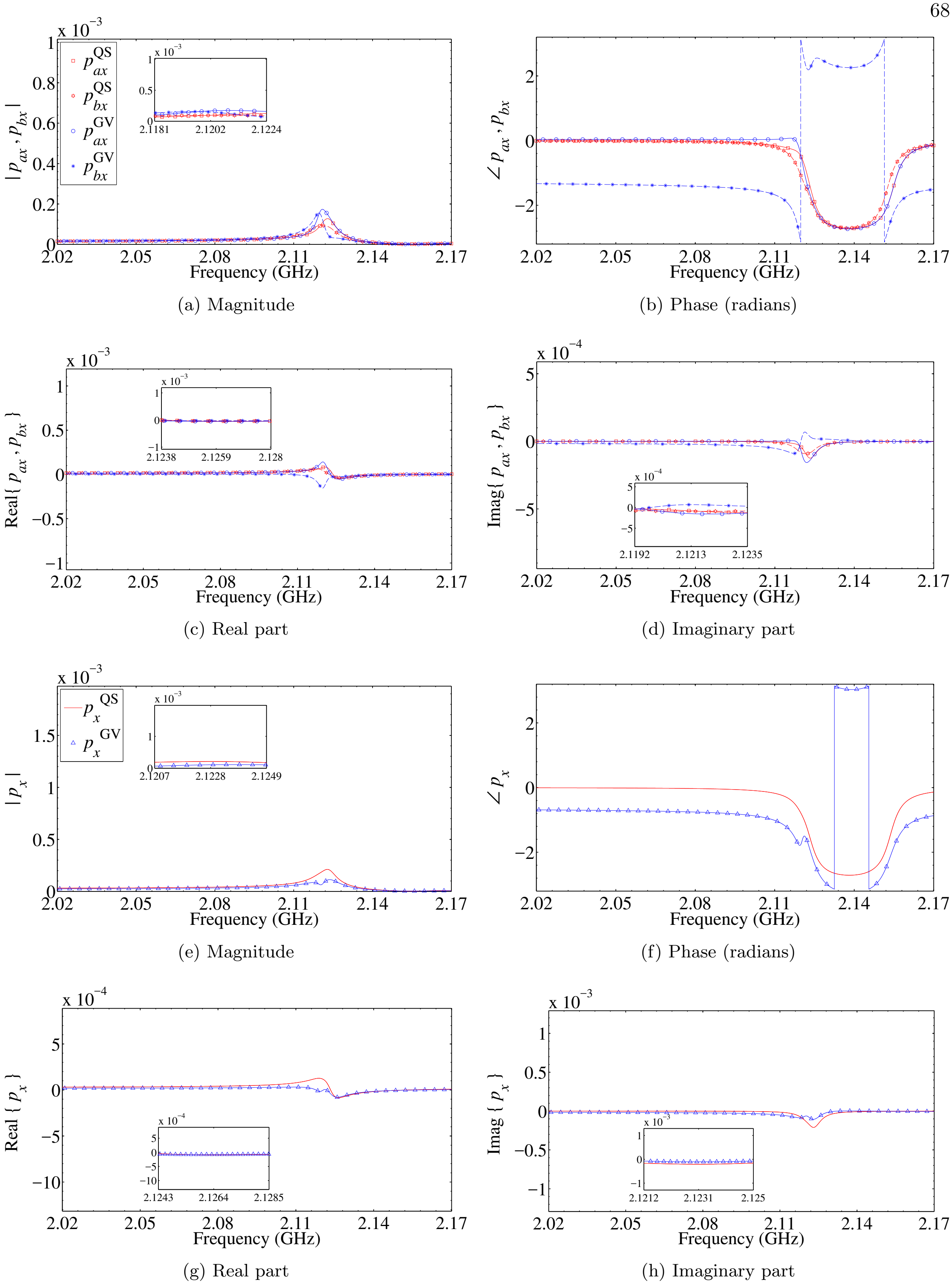

(a) Magnitude

(b) Phase (radians)

(c) Real part

(d) Imaginary part

(e) Magnitude

(f) Phase (radians)

(g) Real part

(h) Imaginary part

Figure 3.30: Pair of dielectric spheres: Case III orientation, radius of b is 0.1% larger than a, spacing 0.03 m, $\epsilon_r = 100$, and $\delta_T = 10^{-2.5}$. Electric dipole moments normalized such that $\epsilon E^{inc} = 1$.

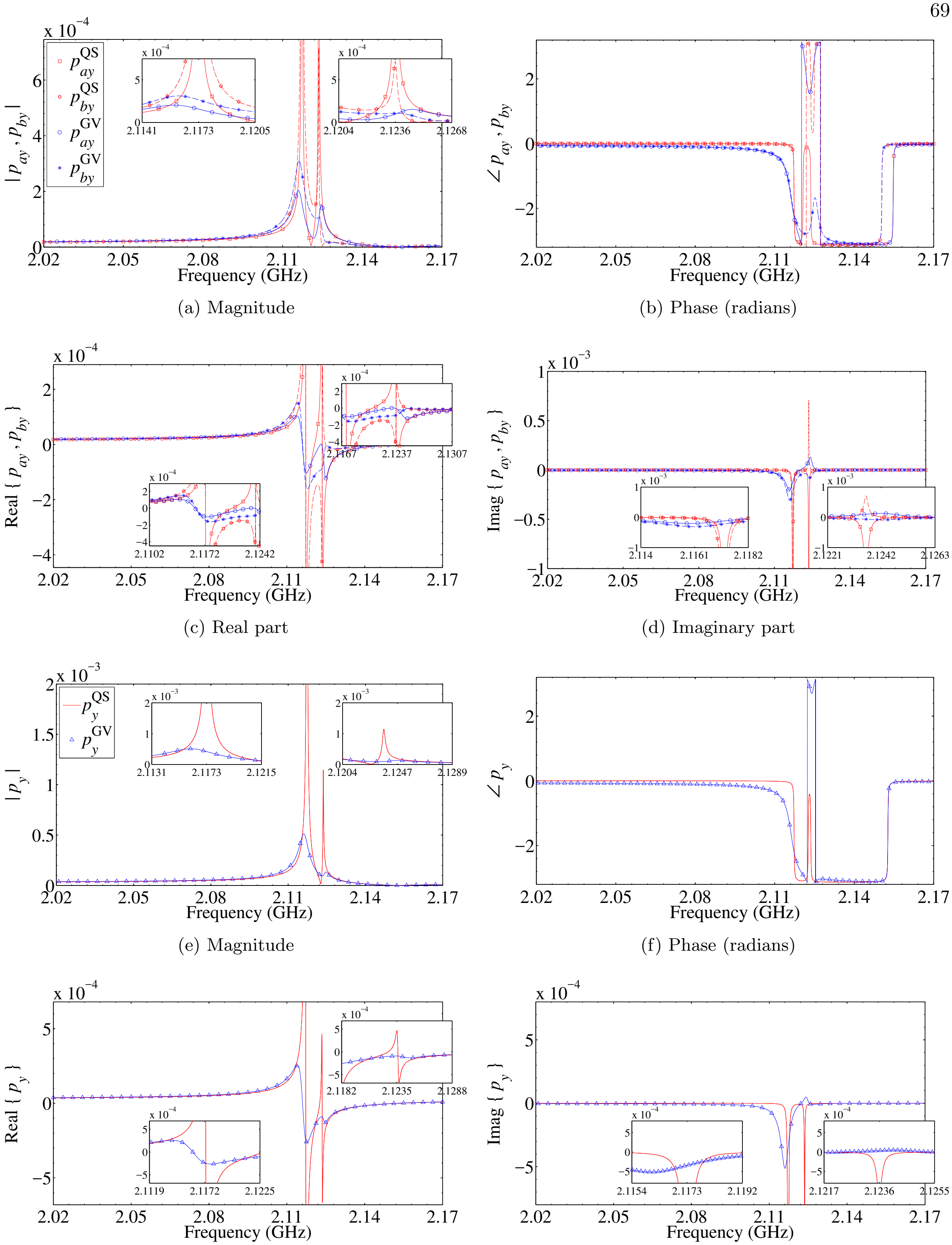

(a) Magnitude

(b) Phase (radians)

(c) Real part

(d) Imaginary part

(e) Magnitude

(f) Phase (radians)

(g) Real part

(h) Imaginary part

Figure 3.31: Pair of dielectric spheres: Case I orientation, radius of b is 0.2% larger than a, spacing 0.03 m, $\epsilon_r = 100$, and $\delta_T = 10^{-4}$. Electric dipole moments normalized such that $\epsilon E^{inc} = 1$.

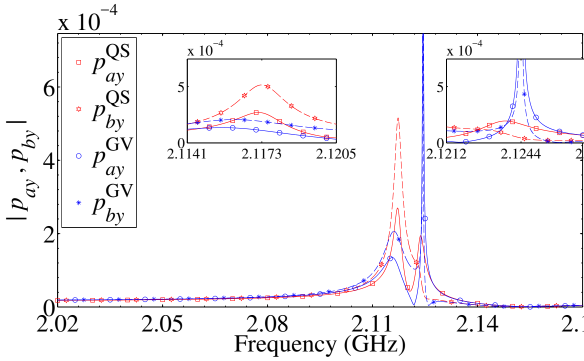

(a) Magnitude

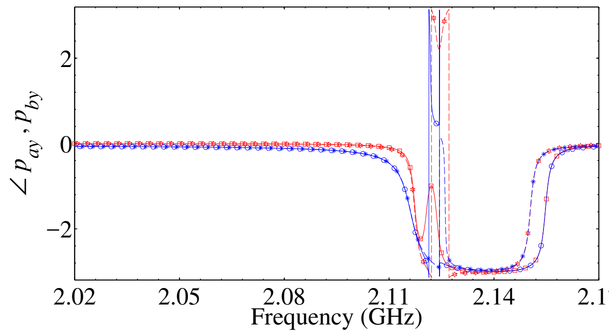

(b) Phase (radians)

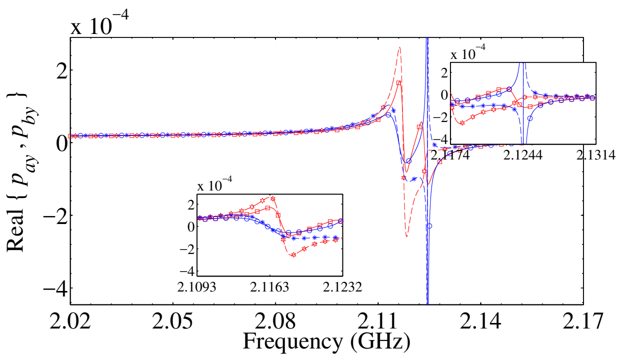

(c) Real part

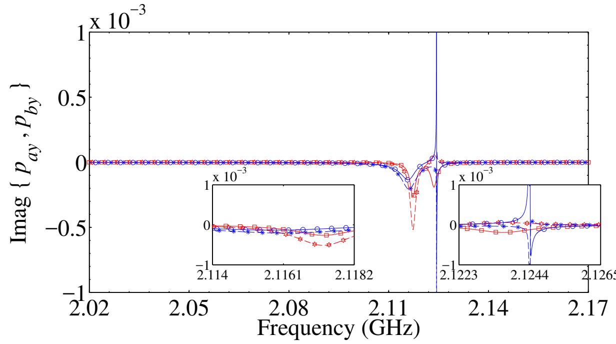

(d) Imaginary part

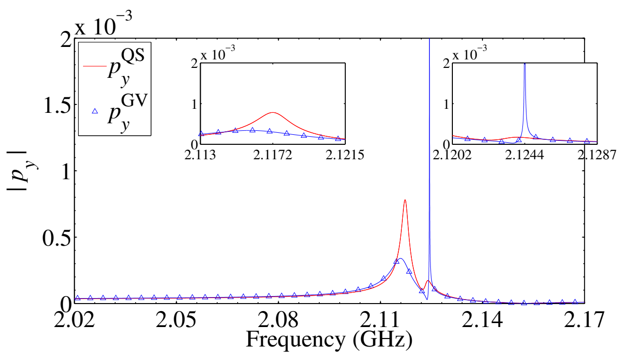

(e) Magnitude

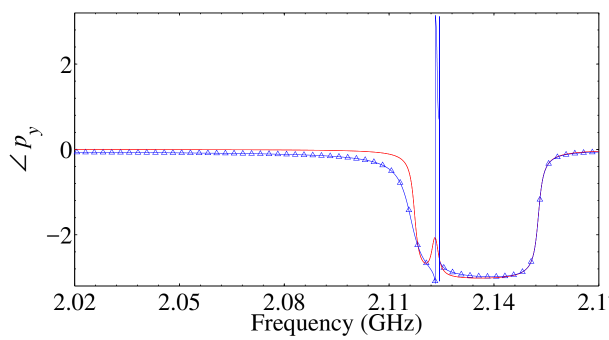

(f) Phase (radians)

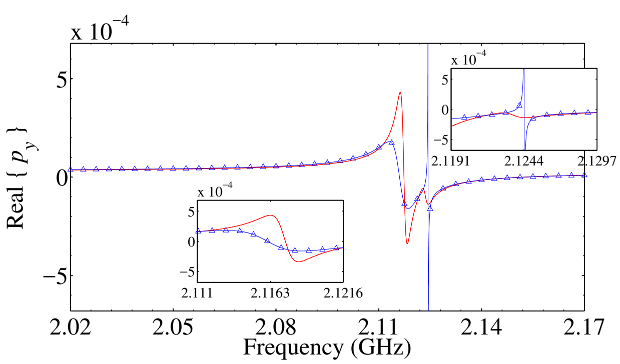

(g) Real part

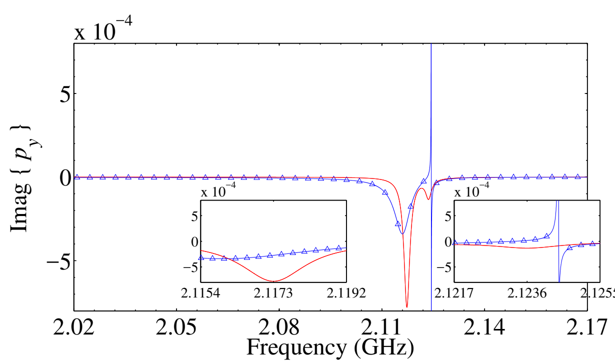

(h) Imaginary part

Figure 3.32: Pair of dielectric spheres: Case I orientation, radius of b is 0.2% larger than a, spacing 0.03 m, $\epsilon_r = 100$, and $\delta_T = 10^{-3}$. Electric dipole moments normalized such that $\epsilon E^{inc} = 1$.

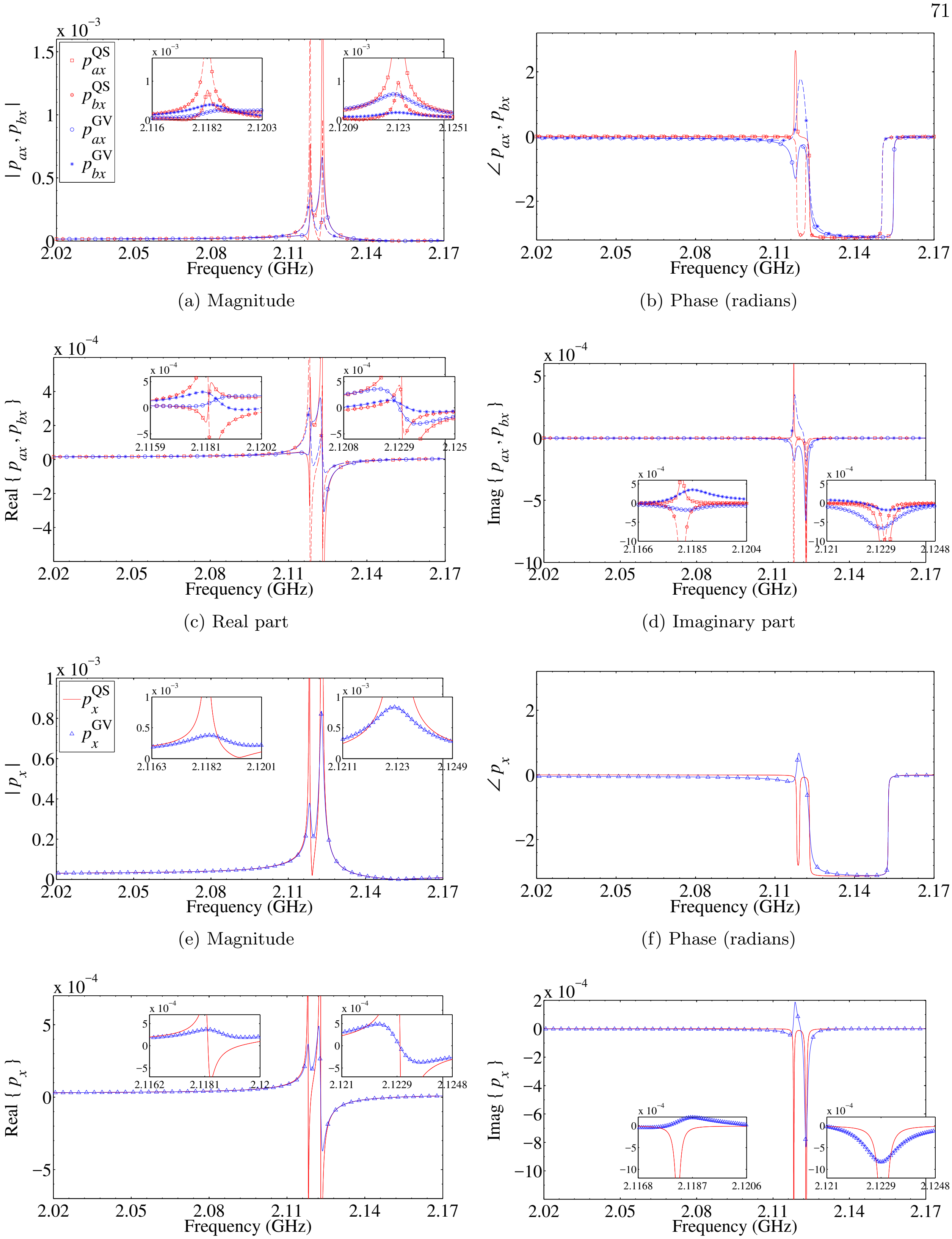

(a) Magnitude

(b) Phase (radians)

(c) Real part

(d) Imaginary part

(e) Magnitude

(f) Phase (radians)

(g) Real part

(h) Imaginary part

Figure 3.33: Pair of dielectric spheres: Case II orientation, radius of b is 0.2% larger than a, spacing 0.03 m, $\epsilon_r = 100$, and $\delta_T = 10^{-4}$. Electric dipole moments normalized such that $\epsilon E^{inc} = 1$.

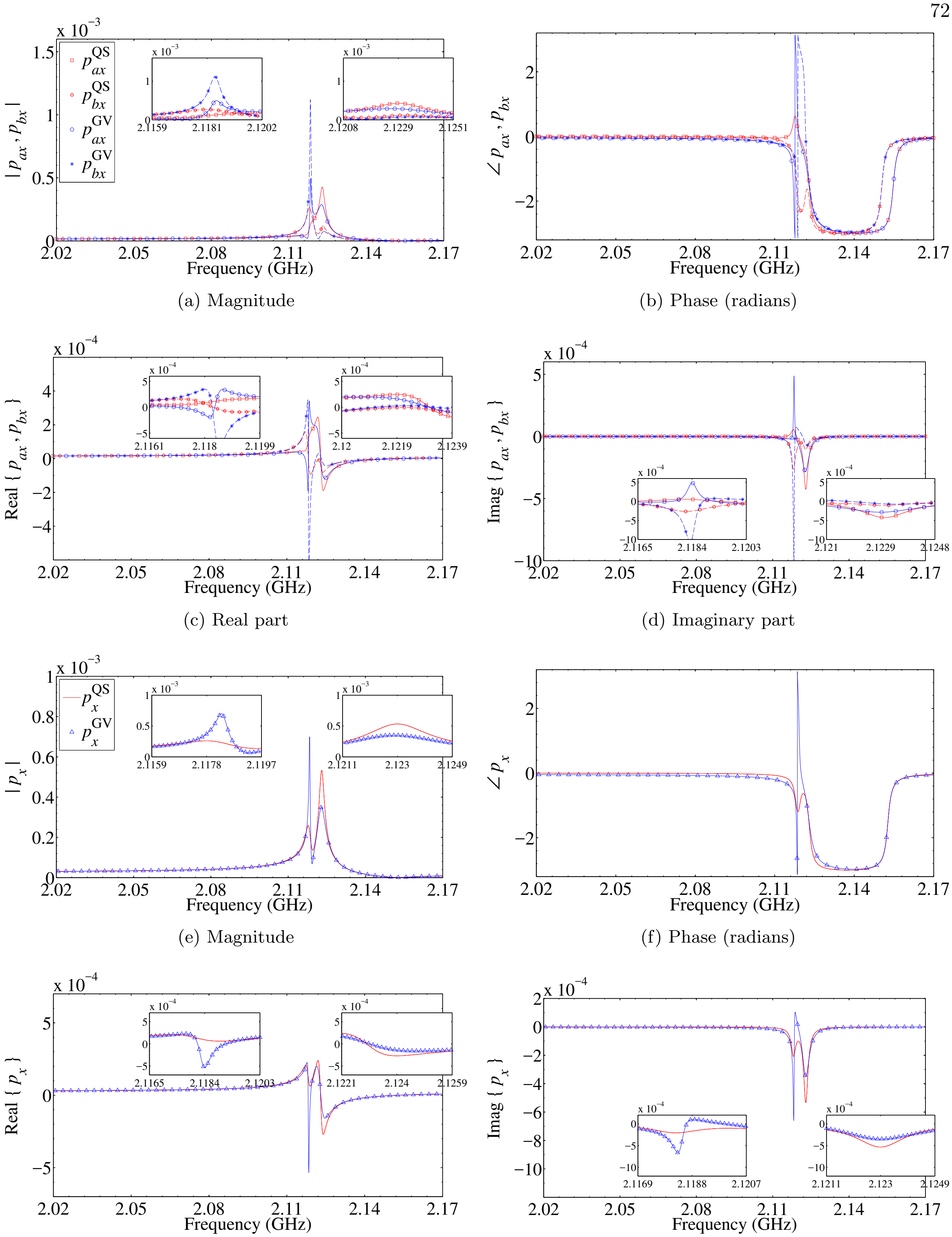

(a) Magnitude (b) Phase (radians)

(c) Real part (d) Imaginary part

(e) Magnitude (f) Phase (radians)

(g) Real part (h) Imaginary part

Figure 3.34: Pair of dielectric spheres: Case II orientation, radius of b is 0.2% larger than a, spacing 0.03 m, $\epsilon_r = 100$, and $\delta_T = 10^{-3}$. Electric dipole moments normalized such that $\epsilon E^{inc} = 1$.

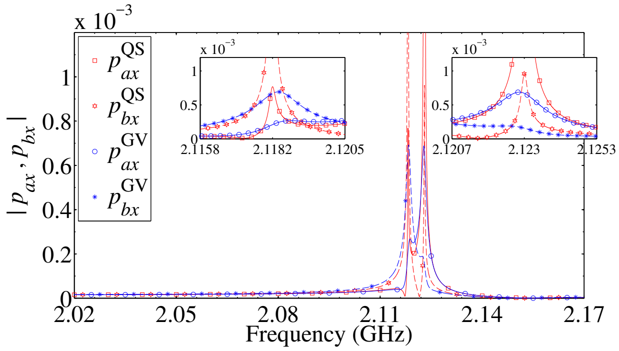

(a) Magnitude

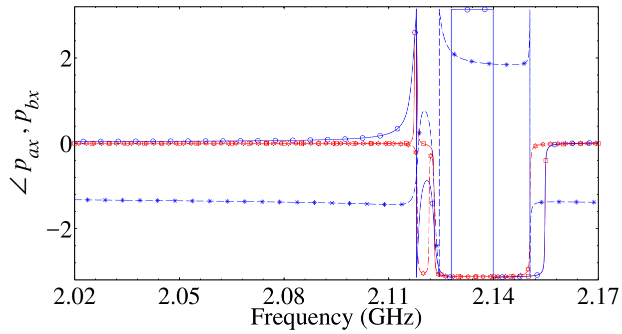

(b) Phase (radians)

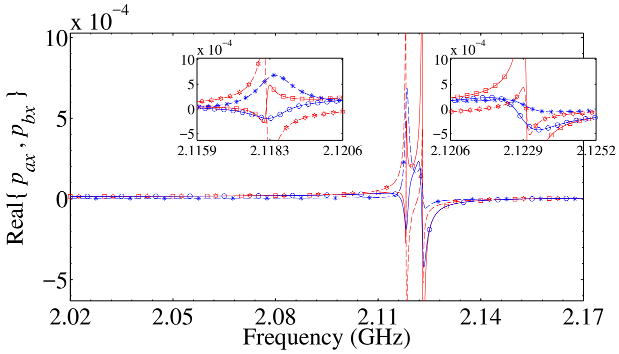

(c) Real part

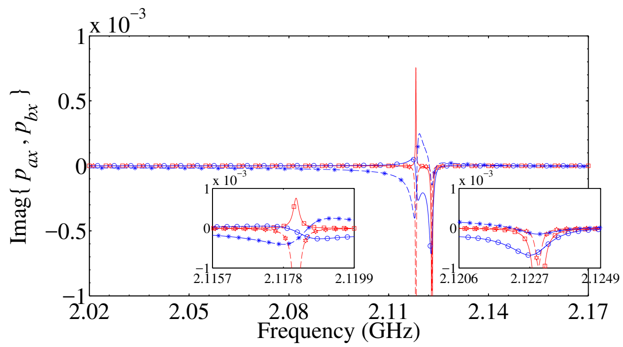

(d) Imaginary part

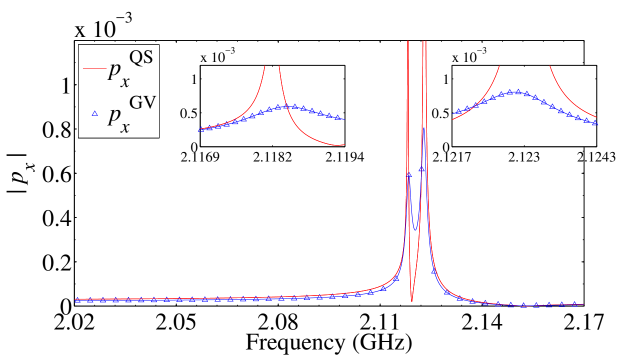

(e) Magnitude

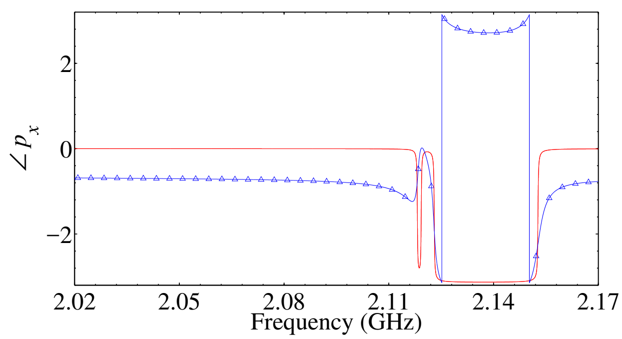

(f) Phase (radians)

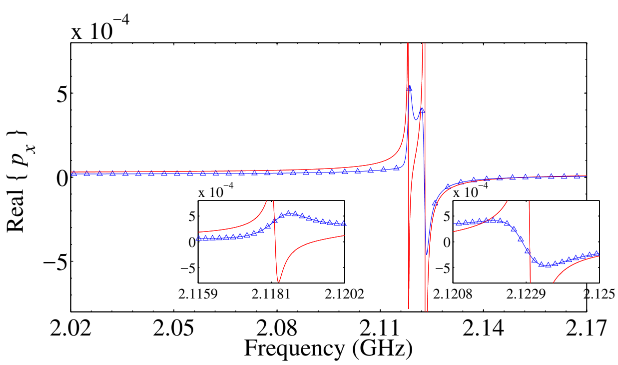

(g) Real part

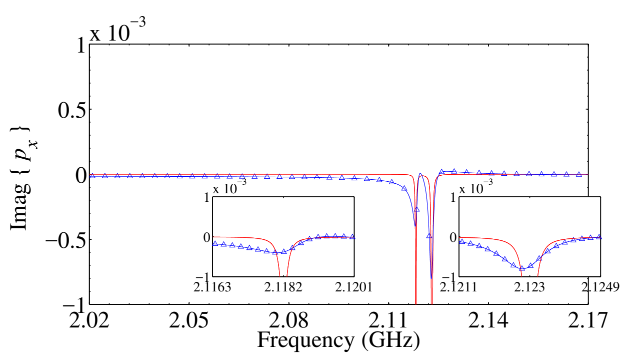

(h) Imaginary part

Figure 3.35: Pair of dielectric spheres: Case III orientation, radius of b is 0.2% larger than a, spacing 0.03 m, $\epsilon_r = 100$, and $\delta_T = 10^{-4}$. Electric dipole moments normalized such that $\epsilon E^{inc} = 1$.

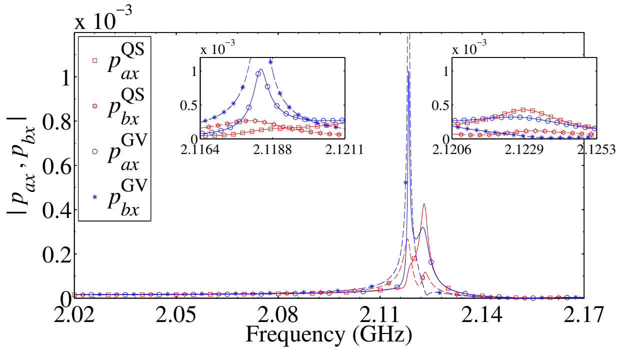

(a) Magnitude

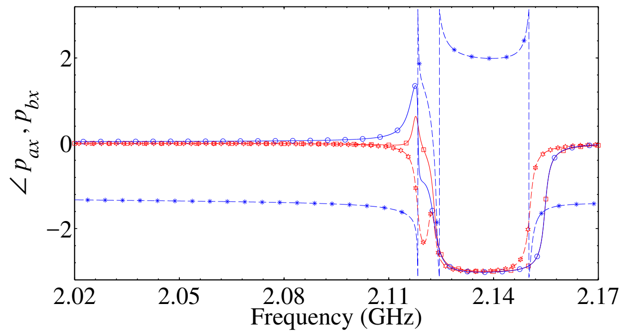

(b) Phase (radians)

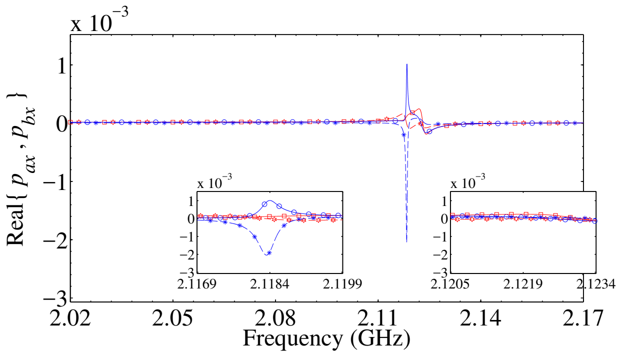

(c) Real part

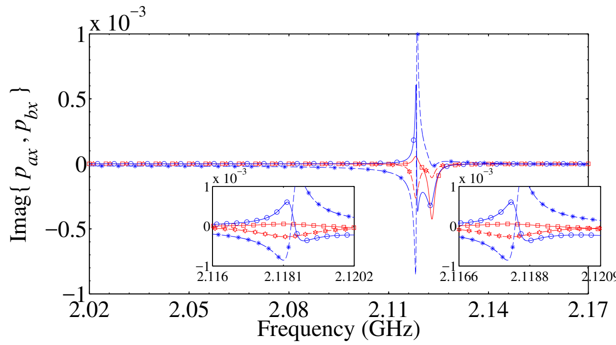

(d) Imaginary part

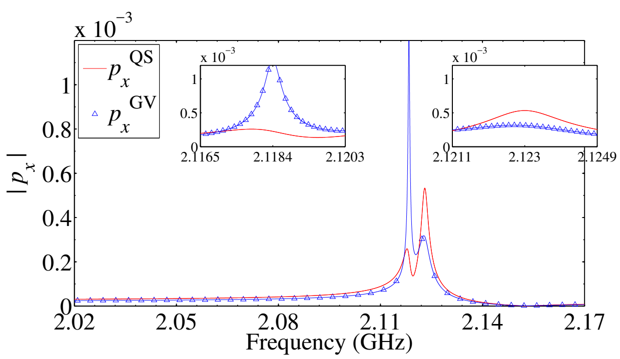

(e) Magnitude

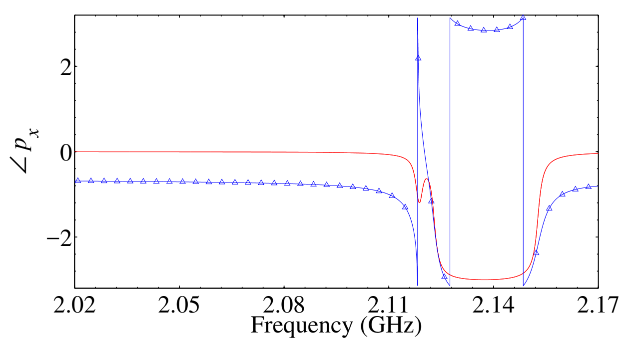

(f) Phase (radians)

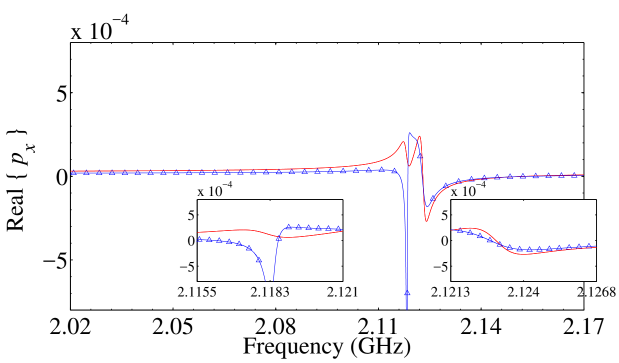

(g) Real part

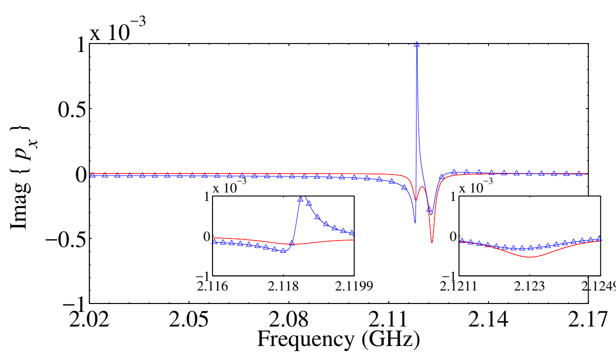

(h) Imaginary part

Figure 3.36: Pair of dielectric spheres: Case III orientation, radius of b is 0.2% larger than a, spacing 0.03 m, $\epsilon_r = 100$, and $\delta_T = 10^{-3}$. Electric dipole moments normalized such that $\epsilon E^{inc} = 1$.

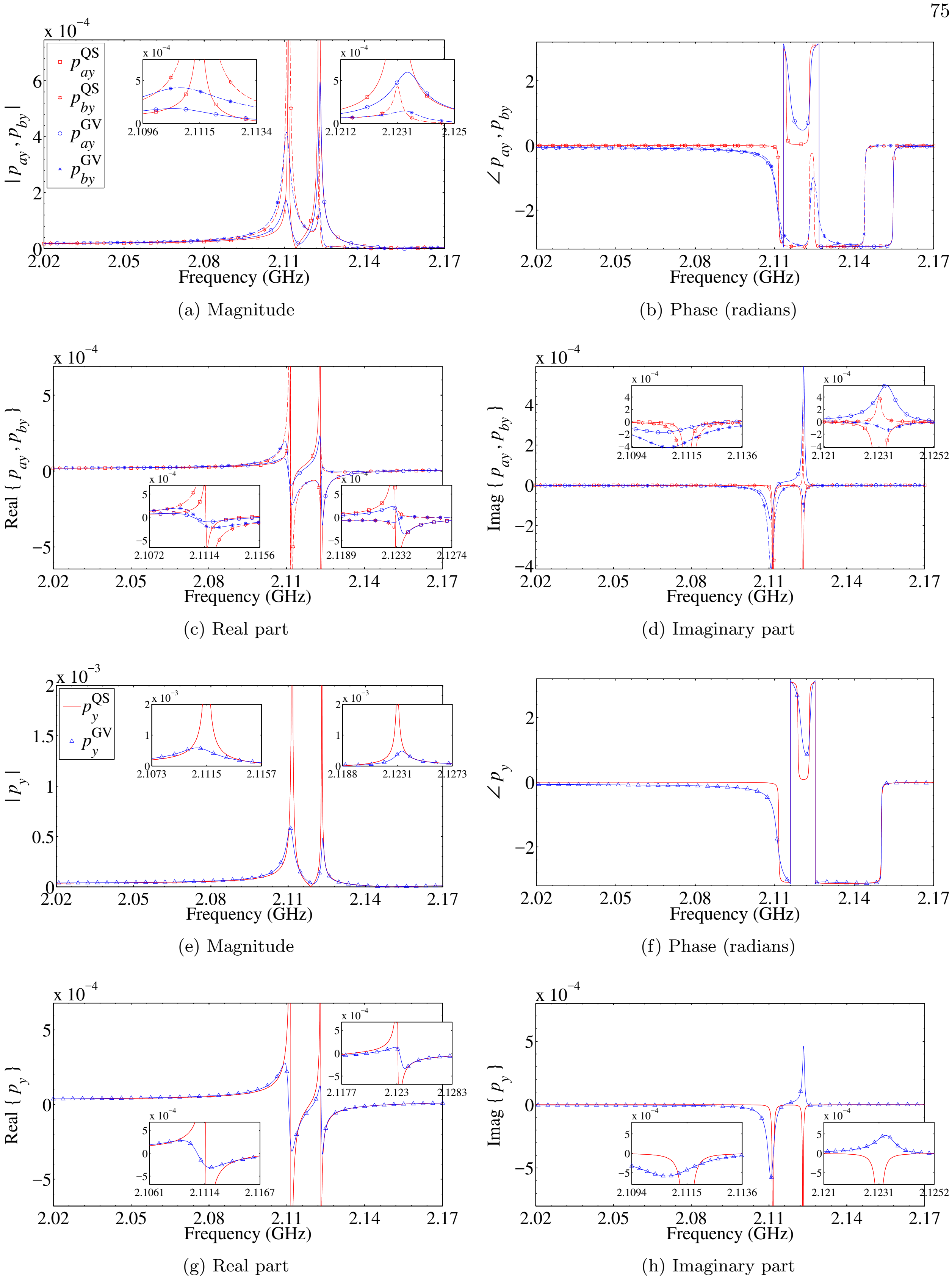

(a) Magnitude

(b) Phase (radians)

(c) Real part

(d) Imaginary part

(e) Magnitude

(f) Phase (radians)

(g) Real part

(h) Imaginary part

Figure 3.37: Pair of dielectric spheres: Case I orientation, radius of b is 0.5% larger than a, spacing 0.03 m, $\epsilon_r = 100$, and $\delta_T = 10^{-4}$. Electric dipole moments normalized such that $\epsilon E^{inc} = 1$.

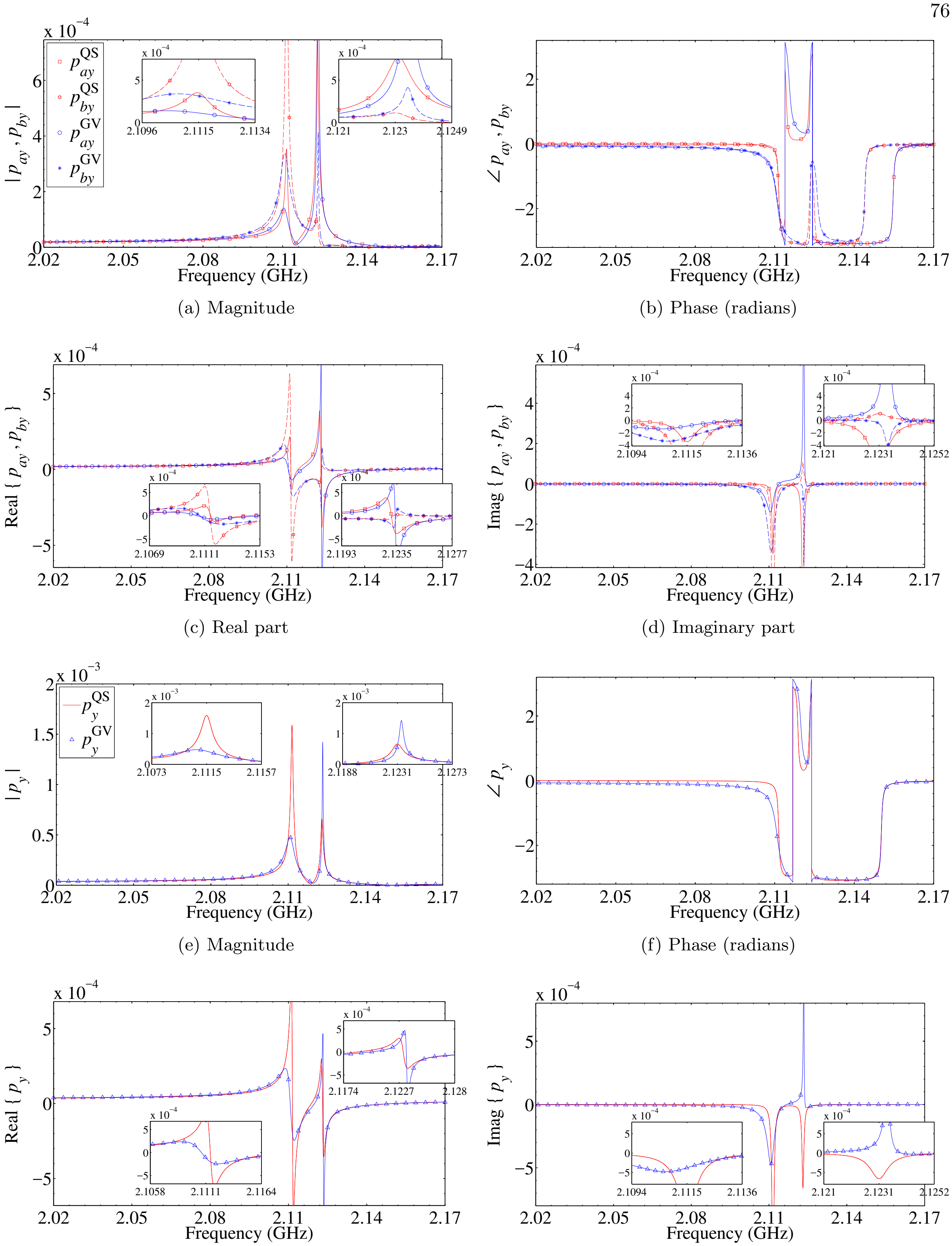

(a) Magnitude

(b) Phase (radians)

(c) Real part

(d) Imaginary part

(e) Magnitude

(f) Phase (radians)

(g) Real part

(h) Imaginary part

Figure 3.38: Pair of dielectric spheres: Case I orientation, radius of b is 0.5% larger than a, spacing 0.03 m, $\epsilon_r = 100$, and $\delta_T = 10^{-3.4}$. Electric dipole moments normalized such that $\epsilon E^{inc} = 1$.

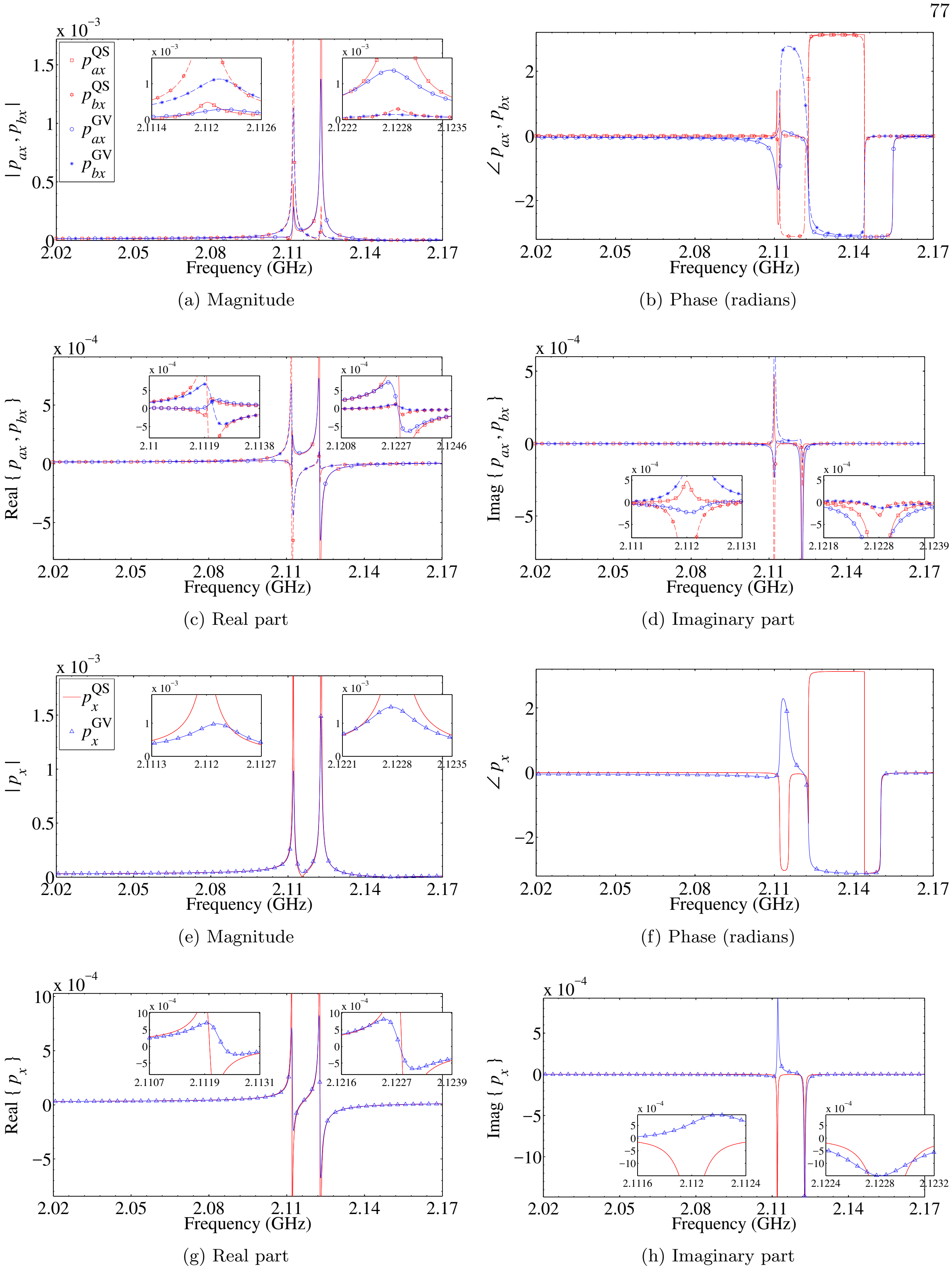

(a) Magnitude (b) Phase (radians)

(c) Real part (d) Imaginary part

(e) Magnitude (f) Phase (radians)

(g) Real part (h) Imaginary part

Figure 3.39: Pair of dielectric spheres: Case II orientation, radius of b is 0.5% larger than a, spacing 0.03 m, $\epsilon_r = 100$, and $\delta_T = 10^{-4}$. Electric dipole moments normalized such that $\epsilon E^{inc} = 1$.

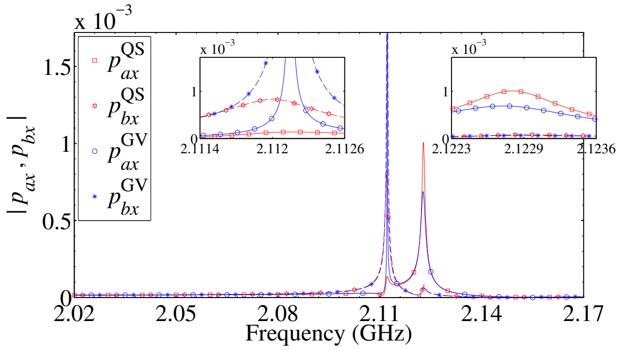

(a) Magnitude

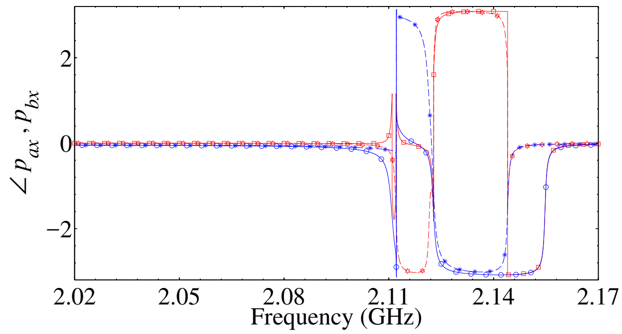

(b) Phase (radians)

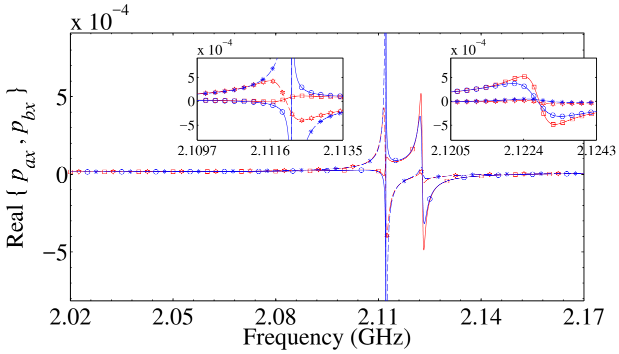

(c) Real part

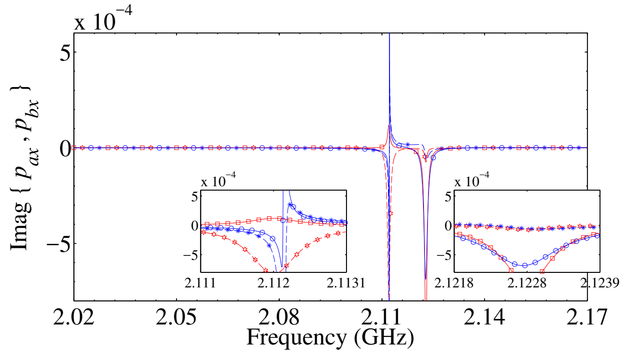

(d) Imaginary part

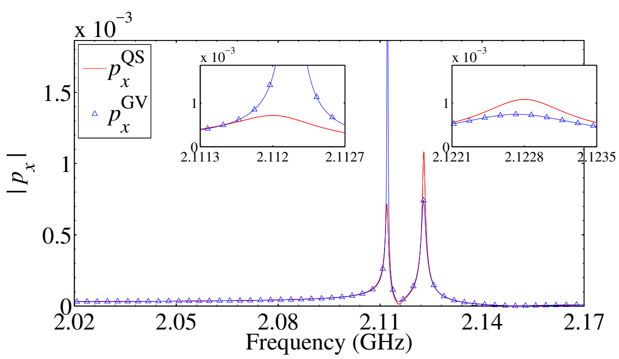

(e) Magnitude

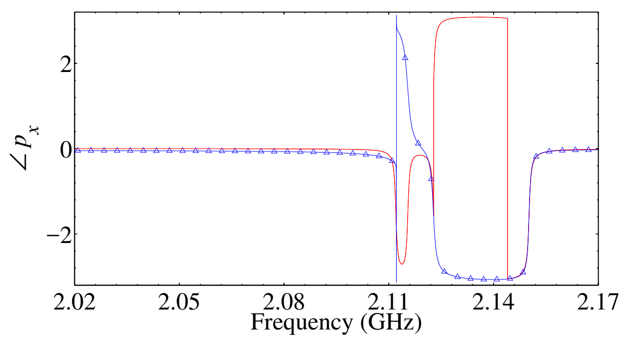

(f) Phase (radians)

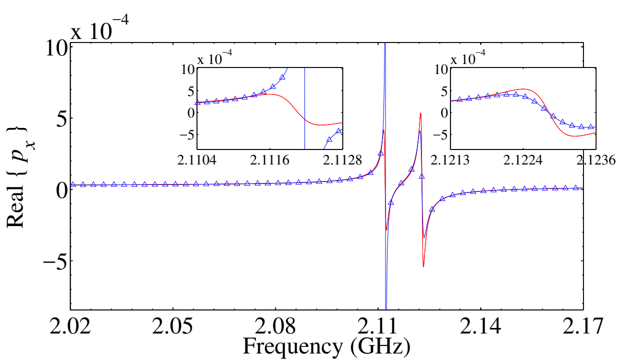

(g) Real part

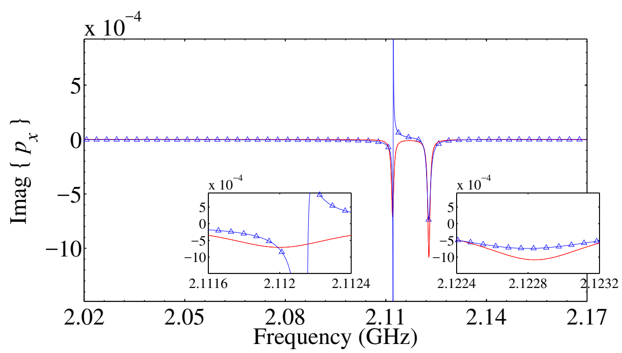

(h) Imaginary part

Figure 3.40: Pair of dielectric spheres: Case II orientation, radius of b is 0.5% larger than a, spacing 0.03 m, $\epsilon_r = 100$, and $\delta_T = 10^{-3.4}$. Electric dipole moments normalized such that $\epsilon E^{inc} = 1$.

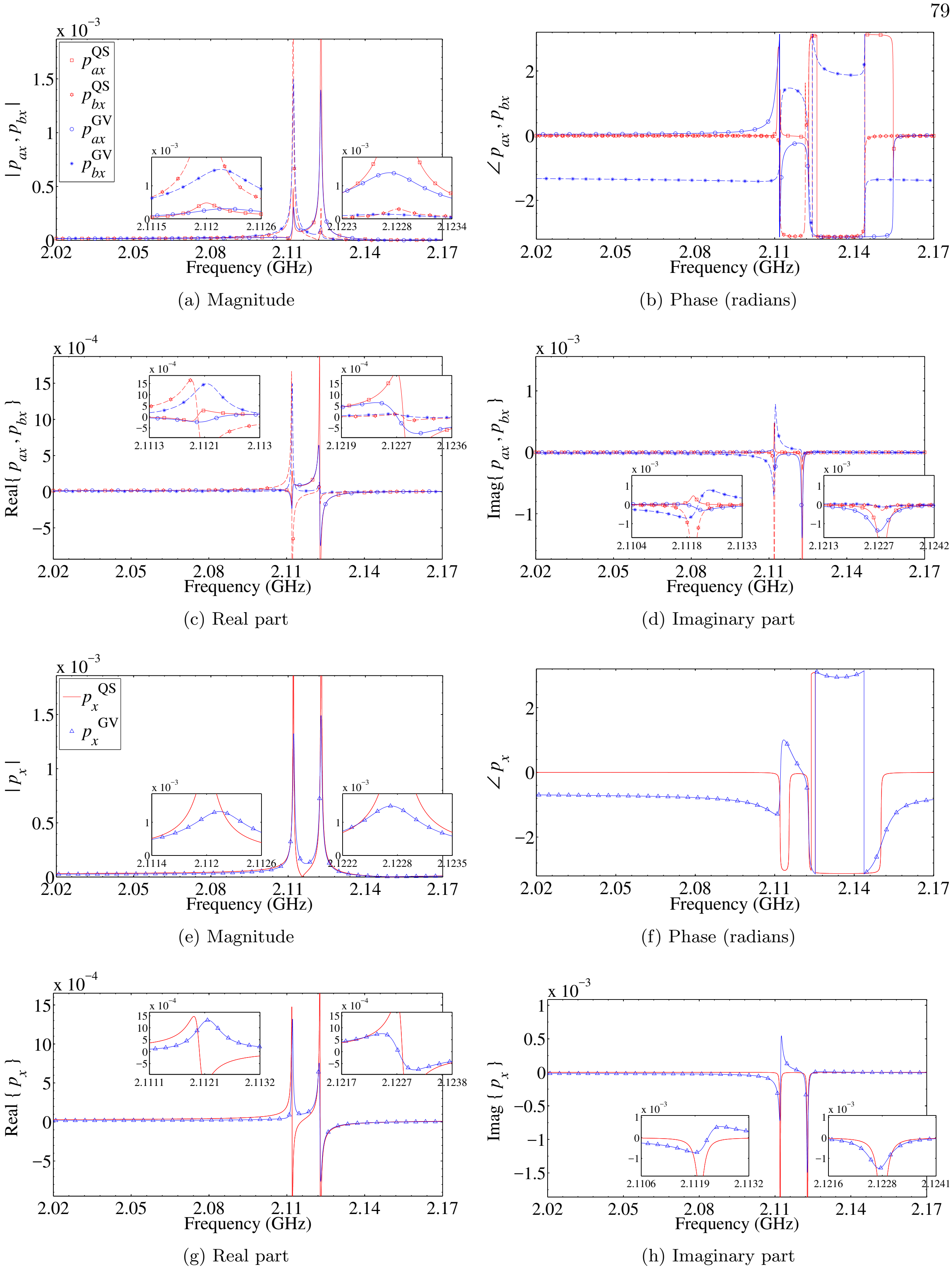

Figure 3.41: Pair of dielectric spheres: Case III orientation, radius of b is 0.5% larger than a, spacing 0.03 m, $\epsilon_r = 100$, and $\delta_T = 10^{-4}$. Electric dipole moments normalized such that $\epsilon E^{inc} = 1$.

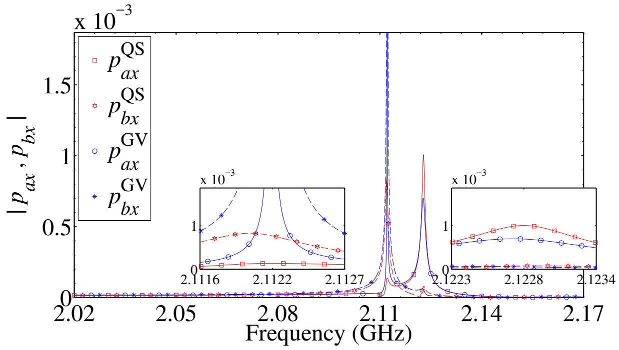

(a) Magnitude

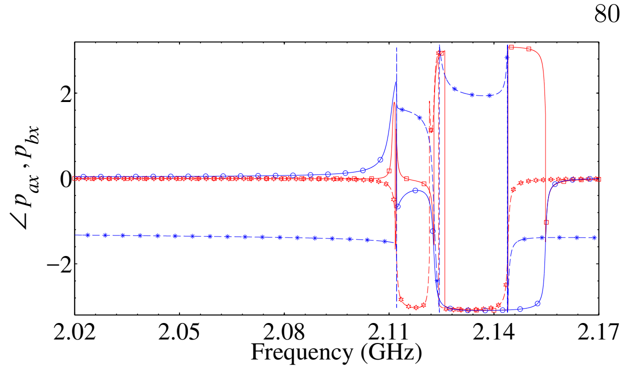

(b) Phase (radians)

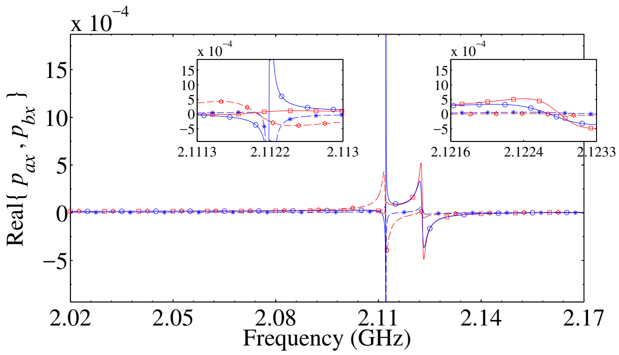

(c) Real part

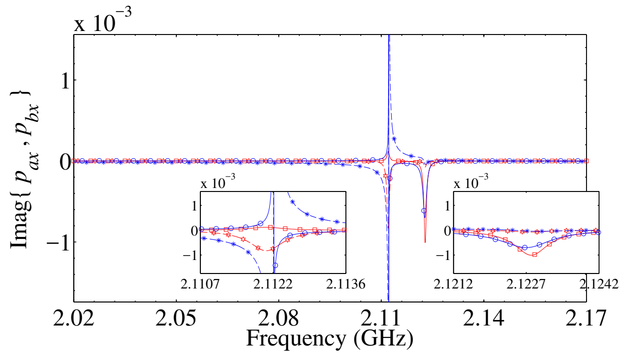

(d) Imaginary part

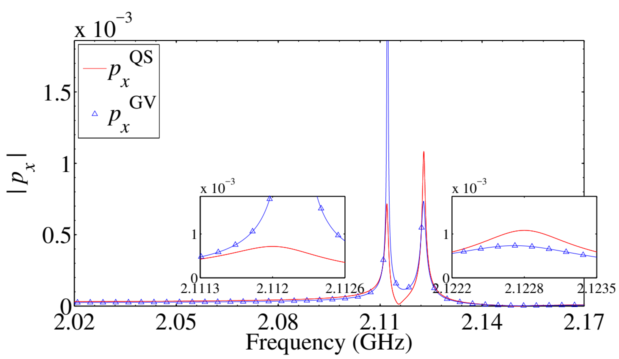

(e) Magnitude

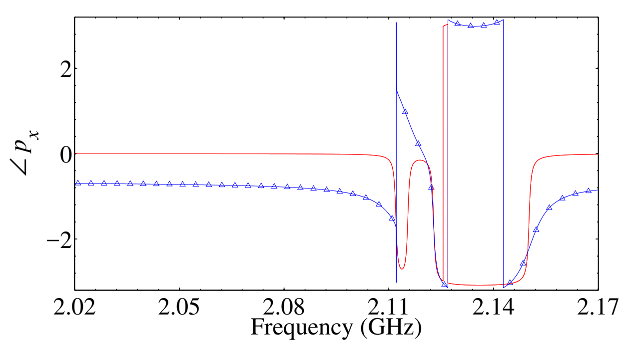

(f) Phase (radians)

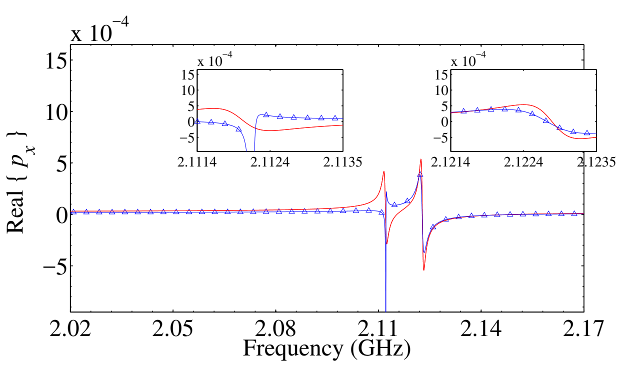

(g) Real part

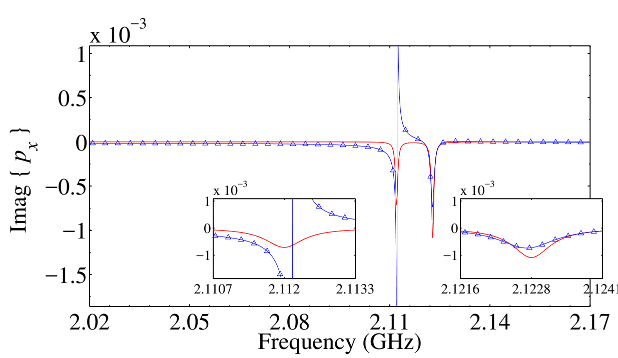

(h) Imaginary part

Figure 3.42: Pair of dielectric spheres: Case III orientation, radius of b is 0.5% larger than a, spacing 0.03 m, $\epsilon_r = 100$, and $\delta_T = 10^{-3.4}$. Electric dipole moments normalized such that $\epsilon E^{inc} = 1$.

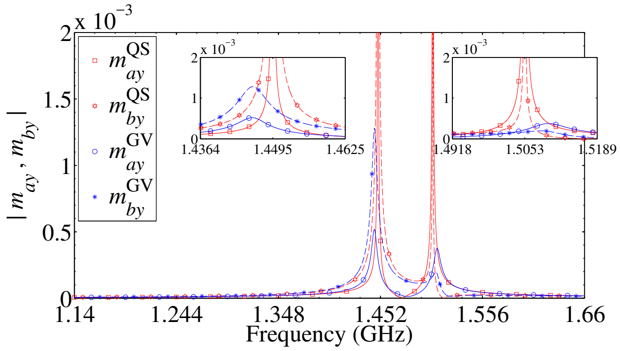

(a) Magnitude

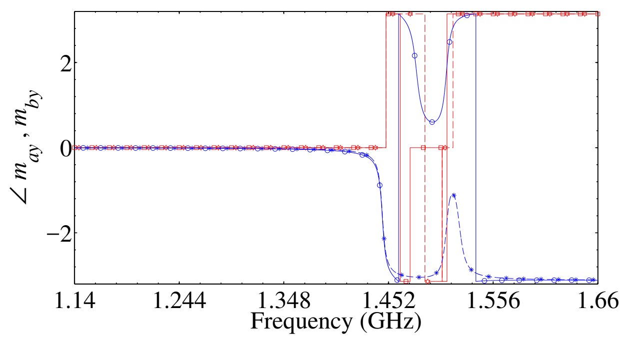

(b) Phase (radians)

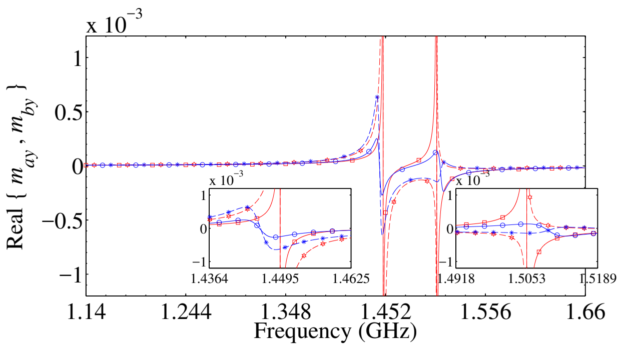

(c) Real part

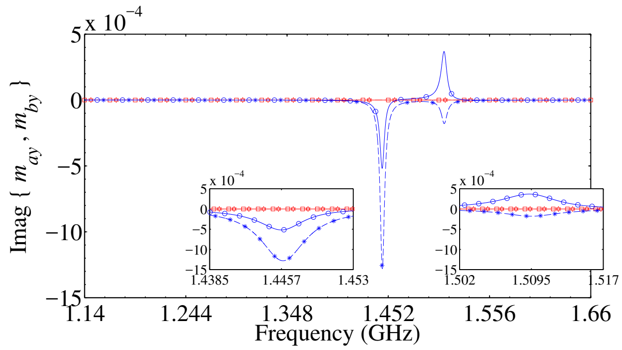

(d) Imaginary part

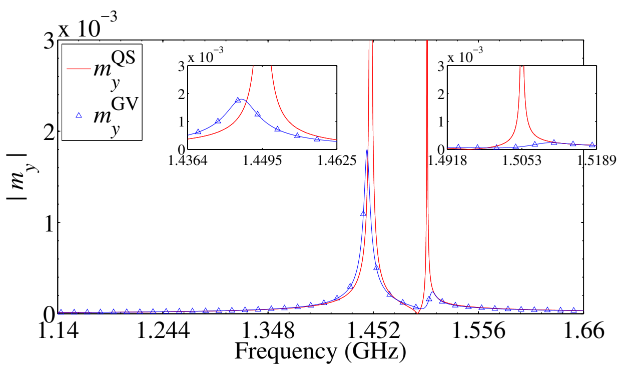

(e) Magnitude

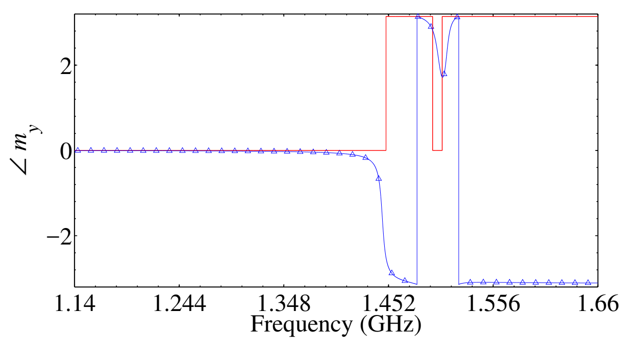

(f) Phase (radians)

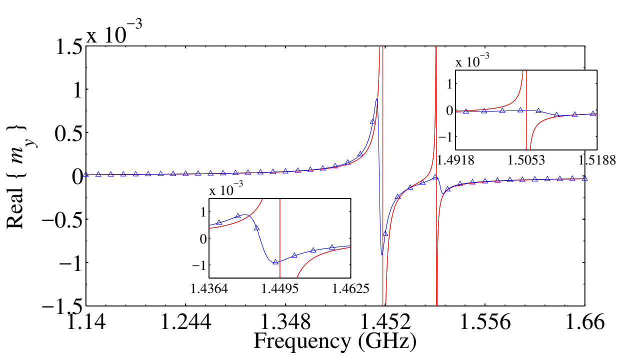

(g) Real part

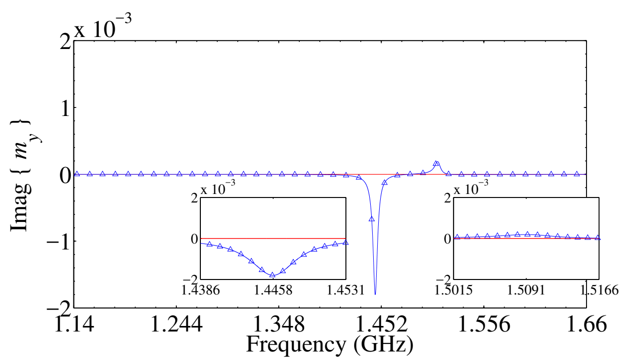

(h) Imaginary part

Figure 3.43: Pair of dielectric spheres: Case I orientation, radius of b is 3% larger than a, spacing 0.03 m, $\epsilon_r = 100$, and lossless. Magnetic dipole moments normalized such that $H^{inc} = 1$.

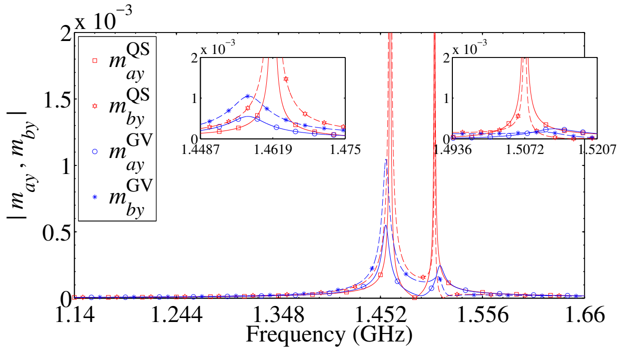

(a) Magnitude

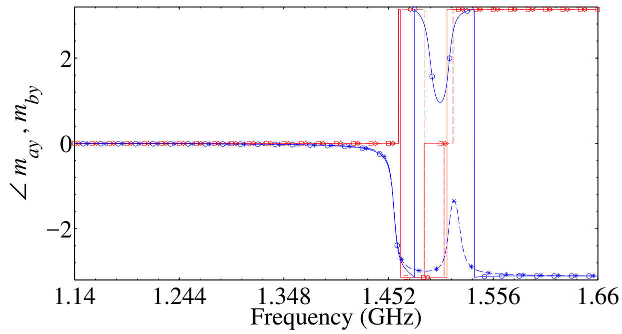

(b) Phase (radians)

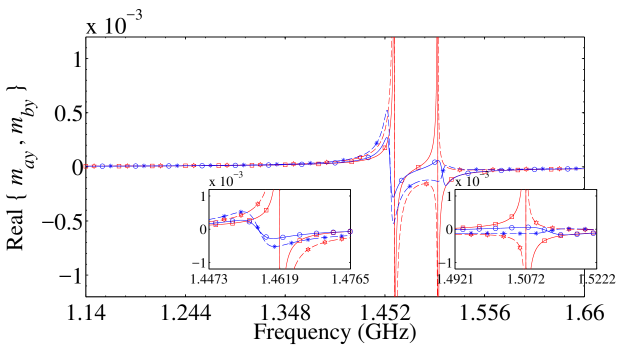

(c) Real part

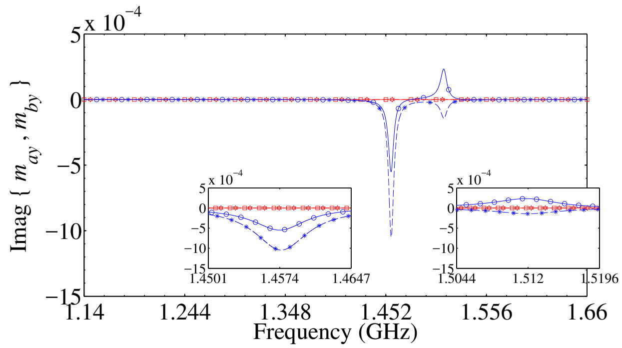

(d) Imaginary part

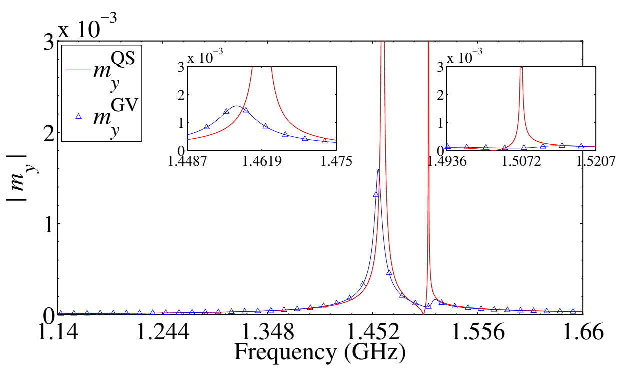

(e) Magnitude

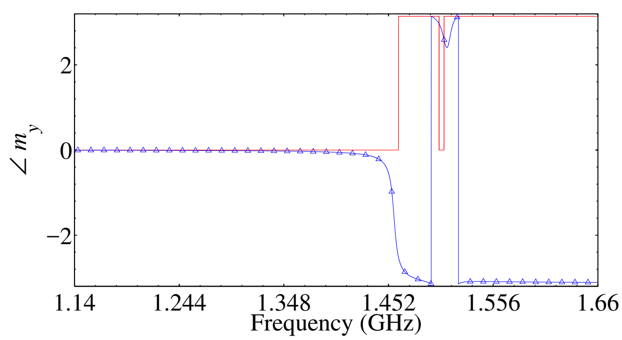

(f) Phase (radians)

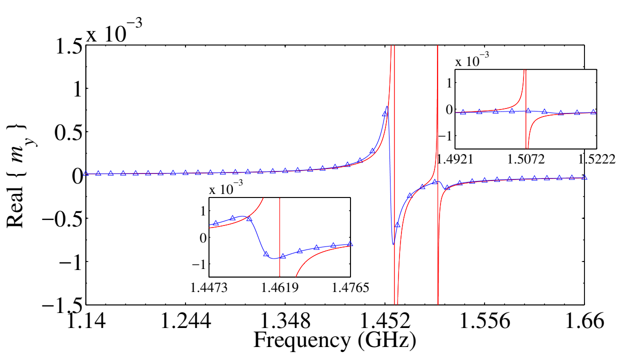

(g) Real part

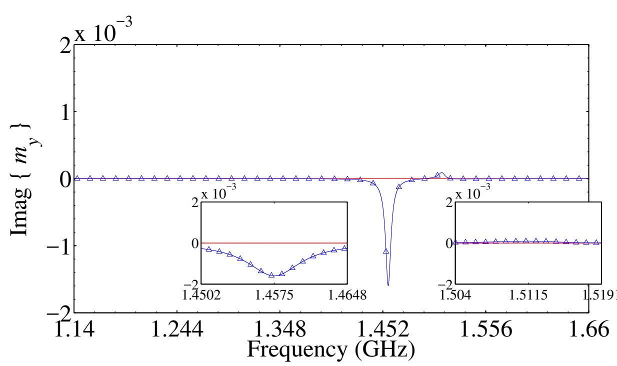

(h) Imaginary part

Figure 3.44: Pair of dielectric spheres: Case I orientation, radius of b is 2% larger than a, spacing 0.03 m, $\epsilon_r = 100$, and lossless. Magnetic dipole moments normalized such that $H^{inc} = 1$.

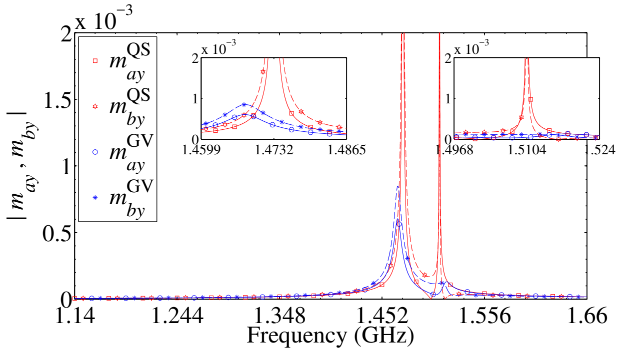

(a) Magnitude

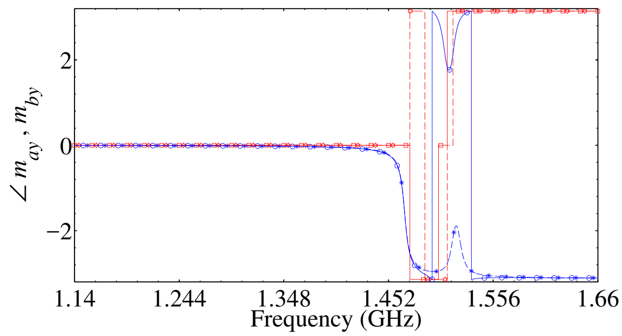

(b) Phase (radians)

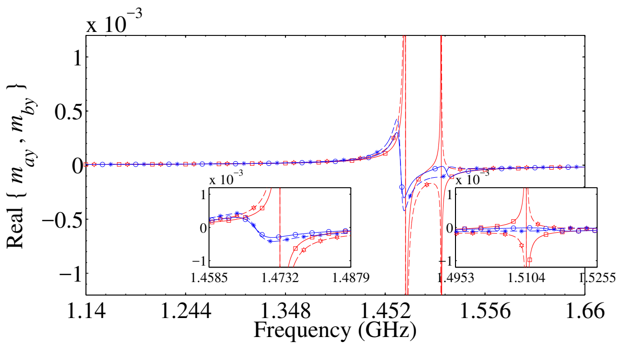

(c) Real part

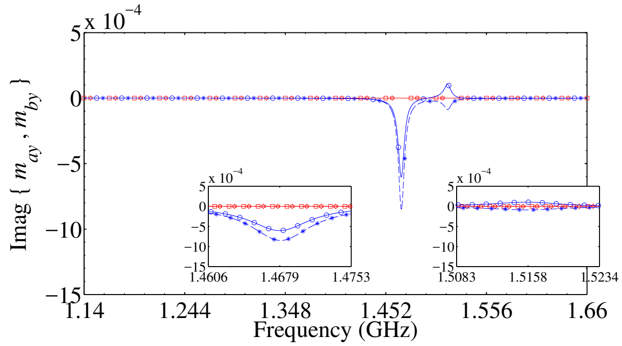

(d) Imaginary part

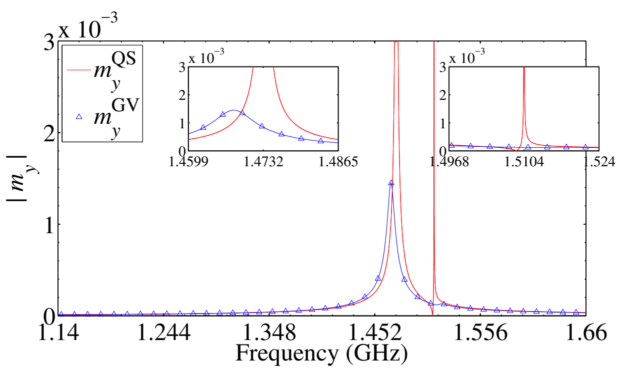

(e) Magnitude

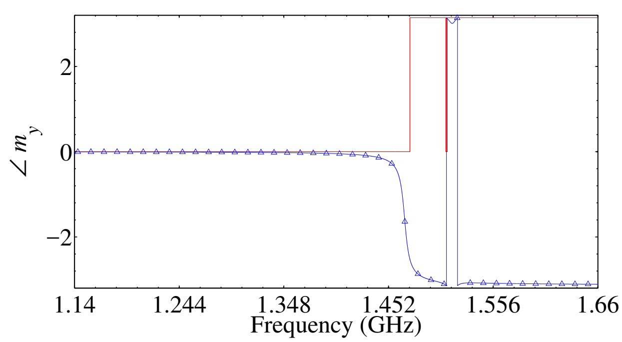

(f) Phase (radians)

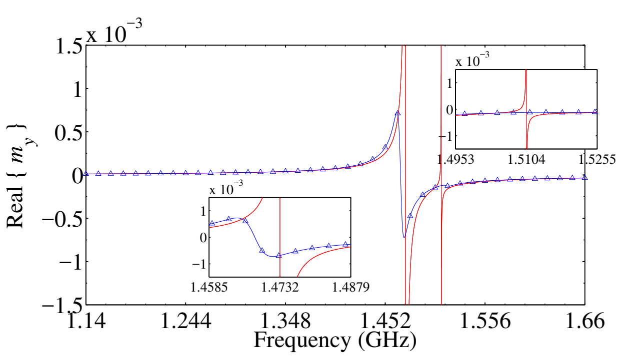

(g) Real part

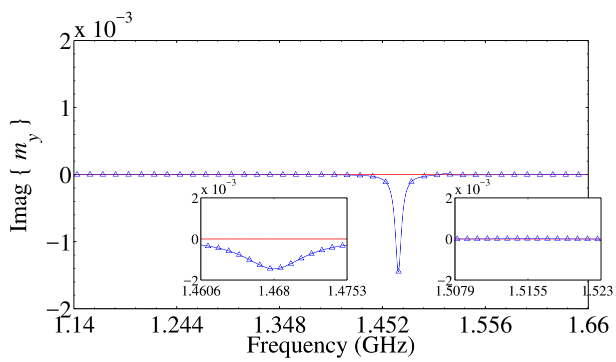

(h) Imaginary part

Figure 3.45: Pair of dielectric spheres: Case I orientation, radius of b is 1% larger than a, spacing 0.03 m, $\epsilon_r = 100$, and lossless. Magnetic dipole moments normalized such that $H^{inc} = 1$.

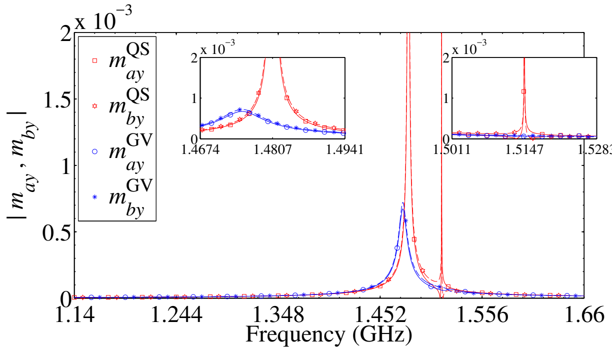

(a) Magnitude

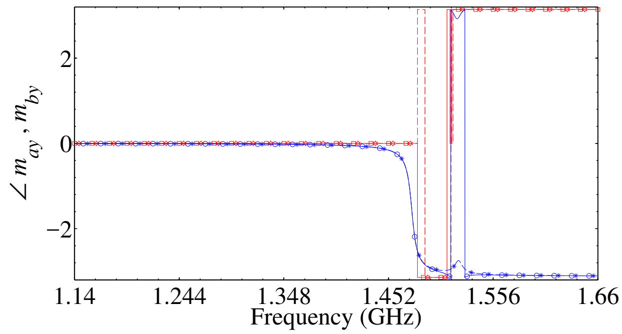

(b) Phase (radians)

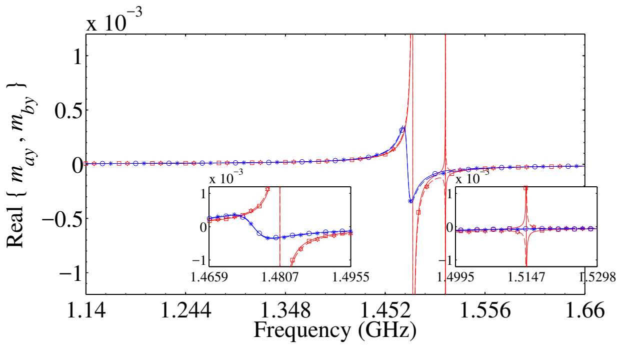

(c) Real part

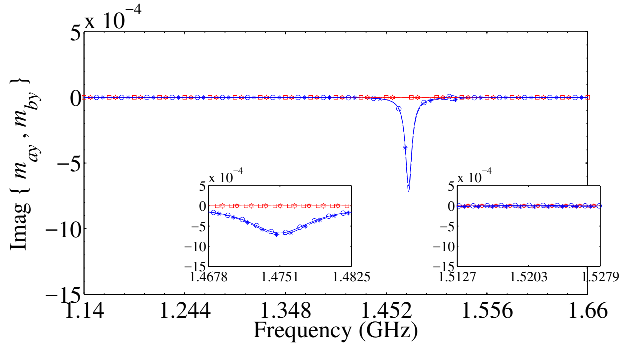

(d) Imaginary part

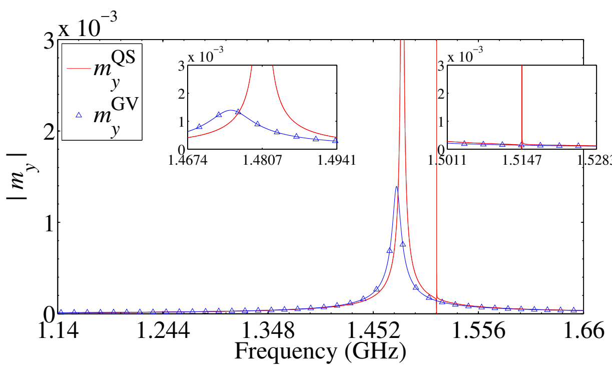

(e) Magnitude

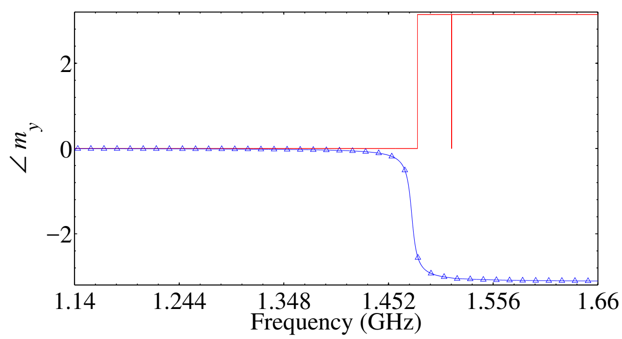

(f) Phase (radians)

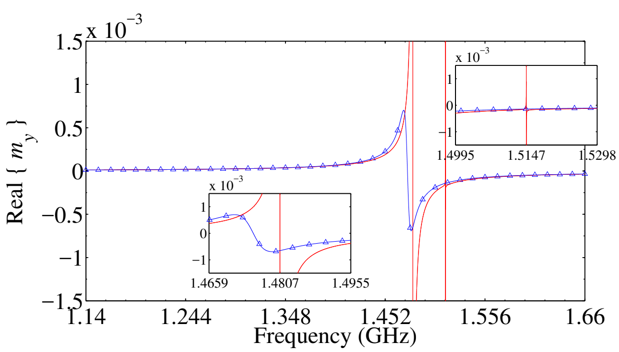

(g) Real part

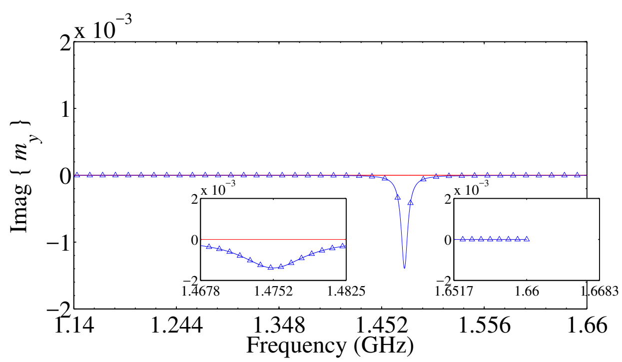

(h) Imaginary part

Figure 3.46: Pair of dielectric spheres: Case I orientation, radius of b is 0.2% larger than a, spacing 0.03 m, $\epsilon_r = 100$, and lossless. Magnetic dipole moments normalized such that $H^{inc} = 1$..

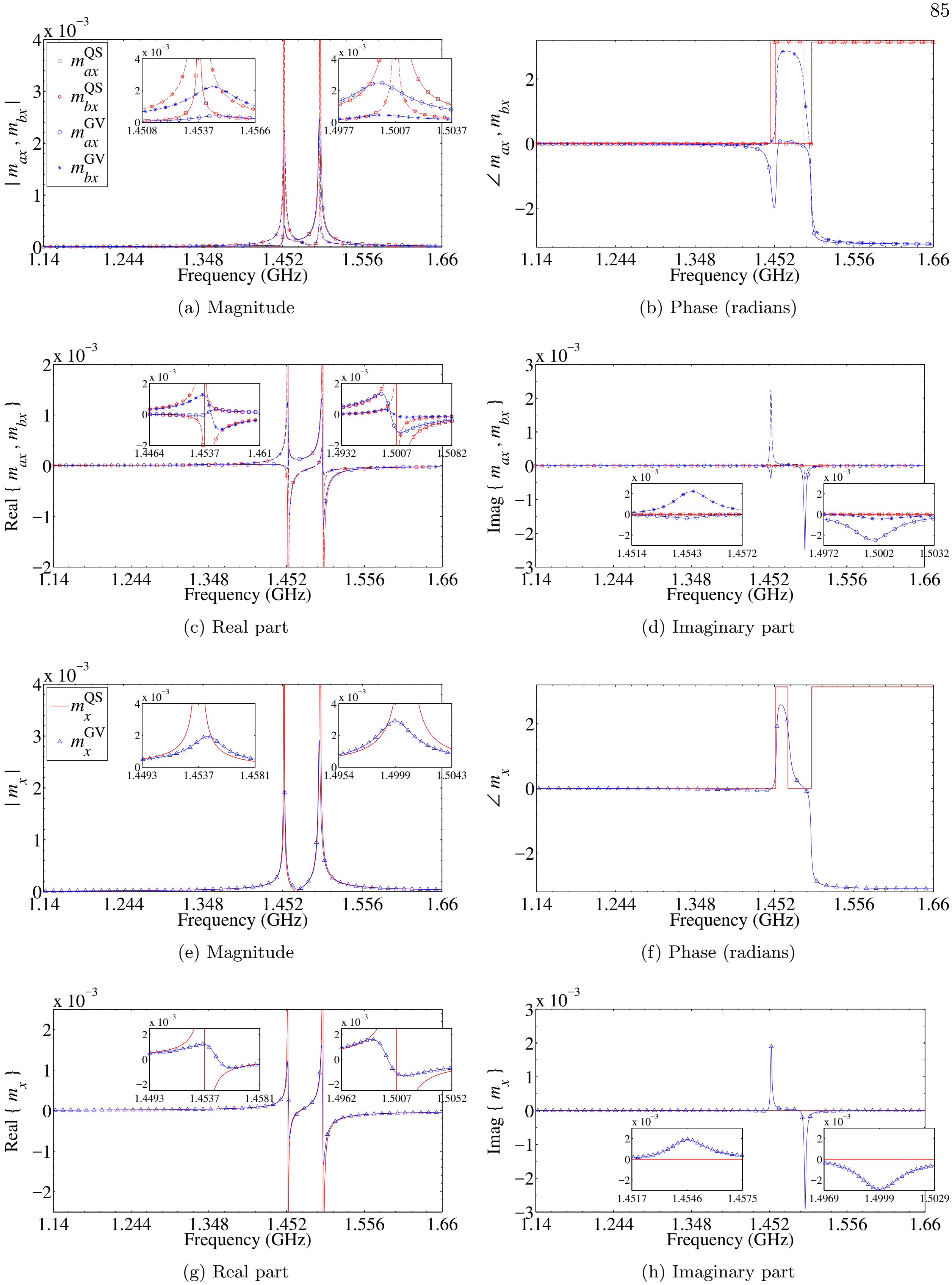

(a) Magnitude

(b) Phase (radians)

(c) Real part

(d) Imaginary part

(e) Magnitude

(f) Phase (radians)

(g) Real part

(h) Imaginary part

Figure 3.47: Pair of dielectric spheres: Case II orientation, radius of b is 3% larger than a, spacing 0.03 m, $\epsilon_r = 100$, and lossless. Magnetic dipole moments normalized such that $H^{inc} = 1$.

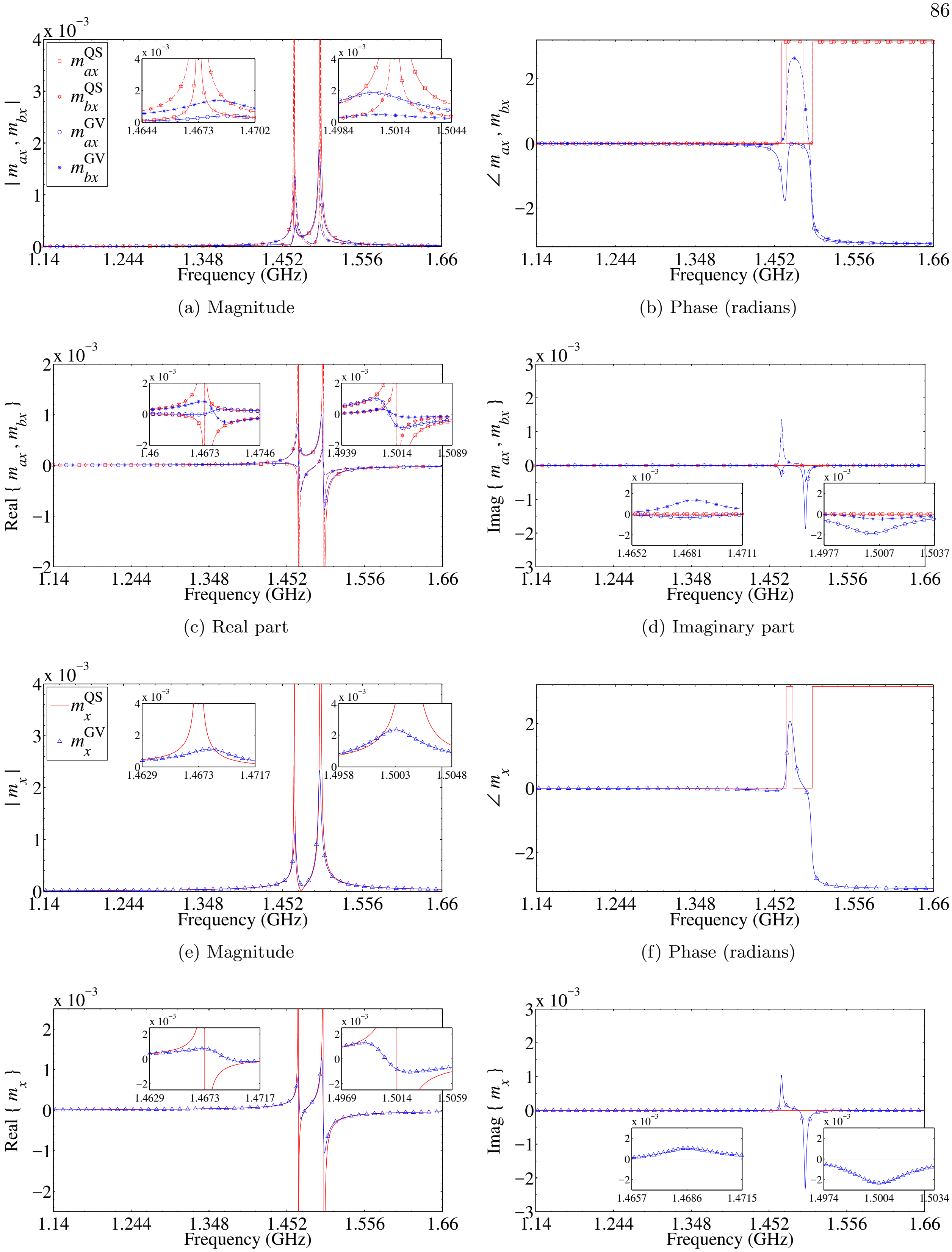

(a) Magnitude (b) Phase (radians)

(c) Real part (d) Imaginary part

(e) Magnitude (f) Phase (radians)

(g) Real part (h) Imaginary part

Figure 3.48: Pair of dielectric spheres: Case II orientation, radius of b is 2% larger than a, spacing 0.03 m, $\epsilon_r = 100$, and lossless. Magnetic dipole moments normalized such that $H^{inc} = 1$.

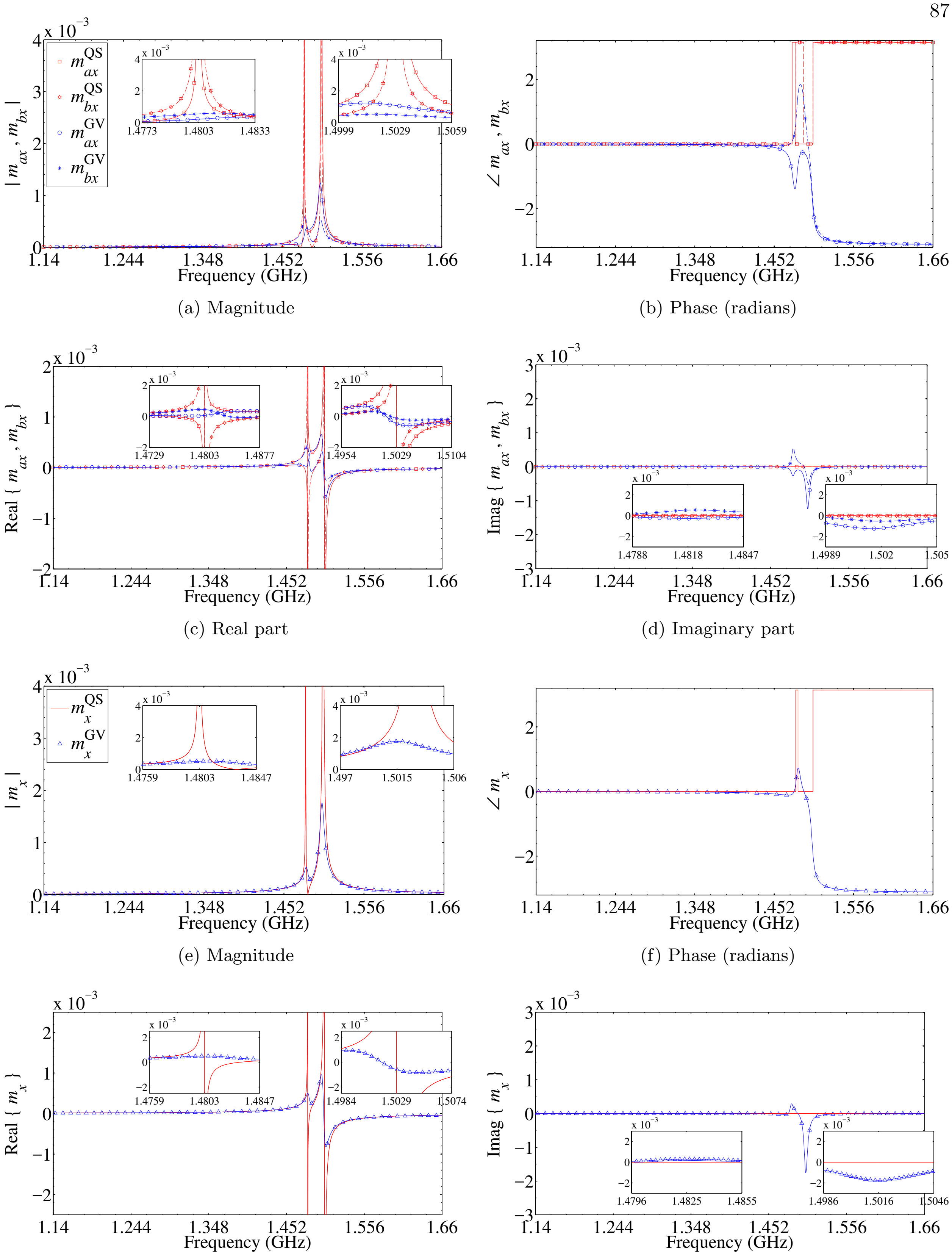

(a) Magnitude

(b) Phase (radians)

(c) Real part

(d) Imaginary part

(e) Magnitude

(f) Phase (radians)

(g) Real part

(h) Imaginary part

Figure 3.49: Pair of dielectric spheres: Case II orientation, radius of b is 1% larger than a, spacing 0.03 m, $\epsilon_r = 100$, and lossless. Magnetic dipole moments normalized such that $H^{inc} = 1$.

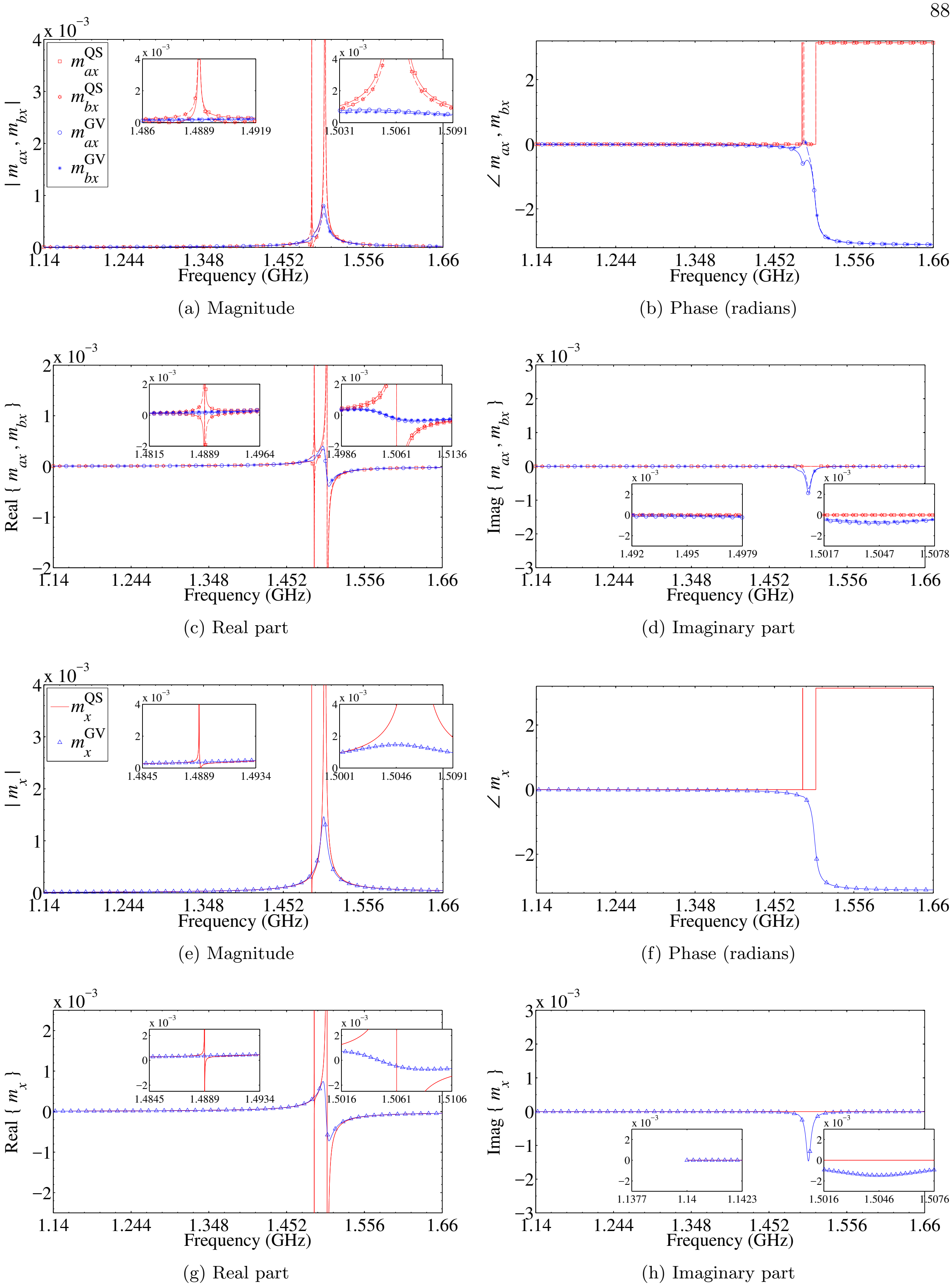

(a) Magnitude (b) Phase (radians)

(c) Real part (d) Imaginary part

(e) Magnitude (f) Phase (radians)

(g) Real part (h) Imaginary part

Figure 3.50: Pair of dielectric spheres: Case II orientation, radius of b is 0.2% larger than a, spacing 0.03 m, $\epsilon_r = 100$, and lossless. Magnetic dipole moments normalized such that $H^{inc} = 1$.

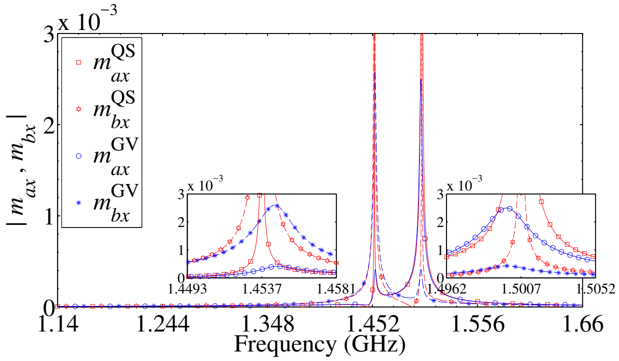

(a) Magnitude

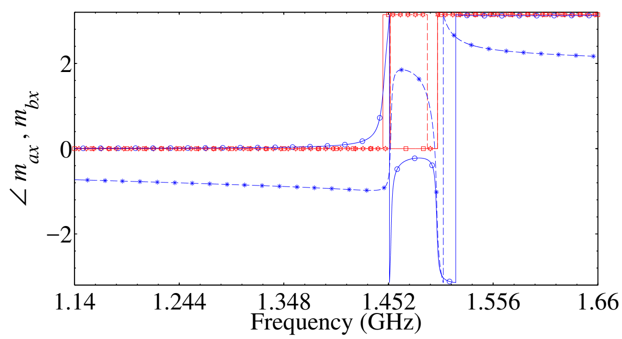

(b) Phase (radians)

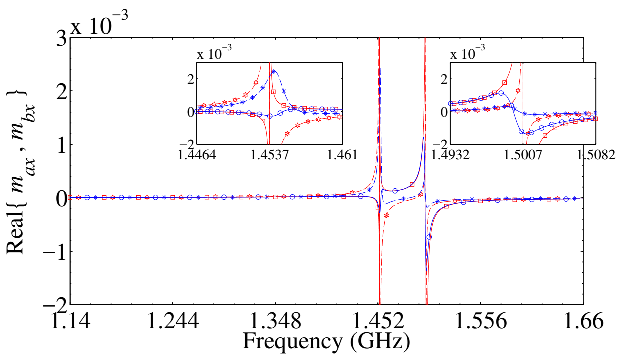

(c) Real part

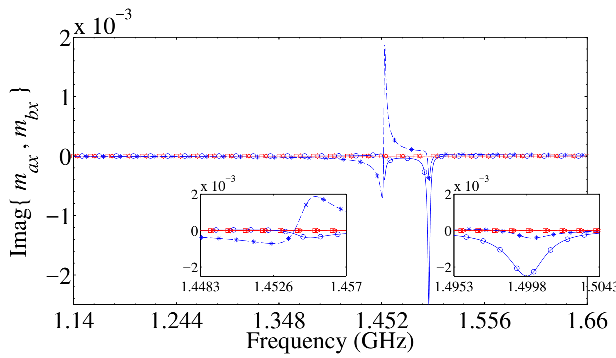

(d) Imaginary part

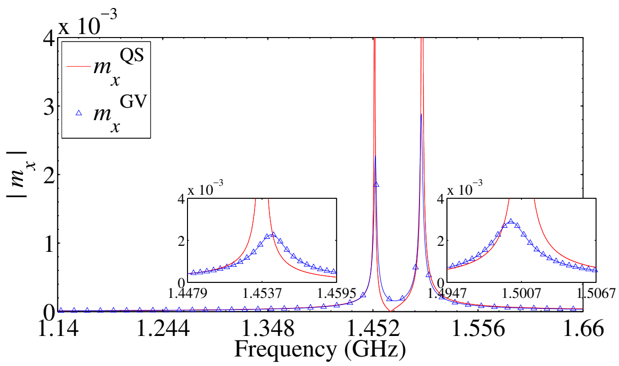

(e) Magnitude

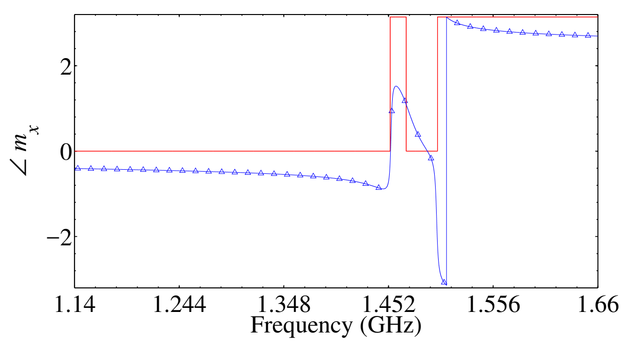

(f) Phase (radians)

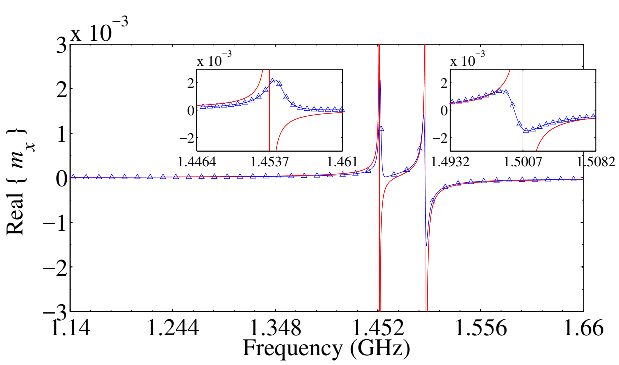

(g) Real part

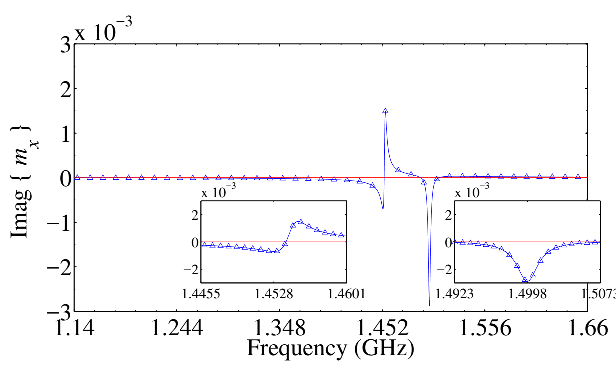

(h) Imaginary part

Figure 3.51: Pair of dielectric spheres: Case III orientation, radius of b is 3% larger than a, spacing 0.03 m, $\epsilon_r = 100$, and lossless. Magnetic dipole moments normalized such that $H^{inc} = 1$.

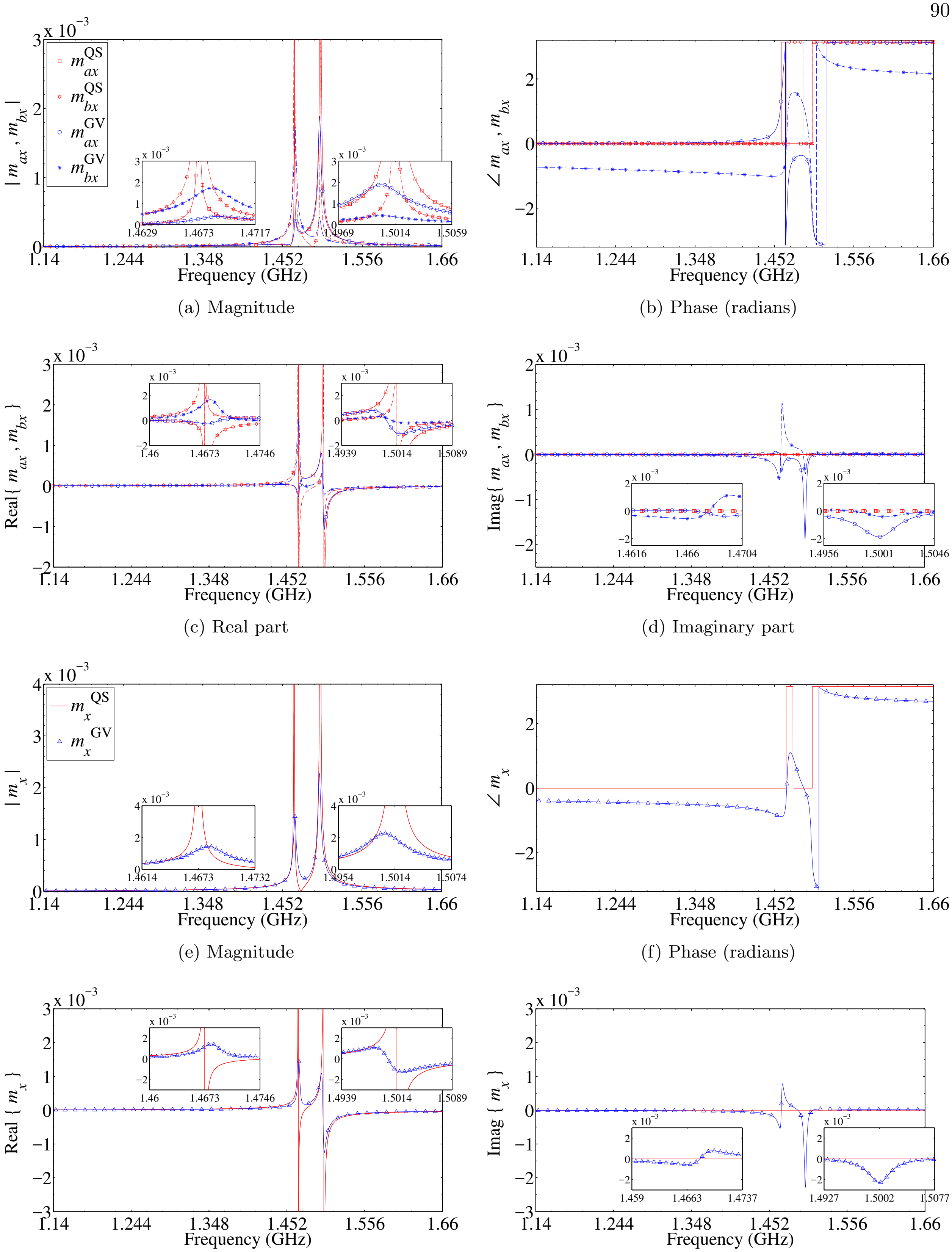

(a) Magnitude

(b) Phase (radians)

(c) Real part

(d) Imaginary part

(e) Magnitude

(f) Phase (radians)

(g) Real part

(h) Imaginary part

Figure 3.52: Pair of dielectric spheres: Case III orientation, radius of b is 2% larger than a, spacing 0.03 m, $\epsilon_r = 100$, and lossless. Magnetic dipole moments normalized such that $H^{inc} = 1$.

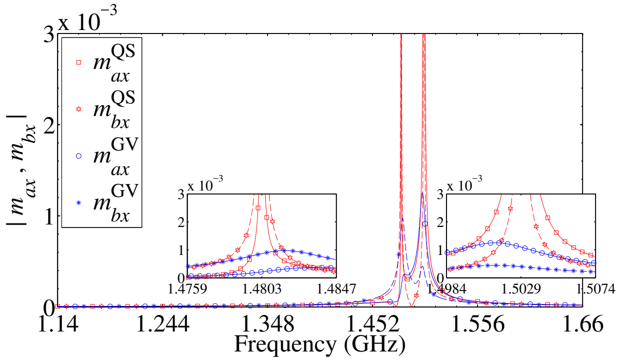

(a) Magnitude

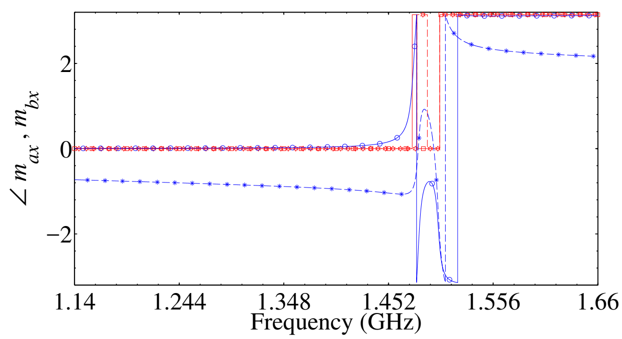

(b) Phase (radians)

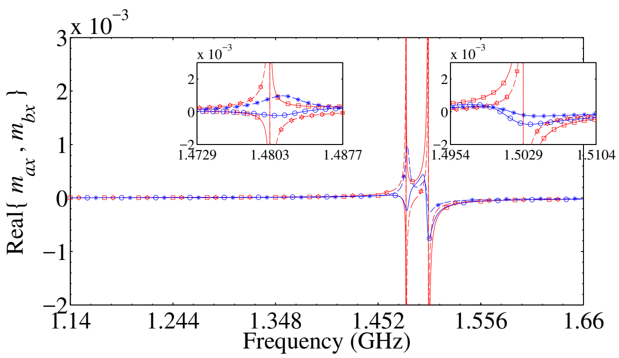

(c) Real part

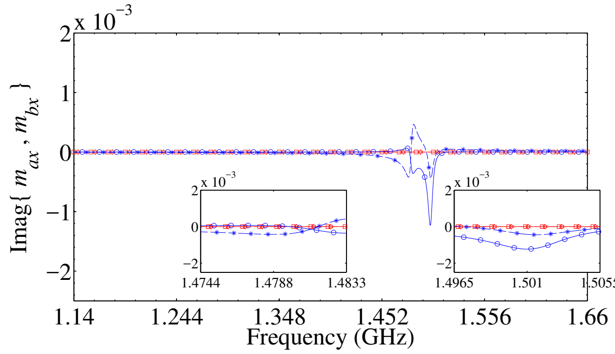

(d) Imaginary part

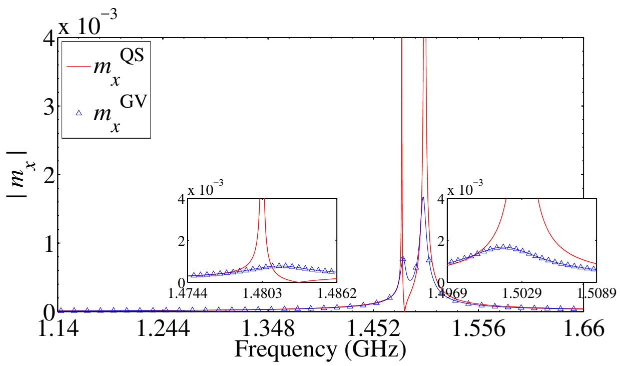

(e) Magnitude

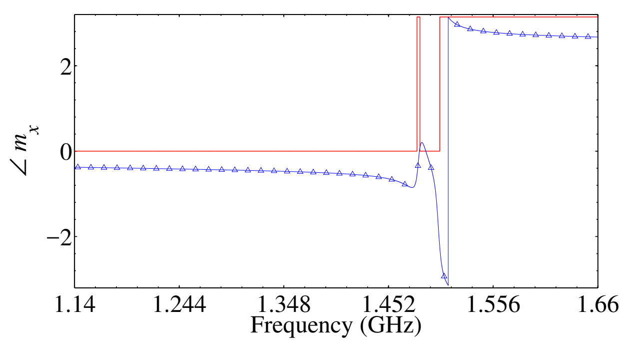

(f) Phase (radians)

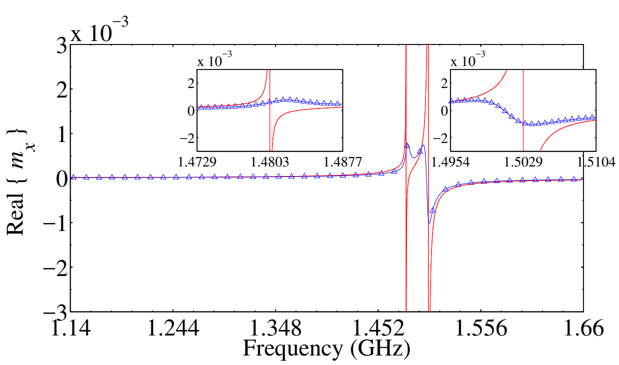

(g) Real part

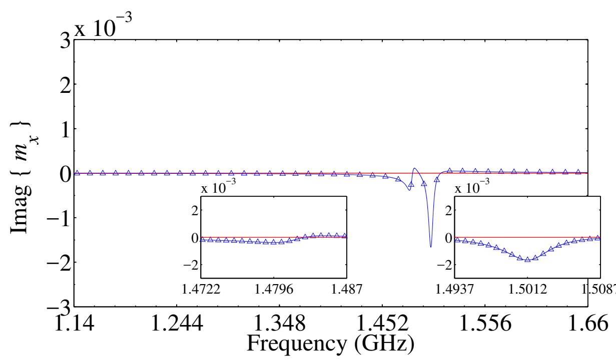

(h) Imaginary part

Figure 3.53: Pair of dielectric spheres: Case III orientation, radius of b is 1% larger than a, spacing 0.03 m, $\epsilon_r = 100$, and lossless. Magnetic dipole moments normalized such that $H^{inc} = 1$.

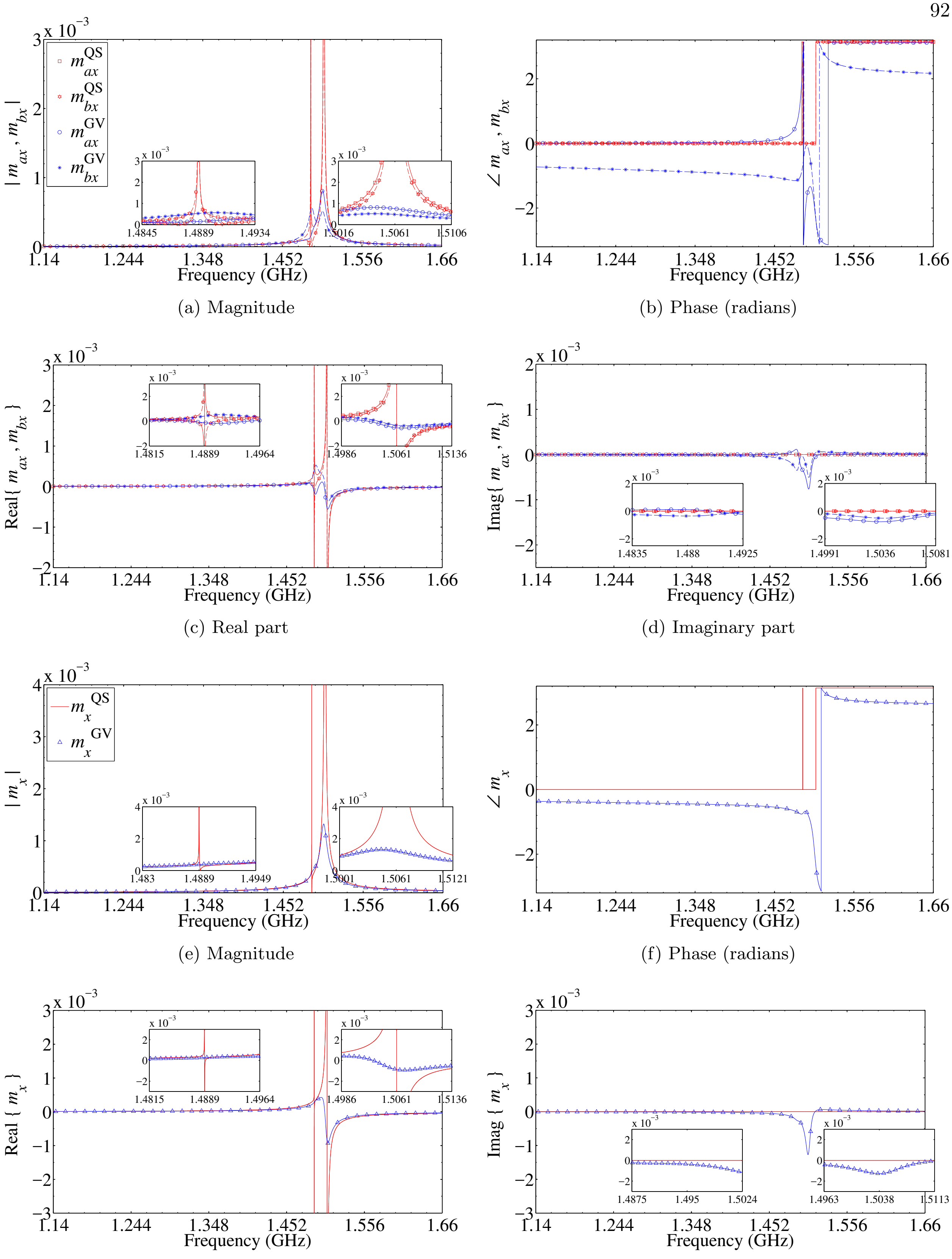

(a) Magnitude (b) Phase (radians)

(c) Real part (d) Imaginary part

(e) Magnitude (f) Phase (radians)

(g) Real part (h) Imaginary part

Figure 3.54: Pair of dielectric spheres: Case III orientation, radius of b is 0.2% larger than a, spacing 0.03 m, $\epsilon_r = 100$, and lossless. Magnetic dipole moments normalized such that $H^{inc} = 1$.

Chapter 4

Metafilm of Polarizable Scatterers Spatial Perturbation Analytical Techniques and Behavior

This chapter and the following chapters will focus on the behavior of a metafilm. In the previous two chapters, the resonator examples investigated were chosen such that their properties would be practical for use as elements in a metafilm. For the purposes of this work, the metafilm will comprise of resonators placed periodically to form a two-dimensional square lattice. Each resonator will be electrically small compared to a wavelength in the background and the lattice constant will be less than a quarter wavelength in the background so that the lattice itself doesn't cause any resonances (i. e. so that there are no propagating Bloch-Floquet modes). As opposed to the design of publication [50], where the lattice is on the order of a wavelength, so the lattice does cause resonances.

The resonators are assumed not to touch each other, and to be sufficiently separated that they may be modeled with only dipole modes and quasi-static field interactions. For a pair of scatterers, the findings of Chapter 3 revealed that any parameter that doesn't effect the resonance will have no significant effect on the behavior of the pair when that parameter varies by a small amount. This chapter will look to see if these results can be extended to a metafilm.

When a metafilm is manufactured, undoubtedly the placement of each resonator will not be perfect. When the element is placed such that it is close to the desired location, but not exactly where it should be, the question arises "Does it matter? If so, by how much?". This chapter will explore this question using GSTCs (Generalized Sheet Transition Conditions) [28] and [20], as an analytic model. The results will be validated with a commercially available finite element method solver: ANSYS *HFSS* (High Frequency

Electromagnetic Field Simulation).

4.1 Background

The GSTCs relate the polarizabilities α, which are microscopic properties of the metafilm, to the surface susceptibilities χ, which are macroscopic properties. The surfaces susceptibilities can then be used to calculate the S-parameters (plane-wave reflection and transmission coefficients), which are measurable quantities used to characterize the performance of the metafilm. This model assumes that the resonators are small compared with a wavelength in the background medium, spaced less than a quarter wavelength in the background, and don't touch. It replaces the thin layer of scatterers with an infinitely thin polarizable sheet. The boundary conditions (GSTCs) were derived by Kuester et al. [28] and are given below:

$$\mathbf{a}_z \times \mathbf{H}|_{z=0^-}^{0^+} = j\omega\epsilon\overleftrightarrow{\boldsymbol{\chi}}_{ES} \cdot \mathbf{E}_{t,\text{av}}|_{z=0} + \mathbf{a}_z \times \nabla_t[\chi_{MS}^{zz} H_{z,\text{av}}]_{z=0} \tag{4.1}$$

$$\mathbf{E}|_{z=0^-}^{0^+} \times \mathbf{a}_z = -j\omega\mu\overleftrightarrow{\boldsymbol{\chi}}_{MS} \cdot \mathbf{H}_{t,\text{av}}|_{z=0} - \nabla_t[\chi_{ES}^{zz} E_{z,\text{av}}]_{z=0} \times \mathbf{a}_z \tag{4.2}$$

$$\mathbf{D}_z|_{z=0^-}^{0^+} = -\nabla_t \cdot (\epsilon\overleftrightarrow{\boldsymbol{\chi}}_{ES} \cdot \mathbf{E}_{t,\text{av}}|_{z=0}) \tag{4.3}$$

$$\mathbf{B}_z|_{z=0^-}^{0^+} = \mu\nabla_t \cdot (\mu\overleftrightarrow{\boldsymbol{\chi}}_{MS} \cdot \mathbf{H}_{t,\text{av}}|_{z=0}) \tag{4.4}$$

For either side of the metafilm, "av" represents the average field quantity, which is one half the sum of the fields at 0^+ and 0^-.

The dyadic electric and magnetic surface susceptibilities, $\overleftrightarrow{\boldsymbol{\chi}}_{ES}$ and $\overleftrightarrow{\boldsymbol{\chi}}_{MS}$ respectively are dependent upon the scatterer geometry. For the highly symmetrical special cases such as elements shaped as a spheres or cubes, the surface susceptibilities have the simple forms

$$\overleftrightarrow{\boldsymbol{\chi}}_{ES} = \chi_{ES}^{xx}\mathbf{a}_x\mathbf{a}_x + \chi_{ES}^{yy}\mathbf{a}_y\mathbf{a}_y + \chi_{ES}^{zz}\mathbf{a}_z\mathbf{a}_z \tag{4.5}$$

$$\overleftrightarrow{\boldsymbol{\chi}}_{MS} = \chi_{MS}^{xx}\mathbf{a}_x\mathbf{a}_x + \chi_{MS}^{yy}\mathbf{a}_y\mathbf{a}_y + \chi_{MS}^{zz}\mathbf{a}_z\mathbf{a}_z \tag{4.6}$$

In the derivation of equations (4.1) - (4.4) expressions for the surface susceptibilities which are unique properties of the metafilm, were derived by [28], [21]. They are based on a dipole interaction approximation that is accurate when the spheres aren't too close together.

$$\chi_{ES}^{xx} = N\frac{\langle \alpha_E^{xx} \rangle}{1 - N\langle \alpha_E^{xx} \rangle / 4R} \tag{4.7}$$

$$\chi_{ES}^{yy} = N\frac{\langle \alpha_E^{yy} \rangle}{1 - N\langle \alpha_E^{yy} \rangle / 4R} \tag{4.8}$$

$$\chi_{ES}^{zz} = N\frac{\langle \alpha_E^{zz} \rangle}{1 + N\langle \alpha_E^{zz} \rangle / 2R} \tag{4.9}$$

$$\chi_{MS}^{xx} = N\frac{\langle \alpha_M^{xx} \rangle}{1 - N\langle \alpha_M^{xx} \rangle / 4R} \tag{4.10}$$

$$\chi_{MS}^{yy} = N\frac{\langle \alpha_M^{yy} \rangle}{1 - N\langle \alpha_M^{yy} \rangle / 4R} \tag{4.11}$$

$$\chi_{MS}^{zz} = N\frac{\langle \alpha_M^{zz} \rangle}{1 + N\langle \alpha_M^{zz} \rangle / 2R} \tag{4.12}$$

Here, the symbol $\langle\rangle$, denotes the average over the resonators, and N is the number of scatterers per unit area. The surface susceptibilities express the effect of the incident field on a certain scatterer, as well as the effect of the fields produced by all the other scatterers on that given scatterer. The parameter R expresses the effect of that second contribution and is given by [28], [39]

$$R = d\frac{2\pi}{\sum'_{n,m}(m^2+n^2)^{-3/2}} \tag{4.13}$$

The parameter R takes into account the placement of the elements in the lattice of the metafilm, and depends on the arrangement; the preceding formula applies to the square lattice. The summation $\sum'_{n,m}$ is an infinite sum from $-\infty$ to ∞ that excludes the case of $m = n = 0$. For periodic spacing (a square array) with a period of d, the quantity R becomes [28], [39]

$$R_0 \cong 0.6956d \tag{4.14}$$

In this chapter, we will modify equation (4.13) to include any distance perturbations from that of a periodic lattice.

Once R has been modified, the surface susceptibility equations (4.7) - (4.12) can be used to determine the S-parameters which are also the transmission (S_{11}) and reflection coefficients (S_{21}). They are derived by applying the boundary conditions (4.1) - (4.4), in a similar manner to that used to derive the Fresnel reflection and transmission coefficients [20]. For a TE polarized incident wave:

$$\Gamma = \frac{-jk_0/(2\cos\theta)(\chi_{ES}^{yy} - \chi_{MS}^{xx}\cos^2\theta - \chi_{MS}^{zz}\sin^2\theta)}{1 + (k_0/2)^2\chi_{MS}^{xx}(\chi_{ES}^{yy} - \chi_{MS}^{zz}\sin^2\theta) - jk_0/(2\cos\theta)(\chi_{ES}^{yy} - \chi_{MS}^{xx}\cos^2\theta - \chi_{MS}^{zz}\sin^2\theta)} \tag{4.15}$$

$$T = \frac{1 - j(k_0/2)^2\chi_{MS}^{xx}(\chi_{ES}^{yy} - \chi_{MS}^{zz}\sin^2\theta)}{1 + (k_0/2)^2\chi_{MS}^{xx}(\chi_{ES}^{yy} - \chi_{MS}^{zz}\sin^2\theta) - jk_0/(2\cos\theta)(\chi_{ES}^{yy} - \chi_{MS}^{xx}\cos^2\theta - \chi_{MS}^{zz}\sin^2\theta)} \tag{4.16}$$

and for a TM polarized incident wave:

$$\Gamma = \frac{-jk_0/(2\cos\theta)(\chi_{MS}^{yy} - \chi_{ES}^{xx}\cos^2\theta - \chi_{ES}^{zz}\sin^2\theta)}{1 + (k_0/2)^2\chi_{ES}^{xx}(\chi_{MS}^{yy} - \chi_{ES}^{zz}\sin^2\theta) - jk_0/(2\cos\theta)(\chi_{MS}^{yy} - \chi_{ES}^{xx}\cos^2\theta - \chi_{ES}^{zz}\sin^2\theta)} \tag{4.17}$$

$$T = \frac{1 - j(k_0/2)^2\chi_{ES}^{xx}(\chi_{MS}^{yy} - \chi_{ES}^{zz}\sin^2\theta)}{1 + (k_0/2)^2\chi_{ES}^{xx}(\chi_{MS}^{yy} - \chi_{ES}^{zz}\sin^2\theta) - jk_0/(2\cos\theta)(\chi_{MS}^{yy} - \chi_{ES}^{xx}\cos^2\theta - \chi_{ES}^{zz}\sin^2\theta)} \tag{4.18}$$

When the incident field is normally incident, then equations (4.16) - (4.16) reduce to [20]:

$$\Gamma = \frac{-j(k_0/2)(\chi_{ES}^{yy} - \chi_{MS}^{xx})}{1 - (k_0/2)^2\chi_{ES}^{yy}\chi_{MS}^{xx} + j(k_0/2)(\chi_{ES}^{yy} + \chi_{MS}^{xx})} \tag{4.19}$$

$$T = \frac{1 + j(k_0/2)^2(\chi_{ES}^{yy}\chi_{MS}^{xx})}{1 - (k_0/2)^2\chi_{ES}^{yy}\chi_{MS}^{xx} + j(k_0/2)(\chi_{ES}^{yy} - \chi_{MS}^{xx})} \tag{4.20}$$

Now that the analytical equations for modeling a metafilm have been introduced, the next section will show how to modify the surface susceptibilities to take into account a square array of scatterers that are perturbed in placement.

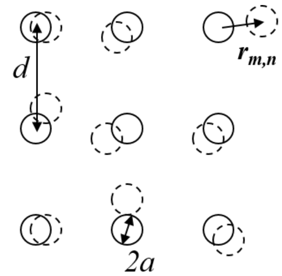

Figure 4.1: A 2D square array of elements whose lattice is perturbed from a periodic spacing. The solid outlined circles indicate periodic spacing, while the dashed outlines indicate perturbations in spacing.

4.2 Perturbed Square Lattice

The begin with, an illustration of what is meant by a perturbed square lattice is illustrated in Figure 4.1. The periodic spacing d of the lattice is indicated with circles that have a solid outline, while the perturbed location of the elements are indicated by the circles outlined with dashes. The vector $r_{m,n}$, originates from the point where the periodic location would be, and extends to the new perturbed location. Therefore, $r_{m,n}$ can be incorporated into the parameter R, equation (4.13) in the following manner

$$R_p = d\frac{2\pi}{\sum'_{n,m}[(m+\mathbf{r}_{m,n}\cdot\mathbf{a}_x/d)^2+(n+\mathbf{r}_{m,n}\cdot\mathbf{a}_y/d)^2)^{-3/2}} \tag{4.21}$$

The parameter R_p, in equation (4.21) takes into account any perturbations from the lattice of period d. It can be used to take into account random variations in spacing, such as those that would occur during the manufacturing process. A random number generator can be used to determine the amount each resonator is displaced from its periodic location. The amount of displacement should prevent the scatterers from touching, to maintain the quasi-static approximation of dipole interactions only.

The summation in the denominator of R_p, converges very slowly. However, this is easily resolved using the Richardson Extrapolation technique [2]. It allows the infinite sum to be approximated with the following expression that uses two finite sums of sizes M_1 x M_1 and M_2 x M_2, denoted $R_{p1}(M_1)$ and $R_{p2}(M_2)$ respectively.

$$R_p \cong \frac{M_1R_{p1}(M_1)-M_2R_{p2}(M_2)}{M_1-M_2} \tag{4.22}$$

A random number generator can be used to create a M_1 x M_1 array of perturbed elements and then equation

(4.21) can be used to determine R_{p1}. Next, while maintaining the values used in the M_1 x M_1 array, the array can be expanded to a larger size M_2 x M_2. Equation (4.21) can then be used to solve for R_{p2}. These values are then directly applied to equation (4.22), to get a final estimate for the infinite summation of parameter R_p.

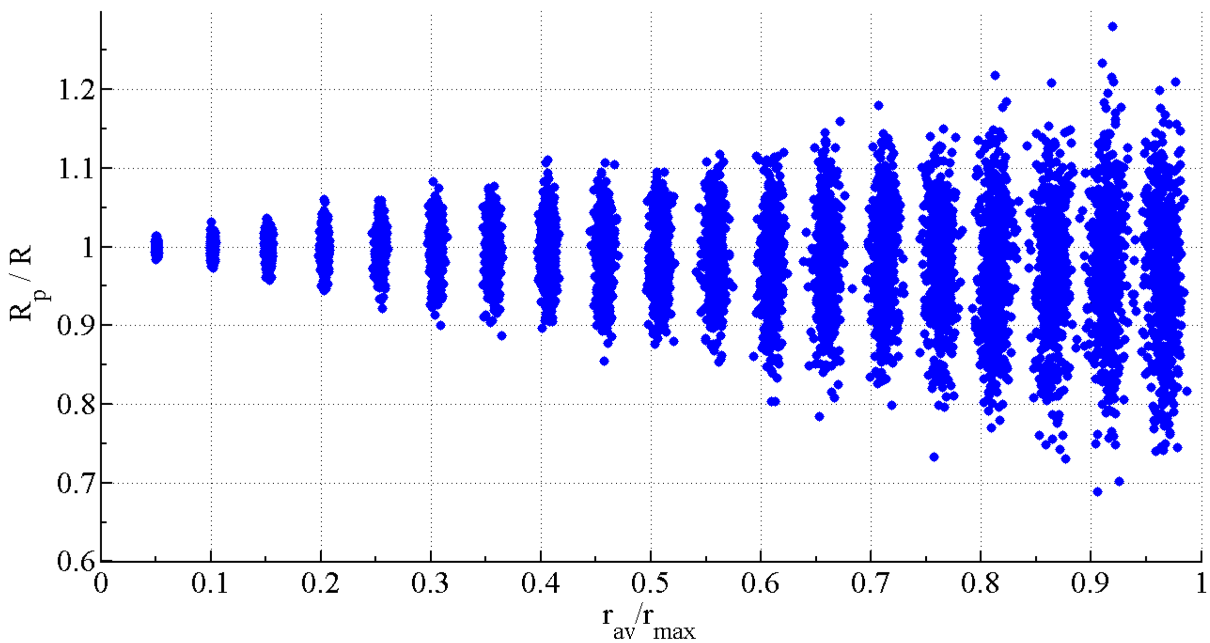

Figure 4.2: An infinite 2D array of identical scatterers with a perturbed lattice. Plot shows the statistical spread of the perturbation parameter R_p as a function of the average deviation.

In Figure 4.2, we show the spread of R_p for various displacement values, where r_{av} is the average value the elements in each array varies from its periodic position, normalized by r_{max}, the maximum value of the deviation of any element from its lattice position. Small values of r_{av}/r_{max} indicate that only small variations in the lattice are allowed, while a value of $r_{av}/r_{max} = 1$ indicates the elements may end up touching.

For this example, the periodic spacing is $d = 30$ mm and the array will be of identical spheres with radius $a = 10$ mm. This is consistent with the nominal values used in the examples of Chapters 2 and 3. To prevent the spheres from touching, the amount the sphere is allowed to be perturbed from its periodic position must be less than $d/2 - a$. A total of 19 different values of r_{max} were used to create 500 metafilms for each. Each metafilm has one value of r_{av} and R_p. They were calculated and the normalized value is represented by a blue dot in Figure 4.2. The parameter R_p is normalized by the value of R for a periodic lattice, R_0 in equation (4.14).

The graph in Figure 4.2 gives an idea of how much the parameter R can vary due to positional perturbation in the lattice. Based on the maximum and minimum values of R_p/R_0, the following values of $R_p = 1.24R_0$ and $0.68R_0$ will be used in the expressions for the surface susceptibilities, equations (4.7) - (4.12). For a normally incident wave on the metafilm, equations (4.19) - (4.20) will be used to determine the S-parameters of the metafilms.

Identical lossless spheres will form an array in free space and will be assigned a permittivity of $\epsilon_r = 100$, a permeability of $\mu_r = 1$, and a radius $a = 10$ mm, and spaced $d = 30$ mm apart. The S-parameter results are plotted versus frequency in Figure 6.1, where (a) and (c) are the magnitude and phase of S_{11}, while (b) and (d) illustrate the magnitude and phase of and S_{21}. The frequency range was chosen to include all frequencies at which the magnetic and electric dipole mode have their first resonances, as were investigated for this example in Chapters 2 and 3. Therefore this range of frequencies also includes the resonant frequencies of the surface susceptibilities. (The resonances of surface susceptibilities will be explored further in Chapter 6, but for this chapter the reader need only note that they occur very close to the resonant frequencies of the dipole moments.) For both values of R_p, the perturbation in the lattice results in simply a small shift of the curves, with essentially unchanged shape from that of the periodic case.

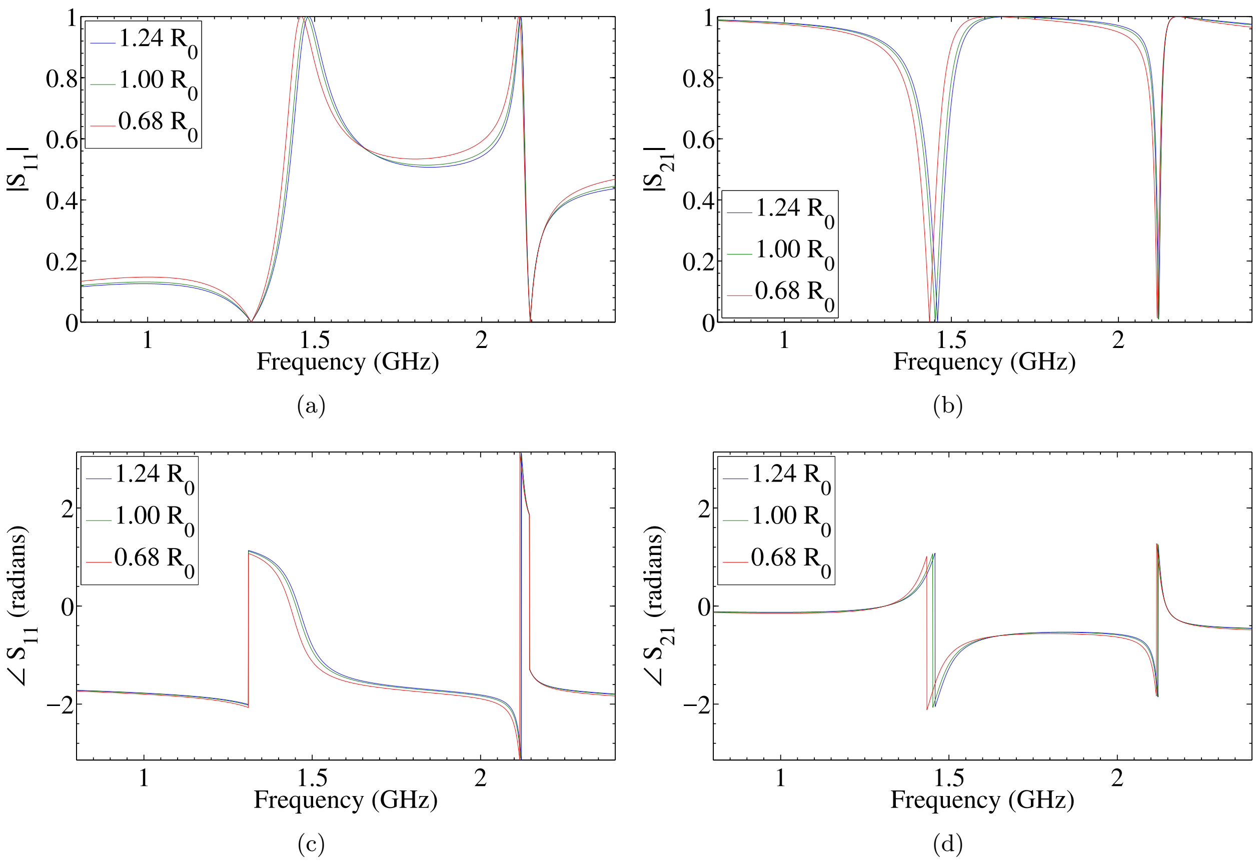

Figure 4.3: An infinite 2D identical array of lossless high dielectric spheres whose S-parameters are plotted versus frequency using the GSTCs when the lattice is perturbed. Each sphere has a radius a = 10 mm, ϵ_r = 100, spaced d = 30 mm apart and is placed in free space.

Lastly, the analytical results from the GSTCs were plotted against the results of an *HFSS* model. The *HFSS* model has a unit cell that consists of an 11 x 11 array of perturbed spheres in free space. The use of boundary conditions then creates a virtual 2D infinite sheet since the unit cell is repeated an infinite number of times. A random number generator created a case where $R_p = 1.013R_0$. The magnitude and phase of S_{11} were calculated using the analytical equations from the GSTCs and from *HFSS* as shown in Figure 6.2 for comparison. There is excellent agreement between HFSS and the GSTCs for both the perturbed and periodic cases.

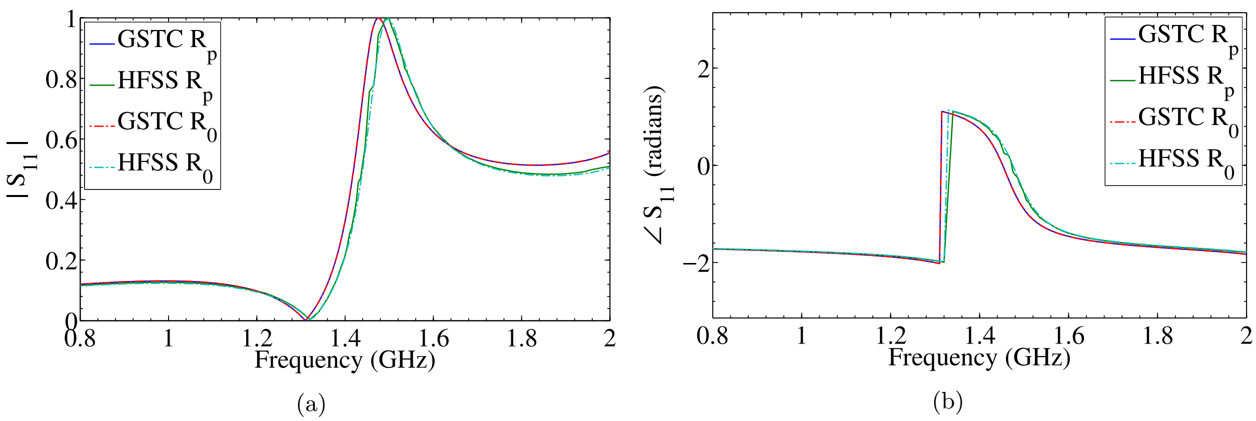

Figure 4.4: An infinite 2D identical array of lossless high permittivity spheres whose S-parameters are calculated with the GSTC model and *HFSS*, are plotted versus frequency for comparison when the lattice is either periodic or perturbed. Each sphere has a radius $a = 10$ mm, $\epsilon_r = 100$, spaced $d = 30$ mm apart, placed in free space, and $R_p = 1.013R_0$. The GSTC periodic case is indicated by a solid blue line and the perturbed case is indicated by a dashed red line. The *HFSS* results of the periodic case are plotted as a solid green curve and the perturbed case as a dashed cyan line.

4.3 Conclusion

This chapter introduced the GSTC's which are an analytical model derived in [28], [20], that properly characterize a uniform metafilm. They utilize a quasistatic approximation such that only dipole iterations are taken into account. This works well as long as the elements are small compared to a wavelength in the background medium, spaced far enough apart that they don't touch, and spaced close enough together to ensure that the lattice doesn't cause any resonances. In this chapter, this model was modified to take into account perturbations in the lattice from that of periodic spacing. The elements of the the array were kept identical so that only the effects due to nonuniformity in the lattice, could be examined. The resonators were allowed to vary from their periodic location by up to approximately half the period, just short of touching each other. The performance of the metafilm was characterized by plotting the S-parameters of the array. Comparisons of the metafilm with a periodic spacing with one having perturbed positioning revealed that the frequency dependence on the S-parameters was essentially unchanged, and exhibited only a minor shift in the overall curves. Lastly, the GSTC's were validated with *HFSS*, and showed excellent agreement. Therefore, just as in the case of the pair of identical spheres from Chapter 3, the metafilm is insensitive to small perturbations of the lattice.

Chapter 5

Metafilm of Polarizable Scatterers Perturbations in Element Parameters Analytical Derivation

In this chapter, we will extend the equations for the single and pair dipole derived in Chapters 2 and 3. To handle the case of an infinite sheet of dipoles so that they make up a metafilm. We will also utilize the ideas discussed in Chapter 4 regarding the GSTC and derive an explicit analytical expression for the surface susceptibilities. This will allow the reflection and transmission coefficients or S-parameters of a metafilm to be determined. In the previous chapter, we utilized analytical equations (4.7) - (4.12), for the surface susceptibilities, which will be referred to as the the averaging polarization approximation (APA) equations. They contain correction terms that take into account the variations in element spacing. They also attempt to approximate the effect that physical parameter variations between elements have on the surface susceptibilities, by taking the average of the polarizabilities:

$$\langle \alpha \rangle = \frac{1}{M} \sum_{m=1}^{M} \alpha_m$$

This chapter will focus on the derivation of an analytical solution which will be called the interactive polarization approximation (IPA) method. They contain coupling terms that take into account interactions between the elements. The IPA equations are more accurate expressions for determining the results of variations between elements. The expressions are more complicated than that of Chapter 3 so we will only focus on the derivation in this chapter. The next chapter will explore the numerical results for similar physical values as used in Chapters 2 - 4.

To begin with, we will consider a discrete expression for the dipole interactions in a uniform array.

Then we will extend these equations to the case of an infinite array whose elements have two different physical parameters, like a checkerboard array. Next, an infinite array with four distinct element parameter variations is considered. Finally, we obtain a general expression that can take into account many variations in the elements.

5.1 Dipole moments in a uniform square array due to an incident electric field

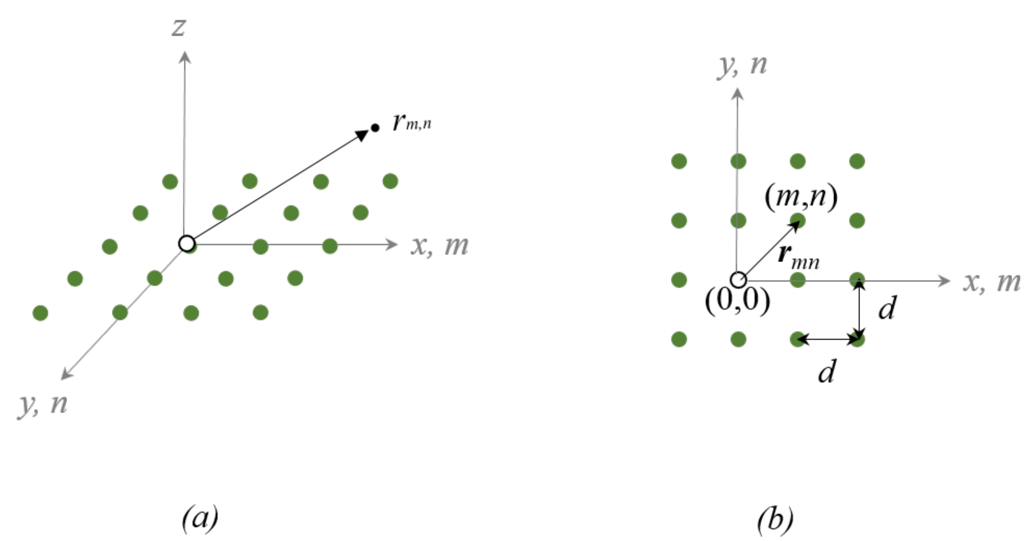

Figure 5.1: Illustration of identical dipoles placed the same distance d apart in a square infinite lattice, with the element at the origin removed.

Having studied two dipoles interacting in Chapter 2, let us extend our analysis to a two dimensional square array of dipoles of infinite extent, placed in an infinite uniform medium. We begin with a square section of the array, as seen in Figure 5.1. The plane of the array is chosen to be in the $x - y$ plane where $z = 0$.. The position of each element in the array is located at the coordinate point (md, nd), where m and n can be any integer ranging from $-\infty$ to ∞ and d is the lattice constant of the array. The origin will refer to the coordinate $(m, n) = (0,0)$. Each dipole will be identical, it's position vector is $\mathbf{r}_{mn} = d[m\mathbf{a}_x + n\mathbf{a}_y]$. Consider the dipole located at the origin. This scatterer will be subjected to an acting field that is due to the incident field and the summation of the fields due to all the other scatterers. This summation can be expressed in terms of a normalized dyadic $\overleftrightarrow{\mathbf{U}}_{m,n}$ as shown below.

Recall that the static electric field due to an electric dipole of moment $\mathbf{p}$ in a medium with permittivity of ϵ is:

$$\mathbf{E} = \frac{1}{4\pi\epsilon}[\frac{-\mathbf{p}}{r^3} + \frac{(\mathbf{p}\cdot\mathbf{r})3\mathbf{r}}{r^5}] \tag{5.1}$$

For an array of dipoles, we can write:

$$\mathbf{E}^{atorigin} = \frac{1}{4\pi\epsilon d^3}\overleftrightarrow{\mathbf{1}}\cdot[\sum{}' \overleftrightarrow{\mathbf{U}}_{m,n}]\cdot\mathbf{p} \tag{5.2}$$

where

$$\overleftrightarrow{\mathbf{U}}_{m,n} = \frac{1}{(m^2+n^2)^{3/2}}[-\overleftrightarrow{\mathbf{1}} + 3\frac{(m\mathbf{a}_x + n\mathbf{a}_y)(m\mathbf{a}_x + n\mathbf{a}_y)}{(m^2+n^2)^{2/2}}] \tag{5.3}$$

and $\overleftrightarrow{\mathbf{1}}$ is the unity dyadic, $\overleftrightarrow{\mathbf{1}} = \mathbf{a}_x\mathbf{a}_x + \mathbf{a}_y\mathbf{a}_y + \mathbf{a}_z\mathbf{a}_z$. The summation over all points except at the origin denoted by $\sum{}'$.

Now, equation (5.2) above gives the electrostatic field, but if d is small compared to a wavelength, we expect this to be reasonably accurate for a time-harmonic field. However, in an infinite array, some dipoles will be on the order of one or more wavelengths away from the origin. We argue that because of the greater distance of these dipoles, the error incurred by the quasi-static approximation will be small. This will be put to the test later in the chapter, when our analytical solution is compared with a full-wave simulation.

Let us next focus our attention on the dyadic $\overleftrightarrow{\mathbf{W}}$, defined as

$$\overleftrightarrow{\mathbf{W}} = \sum{}' \overleftrightarrow{\mathbf{U}}_{m,n} \tag{5.4}$$

which are the contributions at the origin due to the other dipoles. For the case of identical dipoles in an infinite array, periodically spaced, we will call the dyadic, $\overleftrightarrow{\mathbf{W}}_{all}$ and express it as:

$$\overleftrightarrow{\mathbf{W}}_{all} = \sum{}' \frac{1}{(m^2+n^2)^{3/2}}[-(\vec{a}_x\vec{a}_x + \vec{a}_y\vec{a}_y + \vec{a}_z\vec{a}_z) + \frac{3m^2\vec{a}_x\vec{a}_x}{m^2+n^2} + \frac{3n^2\vec{a}_y\vec{a}_y}{m^2+n^2}] \tag{5.5}$$

Notice $\overleftrightarrow{\mathbf{W}}_{all}$ is dependent upon the distances from the origin to all the other dipoles. Let us look at different parts of the equation and try to find a closed-form solution. This is done by considering two scalar sums separately.

$$I_3 = \sum{}' \frac{1}{(m^2+n^2)^{3/2}} = \frac{2\pi}{0.6956} = 9.03... \tag{5.6}$$

Next, consider a similar sum I_5, written in either of the following forms:

$$I_5 = \sum{}' \frac{m^2}{(m^2+n^2)^{5/2}} = \sum{}' \frac{n^2}{(m^2+n^2)^{5/2}} \tag{5.7}$$

Which are equivalent because m and n are dummy indices. Adding both of the expressions for I_5 will give us an expression for I_5 in terms of I_3:

$$I_5 + I_5 = \sum{}' \frac{m^2+n^2}{(m^2+n^2)^{5/2}} = I_3$$

Thus, $I_5 = \frac{1}{2}I_3$. Since I_3 is a known constant, so now we have a much more compact way to express $\overleftrightarrow{\mathbf{W}}_{all}$:

$$\overleftrightarrow{\mathbf{W}}_{all} = I_3[-(\vec{a}_x\vec{a}_x + \vec{a}_y\vec{a}_y + \vec{a}_z\vec{a}_z) + 3/2((\vec{a}_x\vec{a}_x + \vec{a}_y\vec{a}_y)] \tag{5.8}$$

Finally we express $\overleftrightarrow{\mathbf{W}}_{all}$. in terms of components transverse and normal to plane of the array by introducing the constants $C_t = 0.5$ and $C_z = -1$:

$$\overleftrightarrow{\mathbf{W}}_{all} = I_3[C_t\overleftrightarrow{\mathbf{1}}_t + C_z\overleftrightarrow{\mathbf{1}}_z] \tag{5.9}$$

We now substitute the closed-form solution of $\overleftrightarrow{\mathbf{W}}_{all}$ (5.9), into the the expression (5.2) for the electric field, separating it into transverse and normal components: $\mathbf{E}_t^{atorigin}$ is the electric field in the direction in the plane of the array and $\mathbf{E}_z^{atorigin}$ is in the direction perpendicular to the plane of the array. Writing the unity dyadic in its transverse $\overleftrightarrow{\mathbf{1}}_t = \mathbf{a}_x\mathbf{a}_x + \mathbf{a}_y\mathbf{a}_y$ and normal $\overleftrightarrow{\mathbf{1}}_z\overleftrightarrow{\mathbf{1}}_z = \mathbf{a}_z\mathbf{a}_z$ components, the electric field at the origin due to an infinite sheet of identical dipoles spaced an equal distance apart, minus the one at the origin, can be expressed as:

$$\mathbf{E}_t^{atorigin} = \frac{1}{4\pi\epsilon d^3}\overleftrightarrow{\mathbf{1}}_t \cdot \overleftrightarrow{\mathbf{W}}_{all} \cdot \mathbf{p} \tag{5.10}$$

$$\mathbf{E}_z^{atorigin} = \frac{1}{4\pi\epsilon d^3}\overleftrightarrow{\mathbf{1}}_z \cdot \overleftrightarrow{\mathbf{W}}_{all} \cdot \mathbf{p} \tag{5.11}$$

Substituting equation (5.9) into (5.10) and (5.11) and defining some additional constants below K_t and K_z as below, we have more convenient forms:

$$E_t^{atorigin} = \frac{K_t}{\epsilon}p_t \tag{5.12}$$

$$E_z^{atorigin} = \frac{K_z}{\epsilon}p_z \tag{5.13}$$

where

$$K_t = \frac{1}{4\pi d^3}I_3C_t = \frac{1}{4\pi d^3}\frac{2\pi}{0.6956}\frac{1}{2} = \frac{0.3594}{d^3} \tag{5.14}$$

$$K_z = \frac{1}{4\pi d^3} I_3 C_z = \frac{1}{4\pi d^3} \frac{2\pi}{0.6956}(-1) = \frac{-0.7188}{d^3} \tag{5.15}$$

Now, we express the electric dipole moment $\mathbf{p}$, as the electric polarizability α_E of the resonator at the origin dotted with acting field, which is the incident field plus the field due to all the other scatterers except at the origin. We assume a uniform medium with permittivity of ϵ:

$$\mathbf{p} = \epsilon \overleftrightarrow{\boldsymbol{\alpha}}_E \cdot \mathbf{E}^{act} = \epsilon \overleftrightarrow{\boldsymbol{\alpha}}_E \cdot (\mathbf{E}^{atorigin} + \mathbf{E}^{inc}) \tag{5.16}$$

Here the electric polarizability is expressed as a dyadic $\overleftrightarrow{\boldsymbol{\alpha}}_E$. To simplify the algebra, we will now restrict the the shape of the scatterer such that it is uniaxial. Examples of scatterers of this nature are spheres, cylinders, long rectangular boxes, a hockey puck, etc. The polarizability dyadic then has the form

$$\overleftrightarrow{\boldsymbol{\alpha}}_E = \alpha_E^{tt} \overleftrightarrow{\mathbf{1}}_t + \alpha_E^{zz} \overleftrightarrow{\mathbf{1}}_z \tag{5.17}$$

Now equation (5.16) becomes:

$$p_t = \epsilon \alpha_E^{tt} (E_t^{atorigin} + E_t^{inc}) \tag{5.18}$$

$$p_z = \epsilon \alpha_E^{zz} (E_z^{atorigin} + E_z^{inc}) \tag{5.19}$$

Next, examine the equation (5.18) for p_t, solve for $E_t^{atorigin}$ and set it equal to equation (5.12):

$$\frac{p_t}{\epsilon \alpha_E^{tt}} - E_t^{inc} = \frac{K_t}{\epsilon} p_t \tag{5.20}$$

We can solve for $\mathbf{p}_t$ and perform similar operations for the normal case. Which results in expressions for the dipole moments of a sheet of identical resonators equally spaced, in terms of the incident field:

$$p_t = \epsilon E_t^{inc} \frac{\alpha_E^{tt}}{1 - \alpha_E^{tt} K_t} \tag{5.21}$$

$$p_z = \epsilon E_z^{inc} \frac{\alpha_E^{zz}}{1 - \alpha_E^{zz} K_z} \tag{5.22}$$

If $N = 1/d^2$ is the number of dipoles per unit square area, then the surface polarization densities can be used to define electric surface susceptibilities for a sheet of dipoles by

$$P_{st} = N p_t = \epsilon E_t^{inc} \chi_{ES}^{tt} \tag{5.23}$$

$$P_{sz} = N p_z = \epsilon E_z^{inc} \chi_{ES}^{zz} \tag{5.24}$$

where

$$\chi_{ES}^{tt} = N \frac{\alpha_E^{tt}}{1 - \alpha_E^{tt} K_t} \tag{5.25}$$

$$\chi_{ES}^{zz} = N \frac{\alpha_E^{zz}}{1 - \alpha_E^{zz} K_z} \tag{5.26}$$

We can compare the equation above for χ_{ES}^{tt} with equation (4.7). Where variable R of equation (4.7) is equal to $d2\pi/I_3$. Looking at K_t and substituting R for $d2\pi/I_3$, we get that K_t becomes $C_t/(2Rd^2)$. Now substitute $N = 1/d^2$ and $C_t = 1/2$ we get that $K_t = N/(4R)$, which agrees with the result of equation (4.7). Once $\mathbf{P_s}$ is substituted into the jump conditions, we get the GSTCs.

Now consider the magnetic case

$$m_t = H_t^{inc} \frac{\alpha_M^{tt}}{1 + \alpha_M^{tt} K_t} \tag{5.27}$$

$$m_z = H_z^{inc} \frac{\alpha_M^{zz}}{1 + \alpha_M^{zz} K_z} \tag{5.28}$$

$$M_{st} = N m_t = H_t^{inc} \chi_{MS}^{tt} \tag{5.29}$$

$$M_{sz} = N m_z = H_z^{inc} \chi_{MS}^{zz} \tag{5.30}$$

Thus, the magnetic surface susceptibility for a sheet of scatterers becomes

$$\chi_{MS}^{tt} = N \frac{\alpha_M^{tt}}{1 + \alpha_M^{tt} K_t} \tag{5.31}$$

$$\chi_{MS}^{zz} = N \frac{\alpha_M^{zz}}{1 + \alpha_M^{zz} K_z} \tag{5.32}$$

where $\mathbf{m}$ is the magnetic dipole moment, $\overleftrightarrow{\mathbf{M}}_s$ is the magnetic surface polarization density.

Now we ask: what if the scatterers are not at all identical? For example, after fabricating the scatterers they are certain to differ by at least a small amount. Can one could handle this situation by simply taking the average of all the polarizabilities? This is a heuristic approach that has not been validated completely. We will question this approach below and ask when it might be valid for nonidentical scatterers. This will show what is the proper way to express the effects of nonidentical scatterers and when we can and can't use the averaging approach.

5.2 Surface Polarization and Magnetization for Non-Identical Scatterers and the GSTC

5.2.1 2x2 Unit Cell of Dipoles with 2 Slightly Different Properties

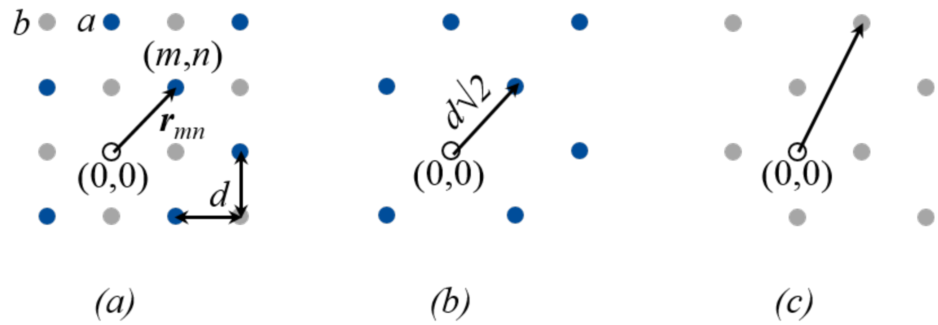

Figure 5.2: Illustration of an infinite checkerboard array of dipoles designated a and b in a square array with period d and placed in free space

We begin with the simplest case of two nonidentical scatterers in a checkerboard lattice. Instead of averaging the polarizabilities, we simply acknowledge that they will have different polarizabilities and see where this analysis leads. An illustration of the checkerboard lattice is shown in Figure 5.2. Each scatterer will have its own dipole moment, $\mathbf{p}_a$ for dipole a and $\mathbf{p}_b$ for dipole b.

We start by expanding the expression for the electric field due to all the other dipoles equation (5.10). Similarly to what was done for identical dipoles, we now have to split the equation into terms for the a and b sites. The dipole moments $\mathbf{p}_a$ and $\mathbf{p}_b$ will each be acting on the reference point. Let dipole a be at the reference point at the origin as shown in Figure 5.2. The electric field at site a due to all the other dipoles will be called $\mathbf{E}_t^{atsitea}$. Since all the a dipoles have a dipole moment of $\mathbf{p}_a$, we need an expression that only includes the distances from the a dipoles to the reference a dipole as shown in Figure 5.2, and we call this interaction dyadic $\mathbf{W}_{aa}$. Similarly we will call the interaction dyadic of all the b dipoles on dipole a as $\mathbf{W}_{ab}$. Lastly, when the reference point is a b dipole the interaction dyadic to the a dipoles will be $\mathbf{W}_{ba}$, and to b dipoles, $\mathbf{W}_{bb}$:

$$\mathbf{E}_t^{atsitea} = \frac{1}{4\pi\epsilon d^3}\overleftrightarrow{\mathbf{1}}_t \cdot [\overleftrightarrow{\mathbf{W}}_{aa} \cdot \mathbf{p}_a + \overleftrightarrow{\mathbf{W}}_{ab} \cdot \mathbf{p}_b] \tag{5.33}$$

$$\mathbf{E}_z^{atsitea} = \frac{1}{4\pi\epsilon d^3}\overleftrightarrow{\mathbf{1}}_z \cdot [\overleftrightarrow{\mathbf{W}}_{aa} \cdot \mathbf{p}_a + \overleftrightarrow{\mathbf{W}}_{ab} \cdot \mathbf{p}_b] \tag{5.34}$$

$$\mathbf{E}_t^{atsiteb} = \frac{1}{4\pi\epsilon d^3}\overleftrightarrow{\mathbf{1}}_t \cdot [\overleftrightarrow{\mathbf{W}}_{aa} \cdot \mathbf{p}_b + \overleftrightarrow{\mathbf{W}}_{ab} \cdot \mathbf{p}_a] \tag{5.35}$$

$$\mathbf{E}_z^{atsiteb} = \frac{1}{4\pi\epsilon d^3}\overleftrightarrow{\mathbf{1}}_z \cdot [\overleftrightarrow{\mathbf{W}}_{aa} \cdot \mathbf{p}_b + \overleftrightarrow{\mathbf{W}}_{ab} \cdot \mathbf{p}_a] \tag{5.36}$$

We first evaluate the interaction dyadic $\overleftrightarrow{\mathbf{W}}_{aa}$. This lattice will only consist of the a dipoles as shown in Figure 5.2. If we rotate our coordinate system by 45 degrees, we notice that we essentially have the same lattice as in the identical dipole case $\overleftrightarrow{\mathbf{W}}_{all}$, but with a different period of $d\sqrt{2}$. So, let $C_1 = 1/2^{3/2}$ and we have that

$$\overleftrightarrow{\mathbf{W}}_{aa} = C_1\overleftrightarrow{\mathbf{W}}_{all}$$

Next, we need an expression for $\overleftrightarrow{\mathbf{W}}_{ab}$. A shortcut is to recognize that this will simply be $\overleftrightarrow{\mathbf{W}}_{all} - \overleftrightarrow{\mathbf{W}}_{aa}$. Let $C_2 = 1 - C_1$ and we have

$$\overleftrightarrow{\mathbf{W}}_{ab} = C_2\overleftrightarrow{\mathbf{W}}_{all} \tag{5.37}$$

Similarly, when b is the reference point, we can apply the same approach as above and get $\overleftrightarrow{\mathbf{W}}_{bb} = C_1\overleftrightarrow{\mathbf{W}}_{all}$ and $\overleftrightarrow{\mathbf{W}}_{ba} = C_2\overleftrightarrow{\mathbf{W}}_{all}$.

Now, we examine the equation for the tangential electric field at site a in equation (5.33) and plug in our equations for $\overleftrightarrow{\mathbf{W}}_{aa}$ and $\overleftrightarrow{\mathbf{W}}_{ab}$:

$$E_t^{atsitea} = \frac{I_3}{4\pi\epsilon d^3}[C_tC_1p_{at} + C_tC_2p_{bt}] \tag{5.38}$$

This can be simplified by defining some new constants K_{1t}, K_{1z}, K_{2t}, and K_{2z}:

$$K_{t1} = K_tC_1 = \frac{1}{4\pi d^3}\frac{2\pi}{0.6956}\frac{1}{2}\frac{1}{2^{3/2}} = \frac{0.1271}{d^3} \tag{5.39}$$

$$K_{z1} = K_zC_1 = \frac{1}{4\pi d^3}\frac{2\pi}{0.6956}(-1)\frac{1}{2^{3/2}} = \frac{-0.2541}{d^3} \tag{5.40}$$

$$K_{t2} = K_tC_2 = \frac{1}{4\pi d^3}\frac{2\pi}{0.6956}\frac{1}{2}(1-\frac{1}{2^{3/2}}) = \frac{0.2323}{d^3} \tag{5.41}$$

$$K_{z2} = K_zC_2 = \frac{1}{4\pi d^3}\frac{2\pi}{0.6956}(-1)(1-\frac{1}{2^{3/2}}) = \frac{-0.4647}{d^3} \tag{5.42}$$

It is now a simple matter to express all the electric field equations (5.33)-(5.36) as:

$$E_t^{at,site,a} = \frac{1}{\epsilon}[K_{1t}p_{at} + K_{2t}p_{bt}] \tag{5.43}$$

$$E_z^{at,site,a} = \frac{1}{\epsilon}[K_{1z}p_{az} + K_{2z}p_{bz}] \tag{5.44}$$

$$E_t^{at,site,b} = \frac{1}{\epsilon}[K_{1t}p_{bt} + K_{2t}p_{at}] \tag{5.45}$$

$$E_z^{at,site,b} = \frac{1}{\epsilon}[K_{1z}p_{bz} + K_{2z}p_{az}] \tag{5.46}$$

Next we shift our attention to expressions for the electric dipole moments $\mathbf{p}_a$ and $\mathbf{p}_b$ for the a and b dipoles respectively. The electric dipole moment is equal to the permittivity of the surrounding media multiplied by the polarizability dyadic, dotted with the acting electric field. In the checkerboard case, the acting field when dipole a is at the origin differs from that of dipole b placed at the origin. This is because a different set of dipoles acts on that site:

$$\mathbf{p}_a = \epsilon \overleftrightarrow{\boldsymbol{\alpha}}_{Ea} \cdot (\mathbf{E}^{atsitea} + \mathbf{E}^{inc}) \tag{5.47}$$

$$\mathbf{p}_b = \epsilon \overleftrightarrow{\boldsymbol{\alpha}}_{Eb} \cdot (\mathbf{E}^{atsiteb} + \mathbf{E}^{inc}) \tag{5.48}$$

Again, let the polarizability be assumed to be uniaxial. The electric polarizability of the a dipoles will be $\overleftrightarrow{\boldsymbol{\alpha}}_{Ea}$, and for the b dipoles $\overleftrightarrow{\boldsymbol{\alpha}}_{Eb}$

$$\overleftrightarrow{\boldsymbol{\alpha}}_{Ea} = \alpha_{Ea}^{tt}\overleftrightarrow{\mathbf{1}}_t + \alpha_{Ea}^{zz}\overleftrightarrow{\mathbf{1}}_z \tag{5.49}$$

$$\overleftrightarrow{\boldsymbol{\alpha}}_{Eb} = \alpha_{Eb}^{tt}\overleftrightarrow{\mathbf{1}}_t + \alpha_{Eb}^{zz}\overleftrightarrow{\mathbf{1}}_z \tag{5.50}$$

Using the equations for the polarizabilities above and performing the dot product on $\mathbf{p}_a$, we get

$$\mathbf{p}_{at} = \epsilon \alpha_{Ea}^{tt}(\mathbf{E}_t^{atsitea} + \mathbf{E}_t^{inc}) \tag{5.51}$$

Next, we solve for $\mathbf{E}_t^{atsitea}$ and do the same for the other cases $\mathbf{E}_z^{atsitea}$, $\mathbf{E}_t^{atsiteb}$, and $\mathbf{E}_z^{atsiteb}$:

$$E_t^{atsitea} = \frac{1}{\epsilon \alpha_{Ea}^{tt}} p_{at} - E_t^{inc} \tag{5.52}$$

$$E_z^{atsitea} = \frac{1}{\epsilon \alpha_{Ea}^{zz}} p_{az} - E_z^{inc} \tag{5.53}$$

$$E_t^{atsiteb} = \frac{1}{\epsilon \alpha_{Eb}^{tt}} p_{bt} - E_t^{inc} \tag{5.54}$$

$$E_z^{atsiteb} = \frac{1}{\epsilon \alpha_{Eb}^{zz}} p_{bz} - E_z^{inc} \tag{5.55}$$

Now we have expressions for the acting electric field at the site in terms of one polarizability and the incident field. Taking these four equations above and setting them equal to equations (5.43)-(5.46) obtained earlier for the acting field in terms of all the dipoles on the sheet. In other words, we solve the 2x2 system of equation for p_{at} and p_{bt} in terms of E^{inc}, and do the same for p_{az} and p_{bz}, the result being:

$$\epsilon E_t^{inc} = (\frac{1}{\alpha_{Ea}^{tt}} - K_{1t})p_{at} + (-K_{2t})p_{bt} \tag{5.56}$$

$$\epsilon E_z^{inc} = (\frac{1}{\alpha_{Ea}^{zz}} - K_{1z})p_{az} + (-K_{2z})p_{bz} \tag{5.57}$$

$$\epsilon E_t^{inc} = (\frac{1}{\alpha_{Eb}^{tt}} - K_{1t})p_{bt} + (-K_{2t})p_{at} \tag{5.58}$$

$$\epsilon E_z^{inc} = (\frac{1}{\alpha_{Eb}^{zz}} - K_{1z})p_{bz} + (-K_{2z})p_{az} \tag{5.59}$$

Solving equations (5.56) - (5.59) above, obtain relations between the dipole moments of the scatterers:

$$p_{at} = p_{bt}(\frac{\frac{1}{\alpha_{Eb}^{tt}} - K_{1t} + K_{2t}}{\frac{1}{\alpha_{Ea}^{tt}} - K_{1t} + K_{2t}}) \tag{5.60}$$

$$p_{az} = p_{bz}(\frac{\frac{1}{\alpha_{Eb}^{zz}} - K_{1z} + K_{2z}}{\frac{1}{\alpha_{Ea}^{zz}} - K_{1z} + K_{2z}}) \tag{5.61}$$

$$p_{bt} = p_{at}(\frac{\frac{1}{\alpha_{Ea}^{tt}} - K_{1t} + K_{2t}}{\frac{1}{\alpha_{Eb}^{tt}} - K_{1t} + K_{2t}}) \tag{5.62}$$

$$p_{bz} = p_{az}(\frac{\frac{1}{\alpha_{Ea}^{zz}} - K_{1z} + K_{2z}}{\frac{1}{\alpha_{Eb}^{zz}} - K_{1z} + K_{2z}}) \tag{5.63}$$

Now take equation (5.62) and put it into equation (5.56); after some simplification we have

$$\epsilon E_t^{inc} = \frac{\frac{1}{\alpha_{Ea}^{tt}\alpha_{Eb}^{tt}} - K_{1t}(\frac{1}{\alpha_{Ea}^{tt}} + \frac{1}{\alpha_{Eb}^{tt}}) + K_{1t}^2 - K_{2t}^2}{\frac{1}{\alpha_{Eb}^{tt}} - K_{1t} + K_{2t}} p_{at} \tag{5.64}$$

Finally we solve for p_{at} and simplify further, and do the same procedure for p_{az}, p_{bt}, and p_{bz}. The final results are:

$$p_{at} = \epsilon E_t^{inc} \frac{\alpha_{Ea}^{tt}(1 + \alpha_{Eb}^{tt}(K_{2t} - K_{1t}))}{1 - (\alpha_{Ea}^{tt} + \alpha_{Eb}^{tt})K_{1t} - \alpha_{Ea}^{tt}\alpha_{Eb}^{tt}(K_{2t}^2 - K_{1t}^2)} \tag{5.65}$$

$$p_{az} = \epsilon E_z^{inc} \frac{\alpha_{Ea}^{zz}(1 + \alpha_{Eb}^{zz}(K_{2z} - K_{1z}))}{1 - (\alpha_{Ea}^{zz} + \alpha_{Eb}^{zz})K_{1z} - \alpha_{Ea}^{zz}\alpha_{Eb}^{zz}(K_{2z}^2 - K_{1z}^2)} \tag{5.66}$$

$$p_{bt} = \epsilon E_t^{inc} \frac{\alpha_{Eb}^{tt}(1 + \alpha_{Ea}^{tt}(K_{2t} - K_{1t}))}{1 - (\alpha_{Eb}^{tt} + \alpha_{Ea}^{tt})K_{1t} - \alpha_{Eb}^{tt}\alpha_{Ea}^{tt}(K_{2t}^2 - K_{1t}^2)} \tag{5.67}$$

$$p_{bz} = \epsilon E_z^{inc} \frac{\alpha_{Eb}^{zz}(1 + \alpha_{Ea}^{zz}(K_{2z} - K_{1z}))}{1 - (\alpha_{Eb}^{zz} + \alpha_{Ea}^{zz})K_{1z} - \alpha_{Eb}^{zz}\alpha_{Ea}^{zz}(K_{2z}^2 - K_{1z}^2)} \tag{5.68}$$

We can express equation (5.65) for p_{at} in a way that showcases the dependence on the elemental spacing d. Since K_{1t} and K_{2t} have the units of m^{-3}, lets use dimensionless quantities instead: $C_{1t} = d^2 K_{1t}$ and $C_{2t} = d^2 K_{2t}$. We now have

$$p_{at} = \epsilon E_t^{inc} \frac{\alpha_{Ea}^{tt}(1 + \alpha_{Eb}^{tt}(C_{2t} - C_{1t})(1/d^3))}{1 - (\alpha_{Ea}^{tt} + \alpha_{Eb}^{tt})C_{1t}(1/d^3)) - \alpha_{Ea}^{tt}\alpha_{Eb}^{tt}(C_{2t}^2 - C_{1t}^2)(1/d^6))} \; [Cm] \tag{5.69}$$

When taking a Clausius–Mossotti approach, we assume that α_{Ea}^{tt}/d^3 is small. If we apply this assumption to equations for equation (5.69), then looking at the numerator, $\alpha_{Ea}/d^3 \gg \alpha_{Ea}\alpha_{Eb}/d^6$ and for the denominator $(\alpha_{Ea} + \alpha_{Eb})/d^3 \gg \alpha_{Ea}\alpha_{Eb}/d^6$. Applying these same approximations to equation (5.67) for p_{bt} and adding p_{at} and p_{bt} we get twice the average as seen below:

$$p_{at} + p_{bt} = \epsilon E_t^{inc} \frac{\alpha_{Ea}^{tt} + \alpha_{Eb}^{tt}}{1 - (\alpha_{Ea}^{tt} + \alpha_{Eb}^{tt})K_{1t}} \cong 2 < \alpha_E > \; (for\ small\ \alpha_{Ea}\alpha_{Eb}) \tag{5.70}$$

Thus, now we have a condition for the validity of the averaging approach: $d^6 \gg \alpha_{Ea}\alpha_{Eb}$. Looking back at Chapter 2, we see that the product of α_{Ea} and α_{Eb} will be small except when resonances occur. At resonance, their values become large, so a more detailed approach is needed. If we want a model that will include the response at resonance (for example when modeling metamaterials), the assumptions for the averaging approach will not apply. This will be apparent in the next chapter when we examine numerical results.

Now we will finish the derivation for surface polarization. We can express the surface polarization in terms of the individual dipole moments. The variable $N' = 1/(d\sqrt{2})^2 = N/2$ is the number of each type of scatterer per unit area. We assume a transversely isotropic scatterers, so we won't need to distinguish between the two different transverse polarizabilities. Then

$$P_{at} = N' p_{at} = \epsilon E_t^{inc} \chi_{ESa}^{tt} \tag{5.71}$$

$$P_{bt} = N' p_{bt} = \epsilon E_b^{inc} \chi_{ESb}^{tt} \tag{5.72}$$

Where, χ_{Ea}^{tt} and χ_{Eb}^{tt} are the partial surface susceptibility, associated with the a and b dipoles respectively. So, for a checkerboard lattice of dipoles, the electric susceptibilities are

$$\chi_{ESa}^{tt} = N' \frac{\alpha_{Ea}^{tt}(1 + \alpha_{Eb}^{tt}(K_{2t} - K_{1t}))}{1 - (\alpha_{Ea}^{tt} + \alpha_{Eb}^{tt})K_{1t} - \alpha_{Ea}^{tt}\alpha_{Eb}^{tt}(K_{2t}^2 - K_{1t}^2)} \tag{5.73}$$

$$\chi_{ESa}^{zz} = N' \frac{\alpha_{Ea}^{zz}(1 + \alpha_{Eb}^{zz}(K_{2z} - K_{1z}))}{1 - (\alpha_{Ea}^{zz} + \alpha_{Eb}^{zz})K_{1z} - \alpha_{Ea}^{zz}\alpha_{Eb}^{zz}(K_{2z}^2 - K_{1z}^2)} \tag{5.74}$$

$$\chi_{ESb}^{tt} = N' \frac{\alpha_{Eb}^{tt}(1 + \alpha_{Ea}^{tt}(K_{2t} - K_{1t}))}{1 - (\alpha_{Eb}^{tt} + \alpha_{Ea}^{tt})K_{1t} - \alpha_{Eb}^{tt}\alpha_{Ea}^{tt}(K_{2t}^2 - K_{1t}^2)} \tag{5.75}$$

$$\chi_{ESb}^{zz} = N' \frac{\alpha_{Eb}^{zz}(1 + \alpha_{Ea}^{zz}(K_{2z} - K_{1z}))}{1 - (\alpha_{Eb}^{zz} + \alpha_{Ea}^{zz})K_{1z} - \alpha_{Eb}^{zz}\alpha_{Ea}^{zz}(K_{2z}^2 - K_{1z}^2)} \tag{5.76}$$

The the total electric susceptibilities are now defined by

$$P_{st} = P_{sat} + P_{sbt} = N'(p_{at} + p_{bt}) = \epsilon E_t^{inc}\chi_{ES}^{tt} \tag{5.77}$$

$$P_{sz} = P_{saz} + P_{sbz} = N'(p_{az} + p_{bz}) = \epsilon E_z^{inc}\chi_{ES}^{zz} \tag{5.78}$$

Recalling that $N' = N/2$, we have finally

$$\chi_{ES}^{tt} = N \frac{(1/2)(\alpha_{Ea}^{tt} + \alpha_{Eb}^{tt}) + \alpha_{Ea}^{tt}\alpha_{Eb}^{tt}(K_{2t} - K_{1t}))}{1 - (1/2)(\alpha_{Ea}^{tt} + \alpha_{Eb}^{tt})2K_{1t} - \alpha_{Ea}^{tt}\alpha_{Eb}^{tt}(K_{2t}^2 - K_{1t}^2)} \tag{5.79}$$

$$\chi_{ES}^{zz} = N \frac{(1/2)(\alpha_{Ea}^{zz} + \alpha_{Eb}^{zz}) + \alpha_{Ea}^{zz}\alpha_{Eb}^{zz}(K_{2z} - K_{1z}))}{1 - (1/2)(\alpha_{Ea}^{zz} + \alpha_{Eb}^{zz})2K_{1z} - \alpha_{Ea}^{zz}\alpha_{Eb}^{zz}(K_{2z}^2 - K_{1z}^2)} \tag{5.80}$$

Let's take a moment to recognize that the average polarizabilities of the two types of dipole moments can be expressed as

$$< \alpha_E^{tt} >= (1/2)(\alpha_{Ea}^{tt} + \alpha_{Eb}^{tt}) \tag{5.81}$$

and

$$< \alpha_E^{zz} >= (1/2)(\alpha_{Ea}^{zz} + \alpha_{Eb}^{zz}) \tag{5.82}$$

$2K_1 = K_t/\sqrt{2}$, since $K_t = N/(4R)$, this is $2K_1 = N/4R\sqrt{2}$, and therefore

$$\chi_{ES}^{tt} = N \frac{< \alpha_E^{zz} > + \alpha_{Ea}^{tt}\alpha_{Eb}^{tt}(K_{2t} - K_{1t}))}{1 - < \alpha_E^{zz} > \frac{N}{4R}\frac{1}{\sqrt{2}} - \alpha_{Ea}^{tt}\alpha_{Eb}^{tt}(K_{2t}^2 - K_{1t}^2)} \tag{5.83}$$

Comparing this with the equation (4.7), for the GSTC of a uniform metafilm, we see that letting $\alpha_{Ea} = \alpha_{Eb}$ in equation (5.83) gives the same result. Thus, for a checkerboard array of scatterers, we get the correction terms $\alpha_{Ea}^{tt}\alpha_{Eb}^{tt}(K_{2t} - K_{1t}))$ in the numerator, and $\alpha_{Ea}^{tt}\alpha_{Eb}^{tt}(K_{2t}^2 - K_{1t}^2)$ in the denominator of (5.83). As well as a corrective multiplication factor of $1/\sqrt{2}$ in the denominator. The significance of these terms will be examined in the next chapter when we will apply the equations derived in this chapter to physical examples and compare their results.

Similarly, we get the following equations for the magnetic case:

$$m_{at} = H_t^{inc} \frac{\alpha_{Ma}^{tt}(1 + \alpha_{Mb}^{tt}(K_{2t} - K_{1t}))}{1 - (\alpha_{Ma}^{tt} + \alpha_{Mb}^{tt})K_{1t} - \alpha_{Ma}^{tt}\alpha_{Mb}^{tt}(K_{2t}^2 - K_{1t}^2)} \tag{5.84}$$

$$m_{az} = H_z^{inc} \frac{\alpha_{Ma}^{zz}(1 + \alpha_{Mb}^{zz}(K_{2z} - K_{1z}))}{1 - (\alpha_{Ma}^{zz} + \alpha_{Mb}^{zz})K_{1z} - \alpha_{Ma}^{zz}\alpha_{Mb}^{zz}(K_{2z}^2 - K_{1z}^2)} \tag{5.85}$$

$$m_{bt} = H_t^{inc} \frac{\alpha_{Mb}^{tt}(1 + \alpha_{Ma}^{tt}(K_{2t} - K_{1t}))}{1 - (\alpha_{Mb}^{tt} + \alpha_{Ma}^{tt})K_{1t} - \alpha_{Mb}^{tt}\alpha_{Ma}^{tt}(K_{2t}^2 - K_{1t}^2)} \tag{5.86}$$

$$m_{bz} = H_z^{inc} \frac{\alpha_{Mb}^{zz}(1 + \alpha_{Ma}^{zz}(K_{2z} - K_{1z}))}{1 - (\alpha_{Mb}^{zz} + \alpha_{Ma}^{zz})K_{1z} - \alpha_{Mb}^{zz}\alpha_{Ma}^{zz}(K_{2z}^2 - K_{1z}^2)} \tag{5.87}$$

$$\chi_{MS}^{tt} = (\chi_{Ma}^{tt} + \chi_{Mb}^{tt}) \tag{5.88}$$

$$\chi_{MS}^{zz} = (\chi_{Ma}^{zz} + \chi_{Mb}^{zz}) \tag{5.89}$$

where χ_{Ma}^{tt} and χ_{Mb}^{tt} are the magnetic surface susceptibilities of the a and b dipoles in the t direction, and χ_{Ma}^{zz} and χ_{Mb}^{zz} in the z direction respectively.

5.2.2 2x2 Unit Cell of Elements with Four Slightly Different Polarizabilities

In Figure 5.3 (a), the case of a 2 by 2 unit cell of 4 scatterers with 4 slightly different polarizabilities is shown. The four types of scatterers are designated as: a in blue dots, b in dots of green crosshatched, c in red circles, and d in yellow dots. The unit cell is replicated an infinite number of times. Again, $\mathbf{r}_{m,n}$ is the position vector that points from the reference dipole to any of the other dipoles. Again, they are uniformly spaced a distance d apart in both the x and y directions. Once again, n designates a point along the y axis and m along x.

Now we need expressions for $\mathbf{K}_1$, $\mathbf{K}_2$, $\mathbf{K}_3$, and $\mathbf{K}_4$, where $\mathbf{K} = \frac{1}{4\pi d^3}\overleftrightarrow{\mathbf{W}}$ for the different subarrays. We remove dipole a at the origin and solve for $\overleftrightarrow{\mathbf{W}}_{aa,4}$, an expression that only includes distances from the reference point a to all the other a elements. In Figure 5.3 (b), we can readily see that $\overleftrightarrow{\mathbf{W}}_{aa,4}$ is simply $\overleftrightarrow{\mathbf{W}}_{all}$

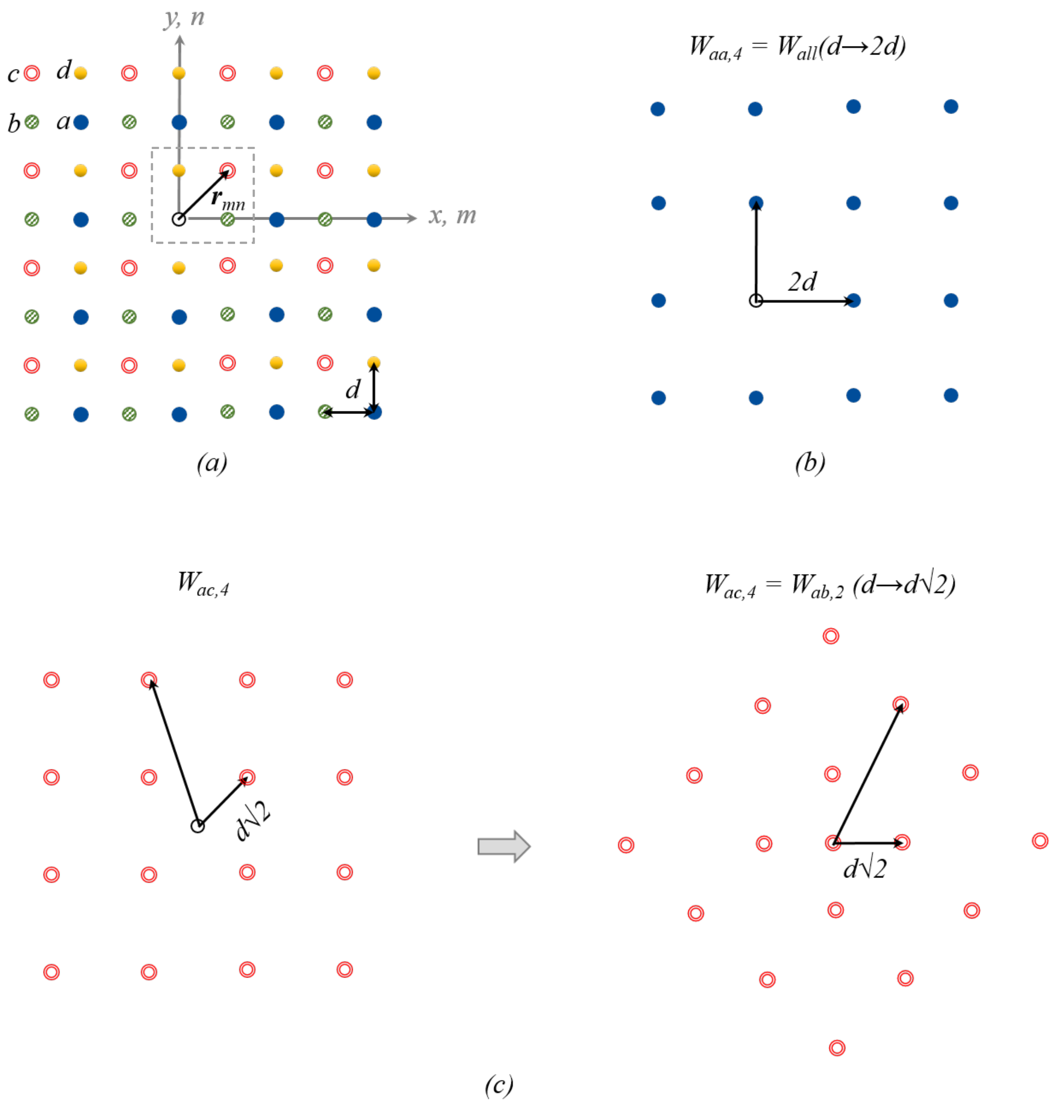

Figure 5.3: Illustration of scatterers placed in a square infinite array of period d, except at the origin with a unit cell of 2x2 dipoles and 4 different types of elements in free space. (a) Depicts unit cell with 4 types depicted in blue dots, red circles, yellow dots, and dots with green crosshatch. (b) Illustrates that $\overleftrightarrow{\mathbf{W}}_{aa,4}$ is simply $\overleftrightarrow{\mathbf{W}}_{all}$ with 2 times the period d. (c) Illustrates that $\overleftrightarrow{\mathbf{W}}_{ac,4}$ is simply $\overleftrightarrow{\mathbf{W}}_{ab,2}$ with the period $d\sqrt{2}$.

with a period of $2d$ instead of d. In the expression for $\mathbf{K}$, d appears as d^{-3}, so we multiply $\overleftrightarrow{\mathbf{W}}_{all}$ by 2^{-3} to obtain our expression of $\overleftrightarrow{\mathbf{W}}_{aa,4}$:

$$\overleftrightarrow{\mathbf{W}}_{aa,4} = \frac{1}{2^3}\overleftrightarrow{\mathbf{W}}_{all} = C_1^2\overleftrightarrow{\mathbf{W}}_{all} = 0.125\overleftrightarrow{\mathbf{W}}_{all} \tag{5.90}$$

Next, we write $\mathbf{K}_1$ in terms of its x, y, and z components and express it in terms of d:

$$K_{1x} = K_{1y} = \frac{1}{4\pi d^3}W_{aa,4,x} = \frac{1}{4\pi d^3}\frac{2\pi}{0.6956}\frac{1}{2}\frac{1}{2^3} = \frac{0.04492}{d^3} \tag{5.91}$$

$$K_{1z} = \frac{1}{4\pi d^3}W_{aa,4,z} = \frac{1}{4\pi d^3}\frac{2\pi}{0.6956}(-1)\frac{1}{2^3} = \frac{-0.08985}{d^3} \tag{5.92}$$

Now we consider the interaction between the reference point a and all the c dipoles. This is illustrated in Figure 5.3 (c). Since the summation for this case is to interchange the $x-$ and $y-$ directions, rotation of the lattice by 45 degrees brings us to a case already familiar to us: $\overleftrightarrow{\mathbf{W}}_{ab,2}$ from the checkerboard array. To utilize this expression, the period must be changed from d to $d\sqrt{2}$: $\overleftrightarrow{\mathbf{W}}_{all,2}(d \to d\sqrt{2})$ minus $\overleftrightarrow{\mathbf{W}}_{aa,2}(d \to d\sqrt{2})$.

$$\overleftrightarrow{\mathbf{W}}_{ac} = \overleftrightarrow{\mathbf{W}}_{ab,2}(d \to d\sqrt{2}) = \overleftrightarrow{\mathbf{W}}_{all,2}(d \to d\sqrt{2}) - \overleftrightarrow{\mathbf{W}}_{aa,2}(d \to d\sqrt{2}) \tag{5.93}$$

$$= (C_1 - C_1^2)\overleftrightarrow{\mathbf{W}}_{all} = (\frac{1}{2^{3/2}} - \frac{1}{2^3})\overleftrightarrow{\mathbf{W}}_{all} = 0.2285\overleftrightarrow{\mathbf{W}}_{all} \tag{5.94}$$

Next, we write $\mathbf{K}_3$ in terms of its x, y, and z components and express in terms of d:

$$K_{3x} = K_{3y} = \frac{1}{4\pi d^3}W_{ac,4,x} = \frac{1}{4\pi d^3}\frac{2\pi}{0.6956}\frac{1}{2}(\frac{1}{2^{3/2}} - \frac{1}{2^3}) = \frac{0.08214}{d^3} \tag{5.95}$$

$$K_{3z} = \frac{1}{4\pi d^3}W_{ac,4,z} = \frac{1}{4\pi d^3}\frac{2\pi}{0.6956}(-1)(\frac{1}{2^{3/2}} - \frac{1}{2^3}) = \frac{-0.16428}{d^3} \tag{5.96}$$

The simple tricks used to find $\mathbf{K}_1$ and $\mathbf{K}_3$, aren't easily extended to $\mathbf{K}_2$ or $\mathbf{K}_4$. However, it is quite easy to use software such as MATLAB to calculate their summations by brute force. To start, recall Figure 5.3 (a). The interaction with the b elements only is associated with $\mathbf{K}_2$. By looking at only the distances from the reference point a to each of the b elements we can write an expression for $\overleftrightarrow{\mathbf{W}}_{ab,4}$. Note that the b dipoles are located at the points where m is odd and n is even.

$$\overleftrightarrow{\mathbf{W}}_{ab,4} = \sum_{m=odd,n=even}{}' \frac{1}{(m^2+n^2)^{3/2}}[-(\vec{a}_x\vec{a}_x + \vec{a}_y\vec{a}_y + \vec{a}_z\vec{a}_z) + \frac{3m^2\vec{a}_x\vec{a}_x}{m^2+n^2} + \frac{3n^2\vec{a}_y\vec{a}_y}{m^2+n^2}] \tag{5.97}$$

Now, separate the $\overleftrightarrow{\mathbf{W}}_{ab,4}$ components of: x, y, and z coordinates.

$$W_{ab,4,z} = \sum_{m=odd,n=even}{}' \frac{-1}{(m^2+n^2)^{3/2}} = -2.9195 \tag{5.98}$$

$$W_{ab,4,x} = \sum_{m=odd,n=even}{}' \frac{1}{(m^2+n^2)^{3/2}}[-1 + \frac{3m^2}{m^2+n^2}] = -2.9195 + 7.1626 = 4.2431 \tag{5.99}$$

Let the second term in $W_{ab,4,x}$ be $S(s) = \sum{}'_{m=odd,n=even} m^2/(m^2+n^2)^{5/2}$. It can be rewritten into a more easily converging sum. As derived by Professor Larry Glasser (L. Glassser, personal communication, September 17, 2016), he wrote: "... a good compuational scheme can be constructed as follows.

$$S(s) = -\frac{1}{\Gamma(s)}\int_0^\infty \frac{dt}{t}\dot{\theta}_3(0,e^{-4t})\theta_2(0,e^{-4t})$$

(The dot denotes the derivative wrt t). Divide the range into $[0,1]+[1,\infty]$. In the first integral use

$$\theta_3(0,e^{-4t}) = \sqrt{\frac{\pi}{3t}}(0,e^{-\pi^2/16t}$$

$$\theta_2(0,e^{-4t})\sqrt{\frac{\pi}{4t}}(0,e^{-\pi^2/16t}$$

In the second integral change t to $1/t$. Then both integrals have the common range [0,1] and converge rapidly. Because the nomes are exponentially small, just keep a few terms in the series representing the theta functions produces a series of integrals that can be evaluated analytically or numerically."

$$W_{ab,4,y} = \sum_{m=odd,n=even}{}' \frac{1}{(m^2+n^2)^{3/2}}[-1 + \frac{3n^2}{m^2+n^2}] = -2.9195 + 1.5960 = -1.3235 \tag{5.100}$$

Now that the summations have been evaluated, we can write $\mathbf{K}_2$ in terms of the period d:

$$K_{2x} = \frac{1}{4\pi d^3} W_{ab,2x} = \frac{0.3376}{d^3} \tag{5.101}$$

$$K_{2y} = \frac{1}{4\pi d^3} W_{ab,2y} = \frac{-0.1053}{d^3} \tag{5.102}$$

$$K_{2z} = \frac{1}{4\pi d^3} W_{ab,2z} = \frac{-0.2323}{d^3} \tag{5.103}$$

The last $\mathbf{K}$ to solve for is $\mathbf{K}_4$ which is associated with the d elements. Again, consider Figure 5.3 (a). Regarding the d elements only, the interaction between the reference point a and all the d elements is written as $\overleftrightarrow{\mathbf{W}}_{ad,4}$. This time, the d dipoles are located at the points where m is even and n is odd. This is the opposite of the case for the b dipoles.

$$\overleftrightarrow{\mathbf{W}}_{ad,4} = \sum_{m=even,n=odd}{}' \frac{1}{(m^2+n^2)^{3/2}} [-(\vec{a}_x\vec{a}_x + \vec{a}_y\vec{a}_y + \vec{a}_z\vec{a}_z) + \frac{3m^2\vec{a}_x\vec{a}_x}{m^2+n^2} + \frac{3n^2\vec{a}_y\vec{a}_y}{m^2+n^2}] \tag{5.104}$$

$$W_{ad,4,z} = \sum_{m=even,n=odd}{}' \frac{-1}{(m^2+n^2)^{3/2}} = -2.9195 \tag{5.105}$$

$$W_{ad,4,x} = \sum_{m=even,n=odd}{}' \frac{1}{(m^2+n^2)^{3/2}} [-1 + \frac{3m^2}{m^2+n^2}] = -2.9195 + 1.5960 = -1.3235 \tag{5.106}$$

$$W_{ad,4,y} = \sum_{m=even,n=odd}{}' \frac{1}{(m^2+n^2)^{3/2}} [-1 + \frac{3n^2}{m^2+n^2}] = -2.9195 + 7.1626 = 4.2431 \tag{5.107}$$

Expressing $\mathbf{K}_4$ in terms of the period d,

$$K_{4x} = \frac{1}{4\pi d^3} W_{ab,4x} = \frac{-0.1053}{d^3} \tag{5.108}$$

$$K_{4y} = \frac{1}{4\pi d^3} W_{ab,4y} = \frac{0.3376}{d^3} \tag{5.109}$$

$$K_{4z} = \frac{1}{4\pi d^3} W_{ab,4z} = \frac{-0.2323}{d^3} \tag{5.110}$$

We now rewrite our results in matrix form so that it can be solved using a commercial code like MATLAB. Once this is done we can solve for the dipole moments. To begin, we'll rewrite equations (5.43) - (5.45) as a matrix and extend it to the 4 variation scatterer case:

$$\begin{bmatrix} \alpha_E^{xx} \end{bmatrix}^{-1} = \begin{bmatrix} \frac{1}{\alpha_{Ea}^{xx}} & 0 & 0 & 0 \\ 0 & \frac{1}{\alpha_{Eb}^{xx}} & 0 & 0 \\ 0 & 0 & \frac{1}{\alpha_{Ec}^{xx}} & 0 \\ 0 & 0 & 0 & \frac{1}{\alpha_{Ed}^{xx}} \end{bmatrix} \tag{5.111}$$

$$\begin{bmatrix} K_x \end{bmatrix} = \begin{bmatrix} K_{1x} & K_{2x} & K_{3x} & K_{4x} \\ K_{2x} & K_{1x} & K_{4x} & K_{3x} \\ K_{3x} & K_{4x} & K_{1x} & K_{2x} \\ K_{4x} & K_{3x} & K_{2x} & K_{1x} \end{bmatrix} \tag{5.112}$$

$$\begin{bmatrix} R \end{bmatrix} = \begin{bmatrix} 1 \\ 1 \\ 1 \\ 1 \end{bmatrix} \tag{5.113}$$

(Not to be confused with the R of equations (4.7) - (4.12).)

$$\begin{bmatrix} p_x \end{bmatrix} = \begin{bmatrix} p_{ax} \\ p_{bx} \\ p_{cx} \\ p_{dx} \end{bmatrix} \tag{5.114}$$

$$\epsilon E_x^{inc} \begin{bmatrix} R \end{bmatrix} = (\begin{bmatrix} \alpha_E^{xx} \end{bmatrix}^{-1} - \begin{bmatrix} K_x \end{bmatrix}) \begin{bmatrix} p_x \end{bmatrix} \tag{5.115}$$

$$(\begin{bmatrix} \alpha_E^{xx} \end{bmatrix}^{-1} - \begin{bmatrix} K_x \end{bmatrix}) \begin{bmatrix} p_x \end{bmatrix} = \epsilon E_x^{inc} \begin{bmatrix} R \end{bmatrix} \tag{5.116}$$

$$\left[p_x\right] = \epsilon E_x^{inc}(\left[\alpha_E^{xx}\right]^{-1} - \left[K_x\right])^{-1}\left[R\right] \tag{5.117}$$

Therefore the electric surface susceptibilities are

$$\left[\chi_{ES}^{xx}\right] = (\left[\alpha_E^{xx}\right]^{-1} - \left[K_x\right])^{-1}\left[R\right] \tag{5.118}$$

$$\left[\chi_{ES}^{yy}\right] = (\left[\alpha_E^{yy}\right]^{-1} - \left[K_y\right])^{-1}\left[R\right] \tag{5.119}$$

$$\left[\chi_{ES}^{zz}\right] = (\left[\alpha_E^{zz}\right]^{-1} - \left[K_z\right])^{-1}\left[R\right] \tag{5.120}$$

Similarly, for the magnetic case we have

$$\left[\chi_{MS}^{xx}\right] = (\left[\alpha_M^{xx}\right]^{-1} - \left[K_x\right])^{-1}\left[R\right] \tag{5.121}$$

$$\left[\chi_{MS}^{yy}\right] = (\left[\alpha_M^{yy}\right]^{-1} - \left[K_y\right])^{-1}\left[R\right] \tag{5.122}$$

$$\left[\chi_{MS}^{zz}\right] = (\left[\alpha_M^{zz}\right]^{-1} - \left[K_z\right])^{-1}\left[R\right] \tag{5.123}$$

This result can be readily extended to the case of N different scatterers and is called the Interactive polarizability approximation (IPA) model. In recent works, [10] derives expressions for the surface susceptibilities of a 2D atomic crystal lattice. They give expressions for square, triangular and honeycomb lattices. For the honeycomb they include an expression for the checkerboard case only. They have generalized dynamic expressions the include full-wave expressions without addressing the issue of getting the slow converging sums to converge. They are missing expressions for dipoles that are perendicular to the lattice, which is required for expressions that take into account oblique incident. Lastly, they don't compare their results to a full-wave simulation or experiment to determine their accuracy. In the next chapter, the IPA model will be validated with a full-wave simulation model and results.

5.3 Conclusion

This chapter derived the the interactive polarizability approximation (IPA) model. It is a set of analytical expressions for electric and magnetic surface susceptibilities that takes into account the variations of the physical parameters of the elements themselves for a metafilm of infinite extent. The expressions are an extension of the result for cluster pair derived in Chapter 3. We will be able to more clearly understand the validity and significance of these equations in the next chapter, where they will applied and compared with a full-wave commercial simulation software that doesn't use the dipole approximation, using physical values similar to those of Chapters 2 - 4.

Chapter 6

Metafilm of Polarizable Scatterers Perturbations in Element Parameter Behavior

For a metafilm, in Chapter 5, the interactive polarization approximation (IPA) equations were derived, allowing the calculation of the surface susceptibilities for an infinite sheet. They include coupling terms that take into account interactions between the elements. The coupling terms allow for variations in the resonant frequency of each element in the unit cell. This chapter compares IPA, the averaging polarization approximation (APA) equations (4.7) - (4.12), and results from a commercially available finite element method software: High Frequency Electromagnetic Field Simulation (*HFSS*).

In Chapter 2, the magneto-dielectric sphere was studied in detail. It was shown that while the permittivity, permeabilty and radius vary the resonant frequency, variations in the radius resulted in the largest shift. This chapter will only look at the high permittivity, nonmagnetic sphere, for which the magnetic dipole modes will be of the nonconfined type such that the resonance has a broad bandwidth and strong field strength outside the sphere. On the other hand, the electric dipole modes will exhibit the special case of confined mode behavior, for which the fields are strong inside the sphere and the resonance has a very narrow bandwidth.

Next, in Chapter 3, a simple case of two elements that couple was considered. For the example of high permittivity spheres, significant coupling occurred when the the two different resonances of the two spheres had bandwidths that overlapped. This occurs easily for wide bandwidths (or nonconfined modes), but narrow resonances (of the confined type) require small differences in the resonant frequencies to achieve coupling. When strong coupling is achieved two distinct resonances occur: a main resonance that is broad where the dipoles of both elements constructively add, and second, from which the dipole moments of the two elements oppose each other causing interference that results in a sharp asymmetric shape or Fano resonance.

The goal of this chapter is to get an intuitive feel for how Fano resonances reveal themselves in measurable quantities used to measure the performance of metafilms, such as the S-parameters. When designers design a metafilm, they often use uniform sheet models to predict its behavior. When a metafilm is designed to have a nominal radius of $a_0 = 10$mm for example, manufacturing tolerances can result in random variations from that nominal value. To simulate this case, a random number generator can be used. For example if one is expecting up to 2% variation in radius, the first four numbers generated were 9.9185, 10.02, 10.056, and 10.074. The percent range of different between these numbers are between 1.6% and 0.14 %. In Chapter 3, a coupled pair of high permittivity spheres with $\epsilon_r = 100$, spaced $d = 30$ mm apart in free space was exhaustively studied. The coupled pair studies revealed that for magnetic dipole moments, a radius variation of less than 3% will result in strong coupling. Such a large difference in radii is possible because they are nonconfined modes. On the other hand, the electric dipole modes are a special case of confined modes that require variations of no more than 0.2% to achieve strong coupling; beyond that weak coupling results.

For a metafilm, in Chapter 4, it was noted from previous works that if one had accurate expressions for the surface susceptibilities, one could analytically calculate the reflection and transmission coefficients or the S-parameters (which are measurable quantities). For the elements of the infinite array, identical high permittivity spheres with practical values were used, allowing small variations in the lattice spacing to be studied. The analytical equations for the normal incidence reflection coefficients were compared with that of *HFSS*. Excellent agreement was achieved, and the results also demonstrated that in the case of identical spheres little difference occurs when the spacing varies randomly by small amounts from that of a perfectly spaced lattice. Therefore lattice spacing is insensitive to small random errors in placement (as is the case during manufacturing) if the frequency is small enough that the lattice doesn't cause resonances to occur. Therefore, only periodic spacing will be considered in this chapter, and only variations in the resonant frequency among elements will be studied.

The practical values used in the metafilm example of Chapter 4 will be also be used again in this chapter. This time the radii of the spheres will be varied while the spacing remains periodic. The three cases of Chapter 5 will be investigated: 1) The array of identical spheres illustrated in Figure 5.1, 2) An array of two alternating spheres or the checkerboard sheet as shown in Figure 5.2, and 3) A unit cell of spheres with four different radii as depicted in Figure 5.3 that are repeated in the plane of the film. The surface susceptibilities derived by IPA will be compared with the less rigorous APA equations. The IPA equations will be validated by comparing the reflection and transmission coefficient results with *HFSS*.

6.1 Infinite Square Identical Array

To begin with, the metafilm will be taken to be that of a uniform array. The metafilm will contain identical spheres whose permittivity is $\epsilon_r = 100$ and have the same radius a. The spheres will be suspended in free space, periodically spaced $d = 30$ mm apart, forming an infinite square array. This spacing is less than a quarter wavelength, therefore the lattice won't cause an additional resonances. The sheet will be placed in the $x - y$ plane as shown in Figure 5.1. We will examine the behavior of the surface susceptibilities and then the reflection and transmission coefficients.

The magnetic and electric surface susceptibilities χ_{MS} and χ_{ES} respectively, are the total magnetic and electric dipole moments per unit area normalized by the incident field (as well as the permittivity of the surrounding medium in the electric case), as defined in equations (5.23), (5.24), (5.27) and (5.28). For a uniform sheet, the x and y directed susceptibilities are equal.

When all the spheres have a radius of $a_0 = 10$ mm, Figure 6.1 illustrates the behavior of χ_{MS} and χ_{ES} as a function of frequency. The first two resonances occur at 1.4631 GHz for χ_{MS}^{xx} (in the blue line) and next at 1.5816 GHz, where χ_{MS}^{zz} resonates (shown in the green dashed line). The magnetic dipoles' nonconfined behavior is also seen in the broad bandwidths of χ_{MS}. Higher in frequency, (in the red line) χ_{ES}^{xx} resonates at 2.1179 GHz and finally (in the cyan dashed line) at 2.1321 GHz χ_{ES}^{zz} resonates. Recall that the electric dipoles exhibit special characteristics since the spheres have a high dielectric constant. The very narrow bandwidths demonstrate the confined mode behavior. Note that all the surface susceptibilities were normalized by d^2.

Next, the reflection and transmission coefficients or S-parameters, for normal incidence are plotted versus frequency in Figure 6.2 using equations (4.15) and (4.16) of Chapter 4. The frequency range includes the regions of both the magnetic and electric dipole resonances. The plots consider three metafilms. For one sheet each sphere has a radius of 10 mm (seen in red), then 10% larger (in blue) and 10% smaller (in green).

There is an overall shift downward in frequency for the S-parameter plot when the sheet has larger spheres, and an overall shift upward when the spheres are smaller. For S_{11}, the dip between the two maxima is highest when the spheres are the biggest and lowest when the spheres are the smallest. Note that the resonant frequencies of the surface susceptibilities occur near the maximum points of the reflection coefficient S11, allowing for total reflection (these plots only consider spheres made of lossless material). We will next examine, the consequences of small variations in the radius of the elements.

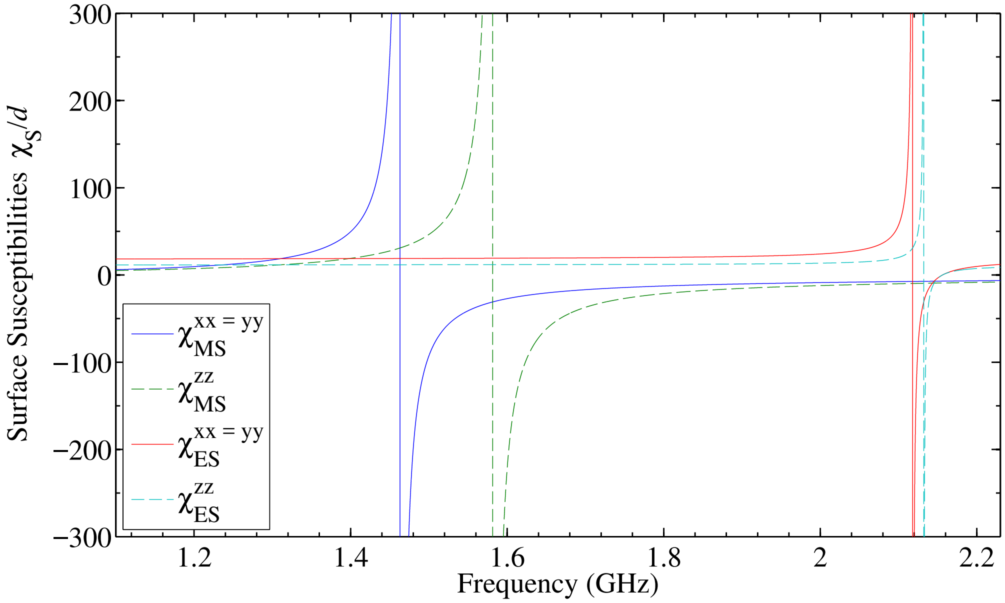

Figure 6.1: Normalized electric and magnetic susceptibilities for an infinite 2D identical array of lossless high permittivity spheres, plotted versus frequency. Each sphere has a $a = 10$ mm and $\epsilon_r = 100$, spaced $d = 30$ mm apart.

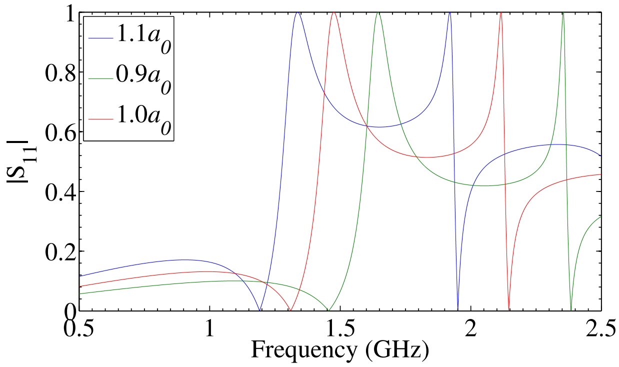

(a) Magnitude of the reflection coefficient

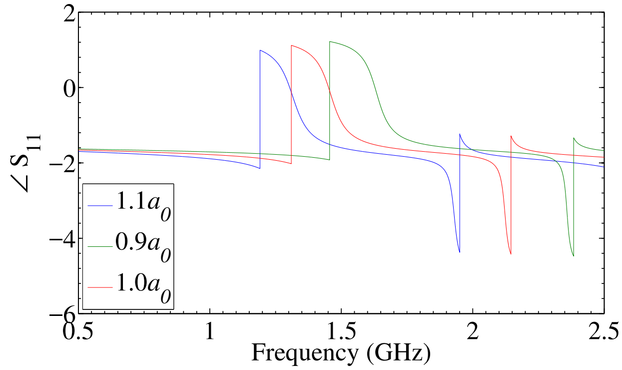

(b) Phase of the reflection coefficient (radians)

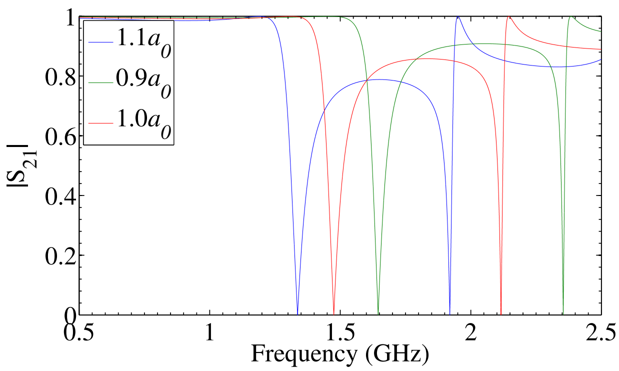

(c) Magnitude of the transmission coefficient

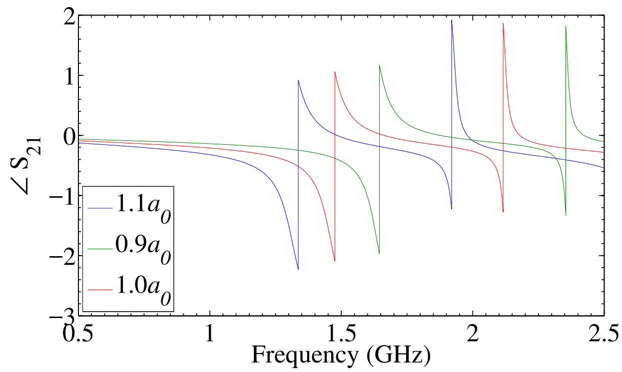

(d) Phase of the transmission coefficient (radians)

Figure 6.2: S-parameters for an infinite 2D identical array of lossless high permittivity spheres, plotted versus frequency. Each sphere has a $\epsilon_r = 100$, spaced $d = 30$ mm apart. Three different identical arrays are compared. One sheet has the nominal radius shown in red, the blue curve indicates a sheet where each sphere is 10% larger than the nominal radius, and in the last one each is 10% smaller, shown in green.

6.2 Checkerboard Array

We next consider, a simple case where an array contains only two different kinds of elements. The same parameters used in the previous section will be used here: $\epsilon_r = 100$, suspended in free space, with a periodic spacing of $d = 30$ mm. However now, each alternating sphere will have a radius of 9.9185 mm or 10.074 mm so they will differ in radius by 1.6%. This implies that the magnetic dipole modes will strongly couple, but that the electric dipole modes will weakly couple. They alternate in placement in such a fashion that it resembles a checkerboard pattern as illustrated in Figure 5.2.

The surface susceptibilities are normalized by d^2 and then plotted versus frequency in Figure 6.3. The results of the IPA equations (5.73) - (5.76), which contain coupling terms, are plotted in red. The results of the averaging technique or the APA equations (4.7) - (4.12) are shown in blue. The dipoles directed in the x direction are equal to those in the y direction indicated by the solid lines, while the z directed susceptibilities are indicated by dashed lines. The magnetic case is shown in (a), while the electric case is shown in (b).

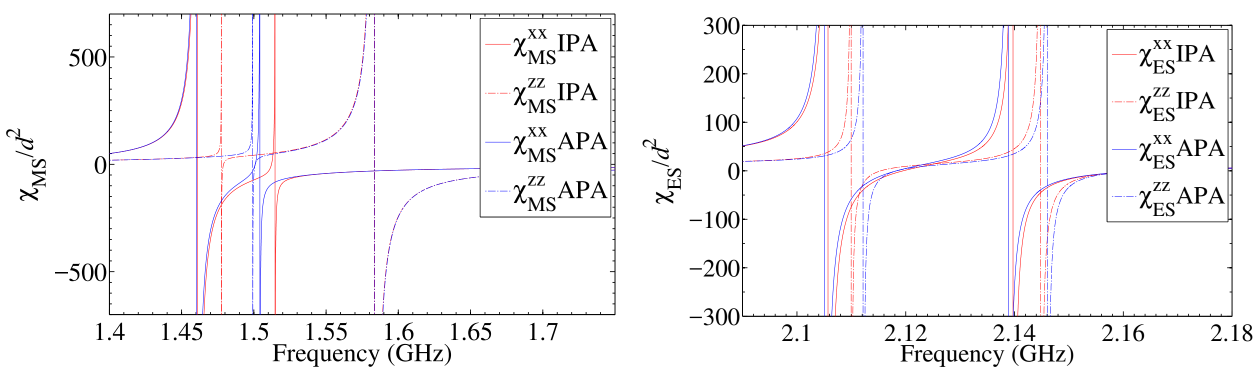

(a) Magnetic dipole resoance frequency range

(b) Electric dipole resoance frequency range

Figure 6.3: Normalized electric and magnetic susceptibilities for an infinite 2D checkerboard array of lossless high permittivity spheres, plotted versus frequency. Each sphere has a $\epsilon_r = 100$, spaced $d = 30$ mm apart, and has a radius of 9.9185 or 10.074 mm. The surface susceptibilities χ were normalized by d^2 and calculated with IPA equations in red, and APA equations in blue. The solid lines indicate x or y polarization and the dashed lines z polarization.

For the magnetic case in (a), each susceptibility has two resonances, the main one with wide bandwidth and the other which is sharp and asymmetric or Fano resonance (see Chapter 3 for details). There is good agreement between IPA and APA in regards to the main resonance, however there is strong disagreement when it comes to the Fano resonances. The behavior of the χ_{MS} terms indicates strong coupling between elements. The electric case also has two resonances, however, the main resonance isn't as wide nor is the Fano resonance as sharp as in the magnetic case, indicating weak coupling between the elements. There is good overall agreement between the APA and IPA equations. This is very similar behavior to that of the coupled pair studied in Chapter 3.

Figure 6.4 illustrates the consequence on the reflection coefficient of two variations in radius for the checkerboard array. Both the IPA and APA equations for the surface susceptibilities were used to calculate the normal incidence reflection coefficient equation (4.15) of Chapter 4. The magnetic dipole resonance frequency range, along with the results predicted by *HFSS*, is plotted in (a) and electric dipole resonance frequency range is plotted in (b).

Looking more closely at Figure 6.4 (b), there is excellent agreement between *HFSS* and the IPA equations and pretty good agreement for the APA equations as well. When the magnitude of S_{11} has a value of nearly 1, all three models predict a major dip in the center. Recall that for the uniform case, no dips are expected over the frequency band of total reflection. The magnetic dipole modes are strongly coupled, which results in the Fano resonances in the χ_{MS}, which then cause a narrow resonance to occur in S_{11}.

Figure 6.4 (b) depicts the range of frequencies where the electric dipole modes resonate. There is excellent agreement between IPA and APA. Again, for the uniform case, no dips occurred across the frequency range of total reflection, yet for the checkerboard case, the Fano resonances seen in χ_{ES} has caused a resonance to occur in the reflection coefficient. Since the electric dipoles of the sheet are weakly coupled, this results in a wide resonance in S_{11}. Next, the case of a metafilm with 4 values of sphere radii of the spheres will be examined.

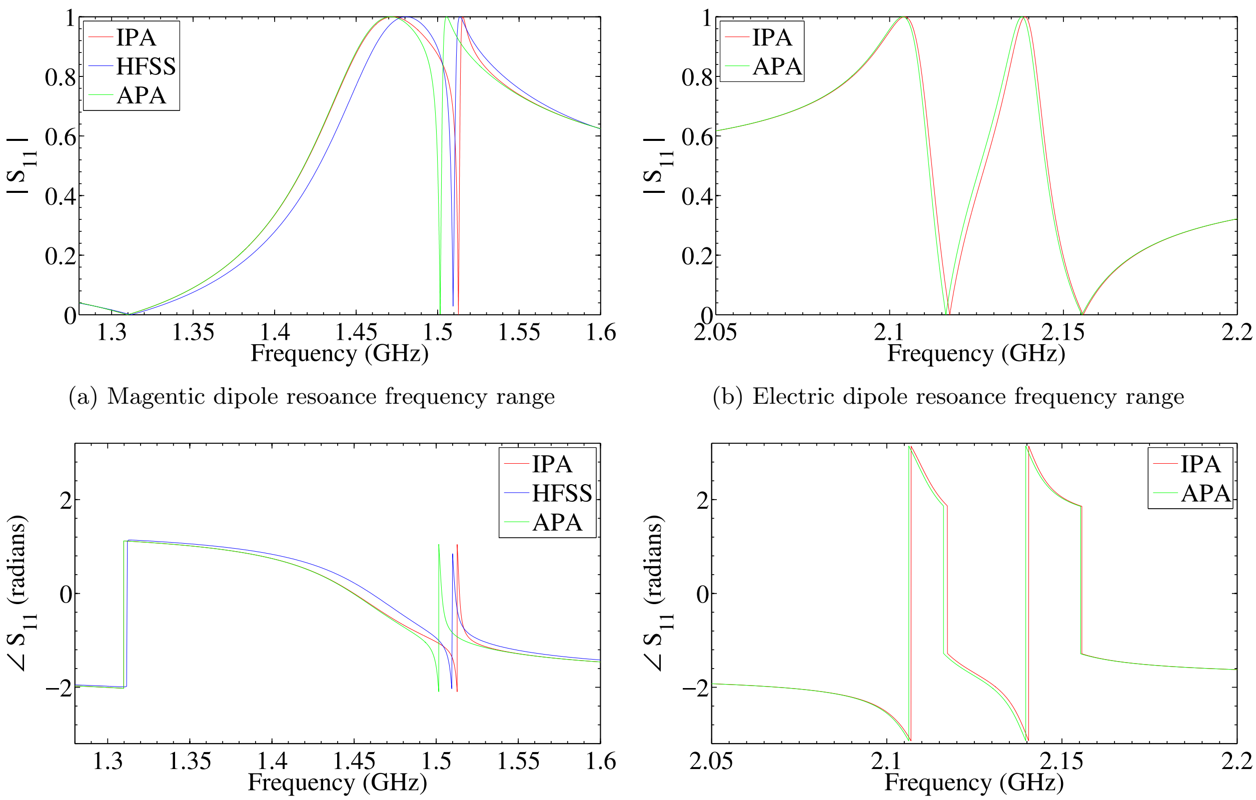

(a) Magentic dipole resoance frequency range

(b) Electric dipole resoance frequency range

(c) Magentic dipole resoance frequency range

(d) Electric dipole resoance frequency range

Figure 6.4: S_{11} parameter for an infinite 2D checkerboard array of lossless high permittivity spheres, plotted versus frequency. Each sphere has a $\epsilon_r = 100$, spaced $d = 30$ mm apart, and has a radius of 9.9185 or 10.074 mm. The reflection coefficients S_{11} were calculated with *HFSS*: shown in blue, IPA equations in red, and APA equations in green.

6.3 Four Radii Unit Cell Array

The previous section considered the case of two different elements. In this section, a unit cell of 4 spheres with 4 different radii will be investigated. The unit cell is repeated an infinite number of times in the $x - y$ plane as illustrated in Figure 5.3. Again the periodic spacing of $d = 30$ mm will be used, and all spheres will have the same lossless dielectric constant of $\epsilon_r = 100$ with a free space background medium. The radii will be 9.9185, 10.02, 10.056, and 10.074 mm. The percent variation in radius thus ranges from 1.6 % to 0.14 %. It's expected that the magnetic dipoles will couple strongly in frequency, while the electric dipole will have a mixed response of weak coupling for the 1.6% variation and strong coupling for the 0.14% variation.

Figure 6.5 depicts the normalized surface susceptibilities as functions of frequency. The results of the IPA equations (5.118) - (5.123) derived in Chapter 4 are compared (shown in red) with the less rigorous APA equations (4.7) - (4.12) of [28] (in blue). The dielectric sphere has polarizabilities that are independent of direction. For the APA equations, the x and y directed susceptibilities are equal, while IPA predicts that this is not always case; therefore they will have some anisotropic behavior. The solid lines of (a) and (b) indicate the x directed susceptibilities, while the dashed lines are the y directed ones. The magnetic case is shown in (a), while the electric case is shown in (b).

Since there are 4 different radii, the isolated spheres has 4 different resonant frequencies that are spaced close together. Each χ_S thus contains 4 resonances. As with the checkerboard case, there is pretty good agreement between IPA and APA, as far as the main resonances and all of the χ_{ES}^{zz} resonances are concerned. There is also good agreement when the x and y directed susceptibilities of the IPA equations have nearly equivalent resonant frequencies. Otherwise there is poor agreement for the Fano resonance frequency points. Again, the χ_{MS} behavior indicates strong coupling, while the χ_{ES} indicates a mixture of weak and strong coupling in frequency. Next, the effect that these resonances have on the S-parameters will be discussed and illustrated.

In Figure 6.6 (a) the magnitude and (c) the phase of the reflection coefficient is plotted, with *HFSS* results shown in blue, IPA equations in red, and APA equations in green, over the frequency range the magnetic dipoles resonate. Overall there is a uniform response except for the three resonances. The uniform response in S_{11}, is the result of the main resonances in the surface susceptibilities constructively adding. This is where IPA and APA equations have excellent agreement. However, the disagreement in the location of two of the Fano resonances in χ_{MS} results in disagreement in two of the resonances seen in S_{11}. There is one Fano resonance where $\chi_{MS}^{xx} = \chi_{MS}^{yy}$ for both the IPA and APA equations, this results in good agreement in *HFSS*, IPA, and APA for one resonance seen in the S_{11}. Since the magnetic dipole moments are strongly coupled, this leads to narrow resonances in the S_{11}. Next, the case of weak coupling across the frequencies where the magnetic dipole moments resonate is considered.

To have weakly coupled magnetic dipole moments, the difference in the radii must be greater than 3%. If the unit cell of a metafilm had the four radii of 9.7, 9.8, 9.9, and 10 mm, we would expect a mix of weak and strong coupling in frequency. The largest variation between which is between 10 and 9.7 mm, is 3% and the smallest range is 1%. For this case, Figure 6.6 (b) reveals the magnitude plots of S_{11} and in (d), the phase. Again there is the case of excellent agreement in the uniform response. *HFSS* and IPA have good agreement in regards to the resonance locations. For the resonances in S_{11}, there is only good agreement between *HFSS*, IPA and APA in the location for one out of the three resonances. Next, the frequency range that includes the resonances of the electric dipole moments will be investigated.

For the case of strong coupling, the variations between the radii of the spheres will need to be very small. Consider a unit cell whose spheres have the following radii: 9.999, 9.9997, 10.003, 10.001 mm. This will result in a maximum of 0.2% variation, which will allow the electric dipole moments to strongly couple. The reflection coefficient magnitude and phase is plotted in Figure 6.7 (a) and (c) respectively over a range of frequencies that includes the electric dipole moment resonances. The IPA and APA equations are compared and show excellent agreement in regards to the uniform response. The Fano bands show good agreement for only one out of three Fano resonances. Since there is strong coupling and the difference between the resonant frequencies of the elements is very small, the Fano resonances in the S_{11} are extremely sharp.

Next, we return to the example of a unit cell comprised of the following radii: 9.9185, 10.02, 10.056, and 10.074 mm. As discussed earlier the electric dipoles will have a mixture of weak and strong coupling. 6.7 (b) and (d) illustrate the response of the magnitude and phase response of S_{11} respectively. The weak coupling results in the wide banded resonances, while strong coupling is responsible for the narrow banded resonance. The IPA and APA equations predict similar results, but the narrow banded resonance reveals more disagreement. A summary of the resonant frequencies and corresponding bandwidths is given in Table 6.1.

In regards to the S-parameter plots, the IPA equations have very good to excellent agreement with *HFSS*, while the APA equations had limited agreement. In the reflection coefficient plots, it's interesting to note that there appears to be a frequency range to which the locations of the Fano resonances is restricted. This frequency range in which Fano resonances reside will be referred to as the Fano band. Consider the case of 2% variations. A random number generator was used to come up with 100 metafilm designs, each of which has a unit cell with four spheres whose radius is randomly varied up to 2 %. The reflection coefficient plots for each metafilm were superimposed to create Figure 6.8 and calculated in (a) using the IPA equations and in (b) the APA equations. Results for the array of identical spheres were also superimposed in both plots to be used a reference. In this figure, the frequency range is wide enough to include both the magnetic and electric dipole moment resonances.

For 2% radius variations, there is strong frequency coupling in the magnetic dipole resonance region and weak to strong coupling in the electric resonance band. In magnetic dipole resonance region, the IPA equations predict three distinct Fano bands that range from: 1.44 -1.47, 1.50 - 1.53, and 1.54 - 1.57 GHz. On the other hand the APA only predicts one: 1.48 - 1.52 GHz. Clearly the APA is only capable of predicting one out of three Fano resonance bands.

When the resonances in S_{11} are are weakly coupled, their bandwidths are wide and there is good agreement between APA and IPA. In this example, the electric dipole resonances are weak to strongly coupled. IPA predicts a Fano band frequency range of 2.10 - 2.15 GHz and for APA the range is 2.10 - 2.165 GHz. For Fano resonances that are so wide, the APA equations should be able to get close agreement with IPA.

Figure 6.9 demonstrates a similar trend when the magnetic dipoles are weak to strongly coupled and the electric dipoles are only strongly coupled. In conclusion, the frequency range of the Fano bands seen in the S-parameters is based on how strongly the dipole moments are coupled with each other. Strong coupling results in narrow bandwidths and narrow Fano bands of frequency, while weak coupling results in a wide Fano band. The general location of the Fano resonances is based on the frequency at which the dipole moments resonate. Lastly, for strong coupling, the APA method is cannot accurately predict the locations of all the Fano resonances, therefore the IPA equations should be used. However, in the case of weak coupling only, either APA or the IPA has shown good agreement with a properly meshed *HFSS* simulation.

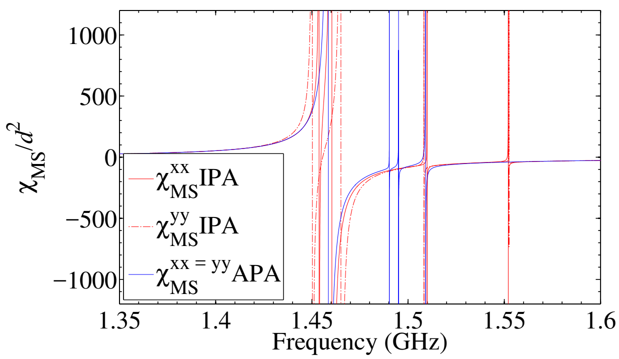

(a) Magnetic dipole resoance frequency range

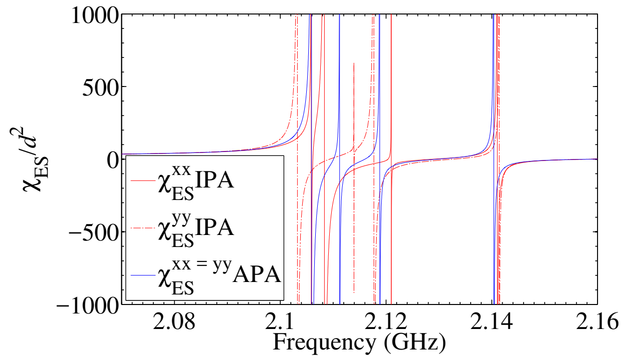

(b) Electric dipole resoance frequency range

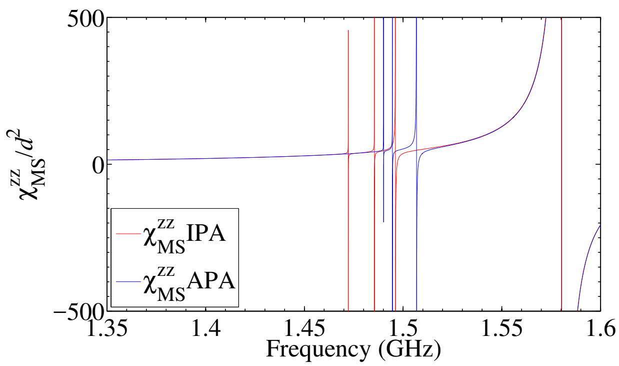

(c) Magnetic dipole resoance frequency range

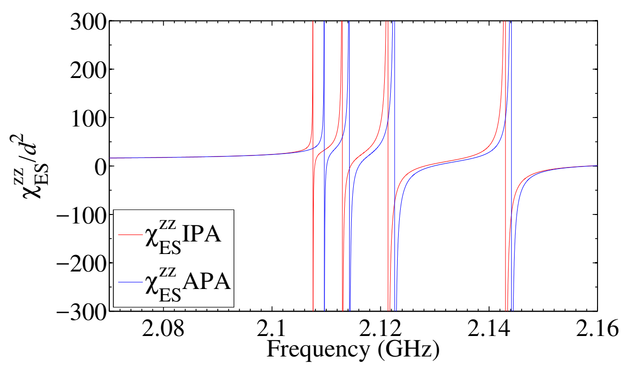

(d) Electric dipole resoance frequency range

Figure 6.5: Normalized electric and magnetic susceptibilities for an infinite 2D array whose unit cell consists of 4 lossless high permittivity spheres, plotted versus frequency. Each sphere in the unit cell has a ϵ_r = 100, is spaced d = 30 mm apart, and has a radius of 9.9185, 10.02, 10.056, and 10.074 mm. The surface susceptibilities χ_S were normalized by d^2 and calculated with IPA equations in red, and APA equations in blue. The solid lines in (a) - (b) indicate the x directed dipoles while for the IPA equations the y directed dipoles are shown using dashes.

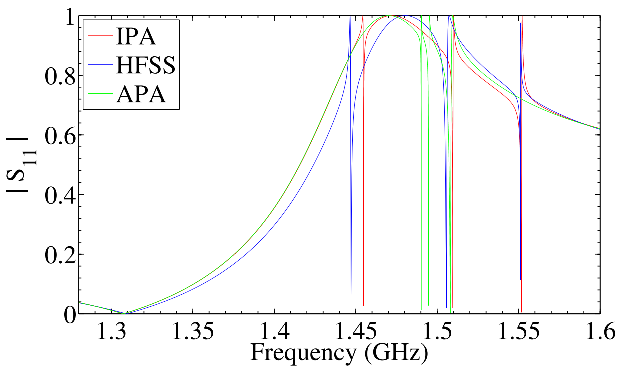

(a) Strong coupling in frequency

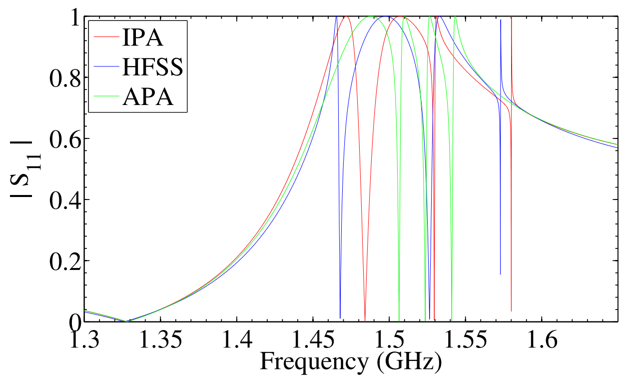

(b) Weak coupling in frequency

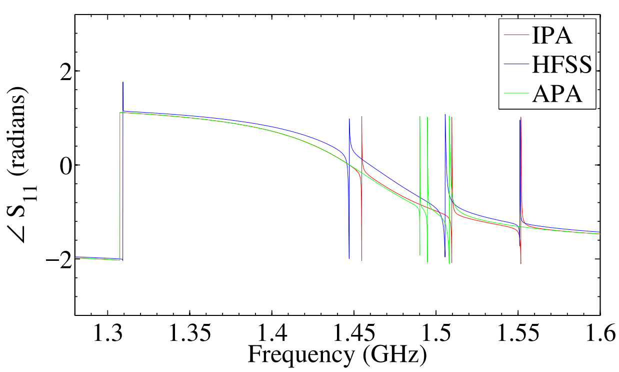

(c) Strong coupling in frequency

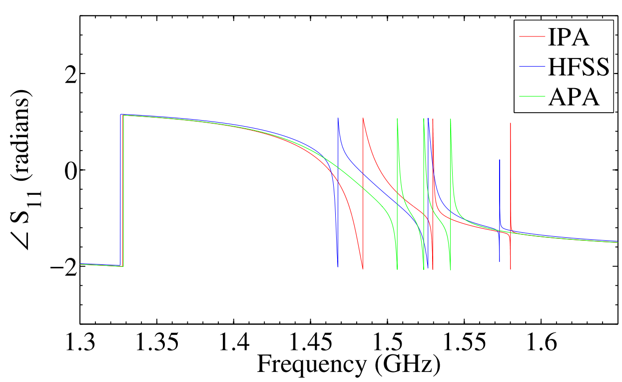

(d) Weak coupling in frequency

Figure 6.6: S_{11} parameter for an infinite 2D array whose unit cell consists of 4 of lossless high permittivity spheres, plotted versus frequency. Each sphere in the unit cell has a $\epsilon_r = 100$, is spaced $d = 30$ mm apart, and each sphere has a radius of (a) 9.9185, 10.02, 10.056, and 10.074 mm and (b) 9.7, 9.8, 9.9, 10 mm. The reflection coefficients, S_{11} were calculated with *HFSS* shown in blue, IPA equations in red, and APA equations in green.

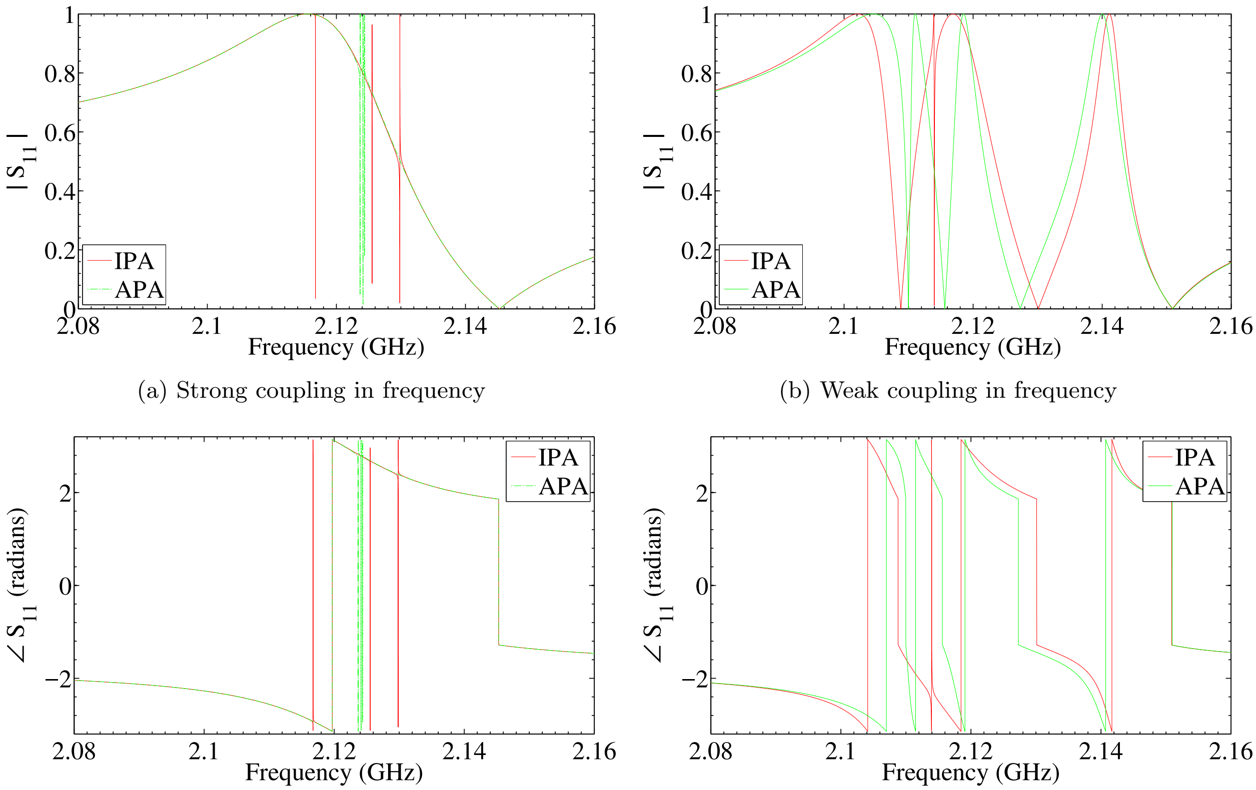

(a) Strong coupling in frequency

(b) Weak coupling in frequency

(c) Strong coupling in frequency

(d) Weak coupling in frequency

Figure 6.7: S_{11} parameter for an infinite 2D array whose unit cell consists of 4 of lossless high permittivity spheres, plotted versus the electric resonant frequency range. Each sphere in the unit cell has a $\epsilon_r = 100$, is spaced $d = 30$ mm apart, and each sphere has a radius of (a) 9.999, 9.9997, 10.003, 10.001 mm and (b) 9.9185, 10.02, 10.056, and 10.074 mm. The reflection coefficients, S_{11} were calculated with the IPA equations in red, and APA equations in green.

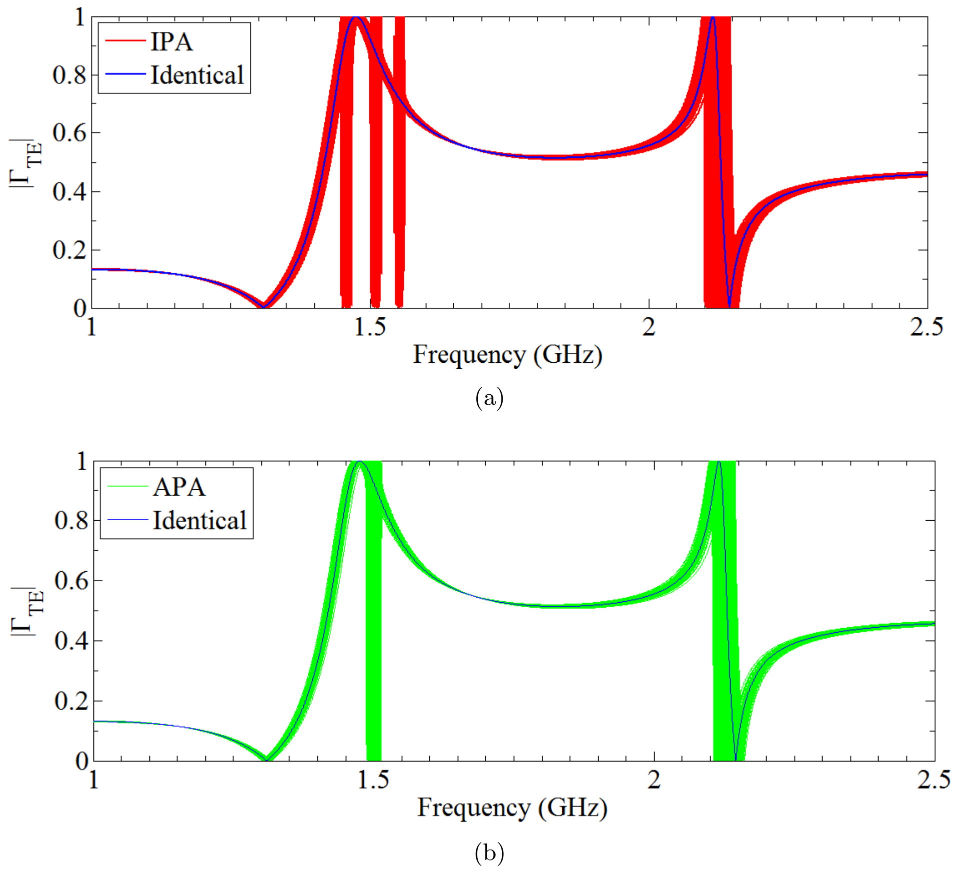

Figure 6.8: The magnitude of S_{11} (Γ_{TE}) for an infinite 2D array whose unit cell consists of 4 of lossless high permittivity spheres, plotted versus a range of frequencies that highlights Fano bands. Each sphere in the unit cell of 4 spheres has a $\epsilon_r = 100$, is spaced $d = 30$ mm apart, and has a nominal radius of $a_0 = 10$ mm. Using a random number generator, 600 metafilms were generated and the results were superimposed for up to a 2% variation in radius from the nominal. The reflection coefficients, S_{11} were calculated with the (a) IPA equations in red, and (b) APA equations in green and compared with a metafilm with identical spheres of nominal radius (in blue).

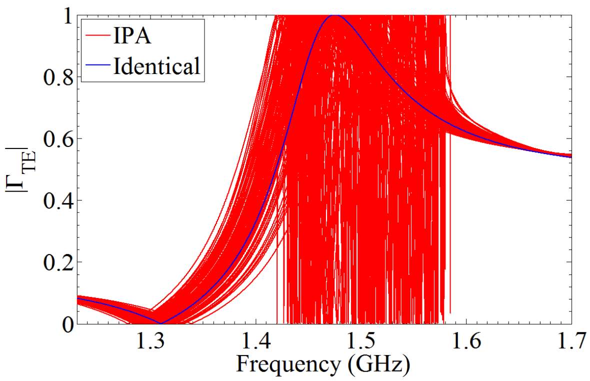

(a) 6 % variation in radius

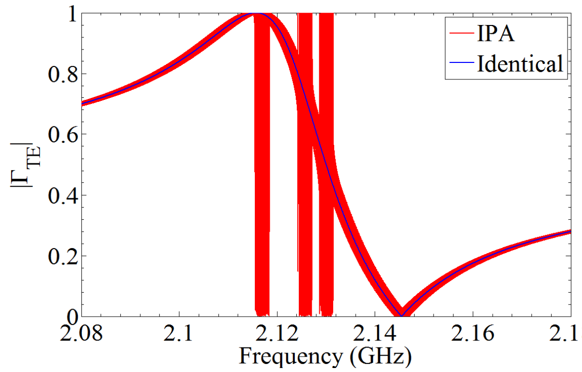

(b) 0.2 % variation in radius

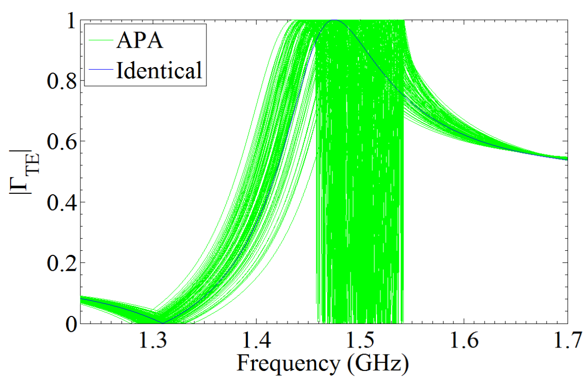

(c) 6 % variation in radius

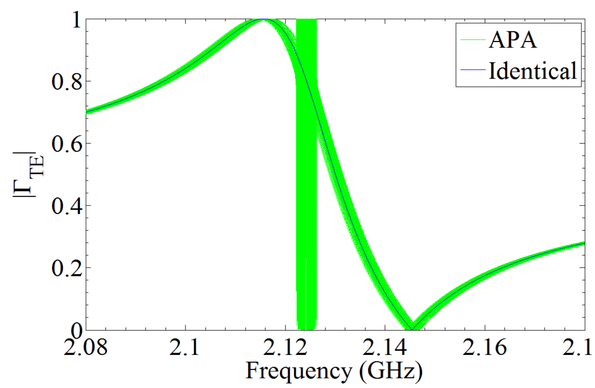

(d) 0.2 % variation in radius

Figure 6.9: The magnitude of S_{11} (Γ_{TE}) for an infinite 2D array whose unit cell consists of 4 of lossless high permittivity spheres, plotted versus a range of frequencies that highlights Fano bands. Each sphere in the unit cell of 4 spheres has a $\epsilon_r = 100$, is spaced $d = 30$ mm apart, and has a nominal radius of $a_0 = 10$ mm. Using a random number generator, 600 metafilms were generated and the results were superimposed for up to a 6% variation in radius from the nominal in (a) and (c) and 0.2% shown in (b) and (d). The reflection coefficients, S_{11} were calculated with the (a) - (b) IPA equations in red, and (c) - (d) the APA equations in green and compared with a metafilm with identical spheres of nominal radius (in blue).

Table 6.1: The resonant frequency and bandwidth with respect to χ_s/d^2 = +/- 130 of the surface susceptibilities of metafilms with up to four radii per unit cell. Calculations that compare the APA and IPA models. The radius values are: a_1 = 9.9185, a_2 = 10.02, a_3 = 10.056, and a_4 = 10.074 mm.

Radii Variations	Radii Used	Eqn. Used	f_r (GHz)	BW (%)	f_r (GHz)	BW (%)	f_r (GHz)	BW (%)
			χ_{MS}^{zz}		χ_{MS}^{xx}		χ_{MS}^{yy}	
1 (Fig. 4.1)	a_1	Id	1.5926	3.74	1.4759	3.33	χ_{MS}^{xx}	χ_{MS}^{xx}
1 (Fig. 4.1)	a_2	Id	1.5791	3.86	1.4599	3.42	χ_{MS}^{xx}	χ_{MS}^{xx}
1 (Fig. 4.1)	a_3	Id	1.5744	3.91	1.4543	3.46	χ_{MS}^{xx}	χ_{MS}^{xx}
1 (Fig. 4.1)	a_4	Id	1.5720	3.94	1.4515	3.20	χ_{MS}^{xx}	χ_{MS}^{xx}
2 (Fig. 4.2)	a_1, a_4	APA	1.4992	0.09	1.4602	3.068	χ_{MS}^{xx}	χ_{MS}^{xx}
			1.5838	3.75	1.5042	0.332	χ_{MS}^{xx}	χ_{MS}^{xx}
2 (Fig. 4.2)	a_1, a_4	IPA	1.4775	0.05	1.4609	3.204	χ_{MS}^{xx}	χ_{MS}^{xx}
			1.5835	3.78	1.5147	0.198	χ_{MS}^{xx}	χ_{MS}^{xx}
4 (Fig. 4.3)	$a_1, a_2,$	APA	1.4901	0.00	1.4585	3.236	χ_{MS}^{xx}	χ_{MS}^{xx}
	a_3, a_4		1.4946	0.01	1.4902	0.013	χ_{MS}^{xx}	χ_{MS}^{xx}
			1.5068	0.05	1.4951	0.047	χ_{MS}^{xx}	χ_{MS}^{xx}
			1.5805	3.80	1.5090	0.119	χ_{MS}^{xx}	χ_{MS}^{xx}
4 (Fig. 4.3)	$a_1, a_2,$	IPA	1.4722	0.00	1.4536	1.341	1.4502	1.420
	a_3, a_4		1.4855	0.01	1.4604	2.034	1.4650	1.959
			1.4961	0.04	1.5099	0.026	1.5083	0.040
			1.5804	3.81	1.5522	0.119	1.5526	0.006
			χ_{ES}^{zz}		χ_{ES}^{xx}		χ_{ES}^{yy}	
1 (Fig. 4.1)	a_1	Id	2.1495	0.19	2.1355	0.49	χ_{ES}^{xx}	χ_{ES}^{xx}
1 (Fig. 4.1)	a_2	Id	2.1279	0.19	2.1136	0.51	χ_{ES}^{xx}	χ_{ES}^{xx}
1 (Fig. 4.1)	a_3	Id	2.1204	0.20	2.1060	0.52	χ_{ES}^{xx}	χ_{ES}^{xx}
1 (Fig. 4.1)	a_4	Id	2.1166	0.20	2.1022	0.52	χ_{ES}^{xx}	χ_{ES}^{xx}
2 (Fig. 4.2)	a_1, a_4	APA	2.1122	0.08	2.1051	0.309	χ_{ES}^{xx}	χ_{ES}^{xx}
			2.1460	0.12	2.1389	0.196	χ_{ES}^{xx}	χ_{ES}^{xx}
2 (Fig. 4.2)	a_1, a_4	IPA	2.1100	0.07	2.1057	0.318	χ_{ES}^{xx}	χ_{ES}^{xx}
			2.1448	0.13	2.1397	0.182	χ_{ES}^{xx}	χ_{ES}^{xx}
4 (Fig. 4.3)	$a_1, a_2,$	APA	2.1096	0.01	2.1059	0.304	χ_{ES}^{xx}	χ_{ES}^{xx}
	a_3, a_4		2.1143	0.04	2.1112	0.057	χ_{ES}^{xx}	χ_{ES}^{xx}
			2.1226	0.08	2.1188	0.076	χ_{ES}^{xx}	χ_{ES}^{xx}
			2.1441	0.07	2.1404	0.084	χ_{ES}^{xx}	χ_{ES}^{xx}
4 (Fig. 4.3)	$a_1, a_2,$	IPA	2.1075	0.01	2.1058	0.157	2.1032	0.252
	a_3, a_4		2.1130	0.03	2.1083	0.251	2.1139	0.000
			2.1214	0.08	2.1210	0.009	2.1177	0.189
			2.1430	0.08	2.1410	0.089	2.1414	0.065

6.4 Effect of Dielectric Material Loss

Until this point, all the analysis of this chapter has considered lossless dielectric spheres. This section will now focus on the impact loss has on Fano resonances in the S-parameters. We consider again the case of a unit cell consisting of four spheres spaced $d = 30$ mm apart, with radii of 9.9185, 10.02, 10.056, and 10.074 mm, and has a relative permittivity of $\epsilon_r = 100$. Current technology allows for high dielectric materials with loss tangents as small as 10^{-4} [44], [43], [42], and [25]. Therefore, for this example all four spheres in the unit cell will have the same dielectric material loss tangent of $\delta_T = 10^{-4}$, 10^{-3}, or $10^{-2.5}$.

Figure 6.10 (a) highlights the response across the magnetic dipole resonance frequency range and (b) the electric dipole resonance frequency range. As expected, the resonances are strongest for low loss, and dampened out when the material loss is higher. In addition, higher material loss also reduces the maximum of the reflection coefficient such that total reflection is no longer achieved. The Fano resonances are substantial for loss tangents of $\delta_T \leq 10^{-3}$ and must be considered during the metafilm design and measurement process.

6.5 Conclusion

This chapter has demonstrated that variations from element to element in parameters that effect the resonance frequency, cause Fano resonances to appear in the S-parameters within the Fano band. Small variations in element resonant frequency lead to strongly coupled elements which leads to narrow banded Fano resonances. Large variations in element resonant frequency lead to weak coupling in the elements and wide banded Fano resonances. The Fano resonances are inherently restricted to a frequency ranges that corresponds to neighborhoods of the frequencies at which the dipole moments resonate called Fano bands. Weak coupling leads to wider Fano bands, while strong coupling leads to narrower Fano bands.

In terms of predicting the S-parameters of the metafilm, the IPA equations derived in Chapter 5 were compared with an averaging approach proposed in previous work. Based on comparisons with *HFSS*, it was concluded that for weakly coupled elements APA or IPA will have very good agreement will *HFSS*. However for strong coupling between elements, only the predictions of the IPA have excellent agreement with *HFSS*.

In this work the examples looked at involved cases where there were either two or four distinct sphere radii. One can surmise that when N different element resonant frequencies are present, $N-1$ Fano resonances will be present in the Fano frequency band. When the elements of metafilm are manufactured, is to be expected that each element will vary in resonant frequency, which will lead to a higher number of Fano resonances. The tighter the manufacturing tolerances, the more narrow the Fano resonances. Therefore, when a metafilm is modeled or measured, a small frequency increment needs to be to chosen in the Fano band so that the Fano resonances are fully accounted for. Material loss will dampen the Fano resonances, while simultaneously dampening the overall performance of the metafilm.

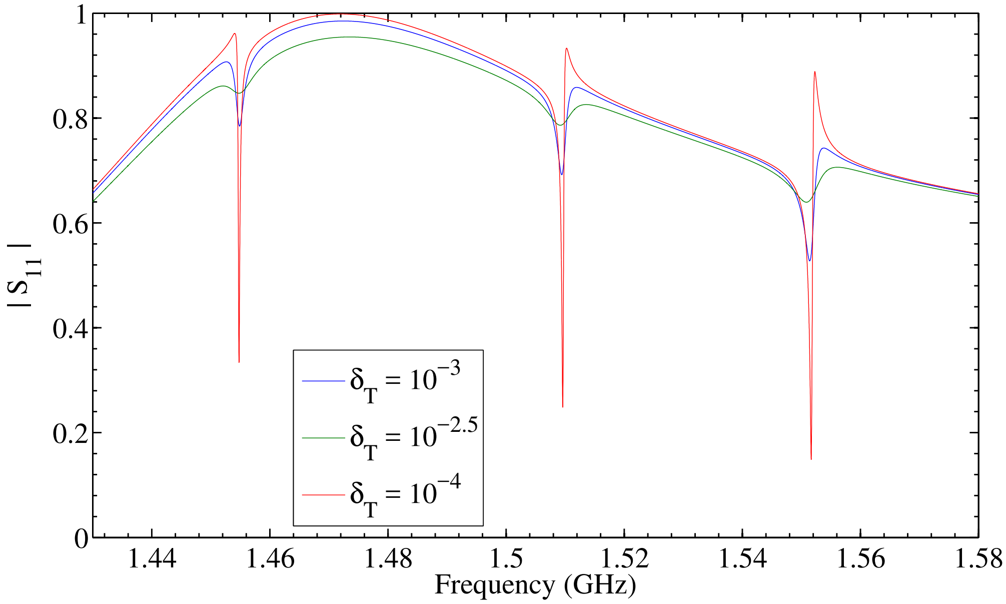

(a) Magnetic dipole resonance region

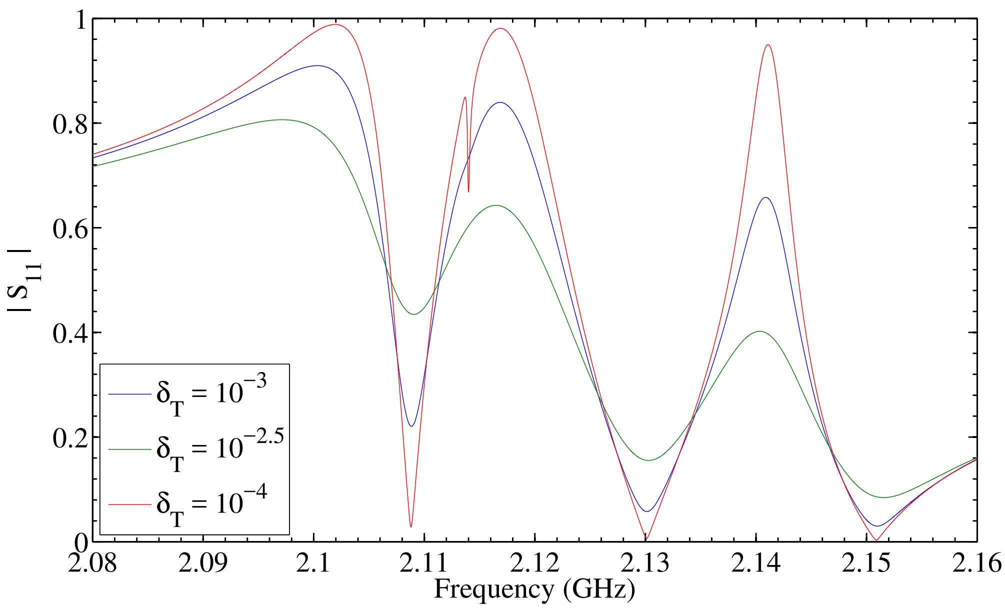

(b) Electric dipole resonance region

Figure 6.10: The magnitude of S_{11} for an infinite 2D array whose unit cell consists of 4 of lossless high permittivity spheres, plotted versus a range of magnetic resonance frequencies for variations in material loss tangent. Each sphere in the unit cell has a $\epsilon_r = 100$, is spaced $d = 30$ mm apart, and each sphere has a radius of 9.9185, 10.02, 10.056, and 10.074 mm. The dielectric loss tangent is $\delta_T = 10^{-4}$ (in red), 10^{-3} (in blue) , and $10^{-2.5}$ (in green).

Chapter 7

Metafilm Measurement and Analysis of Dielectric Cube Array

7.1 Introduction

So far, we have looked at a resonator whose properties allow it to resonate despite being electrically small compared the background medium. So far we have considered the following: one resonator in free space, then a pair, and finally an array of them spaced so that they are non-touching but close enough together that the lattice doesn't resonate. We have throughly investigated their resonant properties using analytical models. Specifically, when there is more than one of them and the physical properties that contribute to the element's resonance vary by a small amount from each other. The fields due to these imperfections constructively and destructively interfere with each other creating resonances with the sharp asymmetric shape that we call a Fano resonance. An analytical model for a metafilm, that takes into account the variations in the physical properties of the elements, was derived and validated by comparing the S parameters results of our analytical model with the numerical models of the commercial finite element code *HFSS*. In this chapter we will demonstrate that Fano resonances can be measured as well as simulated, a significant result.

The metafilm element of choice in previous chapters was the dielectric sphere, since equations for the frequency dependent polarizabilities already exists. However, in this chapter we will show that the result of Fano resonances, due to small physical imperfections between elements (so long as those imperfections effect the resonant properties of the the element), isn't limited to dielectric spheres. That as expected, they also exist for other elements such as dielectric cubes. In previous works by Kim [26], he stacked metafilms comprised of dielectric cubes to create metamaterials. In this chapter we will re-purpose those dielectric cubes and the Styrofoam used to hold the cubes in place. We will model a uniform array (that is, an array of identical cubes) and a nonuniform array (whose cube lengths vary due to fabrication error for example) and compare these models with measurements. This will validate the numerical models as well as demonstrate that Fano resonances do occur for physical variations between elements, when those variations effect the resonant properties of the elements.

There are several ways to measure a metafilm; however, we must consider the measurement facilities available for this work. We will measure a metafilm in a waveguide using a Power Network Analyzer and in order to improve accuracy over a short band of frequencies perform a Thru, Reflect, Line (TRL) calibration. Consider a unit cell with a 2 x 8 array of cubes which, for the remainder of this chapter, will be referred to as "the metafilm". We will approximate a virtual infinite sheet by placing the metafilm into a waveguide. If the waveguide walls were made of perfect electric conductor (pec), then utilizing image theory, we would have the equivalent of an infinite array of cubes. Recall, for the analytical equations derived in Chapter 4, the concept of a unit cell repeated an infinite number of times was also used to create an infinite sheet. Now, we have a way of measuring a metafilm of infinite extent.

Previously, Kim [26] (see dissertation page 104) designed metamaterials by stacking metafilms and alternating pieces of Styrofoam prior to placing them into a waveguide. The metafilm consisted of a 2 x 4 array of cubes supported by Styrofoam. During his work he selected the cube size, dielectric constant, size of the array, the waveguide, and all foam pieces to hold the array in place, as well as the frequency band of interest. While this work also uses these materials, the exact locations of the exact cubes and pieces could not be preserved. However, his measurement data is looked upon to determine what frequency band to consider for the simulations and measurements done here. Incidentally, thank you to Christopher L. Holloway and Sung Kim for allowing me to perform measurements at NIST. Also, thank you to Professor Dejan Filipovic for the measurements taken and consequently presented in this thesis.

First, we will characterize the variations in the dielectric cube lengths by measuring the opposite sides of the cubes. Next, this information is used to create two simulation models: a uniform array and a nonuniform one. We will compare the S parameter results, mesh and electric field plots for nonresonant and resonant frequency points, and the effects of material loss tangent variations among the dielectric cubes. These results will show multiple Fano resonances in the nonuniform case, as opposed to the smooth curves of the uniform one. The loss tangent study will show that the larger the material loss within the cubes, the more the Fano resonances are dampened out. These results will be compared with measurements of 5 different metafilms where multiple Fano resonances are clearly present, thus validating the numerical simulations and the theory that Fano resonances result from variations in the physical parameters of the elements that affect the resonant behavior of the element. Lastly, all 5 metafilms will be stacked together with alternating pieces of Styrofoam to form a metamaterial and measured. Fano resonances are also present but less pronounced.

7.2 Measurement of Manufactured "Cubes" Length, Width, and Height

The dielectric cubes used in this work came from the same group of cubes used in Kim's work [26]. The company TCI Ceramics, Inc. fabricated the cubes by creating a rectangular slab of dielectric material and then cutting it into cubes with side lengths of 9.8 mm using a saw. The nominal dielectric constant ϵ_r of 108.2 and the material loss tangent δ_T of 4.89 x 10^{-4} was provided by the manufacturer. While the exact chemical makeup of the material is unknown for proprietary reasons, Kim [26], p. 104 refers to it as a TiO_2 material and the manufacturer TCI Ceramics, Inc. states in supporting documents on their website, that the material is a ceramic [44] "These ceramics consists of solid solutions within the complex series Ba_{6-3x} Ln_{8+2x} Ti_{18} O_{54} where Ln is La^{3+}, Nd^{3+}, Sm^{3+} and/or Gd^{3+}. Substitutions of Sr^{2+} and Pb^{2+} for Ba^{2+} and of Bi^{3+} for Ln^{3+} are made to tune dielectric constants and temperature coefficients." The parameters that effect the resonances of the cubes are the permittivity, material loss and side lengths. While, it's likely that the permittivity and material loss tangent varies from one cube to another, those variations won't be pursued in this thesis. However, the side lengths errors will be investigated next.

Since this work is concerned with manufacturing tolerances that affect resonant behavior, the actual size of the cubes were measured to determine how much they vary from nominal values. More precisely, the "cubes" are actually cuboids since the length, width, and height can vary from each other due to unavoidable error in the manufacturing process. However, it is common for this to be implied even when these variations have significant effects on the performance. A total of 49 "cubes" were measured with a micrometer, each one with three pairs of opposing faces. The ends of the micrometer were placed at the approximate center of the opposing faces and measured and then recorded. Each cube was measured three times using different opposing faces, determining the length, width, and height. A histogram (Figure 7.1) of the data was created using 0.010 mm sized bins.

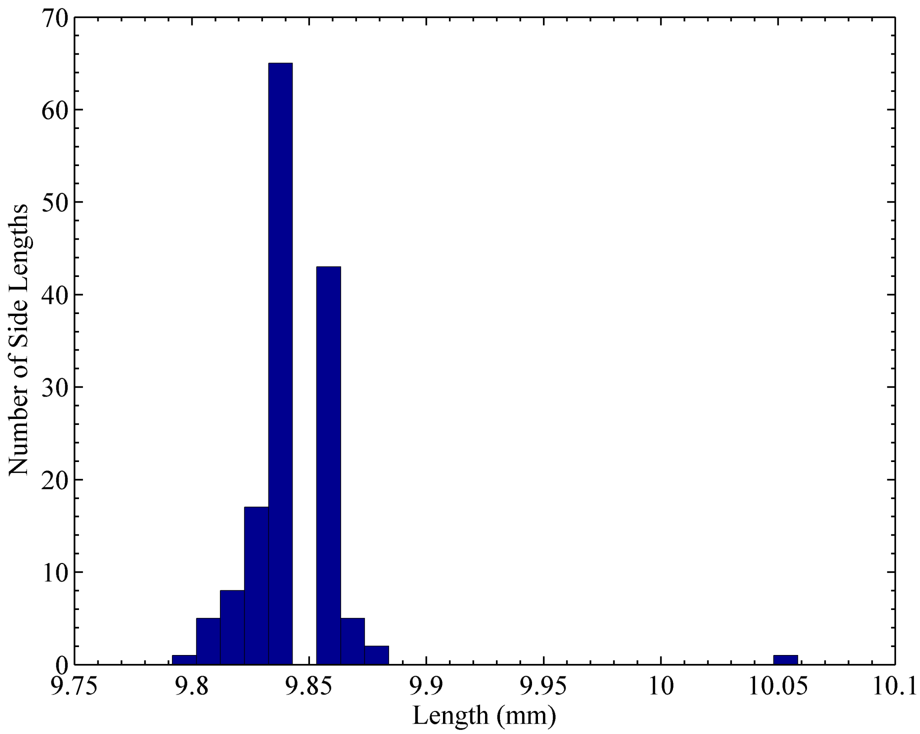

Figure 7.1: Histogram of the physical length measurement results of 49 dielectric cubes. The approximate centers of each opposing pair of faces (length, width, and height) of each cube was measured. Each bin is 0.010 mm wide.

Table 7.1: Summary of measurements of physical values of the length, width, and height of 49 dielectric cubes. The approximate centers of each opposing faces were measured. The manufacturer specification of the side lengths was 9.84 mm.

	Length, L (mm)	Deviation of L	Deviation of Volume, L^3
Nominal	9.843	0%	0%
Minimum	9.792	-0.5%	1.5 %
Maximum	9.881	+0.4%	1.2%
Outlier	10.010	+2.2%	6.7%

(Outlier length was only one length of one cube.)

Using the cube length data shown, a modal, minimum, maximum, and outlier value was found and is listed in Table 7.1. The most common or modal length was found to be about 9.843 +/- 0.025 mm. Recall the manufacturer was trying to cut the cubes to a nominal 9.84 mm side length. There was one clear outlier measured for one opposing face, which deviated by 2.2% of the nominal value. If we consider the case where the length, width, and height are all equal to the minimum measured length of 9.792 mm, we get a 1.5% variation in the volume of the cube. Similarly for a cube of maximum lengths we get 1.2 % variation in volume. Three outlier lengths on one cube would result in a 6.7 % variation. For these high dielectric constant resonators, recall that Chapter 2 suggests that volume variations on the order of 1% will result in a significant change in the resonant frequency. Next, we will look at how these resonant cubes behave with size variations and without, when used to form an array to create a metafilm.

Table 7.2: List of values of the 2 x 4 dielectric cube array length, width, and height used in the metafilm simulation model.

Cube No.	Length (mm)	Width (mm)	Heigth (mm)	Volume (m^3)
	x	y	z	
1	9.893	9.8425	9.8831	1.4917
2	9.8806	9.8171	9.8882	1.4867
3	9.8831	9.8552	9.8425	1.4859
4	9.7536	9.8806	9.8679	1.4740
5	9.7917	9.8806	9.7536	1.4626
6	10.0076	9.7917	9.8552	1.4969
7	9.8806	9.8806	9.8806	1.4951
8	9.8400	9.840	9.840	1.4768

7.3 Numerical Simulations for a 2 x 4 Unit Cell Array of Dielectric Cubes

Now that we've completed the cube size measurements, we will use this information to create a metafilm of cubes. We will use the same metafilm configuration as Kim in Chapter 7 of [26]. To create the metafilm, an array of cubes are placed into a waveguide perpendicular to the wall. For the standard size waveguide WR-284 that operates at S-band (2.60 - 3.95 GHz), the dimensions are 34.036 x 72.14 mm. This leaves enough room for a 2 x 4 array of cubes. The cubes placed in the widest section of the waveguide will have a period of 18.035 mm and the shortest section will have a period of 17.018 mm. A depiction of the element, array, and metafilm simulation model are shown in Figure 7.2.

For the numerical simulations, we will look at two models. As was done for the previous chapters, a 3D finite element method commercial software *HFSS* was used. One model is a uniform array where all the side lengths have the manufacturer listed cube lengths of 9.84 mm. The other is a nonuniform array whose side lengths vary based on values used from the side length measurements of the previous section. The side lengths are listed in Table 7.2. The two models are referred to as the uniform and the nonuniform array models.

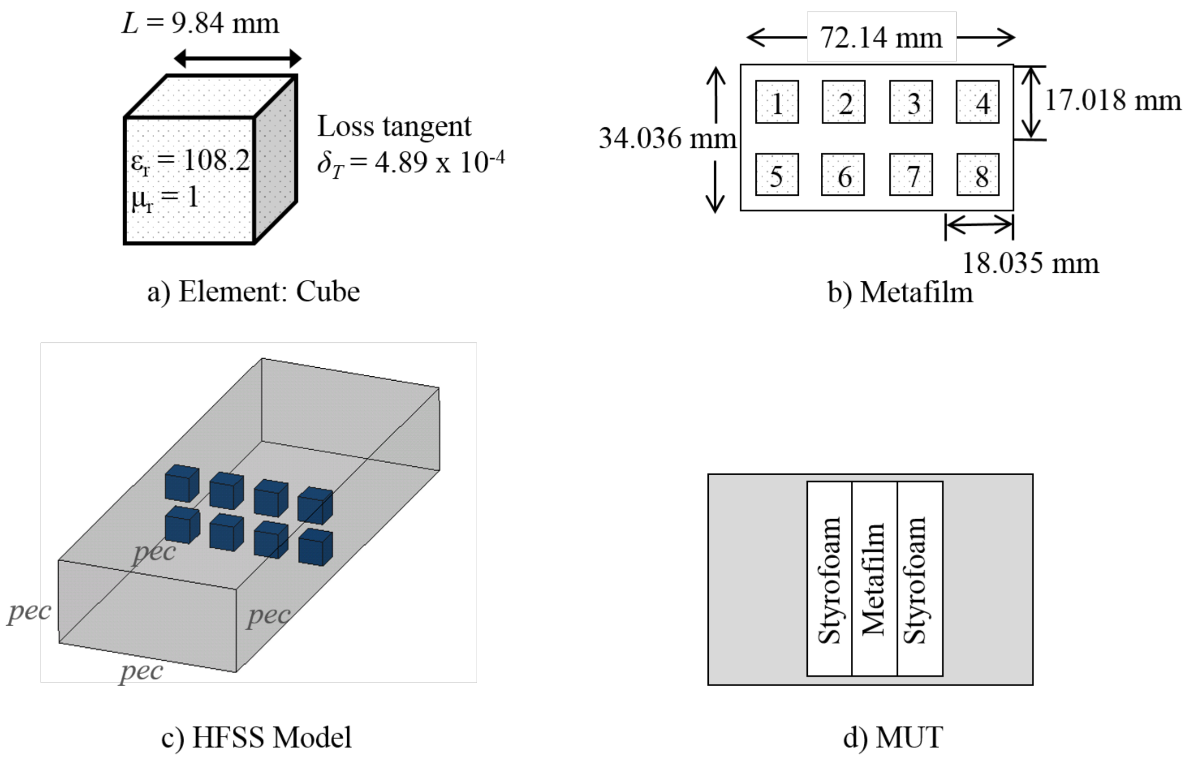

Figure 7.2: Details of the metafilm used for measurements: a) Dielectric cube with manufacturing specs. b) 2 x 4 lattice of dielectric cubes with lattice spacing and waveguide dimensions indicated. c) Numerical simulation model of the metafilm placed perpendicularly in the waveguide. d) Depiction of a the MUT or material under test which includes a layer of Styrofoam, metafilm, and then another layer of Styrofoam placed perpendicular in the waveguide.

We expect Fano resonances to occur when one or more elements in the metafilm has a resonant frequency that varies slightly from the other elements in the array. The frequency band of interest is chosen so that lattice remains less than a quarter of a wavelength and doesn't create resonances. Chapter 3 demonstrated that small variations in parameters that don't cause resonances, result in no Fano resonances. Thus, for the 2 x 4 array of cubes depicted in Figure 7.2 with lattice periods that are less than a quarter of a wavelength, no Fano resonances should be observed resulting from small variations in the lattice periods. However, we do expect the parameters of permittivity and cube side length to shift the resonant frequency of the elements themselves. As shown in Chapters 2 and 5, variations in parameters that effect the resonances of the metafilm create Fano resonances within a band of frequencies we call the Fano band.

To determine the frequency band of interest, a closer look was taken at Kim's measurements in Chapter 7 of [26], of a two layer and three layer metamaterial. He placed the metafilm perpendicularly in the guide and then added a Styrofoam layer of thickness 8 mm, and then another metafilm, alternating metafilms and Styrofoam to create the metamaterials. The two layer metamaterial, contained two metafilms and the three layer metamaterial contained three metafilms. Looking closely at the S parameter data shown in Figures 7.10 (a) and (c) respectively of [26]. One can tell that the data is very smooth overall with occasional shallow dips. This raises the following questions:

(1) Have the Fano resonances been completely dampened out by the material loss in the elements?

(2) Was the frequency increment too large to capture many of the Fano resonances?

(3) Was a post processing smoothing function applied to the measurement data therefore averaging out the Fano resonances?

Close inspection of the magnitude plots of the S_{11} reveals that notable dips occur around 3.4 GHz. We will carefully investigate these dips by simulating and measuring a metafilm over the narrow frequency band of 3.3 to 3.45 GHz.

A narrow frequency band is important, so that the frequency increment can be small. Recall in Chapters 2 and 5, for the case of an array of dielectric spheres in a metafilm. The smaller the variations in parameter that effect resonance between elements, the more narrow the Fano resonances become. As shown in Chapter 5, the higher the number of elements that vary in parameters that effect resonance, the more Fano resonances that will occur and will result in a wider Fano band. The Fano band is the region the Fano resonances occur. Since the variations in cube sizes are small, this gives the expectation that the Fano resonances will be narrow. When considering the availability of the measurement tools used in this work, this frequency band is narrow enough to ensure a small enough frequency increment to give the most likelihood of capturing Fano resonances.

The sharpness of the Fano resonances are dampened by loss within the dielectric resonator. Recall the non-spherical shaped resonators have modes that are confined and the spheres have non-confined modes. We expect the resonances of the cubes to become dampened for smaller values of loss tangent than was seen in Chapters 2 and 5 for the spherical resonators.

7.3.1 Comparison of the S parameters for a Uniform and Nonuniform Array

For the initial simulations of the uniform and nonuniform array of cubes the green and blue curves respectively. The array (shown in Figure 7.2) contains a 2 x 4 unit array of either identical dielectric cubes for the uniform case, or the size varying elements whose values are listed in Table 7.2 for the nonuniform case. The material loss tangent and permittivity given by the manufacturer (δ_T of 4.89 x 10^{-4} and ϵ_r is 108.2, respectively) are used. The S parameters results are shown in Figure 7.3. Not shown are S_{22} and S_{12} since they didn't differ by any significant amount from S_{11} and S_{21}. The magnitude and phase of S_{11} and S_{21} are plotted, as well as the power absorbed determined by $|S_{11}|^2 + |S_{21}|^2$.

Overall there is good agreement between the uniform case and the nonuniform case. The general shape of the magnitudes and phases are comparable aside from the dips. For the magnitude of S_{11}, there is a deep null around 3.353 GHz where they both have the greatest amount of power loss. After the null, there is a stopband that is between approximately 3.35 and 3.4 GHz. The bandstop region in S_{11} for the uniform case is wider than the nonuniform case. The overall shape is the similar with exception to the dips that occur in the nonuniform case (which have the most apparent impact in the power loss plot) versus the smooth curves in the uniform case.

Specifically, the uniform case has a very smooth shape overall. There is one small disruption at 3.385

GHz in the stop band. This is unexpected since all resonant parameters of the elements are the same. Some other phenomena not studied in this work is causing this. The power absorbed is only greatest at the large null discussed at approximately 3.35 GHz. The unexpected shallow one at around 3.385 GHz has a 0.5 amount of power loss.

For the nonuniform case, multiple shallow dips that occur as expected, based on previous chapters, we can attribute these dips to be the result of the variations in the cube sizes which are resonant varying parameters. Therefore the dips are Fano resonances whose sharp corners have been dampened out by the material loss within the elements. They are greatest in number within the stopband. Above 3.4 GHz the resonances in all the S parameter plots, no longer occur, indicating the approximate upper limit to the Fano band. The power absorbed is more substantial for the nonuniform case due to the multiple resonances. There is a wide band of power loss around 30% or more between approximately 3.34 - 3.36 GHz, at 3.375, and at 3.385 GHz. While the uniform model is a good predictor in the overall shape, the effects of the Fano resonances are large enough that the nonuniform case should also be simulated.

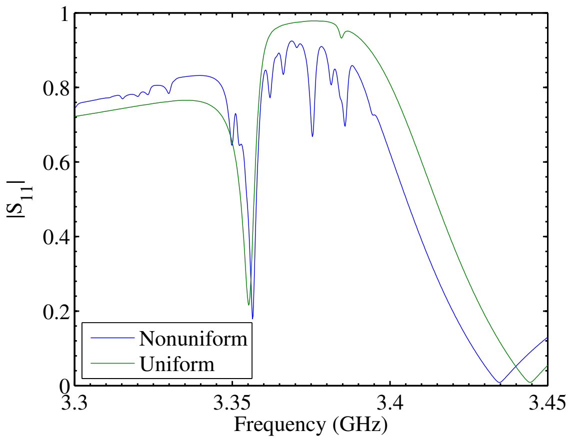

(a) Magnitude of S11

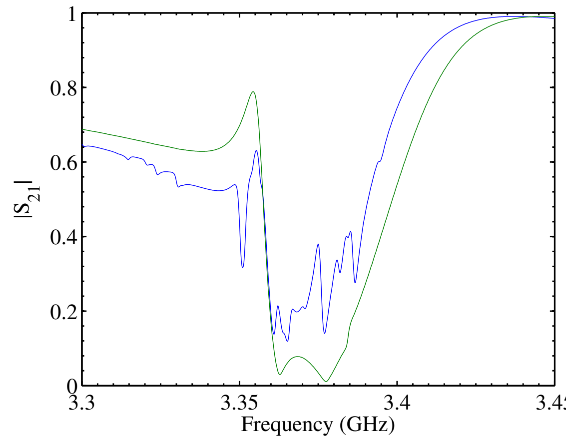

(b) Magnitude of S21

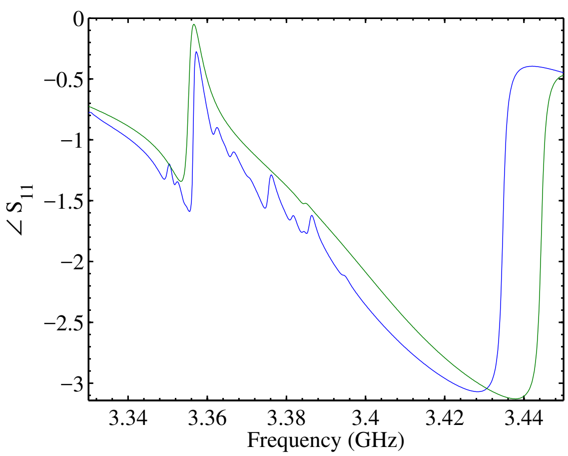

(c) Phase of S11 in radians

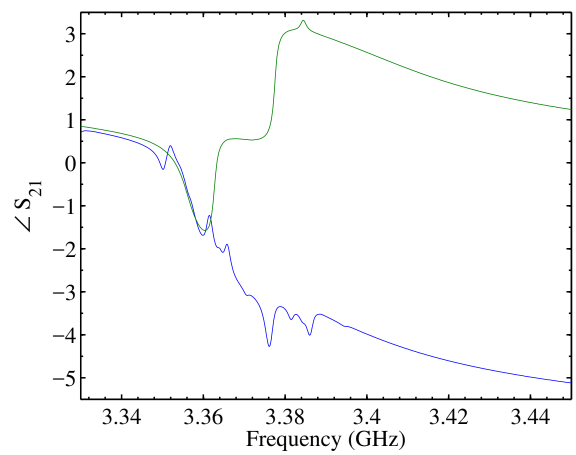

(d) Phase of S21 in radians

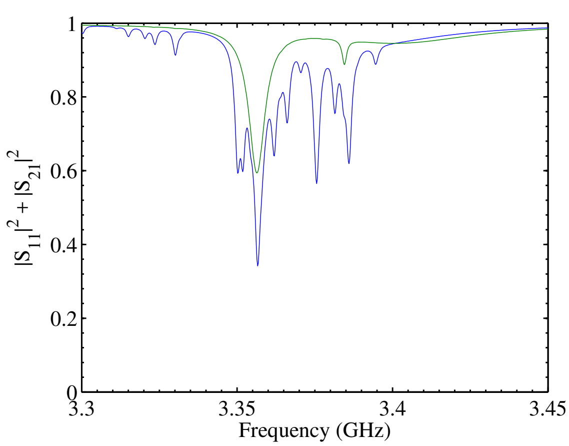

(e) Power absorption

Figure 7.3: HFSS simulation results comparing a uniform (green curve) and nonuniform array (blue curve) of cubes.

7.3.2 Comparison of the Adapted Mesh and Electric Fields for a Uniform and Nonuniform Array

Next, we will take a close look at the calculated fields and converged mesh created by *HFSS* for three frequency points. *HFSS* initially creates a tetrahedral mesh based on the geometry of the model and input user parameters. Then it calculates the gradient of the electric fields and S parameters. It will then locally refine the mesh again and compare the S parameters of the last attempt with the current one, at one frequency. This will continue until a user defined parameter has been reached, determining the model has converged [1]. In Figure 7.4, the left column shows the adapted mesh generated by *HFSS* used to calculate the corresponding Electric fields for a cross-section of the waveguide that contains the cubes, shown in the right column. Figure 7.4 a) and b) are the results for the uniform model at 3.4 GHz and 3.353 GHz respectively. For the nonuniform model, Figure 7.4 c) at 3.4 GHz and d) at 3.361 GHz.

The frequency point of 3.4 GHz was chosen for both models since it is above the Fano band, to ensure the frequency response will be smooth and a low amount of power lost of around 6%. The other two points were chosen to purposefully lie with a region that has a resonance. For the uniform case, 3.353 GHz was chosen since it lies in the region of maximum power absorbed or 35% indicating a strong resonance. For the nonuniform case, a region that contains one of the many Fano bands was chosen, specifically 3.361 GHz with 38% power absorbed. We expect the fields will be more complicated and will have a tighter mesh than for the results outside the Fano band at 3.4 GHz.

For the uniform case, both frequency points show a uniform field from left to right. Figure 7.4 a) For 3.4 GHz, the field plot shows a mode that is similar to that of the waveguide. The center cubes number 2, 3, 6, and 7 from Figure 7.2 have the greatest field, while the outermost cubes 1, 4, 5, and 8 are weakly excited. The mesh plot to the left shows a tigher mesh for the center cubes versus a loose one for the outermost cubes. Next, at the frequency point of 3.353 GHz, Figure 7.4 b) more a complicated mode within all the cubes. There appears to be a significant quadrapole component excited within the cubes. The corresponding mesh for this resonant frequency point is much tighter for all cubes, especially in the outer most columns. Conversely, the nonresonant frequency point shows the outer most cubes have the loosest mesh.

For the nonuniform case, the cube sizes are listed in Table 7.2. Cubes with the most similar volumes, listed from largest to smallest are cubes: 6 and 7, 2 and 3, and 4 and 8. Cube 6 has the smallest volume and cube 1 has a volume that is smaller than cubes 6 and 7, but larger than 2 and 3. For the nonuniform case with no resonance in the S parameters at 3.4 GHz (Figure 7.4 c)), we see the fields are excited similarly to the uniform case, expect that only two of the innermost cubes, 2 and 3 are strongly excited. Also for the outer most cubes, 1 and 8 are more weakly excited than 4 and 5. The mesh is tightest for cubes 2 and 3, and loosest for cube 1. The deviation in the field response from that of the uniform model of a uniform excitation from left to right, is strongly dependent on the variation of the resonant parameters of the cubes themselves.

Next, for the Fano resonant frequency point of 3.361 GHz in Figure 7.4 d), again we have a similar situation as the uniform case the modes within the cubes that are similar to a higher order mode such as a quadrapole. However, cubes 4 and 8 are dominate with a very tight mesh for both, while cubes 1, 3, 5, and 7 are more weakly meshed. The plots of the nonuniform case show the cubes don't have a uniform field from left to right as seen in the uniform model, due to the resonator variations in size which leads to the Fano resonances.

There are very different variations in the mesh of the cubes between frequency points where the S parameters are showing a resonance versus not. This shows great care must be taken when simulating metafilms due to their resonant nature. A very fine mesh is needed to accurately capture all the variations from one frequency point to another, since the fields can vary widely from one another.

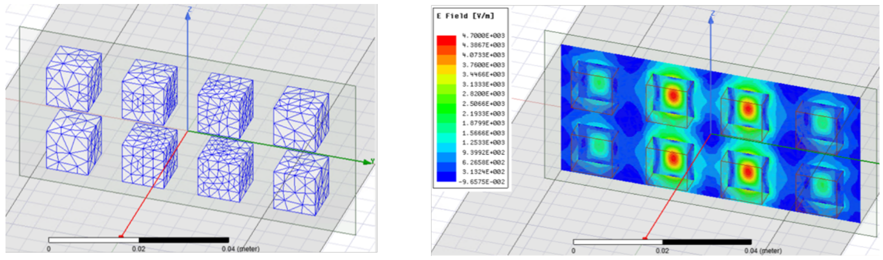

(a)

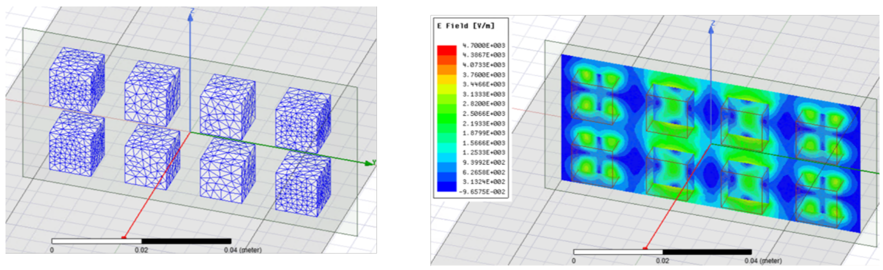

(b)

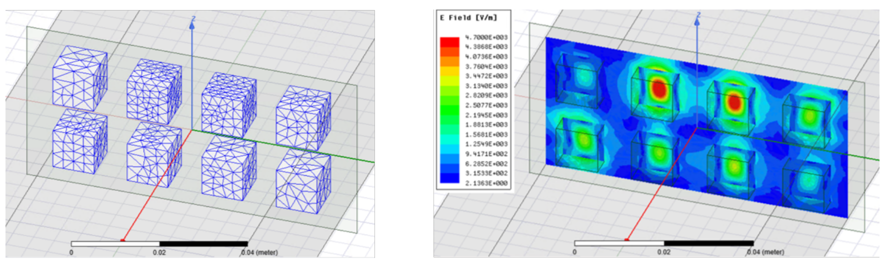

(c)

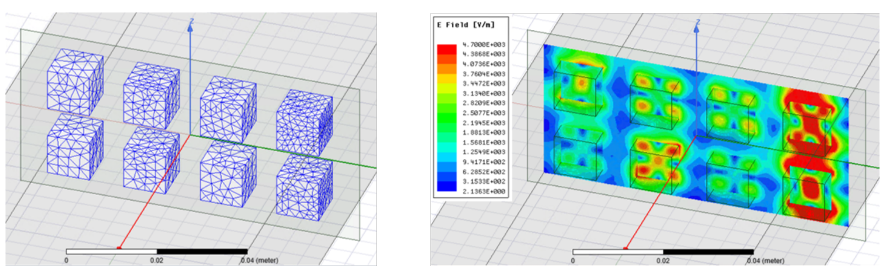

(d)

Figure 7.4: Comparison of the numerical simulation results of the mesh (on the left) and electric fields (on the right) for the uniform and nonuniform cases as shown in Figure 7.2. The uniform array contains identical elements while the nonuniform array has the various cube lengths listed in Table 7.2. For the uniform array at a (a) nonresonant frequency of 3.4 GHz and (b) a resonance at 3.3530 GHz. For the nonuniform array at a (c) nonresonant frequency of 3.4 GHz and (d) resonance at 3.3610 GHz.

7.3.3 Comparison of a Cube Material Loss Tangent of the Nonuniform Array

Lastly, before looking at measurements, we will look at a how material loss tangent within the cubes effects the sharpness of the Fano resonances. Reconsider the previous nonuniform model whose properties are listed in Table 7.2 and the model is illustrated in Figure 7.2. Two cases are considered, when all the cubes have the same loss tangent of δ_T of 4.8 x 10^{-4} and then 1 x 10^{-4}. The S parameter results are given in Figure 7.5. The Fano resonances are sharper for the lower loss model (the blue curve) and absorbed less power. This gives us a good idea of what to expect from material loss tangent for an array of cubes. Small variations in the material loss of the cubes does effect the sharpness of the Fano resonances. Of course, the cubes that will be measured in the laboratory will have materail loss tangents that vary within each cube and also vary from cube to cube. While this work doesn't measure the acutall material loss tangent of each cube, one could expect differnt combinations of material loss from cube to cube. Therefore the cubes with the least loss will contribute the most to the Fano resonances.

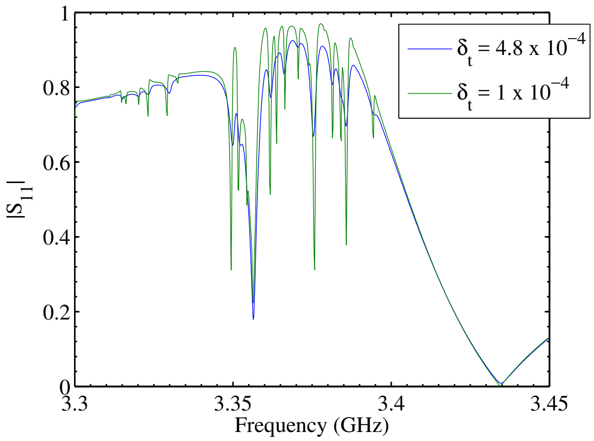

(a) Magnitude of S11

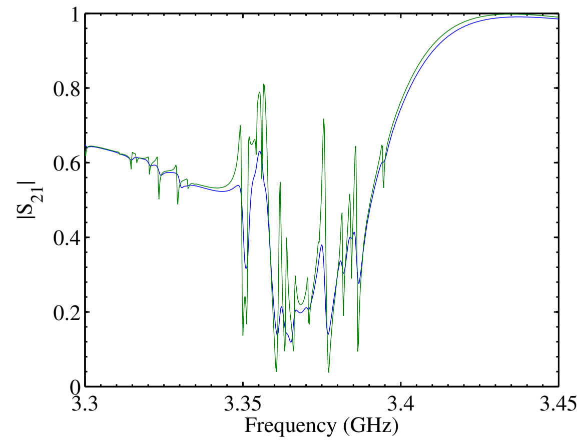

(b) Magnitude of S21

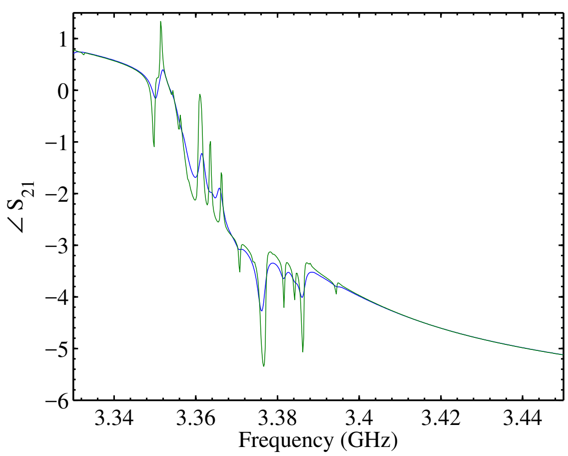

(c) Phase of S11 in radians

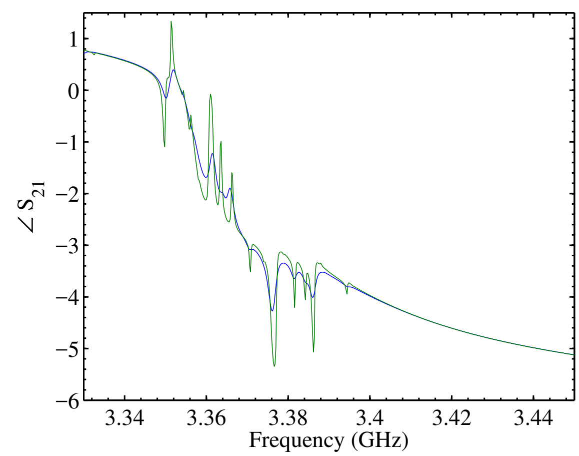

(d) Phase of S21 in radians

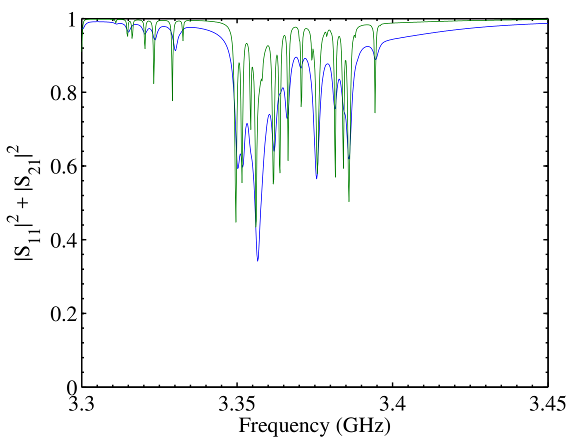

(e) Power absorption

Figure 7.5: A loss tangent study using HFSS simulations of a nonuniform array. All the cube have a loss tangent of 4.8 x10^{-4} (the blue curve) or 1x10^{-4} (the green curve).

7.4 VNA Measurements of the Metafilm Comprising of a 2 x 4 Array of Cuboids

7.4.1 Measurement Setup

By quantifying how much the physical dimensions of the manufactured cuboids vary, and then modeling that behavior. This gives a good idea of how best to proceed with the measurements so that we may observe the Fano resonances. A Power Network Analyzer (PNA) E8363B was used to perform the measurements. The chosen cables were lightly used, unconstrained, and well cared for. All connectors were properly tightened with a torque wrench to protect all connectors and cables. The waveguides used were standard WR-284 with a frequency range of 2.60 - 3.95 GHz or S-band whose inside dimensions are 2.840 x 1.340 inches. Prior to the measurement, a TRL calibration was performed. The chosen frequency range for the measurements was 3.3 - 3.45 GHz so that a small frequency increment of 9.375 kHz or smaller could be used. Also, absolutely no post processing functions were applied. They could smooth out the very Fano resonances we are looking for.

To form the array of cubes or metafilm, a piece of very low loss Styrofoam was used to hold the cuboids in the intended location. The Styrofoam was chosen to have the approximate thickness of the cubes. An exacto knife was used to cut several pieces so that the height and width of the Styrofoam matched that of the inner dimensions of the waveguide. Five of the Styrofoam rectangles were used to create the metafilm lattice. A 2 x 4 array of holes that approximate the size of the cuboids was cut into the Styrofoam. The other Styrofoam rectangles without holes were used as covers for the metafilms to prevent the cubes from moving or falling out of place during testing. According to Kim's work [26] in Chapter 7, the Styrofoam has a relative permittivity of around 1.03. The lattice periods of the array are same as the simulations as shown in Figure 7.2 or 17.018 and 18.035 mm. Two sets of measurements were performed, we will begin by discussing the first set.

For the first set of measurements all post processing functions were turned off and one calibration was preformed. The subsequent materials under test will be called MUT 1, MUT 2, MUT 3, MUT 4, and MUT 5. A total of 48 cubes were used. Five arrays of eight created five different lattices that will be referred to as lattice 1, lattice 2, lattice 3, lattice 4, and lattice 5. Each material under test consists of 3 layers: solid foam, metafilm, and solid foam. The metafilm was placed in between solid foam covers so that the lattice would be as perpendicular as possible within the waveguide and no elements would fall out of place. The foam cover, lattice 1 and the other foam cover, made up MUT 1. Similarly, lattice 2-5 were used to create MUT 2 - 5.

The measurement section of the waveguide ends where then connected to the waveguide to coaxial adapter and held in place with screws. Once the measurement was finished and saved, the measurement section of the waveguide was removed from the test setup so that the MUT could be properly removed. The frequency increment of 9.375 kHz was used first. Then for two smaller frequency ranges, an increment of 1.875KHz was used and plotted against the larger one. The plots lined up perfectly indicating that a frequency step of 9.375 kHz would be as accurate as the smaller one.

7.4.2 Measurement Results

First we will look at the the S-parameters of one MUT. Plotted in Figure 7.6 is MUT 3. The overall shape has a deep null followed by a bandstop. The data distinctly shows many dampened Fano resonances. They are narrow banded, some are very shallow, and others are deeper. It appears that the region the Fano band exists is between approximately 3.325 and 3.425 GHz. Outside the Fano band, there doesn't appear to be anymore Fano resonances. In the bandstop region of the magnitude, the maximum value is around 0.95 while the deepest dip is below 0.8. For some applications, this might be unacceptable. However this variation could be missed if a post processing smoothing functions was applied.

The S-parameter data of MUT1-MUT5 is plotted in Figures 7.7. The overall shape is the same. Again we see dampened Fano resonances in the Fano band and a smooth line outside. However, the Fano band appears distinctively wider and lower for MUT 2 and 4. While all MUTs show agreement that the Fano band ends around 3.425 GHz, MUT 2 and 4 Fano band begins at around 3.31GHz. Interestingly, while looking closely at the $|S_{11}|$ plot of MUT 4 at around 3.35 GHz, there is a very deep and narrow dip that doesn't appear in the other cases. While, all five MUTs have a similar pattern, the exact location and depth of the resonances differ. Clearly, using a post-processing smoothing function or too large of frequency increment would make it difficult to properly capture these Fano resonances which are very sensitive to small variations in element parameters that effect the resonance of the element.

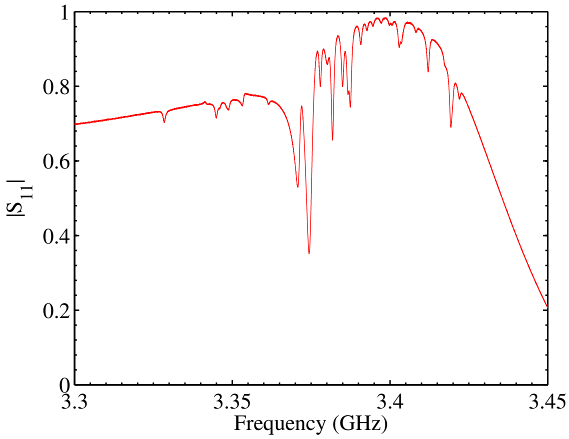

(a) Magnitude of S11

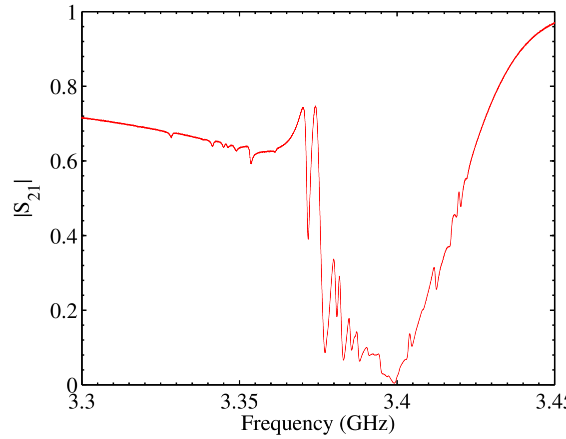

(b) Magnitude of S21

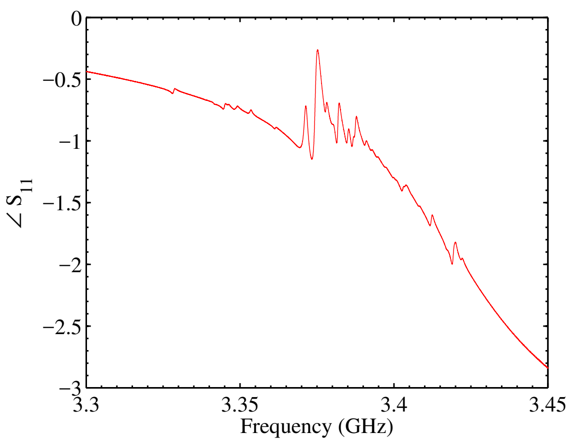

(c) Phase of S11 in radians

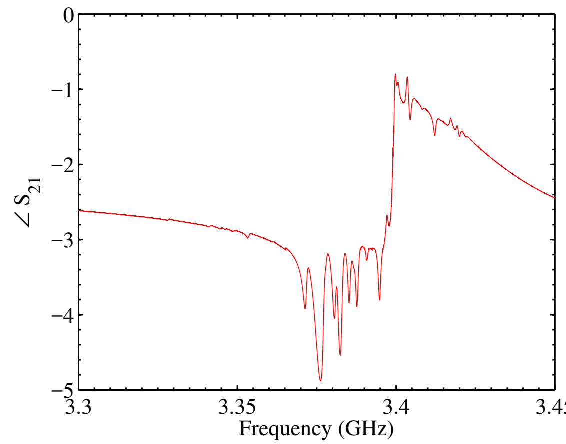

(d) Phase of S21 in radians

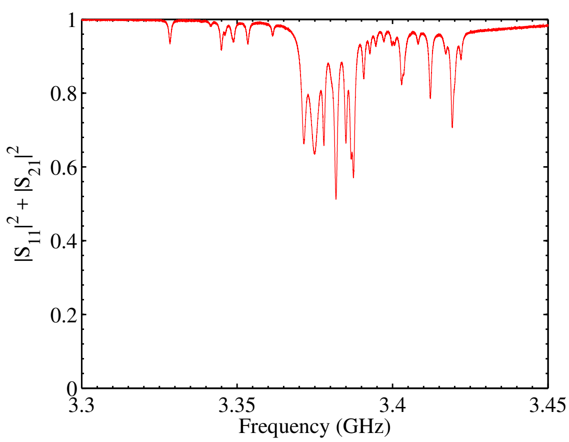

(e) Power absorption

Figure 7.6: The measurement results of the material under test or MUT 3 where the frequency increment used was 9.375 kHz.

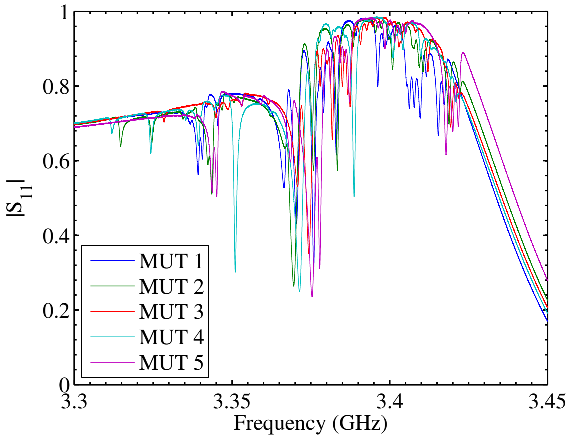

(a) Magnitude of S11

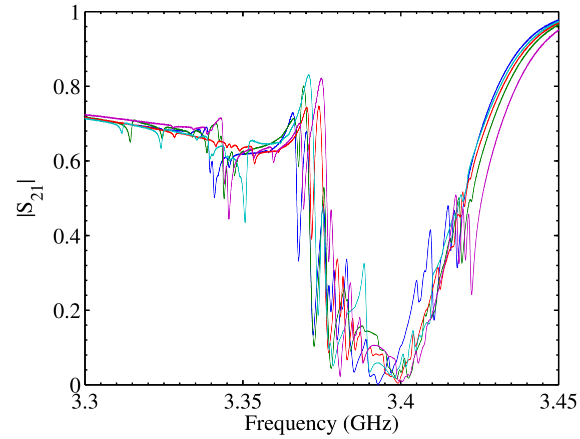

(b) Magnitude of S21

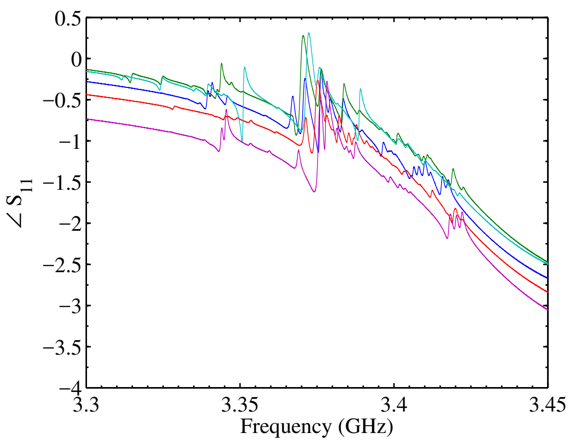

(c) Phase of S11 in radians

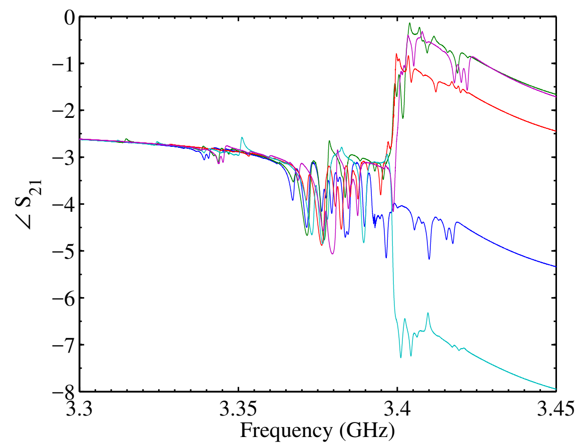

(d) Phase of S21 in radians

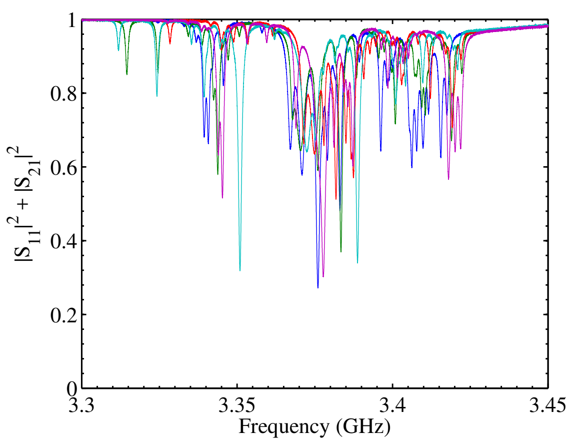

(e) Power absorption

Figure 7.7: The S parameter results for measurements of the material under test or MUT 1 - MUT 5. The same TRL calibration with a frequency increment of 9.375 kHz was used for all five measurements.

7.4.3 Comparison of Measurement Results with Numerical Results

Now, we will compare the numerical simulations results with the measured results. For this comparison, MUT 3 was chosen (see Fig. 7.8 for the S parameters). The numerical simulation model used is the nonuniform one described in Figure 7.2, whose side lengths are listed in Table 7.2. The only parameter adjustment made is the permittivity for all the cubes, from 108.2 to 107.2. This results in an overall shift of the bandstop region to the right. Which makes the comparison of the measured data and simulation data easier. While the overall permittivity of the dielectric slab cut into cubes was quoted by the manufacturer to be 108.2, this likely varied throughout the slab causing each cube to vary in permittivity from cube to cube. This likely causes an overall shift in the data and influenced the location and depths of the Fano resonances (see Chapter 2 for details).

Looking at the S parameter data, the numerical model is plotted in the color blue and the measurement of MUT 3 is plotted in red. Overall there is very good agreement between both. The numerical code did a very good job predicting the overall behavior of the metafilm. We don't expect the location and depth of the Fano resonances to agree. Since the actual cubes measured weren't completely characterized to determine all variations in parameters that effect the resonant behavior of the element. The power absorption plot indicates that the cubes weren't as lossy as indicated by the manufacturer since we see more power is absorbed for the numerical model. The phase of S_{21} varies approximately by multipoles of π. This is likely due to the length of the waveguide used for the measurement that wasn't included in the simulations. The MUT was placed close to the port 1 but far from port 2. Clearly, for both the numerical simulations and the measurements, Fano resonances interrupt the smooth shape the curves a uniform array would have and have a significant contribution to the behavior of metafilm.

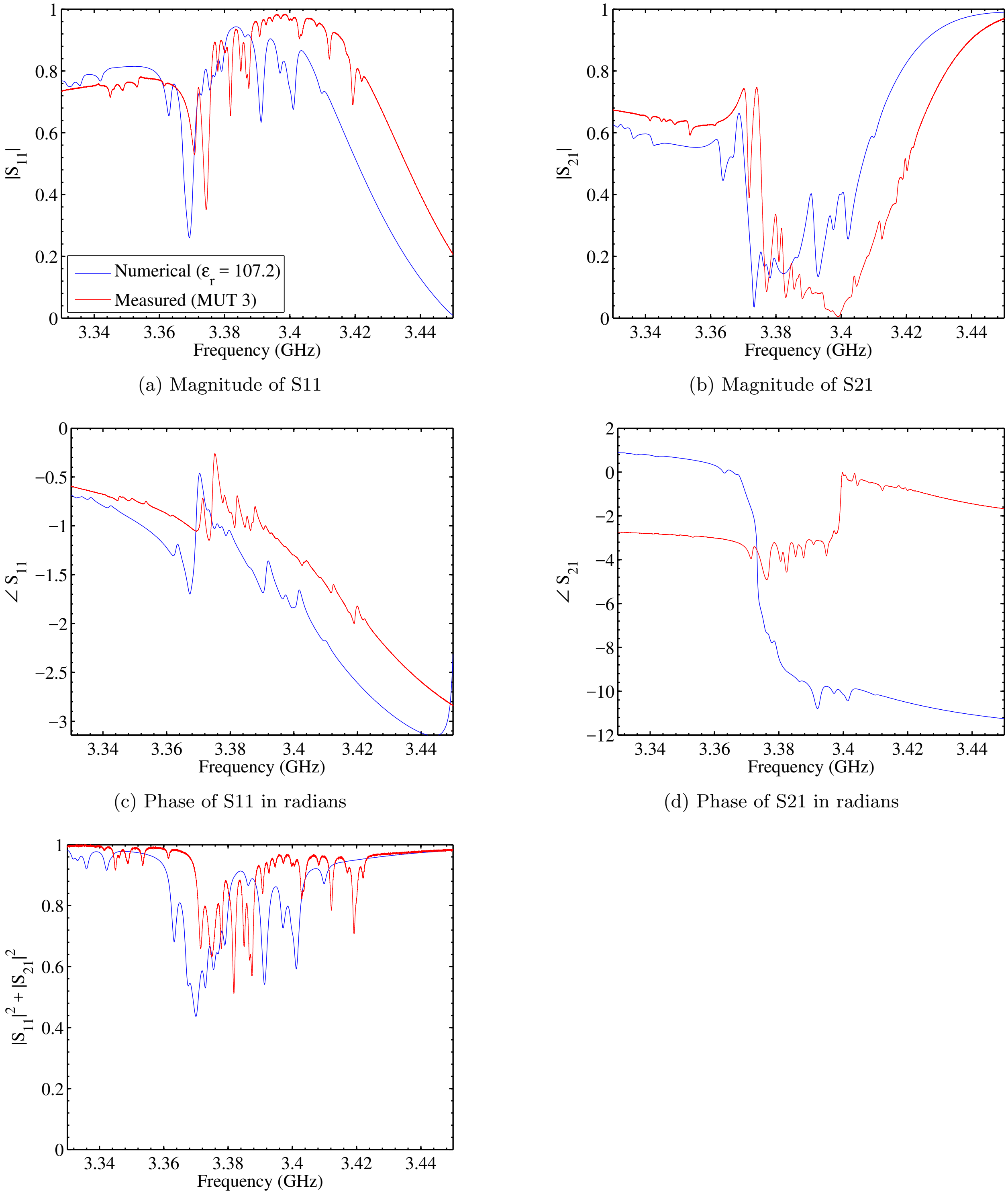

(a) Magnitude of S11

(b) Magnitude of S21

(c) Phase of S11 in radians

(d) Phase of S21 in radians

(e) Power absorption

Figure 7.8: Comparison of the numerical simulation results of the nonuniform array (the blue curve) with measured results of MUT 3 (the red curve) .

7.4.4 Measurement Results of a Metamaterial Made of stacked MUTs

Lastly, a stack of all 5 metafilms with alternating foam layers creating a period between lattices of 8mm, was measured forming a metamaterial which will be referred to as MUT STACK. Figure MUT stack shows the S parameter results. The bandstop region of the magnitude plots is wider for the metamaterial versus the metafilm. Fano resonances even appear in the metamaterial but less pronounced. No Fano resonances are seen above 3.44 GHz, indicating the upper limit of the Fano band. Since the stack is much thicker than the metafilms, we see the phase has a large variation as frequency increases. Still Fano resonances are present for the 5 metafilm stack. Users should use cation while measuring metafilms and metamaterials to properly characterize the behavior of the material. The frequency increment needs to be small enough to capture the narrow banded resonances and any post processing smoothing functions should be turned off.

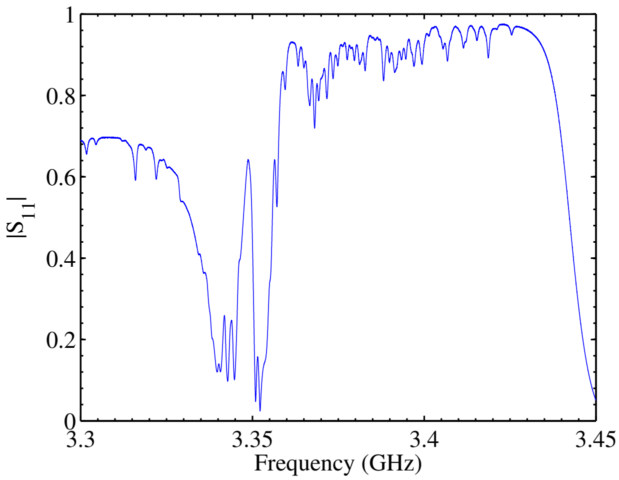

(a) Magnitude of S11

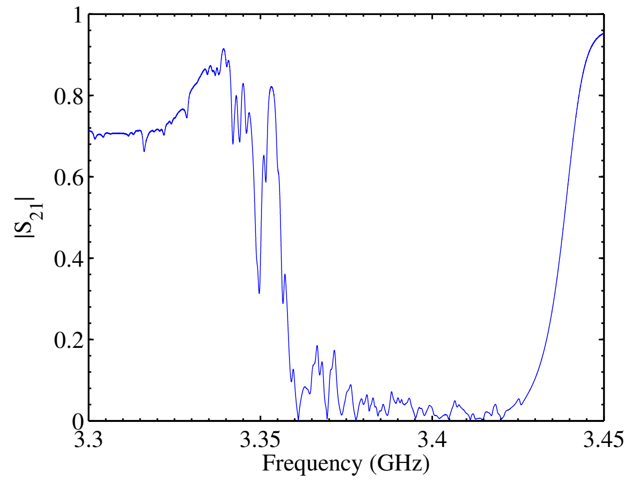

(b) Magnitude of S21

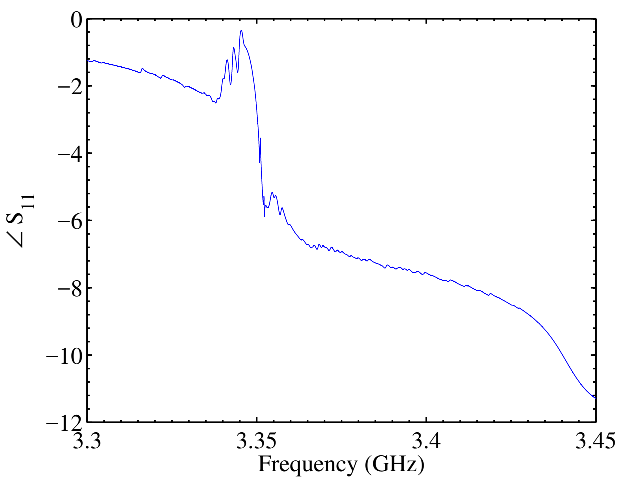

(c) Phase of S11 in radians

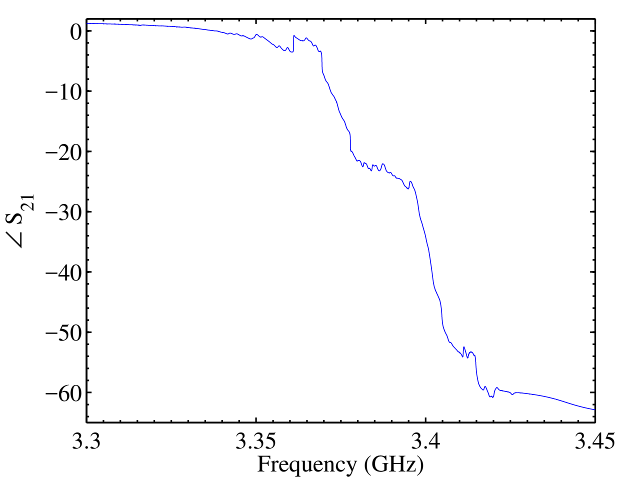

(d) Phase of S21 in radians

Figure 7.9: Measurements of a metamaterial containing all five metafilms with alternating foam layers.

7.5 Conclusion

In this chapter, a metafilm comprised of an array of 8 cubes placed in a waveguide was simulated and measured. The lengths of manufactured cubes were measured using opposing faces. The manufacturing error was found to be about +/-0.5%. This indicated that Fano resonances resulting from this small amount of error in parameters the effect the resonant frequency, would likely be very narrow. When considering the simulations and measurements, we can conclude that a very small frequency increment should be pursued so that we will capture as many Fano resonances as possible.

This information was used to design two numerical models: one uniform array consisting of identical cubes and the other a non-uniform array consisting of cubes that vary in length. S parameters of the uniform array consisted of a smooth bandstop region while the non-uniform array had multiple Fano resonances in the bandstop region and to the left of it indicating a Fano band region. Field and Mesh plots of two sets of frequency points of resonant and nonresonant points. Showed a large variation between frequency points. Demonstrating a very fine mesh is required to capture all variations in the fields accurately. A loss tangent study was preformed on the nonuniform model, showing the dampening effects that cube material loss has on the Fano resonance. Despite the material loss tangent of the elements, the Fano resonances are still a strong contributor the performance of the metafilm.

Next, measurements of the manufactured cubes supported by Styrofoam was preformed using a PNA. Since the resonances are very sharp, a TRL calibration was preformed and all smoothing functions were turned off. For 5 different metafilms, multiple Fano resonances exist in the Fano band. A comparison was made between the simulation model and the measurements and they had very good agreement. This demonstrates that Fano resonances result from variations in the physical parameters of the elements that affect the resonant behavior of the elements. Also, material loss in the elements themselves will dampen the sharpness of those resonances but they will retain a significant amount of depth for low loss materials.

Lastly, all 5 metafilms were stacked together with alternating pieces of Styrofoam to form a metamaterial, then they were measured. Fano resonances are also present but less pronounced.

Chapter 8

Conclusions and Future Work

In Chapter 2, we reviewed the dipole moment behavior of the magnetodielectric sphere that is designed to resonate as frequency changes. The dielectric sphere was studied the most, since it is consistently used for analysis purposes throughout this thesis. In future work, the analytical equations for the frequency dependent polarizabilities of the sphere could be extended to include multipoles at the expense of a more complicated expressions, as was discussed in that chapter.

The theory presented throughout this thesis can be easily extended to magnetodielectric spheres as well as other resonator shapes. An example of this was provided in Chapter 7, wherein dielectric cubes were the chosen element shape. The frequency dependent polarizability for elements with dipole moment behavior occurs for structures other than the magnetodielectric sphere. For arbitrarily shaped elements, the frequency dependent polarizabilities can be determined using numerical software (such as *HFSS* or *CST*). This could be the subject of future research.

Chapter 3 contains a comprehensive study of an isolated pair of scatterers. If the two elements are identical, the individual and total induced dipole moments will exhibit one resonance with a wider bandwidth, than that of a single element. If the distance between identical elements becomes smaller or larger, no significant changes in polarizability occur. When the resonant frequencies of both elements of a cluster pair are no longer equal and their bandwidths overlap, a more complicated coupling process occurs. This work demonstrated that the frequency coupling between the two scatterers will have a paired response: a main resonance and a Fano resonance. The main resonance will exhibit an approximately even mode characteristics, in which the polarizabilities will add constructively, widening the bandwidth as is the case for the identical pair. The Fano resonance displays approximately odd mode behavior, where the polarizabilities of the two elements oppose each other, thereby interfering with each other and causing a narrowing of the resonance and an asymmetric shape.

As the resonant frequencies of both elements become closer together, more of their bandwidths overlap and the pair couples more strongly. The bandwidth of the main resonance increases, while that of the Fano resonance becomes sharper. If the distance between the elements is smaller, the non-identical elements couple in frequency more easily. This was demonstrated by plotting the polarizability versus frequency using analytical equations derived in chapter 3. They are based on a quasi-static dipole mode approximation, and are validated using previous work. It was also demonstrated that the simple additive approach is only a good approximation for the weakly coupled pair. For medium to strong coupling the equations derived in chapter 3, as well as other rigorous equations should be used instead.

The coupled pair analytical equations could be made more accurate, at the expense of becoming more complicated. For example, conservation of energy doesn't hold for either of the dipole moment approximations presented in this thesis. Methods for improving the accuracy of the dipole approximation were outlined in chapter 3.

The implications of a dipole pair behavior for that of a two-dimensional version of a metamaterial known as a metafilm were examined next. The elements of a metafilm are physically small compared with the background medium, but large enough to resonate with changes in frequency, and the scatterers are placed periodically to form a lattice. The spacing between elements is limited to less than a quarter wavelength so that the lattice cannot resonate, but far enough apart such that they do not touch.

In chapter 4, analytical equations that modeled the behavior of a metafilm as an infinite sheet of identical scatterers placed periodically or aperiodically apart were reviewed. The averaging polarizability approximation (APA) equations relate the polarizabilities of the individual elements to the surface susceptibilities, and thence to the measurable quantities (the S-parameters: reflection and transmission coefficients). It is common in the case of modeling metafilms to approximate aperiodic spacing with periodic spacing. Using the APA equations and finite element method software (*HFSS*), it was demonstrated that periodic models are very good approximations for aperiodic models, so long as the elements are all identical. Variations in the spacing of elements, so long as they aren't allowed to touch, only result in a slight overall shift in the S-parameters.

Next, the case of variations in the elements themselves was investigated. The APA equations take this into account by taking the average of the polarizabilities. In chapter 5, a more rigorous set of equations was derived, the interactive polarizability approximation (IPA) model. They are based on the equations derived in chapter 3, but extended to the case of a metafilm. They include coupling terms that take into account frequency coupling between elements.

In chapter 6, results based on the analytical APA and IPA equations, and *HFSS* are compared. For a sheet of identical resonators, the frequency response of the reflection and transmission coefficients exhibits smooth behavior when plotted on a graph. However, when the spacing is periodic and the elements of the metafilm have different resonant frequencies with small or large variations, interactions analogous to those of the approximate odd modes of the dipole pair cause interference that manifests itself as a collection of Fano resonances. The Fano resonances appear in the frequency response of the reflection and transmission coefficients near the individual elements' resonant frequencies. This restricts the range of frequencies in which the Fano resonances will appear, which is referred to as a Fano band. Outside the Fano band the reflection and transmission coefficients have a smooth frequency dependence, like that of a uniform sheet.

Within the Fano band, each dip varies in bandwidth and depth. The bandwidth will depend on how strongly the elements couple with each other. Like the cluster pair, strong coupling results in very narrow dips while weak coupling results in wide dips. Therefore, for a physically realizable metafilm with tight tolerances, the Fano resonances will be sharp. During the measurement process (and for that matter in simulations as well), a fine sampling (or frequency increment) will be required to get an accurate measurement of these phenomena. The depth of a dip is dependent upon the material loss of the elements as well as the medium they are placed in. Very lossy materials will show few or no Fano resonances, and the even mode resonances will be heavily damped as well.

The APA showed good agreement with the IPA and *HFSS* equations for weak frequency coupling. When the coupling increases the APA becomes less accurate. For strong coupling, the accuracy is poor. The IPA equations show very good agreement with *HFSS* for weak to strong coupling.

The examples used in chapter 6 are for the checkerboard case, in which there are two scatterers that alternate in the sheet forming a checkerboard pattern. The other example has four variations in a 2x2 unit cell that is repeated indefinitely to form the infinite sheet. To extend this work, larger unit cells could be investigated. A study could be preformed to determine how large the unit cell needs to become to model an infinitely random sheet. Another way to extend this work would be to consider unit cells that are hexagonally shaped.

The reflection and transmission coefficients were investigated for normally incident plane waves only. In future work, oblique incidence should be examined. It would be very interesting to find out what happens to the Brewster angle when Fano resonances occur. Another future work opportunity is to investigate what happens when the the elements of the metafilm are anisotropic. How does this effect the Fano resonances?

Lastly, in chapter 7 measurements were preformed for a metafilm comprised of a 4 x 8 array of dielectric cubes. The metafilm was placed in a waveguide in such a manner that the metafilm becomes a unit cell as a result of image theory. Therefore there are 8 different resonant frequencies in the infinite sheet which is formed in this way. The experimental measurements carried out confirmed the existence of Fano resonances for a metafilm.

Further measurements could be performed in future work. For instance, a wider range of frequency could be investigated. Only 5 metafilms were measured in this thesis. A larger number of metafilms measured would give a more accurate picture of the upper and lower frequency limits of the Fano band. Other scatterer shapes in the metafilm could be pursued such as the (more complicated to manufacture) dielectric sphere, anisotropic shapes, etc. A very accurate free space measurement system could be used for a large array. This would allow more freedom choice of the resonator, size of the array, spacing, etc.

This thesis demonstrates that Fano resonances result from variations in the resonance parameters. There are other single layer periodic media, where the spacing is allowed to be larger than that of a metafilm, on the order of half a wavelength or larger. In this case, one additional resonant parameter (than that of a metafilm) is the lattice spacing. The publication [50], compares a periodic and aperiodic spacing. At frequencies where the lattice spacing is on the order of half a wavelength, the authors show resonances for the aperiodic case versus a smooth line for the periodic case. This thesis demonstrates that those resonances are Fano resonances that result from variations the resonant parameter, lattice spacing.

This thesis demonstrated the existence of Fano resonances by measurements, how to model them accurately, and the theory of why they appear. Finally, Fano resonances are demonstrated to be an inherent part of realistic metafilm behavior. Designers can try to work outside the Fano band or take advantage of their highly sensitive properties and work within the Fano band. Either way, the Fano band must be considered.

Fano bands can be a problem if a designer was hoping to design a filter to operate within the Fano band range, wherein rapid high and low variations in S-parameters could result in overall system failures. On the other hand, very sensitive rapid variations could be very handy when designing a highly sensitive sensor that is highly sensitive to changes in its environment.

Bibliography

[1] ANSYS Broadband adaptive meshing application brief. `https://www.ansys.com/-/media/ansys/corporate/resourcelibrary/application-brief/ab-ansys-hfss-adaptive-broadband-meshing.pdf`.

[2] Sidi Avram. Practical extrapolation methods: Theory and applications (Cambridge Monographs on Applied and Computational Mathematics), volume 1. Press Syndicate of the University of Cambridge, New York, New York, 2003.

[3] Mohamed Hicham Belyamoun, Olivier Dubrunfaut, and Said Zouhdi. Dynamic homogenization of split-ring metamaterials by floquet–bloch decomposition. Applied Physcis A, 109(4):1043–1051, 2012.

[4] J Van Bladel. The excitation of dielectric resonators of very high permittivity. IEEE Transactions on Microwave Theory and Techniques, 23(2):208–217, 1975.

[5] J. Van Bladel. On the resonances of a dielectric resonator of very high permittivity. IEEE Transactions on Microwave Theory and Techniques, 23(2):199–208, 1975.

[6] J. Van Bladel. Weakly coupled dielectric resonators. IEEE Transactions on Microwave Theory and Techniques, 30(11):1907–1914, 1982.

[7] Caiazzo, Maci, and Engheta. A metamaterial surface for compact cavity resonators. Antennas and Wireless Propagation Letters, IEEE, 3:261–264, 2004.

[8] Tuck C. Choy. Effective medium theory: principles and applications. Oxford University Press Inc., New York, 1999.

[9] R. Collin. Rayleigh scattering and power conservation. IEEE Transactions on Antennas and Propagation, 29(5):795–798, 1981.

[10] Luca Dell'Anna and Michele Merano. Clausius-mossotti lorentz-lorenz relations and retardation effects for two-dimensional crystal. Physical review A, 93(053808), 2016.

[11] N. Engheta. An idea for thin subwavelength cavity resonators using metamaterials with negative permittivity and permeability. Antennas and Wireless Propagation Letters, IEEE, 1:10–13, 2002.

[12] U. Fano. Effects of configuration interaction on intensities and phase shifts. Physical Review, 124:1866–1878, 1961.

[13] O. N. Gadomskii and Yu. Yu. Voronov. Near-field effect in optics of small objects composed of dipole atoms. Journal of Applied Spectroscopy, 66(6):882–889, 1999.

[14] Raimond Grimberg. Electromagnetic metamaterials. Material Science and Engineering B, 178:1285–1295, 2013.

[15] Thomas. Hand, Steven A. Cummer, and Nader Engheta. The measured electric field spatial distribution within a metamaterial subwavelength cavity resonator. Transactions on Antennas and Propagation, IEEE, 55(6):1781–1788, 2007.

[16] R. A. Hill and B. A. Munk. The effect of perturbating a frequency-selective surface and its relation to the design of a dual-band surface. IEEE Transactions on Antennas and Propagation, 44(3):368–374, 1996.

[17] R. A. Hill and B. A. Munk. The effect of perturbating a frequency-selective surface and its relation to the design of a dual-band surface. IEEE Transactions on Antennas and Propagation, 44(3):368 – 374, 1996.

[18] C. L. Holloway, E. F. Kuester, J. Baker-Jarvis, and P. Kabos. A double negative (dng) composite medium composed of magnetodielectric spherical particles embedded in a matrix. Antennas and Propagation, IEEE Transactions on, 51(10):2596–2603, 2003.

[19] C. L. Holloway, D. C. Love, E. F. Kuester, A. Salandrino, and N. Engheta. Sub-wavelength resonators: on the use of metafilms to overcome the lambda/2 size limit. IET Microwaves, Antennas & Propagation, 2(2):120–129, 2008.

[20] C. L. Holloway, M. A. Mohamed, E. F. Kuester, and A.S Dienstfrey. Reflection and transmission properties of a metafilm: with an application to a controllable surface composed of resonant particles. IEEE Transactions on Electromagnetic Compatibility, 47(4):853–865, 2005.

[21] Christopher L. Holloway, Andrew Dienstfrey, Edward F. Kuester, John F. O'Hara, Abul K. Azad, and Antoinette J. Taylor. A discussion on the interpretation and characterization of metafilms/metasurfaces: the two-dimensional equivalent of metamaterials. Metamaterials, 3(2):100–112, 2009.

[22] Christopher L. Holloway, Edward F. Kuester, Joshua A. Gordon, John O'Hara, Jim Booth, and David R. Smith. An overview of the theory and applications of metasurfaces: The two-dimensional equivalents of metamaterials. IEEE Antennas and Propagation Magazine, 54(2):10–35, 2012.

[23] Kwok-Kueng Fung Jon Applequist, James R. Carl. An atom dipole interaction model for molecular polarizability. application to polyatomic molecules and determination of atom polarizabilities. Journal of American Chemical Society, 94(9):2952–2933, 1972.

[24] Alexander B. Khanikaev, Chihhui Wu, and Gennady Shvets. Fano-resonant metamaterials and their applicaitons. Nanophotonics, 2(4):247–264, 2013.

[25] A.P.S. Khanna. Dielectric resonator oscillators theory and state-of-the-art. Proceedings of the 21st Annual Precise Time and Time Interval Systems and Applicaitons Meeting, pages 371–384, 1989.

[26] Sung Kim. Effective properties extraction of metamaterial taking boundary effects into account. PhD thesis, University of Colorado, Boulder Colorado, 2009.

[27] E. F. Kuester and C. L. Holloway. A low-frequency model for wedge or pyramid absorber arrays-i: theory. IEEE Transactions on Electromagnetic Compatbility, 36(4):300–306, 1994.

[28] E. F. Kuester, M. A. Mohamed, M. Piket-May, and C. L. Holloway. Averaged transition conditions for electromagnetic fields at a metafilm. IEEE Transactions on Antennas and Propagation, 51(10):2641–2651, 2003.

[29] Silberstein L. Molecular refractivity and atomic interaction. Philos. Mag., 33:92–128, 1917.

[30] Silberstein L. Molecular refractivity and atomic interaction. Philos. Mag., 33:521–533, 1917.

[31] Silberstein L. Molecular refractivity and atomic interaction. Philos. Mag., 33:215–222, 1917.

[32] Horace Lamb. On group-velocity. Proceedings of London Math Society, 1:473–479, 1904.

[33] Mathieu Langlais, Jean-Paul Hugonin, Mondher Besbes, and Philippe Ben-Abdallah. Cooperative electromagnetic interactions between nanoparticles for solar energy harvesting. Optics Express, 22(S3):A577–A588, 2014.

[34] M. Lapine and S. Tretyakov. Contemporary notes on metamaterials. IET Microwaves, Antennas & Propagation, 1(1):3–11, 2007.

[35] Glasser Larry. Personal communication. September 17, 2016.

[36] Khai Q. Le, Andrea Alù, and Jing Bai. Multiple fano interferences in a plasmonic metamolecule consisting of asymmetric metallic nanodimers. Journal of Applied Physics, 117(2):023118, 2015.

[37] L. Lewin. The electrical constants of a material loaded with spherical particles. Proceedings Institute of Electrical Engineers - Part III: Radio and Communication Engineering, 94(27):65–68, 1947.

[38] Mikhail F. Limonov, Mikhail V. Rybin, Alexander N. Poddubny, and Yuri S. Kivshar. Fano resonances in photonics. Nature Photonics, 11:543–554, 2017.

[39] Stanislav Maslovski and S. A. Tretyakov. Full-wave interaction field in two-dimensional arrays of dipole scatterers. AEU International Journal of Electronics, 53:135–139, 1999.

[40] Andrey E. Miroshnichenko, Sergej Flach, and Yuri S. Kivshar. Fano resonances in nanoscale structures. Rev. Mod. Phys., 82(3):2257–2298, 2010.

[41] B. A. Munk. Frequency selective surfaces: theory and design. A Wiley-Interscience publication. Wiley, 2000.

[42] First Technology Products Page. `http://www1.isti.cnr.it/~salerno/Microonde/dielectric_resonators`.

[43] Skyworks Products Page. `http://www.skyworksinc.com/Products/1147/Dielectric_Resonators`.

[44] TCI Ceramic Inc Products Page. `https://www.magneticsgroup.com/m_di_res`.

[45] J. B. Pendry. Negative refraction make a perfect lens. Physics Review Letters, 85:3966–3969, 2000.

[46] H. C. Pocklington. Growth of a wave-group when the group velocity is negative. Nature, 74:607–608, 1905.

[47] A. Schuster. An introduction to the theory of optics. London, 1:313–318, 1904.

[48] Thomas. B. A. Senior and John Leonidas Volakis. Approximate boundary conditions in electromagnetics. The Institution of Electrical Engineers, London, United Kingdom, 1995.

[49] E. Shamonina and L. Solymar. Metamaterials: How the subject started. Metamaterials, 1(1):12–18, 2007.

[50] Nishhant Shankhwar, Ravindra Kumar Sinha, Yogita Kalra, Sergey Makarov, Alexander Krasnok, and Pavel Belov. High-quality laser cavity based on all-dielectric metasurfaces. Photonics and Nanostructures Fundamentals and Applications, 24:18–23, 2017.

[51] A. Sihvola. Metamaterials in electromagnetics. Metamaterials, 1(1):2–11, 2007.

[52] Ari Sihvola. Metamaterials: a personal view. Radio Engineering, 18(2):90–94, 2009.

[53] Ari Sihvola, Igor Semchenko, and Sergei Khakhomov. View on the history of electromagnetics of metamaterials: evolution of the congress series of complex media. Photonics and Nanostructures Fundamentals and Applications, 12(4):279–283, 2014.

[54] Daniel Sjöberg, Christian Engström, Gerhard Kristensson, David J. N. Wall, and Niklas Wellander. A floquet–bloch decomposition of maxwell's equations applied to homogenization. Multiscale Modeling and Simulation, 4(1):149–171, 2005.

[55] Julius Adams Stratton. Electromagnetic theory. McGraw-Hill Book Company, Inc., 1941.

[56] S. A. Tretyakov, F. Mariotte, C. R. Simovski, T. G. Kharina, and J.-P. Helit. Analytical antenna model for chiral scatterers: comparison with numerical and experimental data. IEEE Transactions on Antennas and Propagation, 44(7):1006–1014, 1996.

[57] Benjamin Vial and Yang Hao. A coupling model for quasi-normal modes of photonic resonators. Journal of Optics, 18(115004), 2016.